Contributions expérimentales et théoriques aux techniques de contraste de phase pour l'imagerie médicale par rayons X

Paul Claude Diemoz

UNIVERSITÉ DE GRENOBLE

THÈSE

Pour obtenir le grade de

DOCTEUR DE L'UNIVERSITÉ DE GRENOBLE

Spécialité : **Physique pour les sciences du vivant**

Arrêté ministériel : 7 août 2006

Présentée par

Paul Claude DIEMOZ

Thèse dirigée par **José BARUCHEL** et **Paola COAN**
codirigée par **Alberto BRAVIN**

préparée au sein du **European Synchrotron Radiation Facility (ESRF)**
dans **l'École Doctorale de Physique**

en cotutelle avec la **Ludwig-Maximilians Universität Munich (Allemagne)**

Contributions expérimentales et théoriques aux techniques de contraste de phase pour l'imagerie médicale par rayons X

Thèse soutenue publiquement le **28 février 2011**,
devant le jury composé de :

Prof. Serge PEREZ
ESRF Grenoble, Président du jury
Prof. Timur E. GUREYEV
CSIRO Materials Science and Engineering (Australie), Rapporteur
Prof. Pekka SUORTTI
University of Helsinki (Finlande), Rapporteur
Dr. José BARUCHEL
ESRF Grenoble, Directeur de Thèse Université de Grenoble
PROF. Paola COAN
LMU University Munich (Allemagne), Directeur de Thèse LMU University Munich
Dr. Alberto BRAVIN
ESRF Grenoble, Co-directeur de Thèse
Prof. Ralf H. MENK
Elettra Synchrotron Light Source (Italie), Examinateur
Prof. Alessandro OLIVO
University College London (Royaume-Uni), Examinateur

Acknowledgements

I would like here to thank all the people who have helped me during these long three years and contributed, in a way or in the other, to the successful completion of this Thesis.

First of all, I wish to express my gratitude to Alberto Bravin for introducing me to the world of synchrotron and phase contrast, for his precious teachings during beamtimes and for always being open to new ideas, and Paola Coan for her guidance, the daily discussions and unflagging help. Thanks Paola and Alberto for having taught me the difficult but rewarding job of the researcher! I would also like to acknowledge José Baruchel, for his kind supervision and encouragement.

I am grateful to Timur Gureyev and Pekka Suortti, who accepted to review this Thesis and gave me valuable comments and suggestions on how to improve the manuscript. I would also like to thank Serge Perez, who acted as President of the Thesis panel, and the examiners Alessandro Olivo and Ralph Menk.

I am particularly indebted to the ESRF and all the people of ID17 for providing me with an excellent work environment and constantly helping me with my work. A big thanks to Christian Nemoz for the informatics support, for his good spirit and the ever-present Pastis, and to Herwig Requardt and Thierry Brochard for their helpfulness and the technical assistance during experiments. I also wish to thank Géraldine Le duc and Dominique Dallery for having taken care of our animals. Merci aussi à mon nouveau collègue Emmanuel Brun pour avoir corrigé les parties en français de cette Thèse, et à mes collègues de bureau, dans l'ordre chronologique Anka, Sukhena, Charlène et Fanny, pour m'avoir si gentiment supporté!

I want to extend my thanks to the ESRF scientific software group, and in particular to Claudio Ferrero, for his continuous helpfulness, his enthusiasm and the many suggestions on how to perform the parallel calculations on the ESRF cluster.

I am grateful to the Institute of Forensic Medicine of the Ludwig-Maximilians University (Munich, Germany) for providing the biological samples that I imaged in this work.

This Thesis would not have been possible without the financial support from the German Cluster of Excellence "Munich Centre for Advanced Photonics", which is gratefully acknowledged.

I am very happy now to thank the people that helped me indirectly in this Thesis by supporting and encouraging me during these three years. A special thanks to my friend Francesco, with whom I shared many good moments, the jokes, the music, the food and, not last, the difficult months of the Thesis redaction (Francesco, grazie per la tua "agreabile" compagnia!). I want to thank also my friend Carlo, for the continuous

support during the good and bad moments and all the wonderful days of skiing we shared together!

I am glad I had the occasion to meet some very special people here in Grenoble, my friends Amalia, Angelo, Carlo M., Davide, Erminia, Imma, Irene, Loredana, Maria, Neda, Raffa, Seb, Sheeba, Silvia, Valentina. I will remember all the nice moments and outings together in Grenoble, the mountains, the dinners, the laughs… And also all the lunches at the canteen and the discussions at the cafeteria, a ray of sunshine in my working day!

Thanks also to Carmen and Elena, whom I met only for a short period. I enjoyed your company, your good mood and spirit. Espero que nos podamos encontrar pronto!

Infine un ringraziamento speciale alla mia famiglia, che nonostante la lontananza mi ha sempre sostenuto nelle mie scelte e costantemente incoraggiato. Ringrazio di cuore in particolare i miei genitori, i miei nonni e i miei fratelli Henri e André.

Grenoble, March 2011

Index

Introduction

X-ray imaging techniques are an indispensable diagnostic tool, which has found widespread use in the clinical practice. Since the first use of X-rays for medical imaging dating back to more than a century ago, these techniques have been developed and optimized. Efforts have particularly focused on technical developments concerning the radiation sources (X-ray tubes) and the detectors. An important step forward was also represented by the introduction, in the 1970's, of computed tomography, which enabled the generation of three-dimensional images of the human tissues. However, the main physical principles upon which these techniques are based have remained the same: the image contrast is generated by variations of the X-ray absorption that arise from density differences and from changes in thickness and composition of the sample. The contrast that can be achieved based on simple differential absorption is in some cases intrinsically limited. This occurs for instance when soft (low atomic number) biological tissues are imaged, since the differences in attenuation are very tiny.

Two emblematic examples are represented by the imaging of articular cartilage and breast tissues, for which the contrast obtained in conventional absorption radiography is limited. A good depiction of these tissues would be very useful for the diagnosis of diseases like osteoarthritis and breast cancers. The detection of early stages of osteoarthritis would enable the realization of longitudinal studies aimed at investigating the progress of the disease and at testing its response to pharmacological treatments; the early detection of breast cancers would dramatically improve the prognosis for the women affected by this disease. An introduction to these subjects is presented in the **chapter 1** of the Thesis.

With the aim of overcoming the present limitations of the clinical X-ray diagnostics, in the last 20 years a number of phase-contrast imaging techniques have been developed. Unlike conventional X-ray methods, which measure the amplitude of the wave exiting the sample, determined by the attenuation properties of the tissues, these techniques derive contrast also from the modulation of the phase produced by the sample. The interest for phase sensitive techniques in medical applications resides in the fact that the X-ray phase shift can be significant even for small details characterized by weak or absent amplitude modulation; as a result, the achievable contrast for soft biological tissues can be greatly increased.

Various techniques have been developed to exploit the phase contrast in the X-ray regime. In this Thesis, the work has been focused on three among the most promising phase-sensitive imaging techniques, namely the propagation-based imaging (PBI), the analyzer-based imaging (ABI) and the grating interferometry (GIFM). The first method, PBI, simply uses free-space propagation between the sample and the detector to convert, through Fresnel diffraction, the beam phase modulations into measurable intensity variations on the detector. ABI employs a perfect crystal placed between the sample and the detector to analyze the radiation refracted inside the

sample, while in GIFM the image contrast is obtained by exploiting the Talbot effect through the use of two diffraction gratings set at an appropriate mutual distance before the detector. The theoretical description of these techniques, as well as the needed experimental setup and their requirements in terms of the spatial and temporal coherence of the radiation illuminating the object, are presented in **chapters 2 and 3.**

The phase-contrast X-ray imaging techniques have been extensively studied in recent years and it has been demonstrated that they are able to provide much improved contrast with respect to conventional absorption imaging. **The aim of this Thesis** is to **contribute**, both theoretically and experimentally, to a **deeper understanding of these techniques** and to study their **potential and** the **best practical implementation for medical imaging applications.**

An important subject considered in this Thesis is the use of mathematical algorithms for extraction of quantitative information from the images of a given sample. In particular, in the ABI technique several extraction algorithms have been proposed and applied in the literature to separate and quantify the absorption, refraction and ultrasmall-angle scattering (USAXS) contributions to the image contrast. These different physical effects, in fact, mix up in the acquired AB images, making the image interpretation sometimes difficult, especially in the case of complex object geometries. An efficient separation of these contributions to the contrast would highlight the different properties of the object and therefore facilitate the image interpretation. Furthermore, the extraction of accurate quantitative information may be very useful for precisely characterizing the sample.

Despite the large number of published works on this subject, however, a comprehensive theoretical and experimental comparison of these mathematical methods was missing in the literature. In particular, their ability to provide quantitatively accurate results in different experimental conditions, which may be important for some biomedical applications, had not been systematically assessed. In this Thesis, five among the most known and used algorithms based on the geometrical optics approximation are considered: diffraction-enhanced imaging (DEI), extended diffraction-enhanced imaging (E-DEI), generalized diffraction-enhanced imaging (G-DEI), multiple image radiography (MIR) and Gaussian curve fitting (GCF). The validity conditions upon which these algorithms are based and the types of images that can be calculated by each of them are discussed. A quantitative comparison of the results obtained with these different methods with those predicted by theory is performed, based on the analysis of experimental images of phantoms with known shape and composition and providing different amounts of absorption, refraction and scattering. These algorithms are also applied to biological samples and the resulting images are compared and discussed. This analysis is reported in the **chapters 4** and **5**, respectively in the case of planar and tomographic imaging.

Grating interferometry (GIFM) is a recently developed phase-contrast technique which is very promising for biomedical applications. However, only the so-called phase stepping method, which is able to separate the sample absorption, refraction and scattering, had been considered in published works for the processing of the acquired images. This method requires a scanning of the gratings and the acquisition of several images, leading to long integral acquisition times and considerable dose delivered to the sample, especially when the tomographic modality is considered. This represents an important limitation of the technique in particular for in-vivo applications, since in this case the imaged tissues cannot be exposed to a too high radiation dose and additionally they may move causing artefacts in the image. It is therefore necessary to investigate alternative imaging procedures that could allow reducing the acquisition times and the dose to the sample.

In the **chapter 6** of the Thesis, a new method for CT acquisition and reconstruction is proposed, theoretically examined and experimentally tested on phantoms and on a biological sample. This method does not allow separating the different physical contributions to the contrast but has important advantages: the diffraction gratings can be kept fixed during the object scan, thus simplifying the imaging procedure, and the acquisition time can be considerably reduced. The proposed method may prove very advantageous for biomedical applications and in particular for in-vivo imaging, where a reduced acquisition time will result in reduced motion artefacts.

The PBI, ABI and GIFM techniques have been extensively investigated and applied in the literature. However, to our knowledge no publication exists on a comparison of the signal obtained in these three techniques. PBI, ABI and GIFM differ not only for the needed experimental setups and for the peculiar coherence requirements, but also for the nature and amplitude of the contrast produced in the images. **Chapter 7** of this Thesis is dedicated to this subject, which is extremely important for determining the advantages and disadvantages of each technique and their potential for different biomedical applications. Analytical formulas for the signal-to-noise ratio and for the figure of merit for both absorption and refraction signals are theoretically derived for these three techniques. An experimental verification is then performed by imaging plastics phantoms of known shape and composition. The obtained images are analyzed and selected extraction algorithms are applied to them. The results are compared: the differences and the similarities between these three phase-contrast techniques are highlighted and their advantages and drawbacks for different kinds of applications are discussed.

This Thesis was performed in the framework of the Cluster of Excellence “Munich Center for Advanced Photonics” (MAP) (Munich, Germany). One of the main aims of this project is to build a compact machine capable of delivering brilliant X-ray beams comparable to classical X-FELs (X-ray free-electron lasers), but reaching higher X-ray energies, which are important for medical diagnostics. The scope of the investigations carried out at the European Synchrotron Radiation Facility (ESRF) within the MAP project is the analysis and development of the phase-contrast

techniques, by using synchrotron radiation as the gold standard, in view of their application to this newly-developed source.

In summary, the Thesis is organized as follows:

Chapter 1. Brief description of the cartilage and breast anatomy and of the modifications originating in these tissues in diseases like osteoarthritis and breast cancer. Overview of the conventional diagnostic techniques to visualize the cartilage and breast tissues.

Chapter 2. Introduction to the general principles of phase-contrast imaging and theoretical description of the phase-contrast techniques considered in this Thesis: propagation-based imaging (PBI), analyzer-based imaging (ABI) and grating interferometry (GIFM). Requirements of the techniques in terms of spatial and temporal coherence of the radiation and achievable spatial resolution.

Chapter 3. Brief introduction to synchrotron radiation and to its particular features with respect to the X-rays emitted by other kinds of sources. Description of the ID17, ID19 and BM5 beamlines at the European Synchrotron Radiation Facility (ESRF), where the experimental investigations were performed, and of the setups used for the different techniques. Presentation of the methods for image acquisition and of general correction and normalization procedures applied to the recorded images.

Chapter 4. Theoretical and experimental comparison of five algorithms for the extraction of quantitative information in planar ABI: diffraction-enhanced imaging (DEI), extended diffraction-enhanced imaging (E-DEI), generalized diffraction-enhanced imaging (G-DEI), multiple-image radiography (MIR) and Gaussian curve fitting (GCF). Discussion of their different validity conditions and comparison of the results obtained on plastics phantoms and on a human bone-cartilage sample.

Chapter 5. Comparison of the previous ABI extraction algorithms in the case of computed tomography, by using phantoms of known geometry and composition and a human bone-cartilage sample. Demonstration of an alternative semi-quantitative method for CT reconstruction and application to human bone-cartilage and breast samples.

Chapter 6. Investigation of a new semi-quantitative method for CT acquisition and reconstruction in GIFM, alternative to the usual phase stepping method. Theoretical demonstration and experimental verification on phantoms and on a human bone-cartilage sample.

Chapter 7. Theoretical and experimental comparison of propagation-based imaging (PBI), analyzer-based imaging (ABI) and grating interferometry (GIFM). Theoretical derivation of expressions for the signal-to-noise ratio (SNR) and figure of merit (FOM) in the various techniques for the absorption and phase (refraction) signals. Analysis of experimental images of plastics phantoms recorded with the three techniques for various acquisition parameters, and application of algorithms for extraction of quantitative information.

Introduction en français

Les techniques d'imagerie par rayons X représentent désormais un outil de diagnostic indispensable, qui a trouvé de nombreuses applications dans la pratique clinique. Depuis la première utilisation des rayons X pour l'imagerie médicale il y a plus d'un siecle, ces techniques ont été développées et optimisées. Les efforts se sont principalement concentrés sur les développements techniques autour des sources de radiation (tubes à rayons X) et des détecteurs. Un important pas en avant a aussi été fait dans les années '70 par l'introduction de la tomographie, qui a permis de produire des images tridimensionnelles de tissus humains. Cependant, les principes physiques sur lesquels ces techniques sont basées sont restés les mêmes : le contraste des images est généré par les variations d'absorption des rayons X qui résultent des différences en intensité et des changements dans l'épaisseur et dans la composition de l'échantillon. Le contraste qui peut être atteint en se basant sur la simple absorption est dans quelques cas limité, ce qui se produit par exemple quand les tissus mous biologiques (charactérisés par de bas numéros atomiques) sont imagés, car les différences en atténuation sont très faibles.

Deux exemples emblématiques sont représentés par l'imagerie du cartilage articulaire et des tissus du sein, pour lesquels le contraste dans la radiographie conventionnelle par absortion est limité. Une visualisation claire de ces tissus pourrait être très utile pour le diagnostic de pathologies comme l'arthrose et les cancers du sein. Une détection précoce de l'arthrose permettrait la réalisation d'études longitudinales ayant pour but d'étudier le progrès de la maladie et tester sa réponse aux traitements pharmacologiques. Une détection précoce des cancers du sein améliorerait dramatiquement le pronostic pour les femmes atteintes par cette maladie. Une introduction sur ces sujets est présentée dans le **chapitre 1** de ce manuscrit.

Avec le but de surmonter les limitations actuelles du diagnostic clinique par rayons X, dans les vingt dernières années un certain nombre de techniques d'imagerie par contraste de phase ont été développées. Contrairement aux méthodes conventionnelles par rayons X, qui mesurent l'amplitude de l'onde sortante de l'échantillon (déterminée par les propriétés d'atténuation des tissus), ces techniques donnent aussi le contraste de la modulation de la phase produite par l'échantillon.

L'intérêt pour ces techniques sensibles au déphasage dans les applications médicales réside dans le fait que le changement de phase des rayons X peut être important même pour des détails charactérisés par une modulation d'amplitude faible ou absente. Par conséquent, le contraste obtenable pour les tissus mous biologiques peut être considérablement augmenté.

Différentes techniques qui exploitent le contraste de phase pour les rayons X ont été développées. Durant ce travail, nous nous sommes concentrés sur trois techniques parmi les plus prometteuses, à savoir la propagation-based imaging (PBI), la analyzer-based imaging (ABI) et la grating interferometry (GIFM). La premiere méthode, PBI, utilise simplement la propagation libre

entre l'échantillon et le détecteur pour convertir les modulations dans la phase du faisceau en variations d'intensité mesurables sur le détecteur (diffraction de Fresnel). ABI utilise un crystal parfait placé entre l'échantillon et le détecteur pour analyser la radiation réfractée dans l'échantillon. Enfin, avec la GIFM le contraste est obtenu en exploitant l'effet de Talbot grâce à l'utilisation de deux réseaux de diffraction placés à une distance mutuelle approprié devant le détecteur. La description théorique de ces techniques, le montage expérimental ainsi que les conditions nécessaires en termes de la coherence spatiale et temporale de la radiation au niveau de l'échantillon, sont présentés dans les **chapitres 2** et **3**.

Les techniques de contraste de phase par rayons X ont été abondamment étudiées dans les dernières années et on a démontré qu'elles sont capables de fournir un contraste beaucoup plus grand par rapport à l'imagerie conventionnelle par absorption. Le but de cette Thèse est de contribuer, de façon théorique et expérimentale, à une compréhension plus profonde de ces techniques et d'étudier leur potentiel et la meilleure implémentation pratique pour les applications en imagerie médicale.

Une part importante de cette Thèse est consacrée à l'utilisation d'algorithmes mathématiques pour l'extraction d'informations quantitatives des images acquises pour un donné échantillon. En particulier, dans la technique ABI de nombreux algorithmes d'extraction ont été proposés et appliqués dans la litérature pour séparer et quantifier les effets d'absorption, de réfraction et de diffusion à très petits angles (USAXS) qui contribuent au contraste de l'image. Ces différents effets physiques, en effet, se mélangent dans les images ABI acquises, ce qui rend l'interprétation des images parfois difficile, en particulier dans le cas d'objets présentant des géométries complexes. Une séparation efficace de chaque contribution au contraste pourrait mettre en évidence les différentes propriétés de l'objet et donc faciliter l'interprétation de l'image. De plus, l'extraction d'informations quantitatives précises pourrait être très utile pour une caractérisation détaillée de l'échantillon.

Cependant, malgré le grand nombre de travaux publiés sur ce sujet, une comparaison complète, théorique et expérimentale, de ces méthodes mathématiques manquait dans la littérature. En particulier, leur abilité à fournir des résultats quantitativement corrects dans des conditions expérimentales différentes, pourtant important pour certaines applications biomédicales, n'avait pas été systématiquement évaluée. Dans cette Thèse, cinq parmi les plus connus et utilisés des algorithmes basés sur l'approximation de l'optique géométrique ont été considérés : diffraction-enhanced imaging (DEI), extended diffraction-enhanced imaging (E-DEI), generalized diffraction-enhanced imaging (G-DEI), multiple image radiography (MIR) et Gaussian curve fitting (GCF). Les conditions de validité sur lesquelles ces algorithmes sont basés et le type d'images qu'ils peuvent permettre de calculer sont examinés. Une comparaison quantitative des résultats obtenus par chacune des différentes méthodes avec ceux prévus par la théorie est réalisée. Cette étude se base sur l'analyse d'images expérimentales de fantômes avec une géométrie et une composition

connues donnant ainsi lieu à des quantités différentes d'absorption, de réfraction et de diffusion. Ces algorithmes sont aussi appliqués à des échantillons biologiques, les images obtenues sont comparées et discutées. Cette analyse est présentée dans les **chapitres 4** et **5**, respectivement dans les case de l'imagerie planaire et tomographique.

La grating interferometry (GIFM) est une technique de contraste de phase récemment développée, très prometteuse pour les applications médicales. Cependant, seulement la méthode du phase stepping, capable de séparer l'absorption, la réfraction et la diffusion introduites par l'échantillon, a été considéré dans la littérature pour le traitement des images acquises. Cette méthode nécessite un scan des réseaux de diffraction et l'acquisition de plusieurs images. Tout ceci conduit à de longs temps d'acquisition et à une dose considérable délivrée, surtout quand la modalité tomographique est utilisée. Cela représente une limitation importante de cette technique en particulier pour les applications in-vivo. En effet dans ce cas les tissus imagés ne peuvent pas être exposés à un taux de radiations trop grand, et peuvent de plus se déplacer causant des artéfacts. Il est donc nécessaire de rechercher des procédures d'imagerie alternatives qui pourraient réduire les temps d'acquisition et la dose à l'échantillon.

Dans le **chapitre 6** de cette Thèse, une nouvelle méthode pour l'acquisition et la reconstruction tomographique est proposée, examinée théoriquement et évaluée expérimentalement sur des fantômes et sur un échantillon biologique. Cette méthode ne permet pas de séparer les différentes contributions physiques au contraste mais présente des avantages importants : les réseaux de diffraction peuvent être maintenus dans une position fixe pendant le scan de l'object, ce qui simplifie la procédure d'acquisition, et le temps d'acquisition peut être considérablement réduit. La méthode proposée peut s'avérer très avantageuse pour les applications biomédicales et en particulier pour l'imagerie in-vivo, où un temps d'acquisition plus court peut permettre de réduire les artéfacts de mouvement.

Les techniques PBI, ABI et GIFM ont été abondamment étudiées et appliquées dans la littérature. Cependant, à notre connaissance il n'existe pas de publications ayant pour objet la comparaison du signal dans ces trois techniques. PBI, ABI et GIFM diffèrent non seulement dans les montages expérimentaux et pour le niveau de cohérence spatiale et temporale requis, mais aussi pour l'origine et l'amplitude du contraste produit sur les images. Le **chapitre 7** de cette Thèse est dédié à ce sujet, extrêmement important pour pouvoir déterminer les avantages et les désavantages de chaque technique ainsi que leur potentiel pour de différentes applications biomédicales. Des expressions analytiques du rapport signal-sur-bruit et de la figure de mérite sont dérivées théoriquement pour ces trois techniques. Une vérification expérimentale est effectuée en imageant des fantômes en plastique avec une géometrie et une composition connues. Les images obtenues sont anaysées et les algorithmes d'extraction sélectionnés sont appliqués. Les résultats sont comparés : les différences et ressemblances entre ces trois techniques de contraste de phase sont mises en évidence ainsi que les avantages et désavantages pour différents types d'applications.

Cette Thèse a été effectuée dans le cadre du Cluster of Excellence "Munich Center for Advanced Photonics" (MAP) (Munich, Allemagne). Un des principaux objectifs de ce projet est de construire une source compacte capable de produire des faisceaux de rayons X à haute intensité comparables à ceux fournis par les X-FELs (X-ray free-electron lasers) classiques, mais pour de plus hautes énergies, essentielles pour le diagnostic médical. Le but des investigations effectuées au European Synchrotron Radiation Facility (ESRF) dans le cadre du projet MAP est l'analyse et le développement des techniques de contraste de phase en utilisant la radiation de synchrotron comme référence, en vue de leur application à cette nouvelle source.

En résumant, la Thèse est organisée de la façon suivante :

Chapitre 1. Brève description de l'anatomie du cartilage et du sein et leurs modifications surgissant lors de pathologies comme l'arthrose et les cancers du sein. Aperçu des techniques conventionnelles utilisées pour visualiser les tissus du cartilage et du sein.

Chapitre 2. Introduction des principes généraux de l'imagerie par contraste de phase et déscription théorique des techniques de contraste de phase considérées dans cette Thèse : propagation-based imaging (PBI), analyzer-based imaging (ABI) et grating interferometry (GIFM). Description des conditions requises par ces techniques concernant la cohérence spatiale et temporale de la radiation, et résolution spatiale qui peut être atteinte.

Chapitre 3. Brève introduction sur la radiation de synchrotron et sur ses particularités et singularités quant aux rayons X émis par d'autres types de sources. Description des lignes de lumière ID17, ID19 et BM5 au European Synchrotron Radiation Facility (ESRF), où les investigations expérimentales ont été effectuées, et des montages utilisés pour les différentes techniques. Présentation des méthodes d'acquisition des images et des procédures générales de correction et de normalisation.

Chapitre 4. Comparaison théorique et expérimentale de cinq algorithmes pour l'extraction d'informations quantitatives dans ABI en modalité planaire : diffraction-enhanced imaging (DEI), extended diffraction-enhanced imaging (E-DEI), generalized diffraction-enhanced imaging (G-DEI), multiple-image radiography (MIR) et Gaussian curve fitting (GCF). Discussion sur leurs différentes conditions de validité et comparaison des résultats obtenus sur des fantômes de plastique et sur un échantillon humain d'os et cartilage.

Chapitre 5. Comparaison des précédents algorithmes d'extraction en ABI dans le cas de la tomographie, en utilisant des fantômes avec géométrie et composition connues et un échantillon humain d'os et de cartilage. Démonstration d'une méthode alternative, semi-quantitative, pour la reconstruction tomographique et application à un échantillon d'os et de cartilage et à un échantillon de tissu mammaire.

Chapitre 6. Etude d'une méthode semi-quantitative, alternative à la méthode du phase-stepping, pour l'acquisition et la reconstruction tomographiques dans la technique GIFM.

Démonstration théorique et vérification expérimentale sur des fantômes et sur un échantillon humain d'os et de cartilage.

Chapitre 7. Comparaison théorique et expérimentale des techniques propagation-based imaging (PBI), analyzer-based imaging (ABI) et grating interferometry (GIFM). Dérivation théorique des expressions pour le rapport signal-sur-bruit (SNR) et pour la figure de mérite (FOM) dans les différentes techniques pour les signaux d'absorption et de phase (réfraction). Analyse d'images expérimentales de fantômes de plastique energistrées pour les trois techniques avec différents paramètres d'acquisition. Application d'algorithmes pour l'extraction d'informations quantitatives.

References and links

J. Ferlay, D. M. Parkin, and E. Steliarova-Foucher, "Estimates of cancer incidence and mortality in Europe in 2008", Eur. J. Cancer **46** (4), 765-781 (2010).

R. C. Lawrence, D. T. Felson, C. G. Helmick, L. M. Arnold, H. Choi, R. A. Deyo, S. Gabriel, R. Hirsch, M. C. Hochberg, G. G. Hunder, J. M. Jordan, J. N. Katz, H. M. Kremers, F. Wolfe, and W. Natl Arthritis Data, "Estimates of the prevalence of arthritis and other rheumatic conditions in the United States", Arthritis Rheum. **58** (1), 26-35 (2008).

L. Ries, D. Melbert, and M. Krapcho, *SEER Cancer statistics review, 1975-2004*, National Cancer Institute, Bethesda, MD (2004).

M. Sant, C. Allemani, R. Capocaccia, T. Hakulinen, T. Aareleid, J. W. Coebergh, M. P. Coleman, P. Grosclaude, C. Martinez, J. Bell, J. Youngson, F. Berrino, and E. W. Grp, "Stage at diagnosis is a key explanation of differences in breast cancer survival across Europe", Int. J. Cancer **106** (3), 416-422 (2003).

1

Cartilage and breast tissues imaging

Table of Contents

Abstract: This chapter is dedicated to an introduction on the subjects of osteoarthritis and breast cancer imaging. The basic anatomy of the cartilage and breast tissues will be described. A brief overview of the available imaging techniques that are currently used for the diagnosis of osteoarthritis and breast cancers will then be given, and their limitations discussed.

1.1 Cartilage and osteoarthritis

Osteoarthritis (OA), also known as degenerative joint disease, is the most common type of arthritis, especially among old people. Statistics indicate that OA affects approximately 14% of adults aged 25 and older, and about 33% of those older than 65 (Lawrence et al., 2008).

Osteoarthritis is a joint disease mostly affecting the cartilage, which is the smooth tissue that covers the ends of bones in a joint. Healthy cartilage allows bones to glide over one another, and the tissue also absorbs energy from the impact of physical movements. In OA, the surface layer of cartilage breaks down and is worn down. This tissue degradation determines subchondral bones to rub together, causing pain, swelling, and loss of motion of the joint. As a result, people with OA usually have joint pain and limited movement.

OA presently has no cure: so far, physician treatment strategies focus on treating the disease symptoms with minimal side effects. In very severe cases, the only solution for reducing the pain and helping restoring functions is partial or complete joint replacement surgery.

1.1.1 The joint anatomy and its modifications in osteoarthritis

Most joints (the place where two moving bones come together) are designed to allow smooth movements between the bones and to absorb stress and strain from walking or other repetitive motions.

In figure 1.1, the general structure of a healthy joint and its components are presented and are compared with those of an osteoarthritic one. In a healthy joint (a), the ends of bones are encased in smooth cartilage. A tough connective tissue membrane (the joint capsule) holds the bones and the other joint structures together. The synovium, a thin epithelial cell-based membrane inside the joint capsule, produces the synovial fluid, which serves the purpose of lubricating the joint and keeping the cartilage smooth and healthy. Ligaments, tendons and muscles are needed to keep the bones stable and allow the joint to bend and move. Ligaments and tendons are tough, fibrous cords that connect respectively one bone to another and muscles to bones.

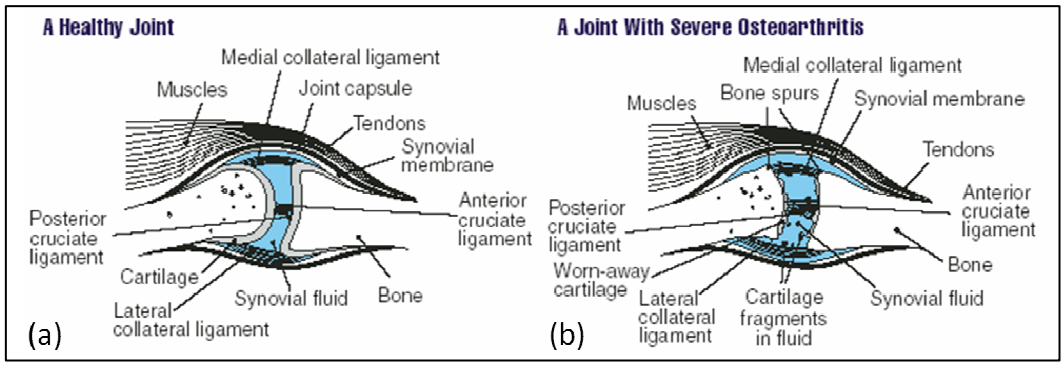

Fig. 1.1. Joint architecture: comparison between (a) a healthy and (b) an osteoarthritic joint.

With OA, the cartilage is worn down (b). Small bone spurs, called osteophytes, grow out from the edge of the bone, and synovial fluid increases. Besides, bits of bone or cartilage may break off and float inside the joint space. Altogether, the joint feels stiff and sore. Usually, OA progresses slowly. Early in the disease, joints may ache after physical work or exercise. OA can occur in many joints, but the main targets are hands, knees, hips, or neck spine.

Articular cartilage

The specific resident cell of the cartilage tissue is the chondrocyte. Typically, each chondrocyte is separated from the neighboring cells by an extracellular hydrated cartilage matrix, which, in absence of vascular elements, is penetrated only by small biomolecules that provide nutrition and also by regulatory biomolecules (i.e. tissue hormones). Chondrocytes are cells possessing different capabilities; besides normal cellular functions, these cells act as autonomous repair and self-defense units, and form the tissue matrix macromolecular framework from three classes of molecules: collagens, proteoglycans, and noncollagenous proteins (glycoproteins). The cartilage matrix is mainly composed by ground substances and by collagen fibers, which give cartilage its elasticity, ability to bear weight and tensile strength.

Throughout life, articular cartilage undergoes internal remodeling as the cells replace matrix macromolecules lost through degradation. Aging decreases the ability of chondrocytes to maintain and restore articular cartilage and thereby increases the risk of its degeneration.

Various horizontal layers with different cell types and molecular composition can be distinguished (fig. 1.2).

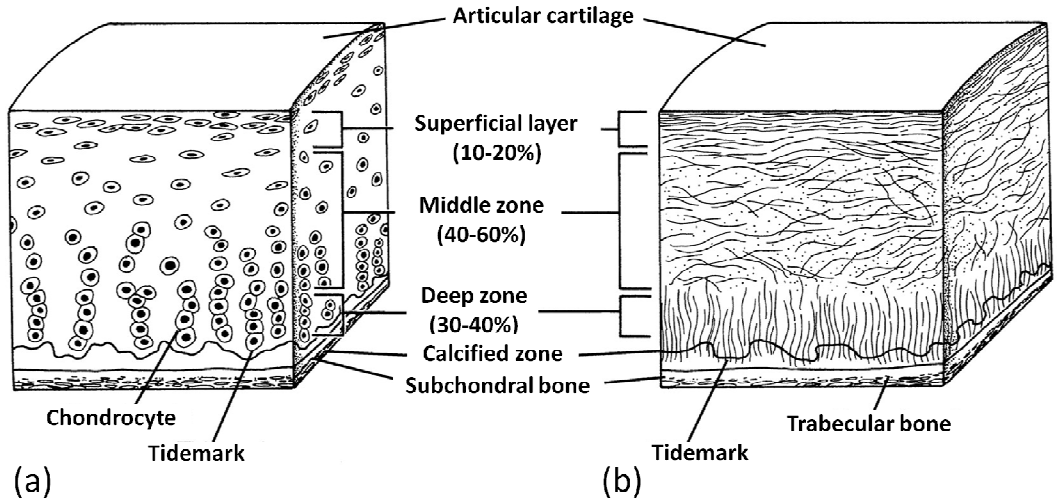

Fig. 1.2. Scheme of healthy intact cartilage: arrangement of (a) the chondrocyte cells and (b) the collagen fibers in the various zones from the cartilage surface to the bone interface.

1. The **superficial (or tangential) zone** consists of one to three layers of flattened chondrocytes. These cells are less than 10% of all the cells in articular cartilage and they produce their own particular subset of extracellular matrix proteins. The chondrocytes in the superficial zone (fig. 1.2(a)) tend to appear as single cells and, together with the collagen fibers (fig. 1.2(b)), they are aligned parallel to the surface. The superficial zone serves as a "basement membrane" equivalent that has the function to separate cartilage from the peripheral tissue and body fluid. Moreover, the superficial cells are very sensitive to irritation and they have capacities similar to those of macrophages.

2. The middle (or transitional) and deep (or radial) zones consist of articular chondrocytes of spherical shape, surrounded by a distinct halo of "territorial" or "pericellular" matrix that has different properties and compositions than the "interterritorial" or "further removed" matrix. These cells are the major providers for the function of the articular cartilage and they represent and control most (over 80%) of the tissue. The chondrocytes of the deeper layers produce all the extracellular matrix components found in the articular cartilage: collagens, proteoglycans, glycoproteins and other substances needed for the tissue turnover.

Depending on the joint and the location within the joint, chondrocytes may exist either as single cells or as "chondrons", which are groups of two or several cells. Chondrons may be defined as functional subcompartments within the cartilage matrix hosting the chondrocytes and without any cellular junction between them. The matrix in which chondrons are embedded is both structurally and functionally different from the interterritorial matrix and it is equivalent to the territorial matrix of single chondrocytes.

In the transitional zone, the chondrocytes and collagen fibers are oriented randomly within the cartilage. In the radial zone, they are oriented perpendicular to the tide mark and 3-5 chondrocytes are closely packed together forming (vertically oriented) the chondrons.

3. The tidemark is a cell-free line of about 10 μm thickness at the border between the uncalcified and calcified cartilage. The tidemark may mark the line of the most recent turnover of the calcified tissue, or a "sink" for metabolic (end) products, since it tends to migrate upward with age.

4. The calcified zone at the subchondral bone interface. The deepest layers of the cartilage tissue are made of chondrocytes situated within a calcified extracellular matrix. These layers form a transitional tissue to the underlying bone whose calcification is sparse with respect to that of the bone tissue. The function of the calcified zone is to prevent the diffusion of nutrients from bone to cartilage.

Effects of OA on the cartilage tissue include: alterations in cartilage contour morphology (surface irregularity, fibrillations and fissures), cartilage thinning, collagen degeneration and increased free-water content.

1.1.2 Limitations of existing techniques for cartilage imaging

Destruction and loss of articular cartilage is one of the key events in osteoarthritic disorders. Detection of very early stages of the tissue degeneration is extremely important for being able to intervene rapidly and effectively. At very advanced OA cases, in fact, when conservative measures fail to control pain and improve joint function, surgery is often the only solution.

The use of a valid and reliable diagnostic tool that is sufficiently sensitive to detect small changes in joints structure and articular cartilage would be therefore of great importance. Such a tool could also prove very useful in understanding the causes of OA and in finding better treatments, by precisely monitoring their effects on the progression of OA.

Unfortunately, tools conventionally used to investigate this disease remain unsatisfactory. For both OA assessment and drug intervention studies, the principal hallmarks are still:

- clinical observation (pain, inflammation, joint function…)
- imaging with clinical conventional techniques, including planar X-ray radiography, Computed Tomography (CT), Magnetic Resonance Imaging (MRI), Ultrasound (US).
- detection of biochemical markers.

Among all, imaging techniques are so far the principal and most widely used tools for OA investigation. Nevertheless, their sensitivity is often insufficient for the detection of early stages of OA and its progression.

The detection of specific biochemical markers, which can be released by the alterations and destruction of the different components of the joint structure (cartilage, synovial tissue and bone) is more and more investigated as a tool for evaluating OA presence and development. The potential for reliable and responsive markers is large. However, further work is still needed to assess how changes measured in some of these biochemical markers of cartilage turnover correlate with OA disease progression.

Hereafter an overview on the use of the main diagnostic imaging modalities for OA, as well as on their limitations, is provided.

- **Conventional X-ray radiography**

Radiography, discovered more than a century ago, is the oldest but also the most used technique for medical imaging. It is based on irradiating the imaged part of the body with an X-ray tube (described in chapter 3) and in recording the transmitted intensity with a 2D detector placed downstream of it. The mechanism that generates the image contrast in this technique is the different absorption encountered by photons traversing the various parts of the sample, which can be due to a different tissue composition, a different tissue density and/or different sample thickness. The intensity transmitted through the sample can be expressed by the following very well-known exponential expression:

$$I_T(x,y) = I_0(x,y)\exp-\left[\int_L dz\mu(x,y,z)\right] \quad (1.1)$$

where (x,y) denotes the spatial coordinates in the plane perpendicular to the beam direction, I_0 and I_T indicate the incident and transmitted intensities, L indicates the sample thickness and μ is the so-called linear attenuation coefficient.

Among the various imaging techniques, conventional radiography has the highest spatial resolution and is the initial, most economical and most abundantly used imaging method in joint abnormalities. However, a strong limitation of conventional absorption radiology for OA imaging is the lack of contrast for cartilage. Like the other soft biological tissues, cartilage is in fact composed by low Z (atomic number) elements and is therefore characterized by low X-ray absorption (see chapter 2, section 2.2). Besides, the measured contrast is further reduced by the scattered radiation, which fogs the image signal and which is not completely eliminated by the anti-scatter devices (e.g. a lead grid) that are typically used. As a result, the tissue itself is not visible, and focal cartilage defects or structural abnormalities diagnostic of early stages of the degenerative joint disease are invisible on conventional radiographs.

However, radiography provides very good contrast for bone, and thus the hallmark radiologic features for OA are:

- joint space narrowing, which is often irregular or asymmetric;
- subchondral sclerosis, which appears as an increased density in subchondral bone;
- bony proliferation with the presence of osteophytes/spurs;
- the presence of cysts in subchondral marrow adjacent to or sometimes remote from the joint (usually seen in later cases);
- soft-tissue changes (small effusions, calcification, and soft-tissue swelling).

Therefore, the radiographic evaluation of the disease severity and progression is made only indirectly and is mainly based on the measurement of the joint space narrowing that occurs between the ends of bones as cartilage is destroyed. For this reason, conventional radiography is sensitive only in the cases of advanced disease.

In figure 1.3, examples of conventional radiographs of a normal and an OA joint are presented. The description of the image features and of the limitations in the tissues visualization are given in the figure caption.

Moreover, even though radiographic measures of joint space width changes have been recommended as primary measure of efficacy for pharmacologic therapy and are commonly used for OA diagnosis, precision of this measurement is quite variable and dependent on standardized radiographic techniques. Small positional changes from one measurement to the other can jeopardize reproducibility of joint space width measurements. The degree of flexion of the knee determines the regions of cartilage taken into account for the measurements. Several methods including fluoroscopy, foot maps and position devices can be employed to obtain satisfactory

measurements, but despite standardization of radiographic techniques the values of joint space narrowing can still vary widely (Brandt et al., 2002, Mazucca et al., 2003).

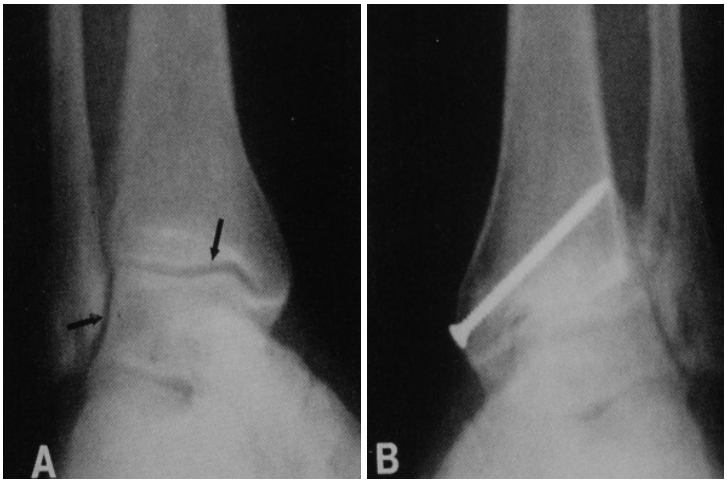

Fig. 1.3. Conventional X-ray radiographs of (A) a normal and (B) an osteoarthritic ankle. In (B) an excess of mineralization and absence of a normal joint space are visible as hallmarks of OA (the screw is part of a joint fusion procedure). In (A), the joint gap visible between the two bones means presence of cartilage tissue; nothing can be said about the status of the cartilage itself.

- **Computed tomography (CT)**

Conventional radiography provides no depth information, as the 3D body structure is projected onto a 2D image, which makes it impossible to determine the three-dimensional position of a feature seen in a radiograph. A tomography is literally a cross-sectional image, a slice of an object: it can be computed from a series of projection images of the object acquired at different view angles around it. The 3D volume can then be reconstructed by piling up the calculated object slices.

The tomography reconstruction algorithms can be classified in two categories: the analytic methods by Fourier transformation and the iterative methods (algebraic and statistical). Among the analytic methods, the filtered backprojection (FBP) algorithm is the most commonly used (Kak and Slaney, 1988, Herman, 2009). Let us consider a coordinate system (x_r,y,z_r) fixed with respect to both the X-ray beam and the detector, with z_r being the beam direction, and rotated with respect to the sample reference frame (x,y,z) by an angle φ around the CT axis y (see fig. 5.1). In the FBP algorithm, the three-dimensional distribution of the linear attenuation coefficient μ is calculated as:

$$\mu(x,y,z) = \int_0^{\pi} d\varphi \mathcal{F}^{-1}\left[|\omega| P(\omega, y, \varphi)\right] \tag{1.2}$$

where $\mathcal{F}^{-1}$ denotes the inverse Fourier transform, ω is the spatial frequency coordinate corresponding to x_r and P represents the Fourier transform of the function p, which is equal to the logarithm of the normalized transmission projection:

$$p\left(x_r, y, \varphi\right) = -\ln\left[I_T\left(x_r, y, \varphi\right) / I_0\left(x_r, y, \varphi\right)\right] = \int_{L_\varphi\left(x_r, y\right)} dz_r \mu\left(x_r, y, z_r\right) \tag{1.3}$$

I_0 and I_T denote the incident and transmitted intensities and $L_\varphi\left(x_r, y\right)$ is the path of the beam inside the object.

Computed tomography is a relatively expensive test. Relative to MRI, it gives poor definition of soft-tissue boundaries, giving rise to misleading cartilage thickness measurements. Computed tomography is particularly helpful in detecting fine details of cortical bone but it lacks sensitivity in early OA stages: as in planar radiology, degenerative signs of cartilage tissue and the entire tissue itself are not visible.

- **Magnetic resonance imaging (MRI)**

MRI has been recognized as having potential for evaluation of joints in OA due to its ability to visualize the morphology and the integrity of the articular cartilage. It also provides a direct image of the soft tissues around the joint. Several studies have been performed in MRI to quantify the cartilage volume and thickness; in addition, in-vivo studies performed on knee joint have shown longitudinal cartilage volume losses in the range 3 to 7% per year in OA patients (Pessis et al., 2003, Raynaud et al., 2003). However, other clinical trials did not detect any change in cartilage volume in patients with knee OA over a 3-year period (Gandy et al., 2002). More concerning is the fact that no strong correlations have been shown between losses of cartilage volume measured by MRI over time and changes in X-ray joint space narrowing or in clinical symptoms. Hence, larger longitudinal studies are still needed to clarify the clinical relevance of MRI measured cartilage volume in OA disease progression.

Promising MRI techniques are also those developed to directly evaluate the changes in cartilage matrix components (e.g. collagen and glycosaminoglycan). These approaches could be of high interest to detect early changes in cartilage components in response to pharmacological interventions. Several studies have shown that the T2 relaxation time can be used as a qualitative probe for the assessment of collagen in the cartilage matrix (Mosher and Dardzinski, 2004, Apprich et al., 2010). A technique known as dGEMRIC (delayed Gadolinium Enhanced MRI of Cartilage) is being developed to directly image the glycosaminoglycan component, which is one of the main constituents of cartilage and which is lost in early OA (Burstein et al., 2001, Taylor et al., 2009). Another approach under investigation is sodium MRI, which is designed to image the loss of proteoglycans associated with early stages of the disease (Madelin et al., 2010).

Magnetic resonance imaging equipment is expensive: for example, the cost of a 1.5 Tesla scanner is usually ranging from 1 million to 1.5 million US dollars; 3 Tesla machines, instead, often cost between 2 million and 2.3 million US dollars.

- **Ultrasound**

Ultrasound is a widespread and very economical imaging technique. However, joint geometry and location often inhibit utilization of the method for most joints since the sound head cannot resolve signals from structures that are not in straight geometry and close connection to the microphone.

- **Arthroscopy**

Arthroscopy is a surgical technique whereby a viewing tube (arthroscope, containing a video camera) is inserted into a body cavity such as the joint space. Abnormalities of and damage to the cartilage and ligaments can be detected and sometimes repaired through the arthroscope. If successful, patients can recover from the arthroscopic surgery much more quickly than from open joint surgery.

Although the arthroscopy technique appears reliable and sensitive to morphologic changes, only the cartilage surface can be evaluated. Moreover, this method is invasive and only semi-quantitative.

1.2 Breast

Another crucial area where an improvement of imaging techniques would be extremely important is breast cancer diagnosis. Breast cancer is the most widespread female cancer, with 421˙000 new cases diagnosed in Europe in 2008 (Ferlay et al., 2010). It is also the primary cause of cancer decease in women.

According to statistics, the 5-year survival rates in women diagnosed of breast cancers has considerably improved in the last years, with a 75% survival rate in 1975, a 79% survival rate in 1985 and a 89 % survival rate in 2003 registered in USA (Ries et al., 2004). Likely explanations for these reductions are early detection by mammographic screening and advances in treatment. There is in fact evidence that the early diagnosis of breast cancer can improve the prognosis. It is estimated that the early detection of a tumour (less than 10 mm in size), which has not invaded the mammary glands, can be successfully treated in about 90% of cases, whereas this value drops to about 55% if glandular invasion has occurred and to about 18% in the case of metastases (Sant et al., 2003).

Despite technical improvements in X-ray sources and digital detectors, however, a substantial fraction (10-20%) of palpable tumours go unnoticed in screening mammography (Durfee et al., 2000, Schulz-Wendtland et al., 2009), which is presently the gold standard employed for breast cancer screening. There is still a strong need, therefore, for improvements of currently available methods for breast imaging.

1.2.1 Breast anatomy and related cancers

The breast is made of lobes of glandular tissue with associated ducts for transfer of the milk to the exterior, and of supportive fibrous and fatty tissues. About 80-85% of normal breast tissue is fat during the reproductive years. The 15-25 lobes are defined by the major lactiferous ducts that open up on the nipple. These lobes are further divided into lobules containing alveoli (small saclike features) of secretor cells and smaller ducts that conduct the milk to the larger ducts (fig. 1.4). In the non-pregnant, non-lactating breast, the alveoli are small. During pregnancy, the alveoli enlarge and during lactation the cells secrete milk substances, i.e. proteins and lipids. Muscular cells surrounding the alveoli contract to express the milk during lactation.

The breast is supported by a highly variable interlacing network of fibrous connective tissue, the so-called Cooper's ligaments. There are two general types of connective tissue in the breast: the nonspecialized connective tissue that holds the breast together and that is found throughout the breast between the lobules (interlobular connective tissue), and the specialized connective tissue that is contained within and surrounds the terminal ducts and lobules (intralobular connective tissue).

The lymphatic system drains the tissues of the breast of excess fluid. Lymph nodes along the pathway of drainage screen for foreign bodies such as bacteria or viruses. The lymph nodes can also become enlarged when migrating cancer cells get lodged in the nodes. This is why lymph nodes located in the arm pit are checked during a breast exam and why they are often cut out along with cancerous tissue when breast cancer surgery has to be applied.

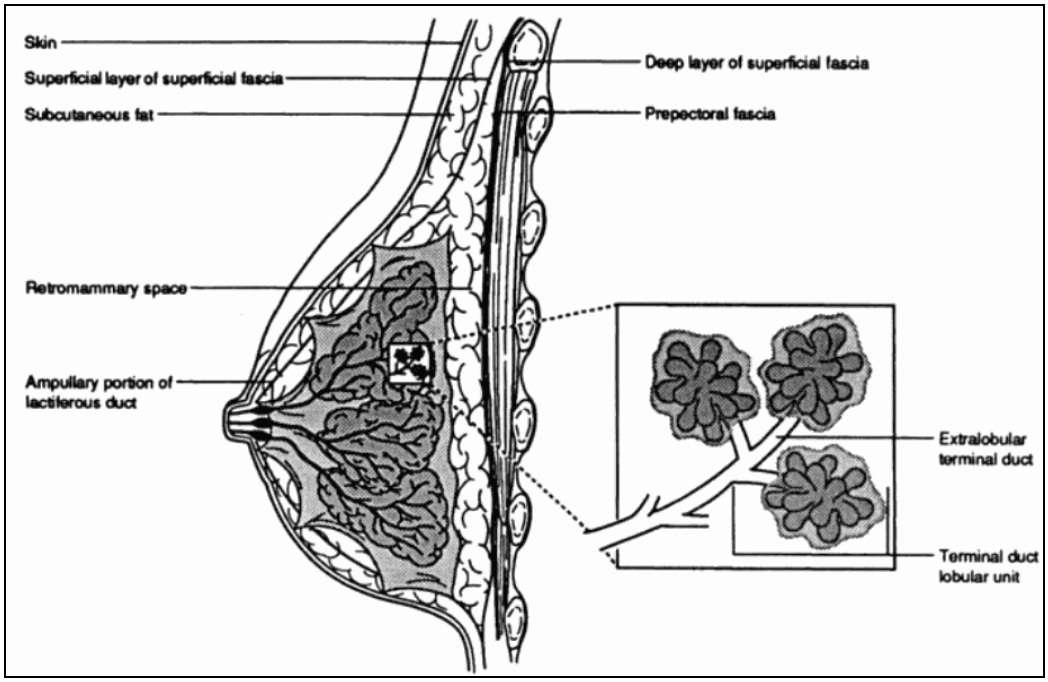

Fig. 1.4. Schematic representation of the basic anatomy of the breast. The glands that produce the milk are called lobules and the tubes that connect them to the nipple are called ducts. The breast is made of lobules, ducts, and fatty, connective and lymphatic tissues.

- Types of breast cancer

A tumour is a swelling or new growth, the cells of which multiply in an uncontrolled manner. Such a growth is also called a neoplasm (*neo* = new and *plasm* = formation). Tumours may be: benign (innocent) or malignant (cancerous).

Benign breast tumours: they show a tendency to invade surrounding structures, but they never give rise to secondary deposits (metastases) and are surrounded by a capsule or fibrous tissue wall. They are slowly growing and are not usually fatal, but can cause breast swelling and pain. They may also secrete hormones in abnormal amounts. Benign breast tumours include fibroadenoma, periductal fibromas (connective tissue tumour), intraductal epithelial tumour, retention cysts, lipomas (fatty tumour), chronic cystic mastitis and fat necrosis. Most often they occur during the reproductive period of life or just after. They are often difficult to distinguish from malignant tumours and must be watched for a change in size, or lymphatic involvement, in which case the growth should be cut out and examined by a precise histology.

Malignant breast tumours: they have no capsules, and can destroy tissues surrounding them. If untreated, they spread to distant sites (metastasis), either by the blood stream or lymphatic system. If the cancer spreads outside the breast and lymph nodes, it tends to go to the bones and lungs and to continue growing, and may eventually prove fatal. They very often recur after surgical removal.

Most breast cancers develop in glandular tissue and are classified as adenocarcinoma. *Ductal carcinoma in situ* (DCIS), which develops in the milk ducts, is the most common type of non-invasive breast cancer. The term “non-invasive” refers to tumours that have not spread beyond the area where they began into the normal surrounding tissue. *Invasive ductal carcinoma* (IDC) develops from DCIS, spreads through the duct walls and invades the breast tissue. DIC is the most common type of invasive cancer, accounting for about 80% of the total number. *Invasive lobular carcinoma* (ILC) instead originates in the milk glands and accounts for 10-15% of invasive breast cancers. The earliest form of the disease is termed *lobular carcinoma in situ* (LCIS). Less common types of breast cancer include the following: inflammatory, medullary carcinoma, mucinous carcinoma, Paget’s disease, Phyllodes tumor, tubular carcinoma.

Despite the fact that breast microcalcifications can be found in normal breasts, in some cases they are correlated with presence of a breast cancer, perhaps invisible on the radiograph. Microcalcifications consist of specks of calcium in breast soft tissue; when they are seen in a cluster, and when they are small, numerous, and variously shaped (rods, branches, teardrops), they are very likely associated with malignant cancer. Their visualization is therefore extremely important and, often, they are the only visible early sign of a neoplasm.

1.2.2 Limitations of existing techniques for breast imaging

- **Mammography**

Among all the available imaging techniques, conventional mammography, based on the absorption of X-rays in the tissues, remains the gold standard employed for breast cancer screening. Presently, it is the most reliable and practical imaging method, and a relatively economical one. It is also the method that provides the highest resolution, exceeding 20 line pairs per millimeter (lp/mm) (Haus and Yaffe, 1994).

Conventional mammography, however, has also some limitations, which derive from the fact that breast soft tissues are composed of light elements and have small density variations, resulting in small inherent absorption contrast in the transmitted beam. Since the differences in X-ray absorption become smaller with increasing X-ray energy, mammography is done at relatively low energies in spite of the entailed increase of the radiation dose. Because of the radiation sensitivity of the breast, the dose to which this organ is exposed to has to be limited in order to minimize the radio-toxicity of the mammographic examination. This inevitably limits the achievable absorption contrast, and affects the visualization/identification of malignancies in a mammogram. In particular, this impairs the detection of small lesions in dense breasts, frequently encountered in young women. The diagnosis, although crucial for young women, in whom the cancer invades more rapidly, becomes even more difficult.

Besides, the image contrast is further decreased by the scattered radiation, which fogs to a certain extent the image signal despite the anti-scatter grids that are typically employed to reduce this effect.

- **Computed tomography (CT) and tomosynthesis**

Lesions are sometimes masked by superimposed normal tissues in planar mammography. Tomographic breast imaging, by providing a three-dimensional image of the tissues, could improve detection of minor diseases in dense breasts or perception of lesions hidden by superimposed structures. However, the application of CT for breast imaging has remained limited. The radiation doses required by a CT, in fact, are often too high for breast, which is a very radio-sensitive organ. Furthermore, the low-spatial resolution (0.1-0.2 mm) together with image noise might limit the visibility of microcalcifications (Boone et al., 2006, Lindfors et al., 2008).

A quite recent and promising technique that can allow overcoming some of the limitations of CT is tomosynthesis. This technique is based on reconstructing a region in the sample by acquiring a limited number of projection images over a limited view angles range, allowing a strong reduction in the required dose compared to CT. Recent studies show that tomosynthesis could be a useful complement to screening mammography for women with suspicious findings (Dobbins and Godfrey, 2003, Poplack et al., 2007).

- **Ultrasound**

For breast imaging, ultrasound is more a complementary technique to X-ray mammography than advocated for a routine screening use. If a lesion is not palpable but detected by mammography, ultrasound can be used to analyze its composition. Ultrasound is principally a method for differentiating cystic lesions from solid masses and serves as a guide for taking a biopsy. However, because of significant overlap in characteristics of benign solid tissues and malignant lesions, ultrasound cannot be considered as an independent diagnostic method but must always be used as a complementary analysis tool. Moreover its main disadvantage resides in its poor ability to detect microcalcifications, which are frequently linked to breast cancer.

- **Magnetic resonance imaging (MRI)**

The advantages of MRI are good resolution (sub mm), non-invasiveness and very low related risk. Disadvantages are the high costs, bulkiness of the equipment and the large acquisition times. T1-weighted MRI with gadolinium-based contrast agents has demonstrated benefits in screening, as a complement to mammography, high-risk women with dense breast (Lord et al., 2007). Contrast-enhanced MRI can also be useful in solving specific problems such as distinguishing between scar from cancer recurrence and in local staging of breast cancers. However, it is not sensitive, in general, to microcalcifications, which can be an early indication of breast disease and represent a frequent finding on mammography. Furthermore, the duration of such an exam is very long, usually between 45 and 60 minutes. MRI without contrast agents is particularly useful in the evaluation of breast implants. However, the differences in T1 and T2 relaxation times between benign and malignant tissues overlap; therefore, used without contrast material, MRI cannot be considered as a diagnostic procedure for breast cancer.

- **Nuclear imaging: scintigraphy and positron emission tomography**

The administration to the patient of a gamma emitting substance allows the imaging and functional study of organs and tissues. The most frequently used tracer applied to breast imaging is Technetium-99m-sestamibi. This radioactive isotope is often attached to biologically active molecules. An external scintillation detector interfaced to a counting device detects the gamma rays emitted by the radionuclide distributed within its target. Sestamibi scanning of the breast has been shown to be effective in relatively large breast cancers but its role in diagnostic imaging is not established. The development of other labeled molecules may permit greater refinement in cancer detection and diagnosis.

Because of the high instrumental cost and the requirements of a cyclotron for the production of short-lifetime radioisotopes, Positron Emission Tomography (PET) systems can normally only be found in large clinical or research facilities. Typical uses include the diagnosis and localization of tumours with the assessment of the metastatic spread.

For breast imaging, PET is also a means to determine some metabolic parameters that are of prognostic value. Glucose labeled with fluorine-18 to form 2-[fluorine-18]-fluoro-2-deoxy-D-glucose (FDG) is one of the most studied molecules. This agent demonstrates the presence of cancer that occurs with an elevated metabolic activity and an increased utilization of glucose.

1.3 Conclusions and perspectives

In this chapter, two crucial medical applications, osteoarthritis disease and breast cancers, where conventional imaging methods still present limitations, have been examined. The anatomy of the joint and of the breast tissues has been briefly described, and the changes undergone in these tissues during pathological states (osteoarthritis and breast cancer, respectively) have been presented. An overview of the conventional imaging methods that are clinically employed for the diagnosis in the two cases has been provided, and their present limitations underlined.

In particular, in the case of osteoarthritis diseases the diagnosis of early degenerative states is very difficult, due to the difficulties in imaging cartilage. The primary method of use for the diagnosis of osteoarthritis, planar radiography, is in fact unable to visualize the cartilage tissue and its degeneration. The diagnosis is thus based only on other signs, like bone structure changes and joint space narrowing, which are however encountered only in advanced stages of the disease.

Planar imaging (mammography) remains the most used method also in breast imaging, and is considered a valid tool for breast cancer screening. However, a certain fraction of small tumours can be invisible in mammography, due to the intrinsic low contrast of soft tissues and to the superposition with normal tissues on the recorded images. The application of computed tomography, which could be a useful complement to screening mammography, is still very limited due to the high radiation dose delivered.

The so-called phase-contrast imaging techniques, which have been investigated in recent years, could provide a great improvement with respect to conventional absorption imaging and could therefore represent a breakthrough for the diagnosis of these pathologies. In particular, they could overcome the limitation of inherent low contrast of conventional radiology when imaging soft tissues. It has been proven, both theoretically and in in-vitro and in-vivo experiments, that phase-contrast techniques could provide greatly increased contrast for soft tissues and at lower radiation doses. For this reason also the application of computed tomography, which is presently limited for the diagnosis of osteoarthritis and breast cancer due to the required high doses, could have an important role also in the diagnosis of these pathologies.

In the next chapter, the most used and promising phase-contrast techniques will be described theoretically, and the intrinsic advantages with respect to conventional absorption imaging will be discussed. At the end of the chapter, an overview of the results obtained until now for cartilage and breast imaging with phase-contrast techniques will be also presented.

References and links

S. Apprich, G. H. Welsch, T. C. Mamisch, P. Szomolanyi, M. Mayerhoefer, K. Pinker, and S. Trattnig, "Detection of degenerative cartilage disease: comparison of high-resolution morphological MR and quantitative T2 mapping at 3.0 Tesla", Osteoarthr. Cartilage **18** (9), 1211-1217 (2010).

J. M. Boone, A. L. C. Kwan, K. Yang, G. W. Burkett, K. K. Lindfors, and T. R. Nelson, "Computed tomography for imaging the breast", J. Mammary Gland Biol. **11** (2), 103-111 (2006).

K. Brandt, S. Mazucca, T. Conrozier, J. Dacre, C. Peterfy, and D. Provvedini, "What is the best radiographic protocol for a clinical trial of a structure modifying drug in patients with osteoarthritis", J. Rheumatol. **29** (6), 1308-1320 (2002).

D. Burstein, J. Velyvis, K. T. Scott, K. W. Stock, Y. J. Kim, D. Jaramillo, R. D. Boutin, and M. L. Gray, "Protocol issues for delayed Gd(DTPA)(2-)-enhanced MRI: (dGEMRIC) for clinical evaluation of articular cartilage", Magnet. Reson. Med. **45** (1), 36-41 (2001).

J. T. Dobbins and D. J. Godfrey, "Digital x-ray tomosynthesis: current state of the art and clinical potential", Phys. Med. Biol. **48** (19), R65-R106 (2003).

S. Durfee, D. Selland, D. Smith, S. Lester, C. Kaelin, and J. Meyer, "Sonographic evaluation of clinically palpable breast cancers invisible on mammography", Breast J. **6** (4), 247-251 (2000).

J. Ferlay, D. M. Parkin, and E. Steliarova-Foucher, "Estimates of cancer incidence and mortality in Europe in 2008", Eur. J. Cancer **46** (4), 765-781 (2010).

S. Gandy, P. Dieppe, M. Keen, R. Maciewic, I. Watt, and J. Waterton, "No loss of cartilage volume over three years in patients with knee osteoarthritis as assessed by MRI", Osteoarthr. Cartilage **10**(12), 929–937 (2002).

A. Haus and M. Yaffe, *Syllabus: a categorical course in physics. Technical aspects of breast imaging*, Chicago: RSNA Publications, pp. 95-97 (1994).

G. T. Herman, *Fundamentals of computerized tomography: Image reconstruction from projections,* 2nd ed., Springer-Verlag (2009).

A. C. Kak and M. Slaney, *Principles of Computerized Tomographic Imaging*, IEEE Press, New York (1988).

R. C. Lawrence, D. T. Felson, C. G. Helmick, L. M. Arnold, H. Choi, R. A. Deyo, S. Gabriel, R. Hirsch, M. C. Hochberg, G. G. Hunder, J. M. Jordan, J. N. Katz, H. M. Kremers, F. Wolfe, and W. Natl Arthritis Data, "Estimates of the prevalence of arthritis and other rheumatic conditions in the United States", Arthritis Rheum. **58** (1), 26-35 (2008).

K. K. Lindfors, J. M. Boone, T. R. Nelson, K. Yang, A. L. C. Kwan, and D. F. Miller, "Dedicated breast CT: Initial clinical experience", Radiology **246** (3) 725-733 (2008).

S. J. Lord, W. Lei, P. Craft, J. N. Cawson, I. Morris, S. Walleser, A. Griffiths, S. Parker, and N. Houssami, "A systematic review of the effectiveness of magnetic resonance imaging (MRI) as an addition to mammography and ultrasound in screening young women at high risk of breast cancer", Eur. J. Cancer **43** (13), 1905-1917 (2007).

G. Madelin, J. S. Lee, S. Inati, A. Jerschow, and R. R. Regatte, "Sodium inversion recovery MRI of the knee joint in vivo at 7T", J. Magn. Reson. **207** (1), 42-52 (2010).

S. Mazucca, K. Brandt, and K. Buckwalter, "Detection of radiographic joint space narrowing in subjects with knee ostearthritis", Arthritis Rheum. **48** (2), 385–390 (2003).

T. J. Mosher and B. J. Dardzinski, "Cartilage MRI T2 relaxation time mapping: Overview and applications", Semin. Musculoskel. R. **8** (4), 355-368 (2004).

E. Pessis, J. Drape, P. Ravaud, A. Chevrot, M. Dougados, and X. Ayral, "Assessment of progression in knee osteoarthritis: results of a 1 year study comparing arthroscopy and MRI", Osteoarthr. Cartilage **11** (5), 361–369 (2003).

S. P. Poplack, T. D. Tosteson, C. A. Kogel, and H. M. Nagy, "Digital breast tomosynthesis: Initial experience in 98 women with abnormal digital screening mammography", Am. J. Roentgenol. **189** (3), 616-623 (2007).

J. Raynaud, C. Kauffman, G. Beaudoins, M. Berthaumie, J. de Guise, and D. Bloch, "Reliability of quantification imaging system using magnetic resonance images to measure cartilage thickness and volume in human normal and osteoarthritic knees", Osteoarthr. Cartilage **11** (5), 351–360 (2003).

L. Ries, D. Melbert, and M. Krapcho, *SEER Cancer statistics review, 1975-2004*, National Cancer Institute, Bethesda, MD (2004).

M. Sant, C. Allemani, R. Capocaccia, T. Hakulinen, T. Aareleid, J. W. Coebergh, M. P. Coleman, P. Grosclaude, C. Martinez, J. Bell, J. Youngson, F. Berrino, and E. W. Grp, "Stage at diagnosis is a key explanation of differences in breast cancer survival across Europe", Int. J. Cancer **106** (3), 416-422 (2003).

R. Schulz-Wendtland, M. Fuchsjager, T. Wacker, and K. P. Hermann, "Digital mammography: An update", Eur. J. Radiol. **72** (2), 258-265 (2009).

C. Taylor, J. Carballido-Gamio, S. Majumdar, and X. J. Li, "Comparison of quantitative imaging of cartilage for osteoarthritis: T2, T1 rho, dGEMRIC and contrast-enhanced computed tomography", Magn. Reson. Imaging **27** (6), 779-784 (2009).

2

Phase-contrast imaging techniques

Table of Contents

Abstract: With the aim of overcoming the limitations of conventional imaging methods, a number of X-ray phase contrast techniques have been developed and applied over the last 20 years. Unlike conventional radiography, these techniques are not only sensitive to the absorption, but also to the phase shift that an electromagnetic wave experiences when passing through the matter. The image contrast potentially achievable is much larger compared to conventional radiography, especially for soft biological tissues that are characterized by small absorption.

In this chapter, three among the most used phase-contrast techniques will be presented: propagation-based imaging (PBI), analyzer-based imaging (ABI) and grating interferometry (GIFM). The basic principles of the image formation in the various techniques will be described and their requirements in terms of experimental setup and needed spatial and temporal coherence will be discussed. The results obtained so far with these phase-contrast techniques in the fields of cartilage and breast imaging will be briefly mentioned.

2.1 Introduction

In conventional radiography the image contrast is generated by variations of the X-ray absorption that arise from density differences and from changes in thickness and composition of the sample (see also chapter 1). These differences, however, can be very tiny for hard X-rays when samples consisting of elements with low atomic number Z are considered. An important example is represented by biological soft tissues, which are mainly composed of oxygen, carbon, hydrogen and nitrogen (ICRU, 1989). The differences in the linear attenuation coefficients for these tissues is of the order of 0.1-0.3 cm^{-1} (Chantler et al., 2005) in the range of energies commonly used in radiology (10-60 keV). As a result, the image contrast is in some cases insufficient for the complete characterization of the healthy and diseased tissues in a given sample.

For these reasons, the application of the so-called phase contrast techniques in the medical physics field has been extensively studied in the last 20 years, with the aim of overcoming the previously stated limitations of standard absorption radiography. It is important to mention that some of these techniques were already largely used in other fields of research in physics at lower energies. Their application to the hard X-rays range was made possible, in the last decades, by the advent of third-generation synchrotron radiation facilities capable of delivering highly coherent X-rays beams at energies of up to tens of keV.

As we will see in section 2.2, the behavior of X-rays as they travel through an object can be described in terms of a complex index of refraction, whose real part, δ, and imaginary part, β, are related to the electromagnetic phase shifts and to the X-ray attenuation in the object, respectively. In the hard X-rays range, the phase term is orders of magnitude higher than the absorption one (fig. 2.2). Therefore, radiographic techniques sensitive to variations of the δ term may potentially provide an increased image contrast with respect to those techniques based only on the X-ray absorption process.

Different X-ray phase-contrast techniques have been developed (Fitzgerald, 2000, Lewis, 2004). They can be classified into four main categories: the interferometric methods based on the use of crystals (Bonse and Hart, 1965, Momose et al., 1996), the free-space propagation methods (Snigirev et al., 1995, Cloetens et al., 1996, Wilkins et al., 1996), the analyzer-based methods (Förster et al., 1980, Davis et al., 1995, Bravin, 2003) and the grating interferometric methods (David et al., 2002, Momose et al., 2003, Pfeiffer et al., 2006, Olivo and Speller, 2008, Wen et al., 2009). These techniques have advantages and disadvantages with respect to the accessible phase information, the complexity of the setup, the beam coherence requirements, the available field of view and the spatial frequency range covered.

In this Thesis work, the phase contrast techniques that have been applied and investigated are the propagation-based imaging (PBI), the analyzer-based imaging (ABI) and the grating interferometry (GIFM). In the next section, the general principles of X-ray phase contrast imaging will be exposed, and in section 2.3 the concept of partial coherence will be introduced. In sections 2.4-2.6, the basic theory of the image formation in the three considered techniques will be

presented, respectively. The needed experimental setup and the requirements in terms of spatial and temporal coherence of the beam will also be discussed.

2.2 The complex refractive index and the phase contrast

The propagation of X-rays in the matter is generally described in terms of the complex refractive index *n*. Since it is very close to unity for hard X-rays, *n* is in general expressed as:

$$n = 1 - \delta + i\beta \tag{2.1}$$

The real part δ is the so-called refractive index decrement, which determines the phase shifts of the electromagnetic wave in the matter, and has its origins in the Thomson elastic scattering of the X-rays with the electrons of the medium (Azaroff, 1968). δ is a positive number in the hard X-rays range. The imaginary part β is the so-called absorption index, and is linked to the effects of the radiation-matter interaction on the wave amplitude. At the considered energies (tens of keV) these effects are mainly due to the photoelectric absorption and to a smaller extent to Compton scattering.

In order to understand the effects of the real and imaginary parts of the complex index of refraction onto the wave propagation, let us consider a thin object described by the 3D complex refractive index distribution $n(x,y,z)$, illuminated by a monochromatic wave field of wavelength λ. The wave exiting the sample can be expressed by:

$$\Psi_{obj}(x,y) = T(x,y)\,\Psi_{in}(x,y) \tag{2.2}$$

where (x,y) denotes the spatial coordinates in the plane perpendicular to the propagation direction *z*, $\Psi_{in}(x,y)$ is the wave incident on the sample and $\Psi_{obj}(x,y)$ the wave at the sample exit surface. The wave-object interaction can be described by the object complex transmission function $T(x,y)$:

$$T(x,y) = A(x,y)\,e^{i\phi(x,y)} \tag{2.3}$$

where the amplitude modulation is given by the projection of the imaginary part β of the refractive index distribution along the beam direction *z*:

$$A(x,y) = e^{-B(x,y)} \quad \text{with} \quad B(x,y) = \frac{2\pi}{\lambda}\int_z dz\,\beta(x,y,z) \tag{2.4}$$

and the phase modulation is provided by the projection along *z* of its real part δ:

$$\phi(x,y) = -\frac{2\pi}{\lambda}\int_z dz\,[1-\delta(x,y,z)] = \phi_0 - \frac{2\pi}{\lambda}\int_z dz\,\delta(x,y,z) \tag{2.5}$$

The integrations along the propagation direction z are made over the entire thickness of the object. By taking the squared modulus of eq. 2.2 and by using eqs. 2.3-2.5, we obtain the following equation that relates the intensity of the wave exiting the sample, I_T, and that of the wave incident on the sample, I_0:

$$I_T = I_0 \, e^{-\frac{4\pi}{\lambda}\int_z dz\beta} \tag{2.6}$$

By comparing eq. 2.6 with the well known equation for the absorption of X-rays in the matter (eq. 1.1), we see that the linear attenuation coefficient μ is related to the absorption index β through:

$$\mu = \frac{4\pi}{\lambda}\beta \tag{2.7}$$

ϕ_0 in eq. 2.5 is the phase of the reference beam in the vacuum and, as we will see in sections 2.3-2.5, has no influence on the intensity recorded on the detector. This constant will therefore be neglected in the following. From eq. 2.5, we see that the component of the phase shift that is due to the object is related to the refractive index decrement δ through:

$$\phi = -\frac{2\pi}{\lambda}\int_z dz\,\delta \tag{2.8}$$

An important effect of the wavefront distortions due to the phase shifts introduced by the object is that the X-rays that passed through the sample are locally refracted by an angle $\Delta\theta_R$ (see figure 2.1) that can be expressed as (Born and Wolf, 1999):

$$\Delta\theta_R\left(x,y;\lambda\right) \simeq -\frac{\lambda}{2\pi}\vec{\nabla}_{x,y}\phi\left(x,y;\lambda\right) \tag{2.9}$$

This relation is valid if $\left|\vec{\nabla}_{x,y}\phi\left(x,y;\lambda\right)\right| \ll 2\pi/\lambda$, which is the so-called paraxial approximation.

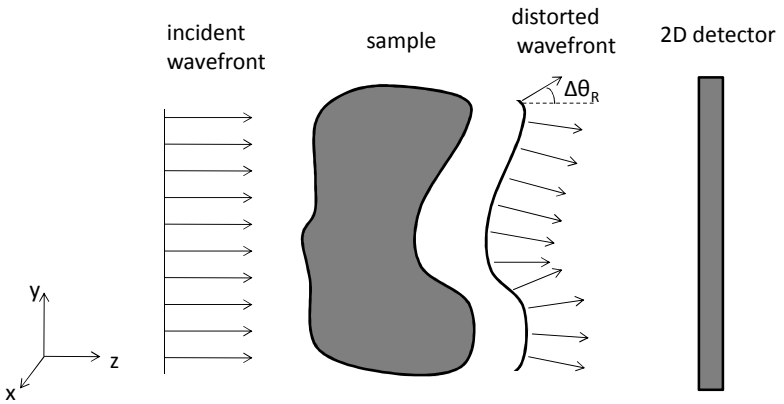

Fig. 2.1. Local angular deflections of the beam due to the wavefront distortions introduced by the sample. The drawing is not in scale (the angles are typically in the order of a few µrad).

Let us now consider the values of the real and imaginary parts of the complex index of refraction and their dependence upon the energy and the atomic number *Z*. The refractive index decrement, which is due to the Thomson elastic scattering of the X-rays with the electrons in the medium, is generally expressed by (Jackson, 1975):

$$\delta = \frac{r_e \lambda^2}{2\pi V} \sum_j \left(Z_j + f_j^{'} \right) \tag{2.10}$$

where r_e is the electron radius, Z_j the atomic number of the atom j in the volume V and $f_j^{'}$ the real part of the wavelength-dependent dispersion correction of the atomic scattering factor. Far from the absorption edges, δ can be approximated to:

$$\delta = \frac{\lambda^2 r_e}{2\pi} \rho_e \approx 1.3 \cdot 10^{-6} \rho \lambda^2 \tag{2.11}$$

where ρ_e is the electron density, ρ is the mass density of the material in g/cm^3 and λ is expressed in Å.

The absorption index β has a complex energy and composition dependence, and varies abruptly near the absorption edges of the element. It can be expressed by (Jackson, 1975):

$$\beta = \frac{r_e \lambda^2}{2\pi V} \sum_j f_j^{''} \tag{2.12}$$

where $f_j^{''}$ is the imaginary part of the wavelength-dependent dispersion correction.

For light elements and for energies in the range 10-100 keV (far from absorption edges), *f'* is approximately zero, whereas *f''*, dominated by the absorption process, behaves with the energy approximately as E^{-2}. The linear attenuation coefficient is often approximated, in this range of energies and for low *Z* elements, to a sum of a photoelectric absorption term and a Compton scattering term:

$$\mu \approx \rho Z^p k_1(\lambda) + \rho k_2(\lambda) \tag{2.13}$$

where p is a number that varies from 3 to 4, and k_1 and k_2 are functions of the wavelength λ.

Numerically, n deviates only slightly from unity, δ and β being extremely small. The index δ is however much larger than β, especially for soft tissues, in the energy range normally used in radiology and differs at least by two orders of magnitude as shown in figure 2.2, where the ratio δ/β is reported as a function of the energy for two biological tissues. This large difference between δ and β is the reason for the advantage of phase-contrast imaging, the phase contribution being the sole source of contrast when the absorption counterpart is undetectable. For example, an X-ray beam of 35 keV passing through a 100-μm-thick sheet of breast tissue will be attenuated by less than 0.1%, while the phase shift is close to π.

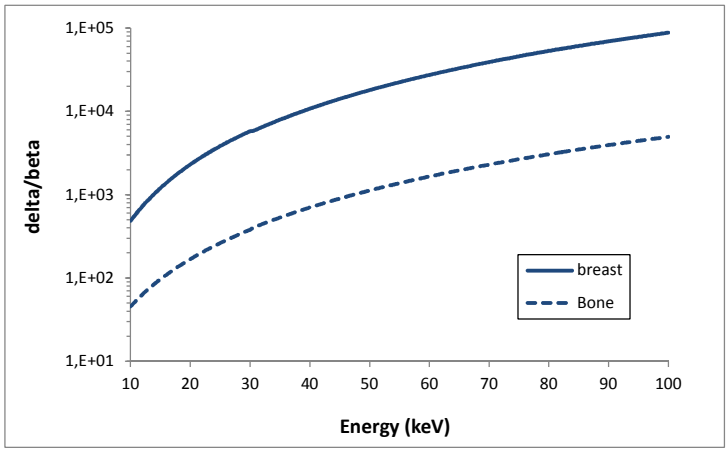

Fig. 2.2. Ratio of the delta and beta indices in the range 10-100 keV for bone and a soft tissue (breast). The values have been calculated with XOP (http://www.esrf.fr/computing/scientific/dabax/) by considering the elemental composition of the two tissues (ICRU, 1989).

The energy dependence of the two terms δ and β, for energies far from the absorption edges, is approximately given by (cf. eqs. 2.11 and 2.12):

$$\delta \propto \frac{1}{E^2} \qquad \text{and} \qquad \beta \propto \frac{1}{E^4} \tag{2.14}$$

The energy dependence of the phase shift ϕ can then be expressed as (see eq. 2.8):

$$\phi \propto \frac{1}{E} \tag{2.15}$$

whereas the linear attenuation coefficient varies with the energy as (see eq. 2.7):

$$\mu \propto \frac{1}{E^3} \tag{2.16}$$

The dependence upon energy for phase sensitive techniques is therefore not as crucial as for absorption methods, thus working at high energies does not necessarily entail a dramatic decrease of contrast. High energies are particularly interesting for medical and biological applications since they tend to reduce the dose deposition, and therefore the damage to the tissues.

2.3 X-ray partial coherence

In this section we will briefly introduce the concepts of spatial and temporal coherence, which are very important for the phase-contrast imaging techniques that will be described later in the chapter. Empirically, "coherence" can be defined as the property that makes a wave capable to produce observable interference and diffraction effects. A monochromatic plane wave in this sense is perfectly coherent, while the light emitted by a standard light bulb is completely incoherent. Intermediate states of coherence also exist, which we will refer to as "partial coherence" states. In

the latter case interference effects will be observable, but with a reduced visibility depending on the degree of coherence of the wave.

The coherence properties of a wave field can be described by time and space dependent correlation functions (Born and Wolf, 1999), respectively linked to the X-ray monochromaticity and to the angular source size:

- **Temporal (longitudinal) coherence** implies a phase relationship between the wave $\Psi(t)$ and the wave $\Psi(t+\Delta t)$ separated by a short time delay. The distance covered by the wave during a time delay over which the correlation remains high is called the longitudinal coherence length $l_t = \lambda^2/\Delta\lambda$, where λ is the wavelength. It is associated to the monochromaticity $(\Delta\lambda/\lambda)$ of the beam.

- **Spatial (transverse) coherence** indicates the correlation of the wave amplitudes between different points transverse to the direction of propagation (between the wave $\Psi(x)$ and the wave $\Psi(x+\Delta x)$ in two points separated by a distance Δx). This property is usually expressed in terms of lateral (or transverse) coherence length $l_t = \lambda/2\alpha$, where $\alpha = S/L$, and L and S are the source-to-object distance and the transverse dimension of the source, respectively (Born and Wolf, 1999).

In a more general treatment, a complete description of the temporal and spatial coherence is given in terms of the mutual coherence function (Paganin, 2006). This function expresses the correlation of the wave in two points separated in both time and space, and it is defined as:

$$\Gamma(x_1, x_2, \tau) \equiv \left\langle \Psi(x_1, t+\tau)\Psi^*(x_2, t) \right\rangle \tag{2.17}$$

where $x_2 = x_1 + \Delta x$ and the angular brackets indicate a time average operation. The complex degree of coherence is obtained by normalizing the mutual coherence function Γ :

$$\gamma(x_1, x_2, \tau) \equiv \frac{\Gamma(x_1, x_2, \tau)}{\sqrt{\Gamma(x_1, x_1, \tau=0)\Gamma(x_2, x_2, \tau=0)}} = \frac{\Gamma(x_1, x_2, \tau)}{\sqrt{I(x_1)I(x_2)}} \tag{2.18}$$

with $I(x_1)$ and $I(x_2)$ the intensities of the wavefield at the two considered locations. The correlation functions related to temporal and spatial coherence are special cases of the mutual coherence function Γ , when the distance between the two points or the considered time difference are respectively set to zero. In this latter case the mutual intensity function, depending only on the spatial coordinates of the two considered points x_1 and x_2 , is defined as:

$$J(x_1, x_2) \equiv \Gamma(x_1, x_2, \tau = 0) \tag{2.19}$$

Let us now assume that a given optical experiment is performed using quasi-monochromatic radiation, with mean angular frequency $\bar{\omega}$ and narrow angular frequency spread $\Delta\omega$. Under the

further assumption that the considered path-length differences have corresponding time differences τ that are much less than $2\pi/\Delta\omega$, it can be demonstrated that:

$$\Gamma(x_1, x_2, \tau) \approx \exp(-i\bar{\omega}\tau) J(x_1, x_2) \quad , \quad \tau \ll 2\pi/\Delta\omega \tag{2.20}$$

Under the stated conditions, therefore, the mutual coherence function factorizes into a product of two functions, one of which is a harmonic function that depends only on the time difference τ, with the other being the mutual intensity that depends only on the spatial coordinates x_1 and x_2 of the two considered points. In the general case, however, the information contained in the mutual coherence function cannot be cleanly separated into properties pertaining to spatial and temporal coherence.

2.4 Propagation-based imaging

In the propagation-based, or "in-line", phase-contrast technique, highly spatially coherent radiation illuminates the object, which can give rise to a spatially varying phase shift. As the radiation propagates after the sample, parts of the wavefront, which have experienced different deflections, interfere giving rise to a characteristic pattern that is then recorded by a detector set at a convenient distance (figure 2.4) (Snigirev et al., 1995, Cloetens et al., 1996). Thanks to the Fresnel diffraction, the phase shifts are therefore transformed into detectable intensity variations (Born and Wolf, 1999).

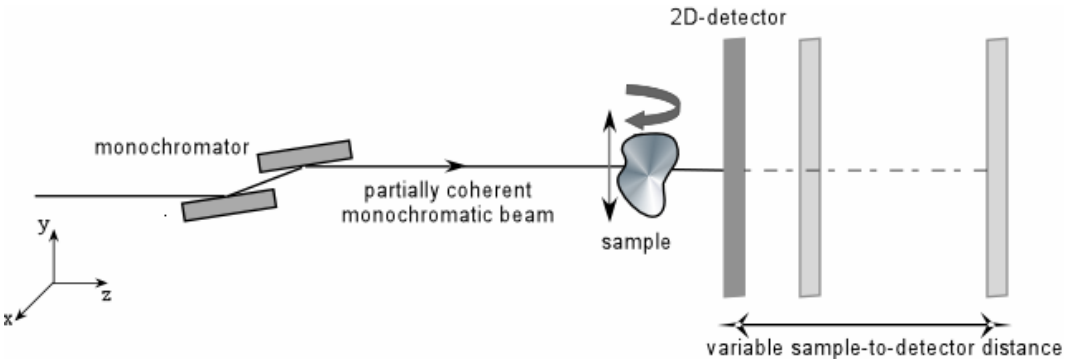

Fig. 2.3. Scheme of the setup of the propagation-based technique.

Compared to the other phase-contrast techniques, this imaging modality presents the advantages of a relatively simple setup (figure 2.3) requiring no optical elements between the sample and the detector. This implies the absence of possible aberrations arising from the optical elements and a high potentially achievable resolution, which depends largely, but not only, on the size of the source (Pogany et al., 1997, Arhatari et al., 2004, Gureyev et al., 2008). Similarly to the analyzer-based and the grating-based techniques, which will be discussed respectively in sections 2.5 and 2.6, the propagation-based technique is a differential phase-contrast imaging modality, in

the sense that the image signal does not depend directly on the phase shift induced by the object but on its spatial variation. In particular, in this case, as it will be described in detail in the following, the image contrast is at a first approximation proportional to the Laplacian of the phase shift in a plane perpendicular to the optical axis.

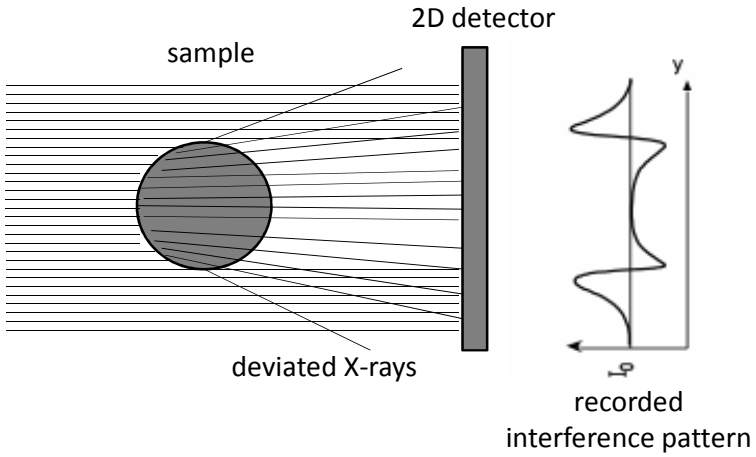

Fig. 2.4. Recorded interference pattern between parts of the incident wavefront affected by different angular deviations. The drawing is not in scale (the refraction angles are typically in the order of a few µrad).

There exists an important dependence of the phase-contrast signal on the so-called effective propagation ("defocus") distance *D*, which is defined as $D = d \cdot l \big/ \left(d + l \right)$, where *l* and *d* are the source-to-sample and the sample-to-detector distances respectively. For $l \gg d$, which is a typical condition for synchrotron-based setups, the defocus distance is simply determined by the propagation distance, i.e. $D \simeq d$. By varying the defocus distance and considering the transverse characteristic length scale *h* of the object and a monochromatic plane wave, four regimes may be distinguished (Mayo et al., 2002, Gureyev, 2003):

- The *absorption* regime, for which the sample to detector distance *d* is close to zero.
- The *edge detection* or *near-field diffraction* regime, characterized by small defocus distances *D* such that: $r_F^2 = \lambda D \ll h^2$.

  The introduced quantity r_F is the radius in the object plane of the so-called first Fresnel zone, which represents the finite region in the object that contributes significantly to a point *P* in the image. In this case, the contrast is formed locally around specific sample features. The boundaries of the object are strongly enhanced and a distinct interference pattern corresponds to every edge, giving valuable geometrical information on the object. If we introduce the Fresnel number $N_F \equiv h^2 \big/ \left(\lambda D \right)$, the above condition for the near-field regime can be expressed as $N_F \gg 1$.

- The *Fresnel* or *intermediate* regime, characterized by defocus distances such that: $r_F^2 = \lambda D \approx h^2$. This condition is also equivalent to $N_F \approx 1$.
- The *Fraunhofer* or *far-field diffraction* regime, characterized by large defocus distances such that $r_F^2 = \lambda D \gg h^2$, and then $N_F \ll 1$.

  In this last case, the interference fringes are well resolved but they can no longer be attributed to a specific edge of the sample. The shape of the object is hardly recognizable: the images increasingly lose direct resemblance to the object and they give little direct information on it.

Therefore, depending on the experimental conditions, the Fresnel diffraction pattern enhances different properties of the sample. In particular, it is possible to demonstrate that the image is most sensitive to a given frequency range *f* of a particular phase feature at a distance *D* given by $D \approx 1/\left(2\lambda f^2\right)$. At this distance, in fact, the phase contrast term of the image intensity (see eq. 2.33) is maximized. As an example, for a λ = 0.5 Å, in order to detect features of 10 μm (40 μm) size, the optimal distance would be 1 m (16 m). Since the propagation distance is limited to the length of the experimental hutch (~10 m), this means that the high frequency range is intrinsically selected to the detriment of the low frequencies. Therefore, this technique is more adapted to image rapid variations than smooth variations in the object's phase.

Several algorithms have been developed in order to retrieve, from propagation-based images, quantitative information concerning the absorption and phase induced by the object. In general, this inverse problem is solved by combining a set of Fresnel diffraction patterns recorded at different distances *D*. Two examples of such algorithms in the near-field regime are the methods based on the transport of intensity equation (TIE) and the methods based on the contrast transfer function (CTF) approximation. Algorithms that calculate the phase and absorption of an object by using a single PB image have been developed (see, for instance, Gureyev et al., 1995, Bronnikov et al., 1999, Paganin et al., 2002, Gureyev et al., 2004, Beltran et al., 2010), which however impose very strong constraints on the object characteristics. In the following, we will present the basic principles of the image formation in the PBI technique and we will derive from these general equations a method for phase retrieval in the near-field regime based on a mixed TIE-CTF approach (Guigay et al., 2007). We will then briefly describe the requirements of PBI in terms of beam coherence and the achievable spatial resolution.

2.4.1 General PBI formalism

The theoretical framework for the PBI description is the Fresnel diffraction theory. Let us consider a monochromatic spatially coherent wave field of wavelength λ incident on a thin object characterized by a complex refractive index distribution $n(x, y, z)$. The expression of the wave at the exit surface of the object, as we saw, can be calculated by multiplying the incoming wave by the object complex transmission function (eq. 2.2).

Now, let us consider that the exiting wave Ψ_{obj} propagates over a distance D before being recorded by the detector. Under the assumption that the coherent wave field Ψ_{obj} is paraxial, that is, all of the non-negligible plane-wave components of the field make a small angle with respect to the optic axis, the expression for the wave after a distance D can be written as:

$$\Psi_D(\mathbf{x}) = P_D(\mathbf{x}) * \Psi_{obj}(\mathbf{x}) \tag{2.21}$$

where $*$ denotes convolution, $\mathbf{x} = (x, y)$ denotes the spatial coordinates in the plane perpendicular to the propagation direction z and $P_D(\mathbf{x})$ is the so-called Fresnel propagator, which is expressed by (Born and Wolf, 1999):

$$P_D(\mathbf{x}) = \frac{\exp(i2\pi D/\lambda)}{i\lambda D}\exp\left(i\frac{\pi}{\lambda D}|\mathbf{x}|^2\right) \tag{2.22}$$

Propagation of a wave in free space can also be calculated in the Fourier domain. The Fourier transform of the Fresnel propagator can be written analytically as:

$$\tilde{P}_D(\mathbf{f}) = \exp(i2\pi D/\lambda)\cdot\exp\left(-i\pi\lambda D|\mathbf{f}|^2\right) \tag{2.23}$$

where $\boldsymbol{f} = (f_x, f_y)$ indicates the spatial frequency coordinates. If we denote with $\tilde{\Psi}_{obj}$ and $\tilde{\Psi}_D$ the Fourier transforms of Ψ_{obj} and Ψ_D respectively, the convolution in eq. 2.21 can be expressed in the Fourier domain as:

$$\tilde{\Psi}_D(\mathbf{f}) = \tilde{P}_D(\mathbf{f})\cdot\tilde{\Psi}_{obj}(\mathbf{f}) \tag{2.24}$$

The intensity impinging on the detector after the effective propagation distance D is given by:

$$I_D(\mathbf{x}) = |\Psi_D(\mathbf{x})|^2 = |P_D(\mathbf{x}) * \Psi_{obj}(\mathbf{x})|^2 \tag{2.25}$$

Its Fourier transform can be written in the near-field diffraction regime as (Guigay, 1977):

$$\tilde{I}_D(\mathbf{f}) = \int T\left(\mathbf{x} - \frac{\lambda D\mathbf{f}}{2}\right)T^*\left(\mathbf{x} + \frac{\lambda D\mathbf{f}}{2}\right)\exp(-i2\pi\mathbf{x}\cdot\mathbf{f})\,dx \tag{2.26}$$

The transport of intensity equation (TIE) can be obtained from eq. 2.26. Under the assumption that the effective propagation distance is small, we can approximate the transmission function T by using a first order Taylor expansion (Turner et al., 2004):

$$T\left(\mathbf{x}+\frac{\lambda D\mathbf{f}}{2}\right)\approx T(\mathbf{x})+\frac{1}{2}\lambda D\mathbf{f}\cdot\nabla T(\mathbf{x}) \tag{2.27}$$

Substituting eq. 2.27 into eq. 2.26 and keeping only the terms linear with respect to D yields:

$$I_D(\mathbf{x})=I_T(\mathbf{x})-\frac{\lambda D}{2\pi}\nabla\left[I_T(\mathbf{x})\nabla\phi(\mathbf{x})\right] \tag{2.28}$$

Eq. 2.28 is equivalent, for small distances D, to the following expression:

$$\nabla\left[I_T(\mathbf{x})\nabla\phi(\mathbf{x})\right]=-\frac{2\pi}{\lambda}\frac{\partial}{\partial z}I_T(\mathbf{x}) \tag{2.29}$$

which is known as the transport of intensity equation (Teague, 1982).

If the intensity of the unpropagated wave Ψ_{obj} is sufficiently slowly varying in the plane perpendicular to the propagation direction, I_T can be moved outside the gradient operator and eq. 2.28 becomes:

$$I_D(\mathbf{x})=I_T(\mathbf{x})\left[1-\frac{\lambda D}{2\pi}\nabla^2\phi(\mathbf{x})\right] \tag{2.30}$$

Under the approximation of small propagation distances and slowly varying object absorption, the contrast is therefore proportional to the object phase Laplacian. Furthermore, it increases linearly with the propagation distance D, until the value of D is sufficiently large for the approximation employed in eq. 2.27 to break down. Eq. 2.30 can be used to retrieve the object phase from the measurement of the intensity at a single propagation distance, under appropriate conditions, as shown by different authors (see, for example, Gureyev et al., 1995, Bronnikov et al., 1999, Paganin et al., 2002, Beltran et al., 2010).

In the next section we will present a more general phase retrieval algorithm due to Guigay et al. (Guigay et al., 2007), similar to a previously developed method by Wu and Liu (Wu and Liu, 2003), which imposes less stringent conditions on the object and on the considered propagation distance.

2.4.2 Phase retrieval in the mixed TIE-CTF approach

As we have seen, the TIE approximation (eq. 2.28) can be obtained under the assumption of large Fresnel numbers. An alternative approach for simplifying eq. 2.26 is the so-called contrast transfer function (CTF) approximation, which is based on linearizing the object transmission function with respect to the amplitude and phase modulations (cf. eqs. 2.3 and 2.4):

$$T(\mathbf{x}) \approx 1 - B(\mathbf{x}) - i\phi(\mathbf{x}) \tag{2.31}$$

This approximation is valid for weak absorption and slowly varying phase:

$$B(\mathbf{x}) \ll 1 \qquad \text{and} \qquad \left|\phi(\mathbf{x}) - \phi(\mathbf{x} + \lambda D\mathbf{f})\right| \ll 1 \tag{2.32}$$

If we substitute eq. 2.31 into eq. 2.26 and we keep only the first-order terms, we get (Guigay, 1977):

$$\tilde{I}_D(\mathbf{f}) = \delta(\mathbf{f}) - 2\cos\left(\pi\lambda D|\mathbf{f}|^2\right)\tilde{B}(\mathbf{f}) + 2\sin\left(\pi\lambda D|\mathbf{f}|^2\right)\tilde{\phi}(\mathbf{f}) \tag{2.33}$$

which is the so-called CTF approximation. Eq. 2.33 can be used for phase retrieval by considering images acquired at different distances. Extraction algorithms based on CTF do not require the images to be acquired at small distances like in the TIE methods, but their validity condition is limited to the case of weak absorption and slowly varying phase. A generalization of both CTF and TIE can be obtained in the following way (Guigay et al., 2007). If we make the assumption of slowly varying phase, eq. 2.26 can be rewritten by linearizing only the phase term:

$$\tilde{I}_D(\mathbf{f}) = \int \exp(-i2\pi\mathbf{x}\cdot\mathbf{f})\, A\left(\mathbf{x} - \frac{\lambda D\mathbf{f}}{2}\right) A\left(\mathbf{x} + \frac{\lambda D\mathbf{f}}{2}\right) \times \left[1 + i\phi\left(\mathbf{x} - \frac{\lambda D\mathbf{f}}{2}\right) - i\phi\left(\mathbf{x} + \frac{\lambda D\mathbf{f}}{2}\right)\right] d\mathbf{x} \tag{2.34}$$

Developing the multiplication, eq. 2.34 can be rewritten as a sum of integrals. Making variable changes $\mathbf{y} = \mathbf{x} - \lambda D\mathbf{f}/2$ and $\mathbf{y} = \mathbf{x} + \lambda D\mathbf{f}/2$, respectively, and recombining terms yields:

$$\begin{aligned}\tilde{I}_D(\mathbf{f}) = \tilde{I}_D^{\phi=0} &+ \sin\left(\pi\lambda D|\mathbf{f}|^2\right)\int A(\mathbf{x})\phi(\mathbf{x})\exp(-i2\pi\mathbf{x}\cdot\mathbf{f}) \times \left[A(\mathbf{x} + \lambda D\mathbf{f}) + A(\mathbf{x} - \lambda D\mathbf{f})\right] d\mathbf{x} \\ &+ i\cos\left(\pi\lambda D|\mathbf{f}|^2\right)\int A(\mathbf{x})\phi(\mathbf{x})\exp(-i2\pi\mathbf{x}\cdot\mathbf{f}) \times \left[A(\mathbf{x} + \lambda D\mathbf{f}) - A(\mathbf{x} - \lambda D\mathbf{f})\right] d\mathbf{x}\end{aligned} \tag{2.35}$$

$\tilde{I}_D^{\phi=0}$ is the Fourier transform of the intensity at distance D if the phase was zero and can be approximated by $\tilde{I}_T$. If the object absorption is slowly varying, we can make the approximations $A(\mathbf{x} + \lambda D\mathbf{f}) + A(\mathbf{x} - \lambda D\mathbf{f}) \approx 2A(\mathbf{x})$ and $A(\mathbf{x} + \lambda D\mathbf{f}) - A(\mathbf{x} - \lambda D\mathbf{f}) \approx 2\lambda D\mathbf{f}\cdot\nabla A(\mathbf{x})$, which give:

$$\tilde{I}_D(\mathbf{f}) = \tilde{I}_T(\mathbf{f}) + 2\sin\left(\pi\lambda D|\mathbf{f}|^2\right)\mathcal{F}\{I_T\phi\}(\mathbf{f}) + \cos\left(\pi\lambda D|\mathbf{f}|^2\right)\frac{\lambda D}{2\pi}\mathcal{F}\{\nabla(\phi\nabla I_T)\}(\mathbf{f}) \tag{2.36}$$

where $\mathcal{F}$ indicates a Fourier transform operation. Eq. 2.36 generalizes both the TIE and the CTF. If $D \to 0$ the TIE is obtained (eq. 2.28), while if the absorption is assumed to be weak the CTF (eq. 2.33) is obtained. Equation 2.36 can be solved by considering the third term as a perturbation term, which vanishes for homogeneous absorption. Different distances are taken into account by a linear least squares fitting. Considering $\mathcal{F}\{I_T\phi\}(\mathbf{f})$ as the unknown, the following minimization problem is posed:

$$\mathcal{F}\{I_T\phi\}(\mathbf{f}) = \arg\min_{\mathcal{F}\{I_T\phi\}} \sum_D \left| C_D(\mathbf{f})\,\mathcal{F}\{I_T\phi\}(\mathbf{f}) + \tilde{I}_T(\mathbf{f}) + \Delta_D(\mathbf{f}) - \tilde{I}_D(\mathbf{f}) \right|^2 + \alpha \left| \mathcal{F}\{I_T\phi\}(\mathbf{f}) \right|^2 \quad (2.37)$$

where $\Delta_D(\mathbf{f}) = \cos\left(\pi\lambda D|\mathbf{f}|^2\right)(\lambda D/2\pi) \times \mathcal{F}\{\nabla(\phi\nabla I_T)\}(\mathbf{f})$, $C_D(\mathbf{f}) = 2\sin\left(\pi\lambda D|\mathbf{f}|^2\right)$ and α is a regularizing parameter. The minimization problem in eq. 2.37 has the solution:

$$\mathcal{F}\left\{I_T\phi^{(n+1)}\right\}(\mathbf{f}) = \frac{\sum_D C_D(\mathbf{f})\left[\tilde{I}_D(\mathbf{f}) - \tilde{I}_T(\mathbf{f}) - \Delta_D^{(n)}(\mathbf{f})\right]}{\sum_D C_D^2(\mathbf{f}) + \alpha} \quad (2.38)$$

where the first estimate of ϕ is obtained by neglecting the third term in eq. 2.36, $\phi^{(n)}(\mathbf{x})$ is the phase at iteration *n* and $\Delta_D^{(n)}(\mathbf{f}) = \cos\left(\pi\lambda D|\mathbf{f}|^2\right)(\lambda D/2\pi) \times \mathcal{F}\left\{\nabla\left(\phi^{(n)}\nabla I_T\right)\right\}(\mathbf{f})$. This procedure converges in three to five iterations in practical cases. Typically three or four distances are used.

It has been observed, however, that phase retrieval using eq. 2.38 often suffers from strong low frequency artefacts. This problem arises from the fact that the transfer function is always small in the low spatial frequency range, thus making the phase retrieval sensitive to noise (Langer et al., 2010). In the same work, an alternative approach for iteratively solving eq. 2.36 has been proposed. In this method a regularization term based upon the absorption image is introduced in order to address the problem of the low frequency distortions. For a homogeneous object, in fact, the phase and the absorption are univocally related, and the absorption information can be used to correct the phase image. Since the regularization term based upon absorption is applied only to the low spatial frequencies in this method, however, this allows the homogeneous object assumption to be introduced only in the low frequency range.

2.4.3 PBI coherence requirements and spatial resolution

In the previous paragraphs we have described the principles of the image formation in PBI for a monochromatic component of the wave-field radiated by the source. However, it is possible to demonstrate that phase-contrast propagation-based images can be obtained even with a fully polychromatic beam, as Wilkins et al. (Wilkins et al., 1996) proved both theoretically and experimentally by using a conventional microfocus X-ray tube. An important feature of PBI is in fact its relative insensitivity to polychromaticity (i.e. lack of temporal coherence) in the radiation source.

However, the method is very sensitive to the lack of spatial coherence of the radiation illuminating the object. If the angular size of an incoherent source as seen from the sample is too large ($\alpha = S/L$, with S being the lateral source size and L the source-to-sample distance), the propagation-based phase contrast is destroyed because the interference fringes visibility vanishes. For long synchrotron beamlines such as ID17 at the ESRF (L ~ 145 m), the transverse coherence length $l_c = \lambda/\alpha$ is as high as 175 μm in the vertical direction at 25 keV (see chapter 3), while a microfocus X-ray tube with a typical source size of 20 μm delivers X-rays with l_c = 1.5 μm at 25 keV and at 0.5 m from the source. Normal X-ray tubes with larger source size instead deliver radiation with insufficient transverse coherence length. Therefore the application of propagation-based imaging to X-ray tubes is limited to microfocus sources, which, however, are characterized by weak integral X-ray fluence. This is one of the reasons that has prevented up to now the widespread use of the PBI method in the current medical practice.

The visualization of the PB signal imposes strong requirements also in terms of the detector spatial resolution. If I_p is the signal obtained with a point-like source and an ideal detector with infinitely small spatial resolution, the recorded signal I_{det} can be written as the following convolution (Born and Wolf, 1999, Gureyev et al., 2008):

$$I_{\mathrm{det}}(x,y) = I_p(x,y) * h(x,y) * PSF_{\mathrm{det}}(x,y) \tag{2.39}$$

where (x,y) is a point on the two-dimensional detector plane, h is a function expressing the projection of the angular source size α scaled by the ratio d/L and PSF_{det} is the point spread function of the detector. The effect of this convolution chain is that of a low-pass filter removing the high frequencies of the interference image.

For untreated images and in the near-field regime, the resolution is limited by the fringe spacing to about $\sqrt{\lambda D}$, which corresponds to the radius of the first Fresnel zone (Born and Wolf, 1999). The resolution in the PBI technique is also linked to the image processing and to the sample thickness (t). The latter contributes with a blurring equal to $\sqrt{\lambda t}$, that is 0.2 μm for a 1 mm thick sample and for an energy of 25 keV: therefore this effect can be usually neglected since smaller than the pixel size.

As we mentioned, in order to observe the interference fringes, a detector with a suitable spatial resolution is required. For instance, for a sample-to-detector distance d = 5 m, very long source-to-sample distance $L \gg d$ (parallel beam geometry) and an energy of 25 keV, at least a resolution of ~16 μm is necessary. This is a drawback for possible clinical applications since the smaller the pixel size the higher is the dose required for achieving a given signal-to-noise ratio (defined in chapter 3). However, this problem can be overcome by using magnification geometries, for example in laboratory X-ray imaging with microfocus sources where $L \sim d$. In this case, in fact,

the object image is magnified by a factor $M = (L+d)/L$. As a direct consequence, the effective pixel size at the object position is smaller than the physical detector pixel size.

2.5 Analyzer-based imaging

The typical ABI setup consists of a parallel quasi-monochromatic X-ray beam, which is used to irradiate the sample, and a perfect crystal, called the analyzer, placed between the sample and the detector. Photons traversing the sample are deviated according to the gradient of the real part of the refractive index (eqs. 2.8-2.9). The analyzer crystal acts as an angular filter, selectively accepting or rejecting such photons: only the X-rays travelling in a narrow window close to the Bragg condition for diffraction ($2d\sin\theta_B = \lambda$, where d is the crystal d-spacing, θ is the grazing angle of incidence to the crystal and λ the radiation wavelength) can reach the detector and then contribute to the image formation (Podurets et al., 1989, Bravin, 2003).

For this reason, as we will see in detail in the following, ABI (conversely to the PBI technique) is sensitive only to the component of the refraction angle that is parallel to the diffraction plane (see fig. 2.5):

$$\Delta\theta_y(x,y) = -\frac{\lambda}{2\pi}\frac{\partial\phi(x,y;\lambda)}{\partial y} \tag{2.40}$$

The angular filter function is given by the rocking curve (RC) of the analyzer (which actually corresponds to the convolution of the monochromator and analyzer reflectivity curves) and typically features an acceptance window (given by the RC full-width at half maximum FWHM) of a few microradians or tens of microradians. As an example, the RC FWHM when the reflection 333 of the silicon is used for both monochromator and analyzer spans the range 3.61-0.77 μrad for the energy interval 15-80 keV (XOP) (http://www.esrf.fr/computing/scientific/dabax/). The analyzer crystal can be set either in Bragg (Förster et al., 1980, Somenkov et al., 1991, Bushuev et al., 1997) or Laue (Ingal and Beliaevskaya, 1995, Chapman et al., 1996) geometry.

This technique is often referred to as “Diffraction Enhanced Imaging” (DEI). This name has been introduced by Chapman et al. (Chapman et al., 1997) to indicate their algorithm for extracting the refraction and apparent absorption images (described in chapter 4) and used later on by other authors for indicating the imaging technique itself. In this work, it has been chosen to utilize the name “analyzer-based imaging” (ABI) since it directly refers to the use of the analyzer crystal, regardless the use of a specific algorithm in the image processing.

In the following sections, the general theoretical framework for the ABI technique will be described and the geometrical optics approximation, which is considered in most of the published works on ABI and represents a very useful simplification of the general formulas, will be introduced. Considerations about the nature of the image contrast, the achievable spatial resolution and the requirements in terms of spatial and temporal coherence of the radiation will be provided.

2.5.1 General ABI formalism

The theoretical description of the ABI technique is based on the dynamical diffraction theory for perfect crystals (Zachariasen, 1945, Authier, 2001). In the following description, the case of a thick non-absorbing crystal set in symmetrical Bragg geometry is considered and any propagation effect is neglected.

The right-handed coordinates system represented in figure 2.5 will be used. The directions of the coordinate axes are chosen in such a way that axis *z* coincides with the propagation direction, (*y*,*z*) is the plane of drawing in figure 2.5 and the axis *x* has the same direction at all points of the optical axis. (*x*,*y*) therefore represents the plane of both the object and the detector, and (*y*,*z*) is the diffraction plane.

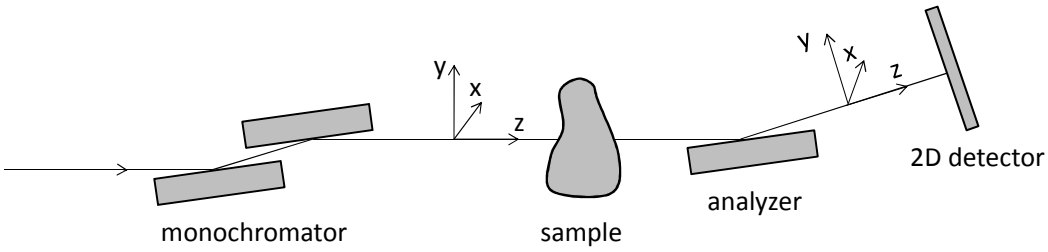

Fig. 2.5. Scheme of the setup of the analyzer-based imaging technique. The axis *z* is directed at each point of the optical axis in the propagation direction, (*y*,*z*) is the plane of drawing and represents the diffraction plane.

Let a monochromatic plane wave with unit amplitude be incident onto the sample, which is placed just before the analyzer crystal. The wave incident onto the crystal is then given by (cf. eqs. 2.2-2.5):

$$\Psi_{obj}\left(x,y\right)=T\left(x,y\right)=\exp\left[i\phi\left(x,y\right)-B\left(x,y\right)\right] \tag{2.41}$$

The amplitude of the wave diffracted by the analyzer can be expressed by the following convolution integral:

$$\Psi_{an}\left(x,y;\theta_{an}\right)=\int_{-\infty}^{+\infty}dy'\,G\left(y';\theta_{an}\right)\Psi_{obj}\left(x,y-y'\right) \tag{2.42}$$

where $G\left(y;\theta_{an}\right)$ is the point spread function of the analyzer and θ_{an} is the angular deviation of the crystal from the Bragg position θ_B. Differently from the case of PBI, where the Fresnel propagator convolves the wave function in both directions perpendicular to the optical axis (eq. 2.21), the convolution is performed in this case only in one direction.

Equation 2.42 can be rewritten as the following multiplication in Fourier space:

$$\tilde{\Psi}_{an}\left(x;v;\theta_{an}\right)=r\left(\theta_{an}+\lambda v\right)\tilde{\Psi}_{obj}\left(x;v\right) \tag{2.43}$$

where v is the spatial frequency coordinate corresponding to y, $\tilde{\Psi}_{obj}$ and $\tilde{\Psi}_{an}$ are the Fourier transforms of the complex amplitudes respectively of the incident and diffracted waves, and $r\left(v;\theta_{an}\right)$ is the amplitude reflection coefficient (ARC) of the analyzer crystal, which is equivalent to the Fourier transform of the analyzer PSF:

$$r\left(\theta_{an}+\lambda v\right)=\tilde{G}\left(v;\theta_{an}\right) \tag{2.44}$$

The function $r\left(v;\theta_{an}\right)$ is also called Takagi propagator and represents the transfer function of the analyzer.

If we consider the case of a semi-infinite perfect crystal, the crystal ARC can be written analytically as (Afanas'ev and Kohn, 1971):

$$G_{\infty}\left(y,\theta\right)=i\frac{\sigma_h}{\sigma}\exp\left(i\alpha\eta y\right)\frac{J_1\left(2\alpha\sigma y\right)}{y}H\left(y\right) \tag{2.45}$$

where J_1 is the Bessel function of the first kind and first order, H is the Heaviside step function, $\alpha=\gamma^2/\sin\left(2\theta_B\right)$, $\gamma=\sin\left(\theta_1\right)$, θ_1 is the angle between the wavevector $\vec{k}$ of the incident wave and the crystal surface, $\eta=2\sigma_0+k\gamma\theta_{an}/\alpha$, $\sigma^2=\sigma_h\sigma_{-h}$, $\sigma_0=\pi\chi_0/\left(\lambda\gamma\right)$, $\sigma_{\pm h}=\pi C\chi_{\pm h}/\left(\lambda\gamma\right)$, $\chi_{0,\pm h}$ are the Fourier components of the crystal susceptibility and C is the polarization factor.

The crystal ARC can instead be expressed by:

$$r_{\infty}\left(\theta\right)=\left\{\begin{array}{ll}\dfrac{\sigma_h}{\xi_1}, & \mathrm{Im}\left(\xi\right)<0\\ \\ \dfrac{\sigma_h}{\xi_2}, & \mathrm{Im}\left(\xi\right)<0\end{array}\right\} \tag{2.46}$$

where $\xi_{1,2}=\left(-\eta\pm\xi\right)/2$ and $\xi=\left(\eta^2-4\sigma^2\right)^{1/2}$.

2.5.2 Geometrical optics approximation

Different approximations have been proposed to simplify eq. 2.42 in order to find an analytical solution for the inverse problem of calculating the object absorption and phase from the intensity recorded on the detector. The most used methods are based on the geometrical optics (GO) approximation, but methods based on the weak object (WO) approximation (Nesterets et al., 2004, Nesterets et al., 2006) and on the linear transfer function (LTF) approximation (Paganin et al., 2004, Pavlov et al., 2004) have also been developed.

WO assumes that the variations in the object absorption are weak and that the object phase is either weak or slowly varying on the characteristic length scale of the system PSF (i.e. on the

length scale of the crystal extinction length). Under these assumptions, the object complex transmission function (eq. 2.41) can be safely linearized (Nesterets et al., 2004).

In the LTF approach, the imaging system transfer function is linearly approximated, under the assumption that the spatial Fourier spectrum of the wave incident onto the analyzer is non-negligible over a frequency range for which the ARC of the analyzer is well approximated by a linear function (Paganin et al., 2004, Pavlov et al., 2004).

The GO approximation (Gureyev and Wilkins, 1997, Bushuev et al., 1998) is valid if the phase of the wave incident onto the crystal is a slowly varying function over the length scales on the order of the crystal extinction length. It can be shown that this condition is equivalent to:

$$N_T = \left(h/\lambda\right)^2 \left| \frac{r\left(\theta_{an}\right)}{r''\left(\theta_{an}\right)} \right| \gg 1 \tag{2.47}$$

where h is the size of the smallest feature in the object, or the resolution limit of the imaging system if this is larger, and $r''\left(\theta_{an}\right)$ denotes the second derivative of the Takagi propagator. N_T was termed "Takagi number" in analogy with the Fresnel number in propagation-based imaging (Pavlov et al., 2004). More complex formulations of the Takagi number taking into account the quasi-monochromaticity and divergence of the beam, the source size and the detector resolution have also been derived (Nesterets et al., 2006, Kitchen et al., 2007). If the condition in eq. 2.47 holds, eq. 2.42 can be approximated, by using the stationary phase method (Gureyev and Wilkins, 1997), by the following expression:

$$\Psi_{an}\left(x,y;\theta_{an}\right) = r\left(\theta_{an} - k^{-1}\frac{\partial\phi\left(x,y\right)}{\partial y}\right)\Psi_{obj}\left(x,y\right) \tag{2.48}$$

By taking the square modulus of eq. 2.48 and using eq. 2.40 for the refraction angle, an expression relating the intensity of the diffracted wave at a point (x,y) in the detector plane to the intensity of the wave exiting the sample at a corresponding point in the object plane can be written:

$$I\left(x,y;\theta_{an}\right) = I_T\left(x,y\right) R_{an}\left[\theta_{an} + \Delta\theta_y\left(x,y\right)\right] \tag{2.49}$$

where I_T represents the intensity transmitted through the object and where we have introduced the reflectivity curve of the crystal, R_{an}, which is equal to the square modulus of the Takagi propagator:

$$R_{an}\left(\theta\right) = \left|r\left(\theta\right)\right|^2 \tag{2.50}$$

In the real experimental case one or more crystals need to be used before the object in order to monochromatize/collimate the beam. The beam illuminating the object, however, is not perfectly monochromatic and parallel, but maintains a small degree of polychromaticity and divergence which depends on the used crystals and on the chosen reflections. Let us indicate with $d_i\left(\theta'\right)$ the

intensity distribution of the beam incident on the first monochromator crystal, such that $I_i(x,y) = \int_{\theta_{\min}}^{\theta_{\max}} d\theta' \, d_i(x,y;\theta')$, where θ' is the detuning angle from the Bragg condition and $I_i(x,y)$ is the integral intensity incident on the first monochromator crystal. The following expression can be written for the intensity distribution $d_0(\theta')$ incident onto the object:

$$d_0(x,y;\theta') = d_i(x,y;\theta') \Pi_{j=1..N} R_j(\theta') \tag{2.51}$$

where $\Pi_{j=1..N} R_j(\theta')$ indicates the product of the reflectivity curves of the N used monochromators. The integrated intensity incident onto the object can be calculated as:

$$I_0(x,y) = \int d\theta' \, d_i(x,y;\theta') \Pi_{j=1..N} R_j(\theta') = d_i(x,y;\theta'=0) \int d\theta' \Pi_{j=1..N} R_j(\theta') \tag{2.52}$$

where we have assumed, in the second equation, that the intensity distribution is constant over the narrow angle range where the reflectivity of the crystals is non-negligible.

Equation 2.49, expressing the intensity of the wave diffracted by the analyzer as a function of the intensity of the wave exiting the object, needs then to be rewritten in the case of a quasi-monochromatic and slightly divergent beam as:

$$I(x,y) = I_T(x,y) \, R\left(\theta_{an} + \Delta\theta_y(x,y)\right) \tag{2.53}$$

where we have introduced the so-called rocking curve R of the analyzer, which is defined as the ratio between the intensity diffracted by the analyzer and the intensity incident on it, and is given by:

$$R(\theta) = \frac{\int d\theta' \, d_i(\theta') \left(\Pi_{j=1..N} R_j(\theta')\right) R_{an}(\theta - \theta')}{\int d\theta' \, d_i(\theta') \Pi_{j=1..N} R_j(\theta')} \tag{2.54}$$

The rocking curve (RC) is then expressed as the normalized convolution of the monochromators and analyzer reflectivities. It is easy to show that eq. 2.53 reduces to eq. 2.49 in the ideal case of a perfectly parallel and monochromatic beam incident onto the first monochromator, that is, $I(\theta') = \delta(0)$, where $\delta(0)$ indicates a Dirac delta function centered on the Bragg angle. As an example, the reflectivity curve for the Si(333) reflection in Bragg geometry and the rocking curve in the case of a polychromatic beam incident on a Si(333)-Si(333) monochromator-analyzer system are reported in figure 2.6, for a selected photon energy of 40 keV.

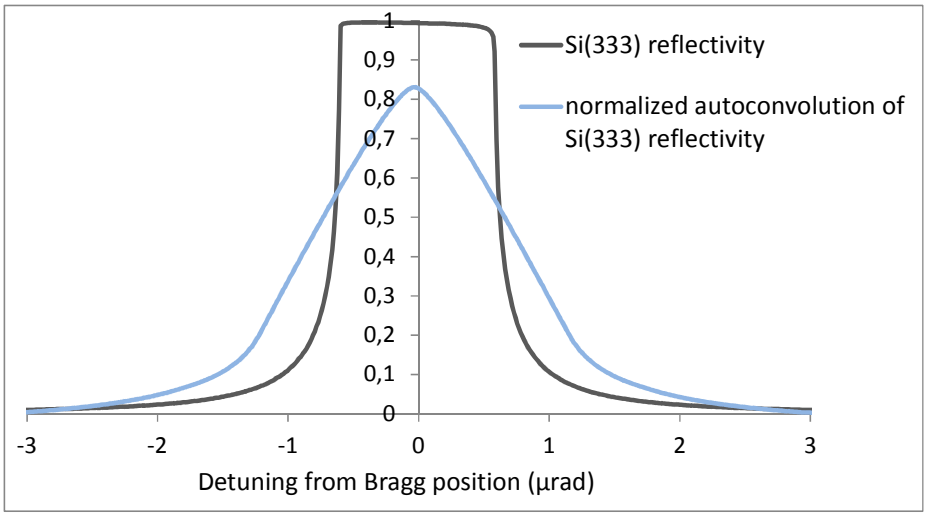

Fig. 2.6. Reflectivity curve for a Si(333) crystal reflection at 40 keV, and rocking curve for a Si(333)-Si(333) monochromator-analyzer system.

The geometrical optics approximation, whose central result is represented by eq. 2.53, allows relating in a simple way the intensity recorded by the detector to the intensity transmitted through the sample. In particular, under this approach the intensity recorded at a point (x,y) on the detector depends only, for a given orientation of the analyzer, on the absorption and refraction angle introduced at the corresponding point (x,y) on the object. Equation 2.53 represents the starting point of the various extraction algorithms that are based on the geometrical optics approximation and aim at solving the inverse problem of calculating the object absorption, refraction and scattering contributions from the recorded images. A theoretical analysis and experimental comparison of five among the most used and well-known GO extraction algorithms will be presented in chapter 4.

2.5.3 Image contrast and sensitivity in ABI

By considering eq. 2.53, it is possible to make some general considerations about the nature of the image contrast in the ABI technique. Besides the contrast generated by the object absorption, formally equivalent to that of conventional X-ray imaging, a second type of contrast determined by the filtration introduced by the analyzer crystal is produced. In particular:

- The Compton scattered X-rays, which represent a source of image blurring in conventional X-ray imaging, are not diffracted by the analyzer and therefore do not contribute to the image contrast. The result is a noise reduction and a consequent improvement of the image quality.
- The small-angle scattered X-rays (SAXS), typically encountered when considering biological tissues, and arising from tissue structures at the nanometer scale, are characterized by angles in the milliradians range and are therefore not diffracted by the analyzer. This gives rise to the so-called “extinction contrast”, which can provide,

potentially, a method to distinguish tissues with equivalent absorption but different SAXS contribution. The ultrasmall-angle scattered X-rays (USAXS), instead, generated by structures in the order of hundreds of nanometers up to micrometers and characterized by angles of several microradians, partially fall within the acceptance window of the analyzer and therefore contribute to the image signal. The effect of USAXS, as we will see in chapter 4, is a broadening of the measured experimental RC.

- The "refraction contrast", finally, is the most important contribution to contrast in ABI. The angular deviations of the beam due to the refraction inside the object are converted, through the modulation provided by the RC, into changes of intensity in the recorded image. When the analyzer is set at the angle corresponding to the peak of the RC, it diffracts the unrefracted X-rays with maximum efficiency, while refracted X-rays are attenuated. The objects edges, where refraction is stronger, tend to appear less intense (darker) than the background. When the analyzer is set at one of the slopes of its RC, the refraction angles in the direction corresponding to increasing values of the RC will give rise to an increased image intensity, while refraction angles in the opposite direction will produce a decrease in intensity. The edges will therefore appear black or white according to the sign of the gradient of the refractive index decrement (see eqs. 2.40 and 2.8).

The sensitivity of the ABI technique is determined by the gradient of the slopes of the analyzer RC, which is at first approximation inversely proportional to the RC width: the narrower the curve width (and then the higher the slopes gradient), the higher the extinction and refraction contrast. This concept will be better formalized and exemplified in chapter 7. As previously discussed, phase sensitive techniques are better suited to higher energies than conventional absorption imaging because of the weaker energy dependence of the delta term ($1/E^2$) with respect to beta ($1/E^4$). The ABI technique particularly benefits from high energies since the rocking curve width for a given crystal reflection decreases linearly with increasing energy, and this partially compensates for the $1/E^2$ behaviour for the refraction angle. Overall, ABI effectiveness is proportional to $1/E$.

The fact that the ABI sensitivity is inversely proportional to the rocking curve width encourages the quest for narrow rocking curves. The latter can be achieved utilizing different crystal reflections (Chapman et al., 1997, Zhong et al., 2000, Rigon et al., 2002). For instance, the use of the Si(333) reflection at 40 keV produces a rocking curve that is about four times narrower than that of the Si(111) reflection (http://www.esrf.fr/computing/scientific/dabax/). Therefore, the associated improvement in refraction contrast can be 4-fold.

2.5.4 ABI coherence requirements and spatial resolution

X-rays incident on the sample must be almost parallel and monochromatic with a typical $\Delta E/E$ of perfect crystal (10^{-4}). Anyway, no particular restrictions have to be fulfilled by the beam arriving on the monochromator since the ABI setup itself generally warrants the necessary beam collimation and monochromaticity. The advantages of the synchrotron radiation for the

implementation of this technique mainly reside in the high beam collimation and in the delivered high photon flux given the unavoidable considerable loss of photons occurring in the monochromatization/collimation process.

The spatial resolution of the technique is intrinsically affected by the presence of the analyzer crystal. In the simplified geometrical optics description, a point of the image corresponds to an angularly deviated X-ray from a given point of the projected object (see eq. 2.53). In reality, when the general dynamical diffraction theory is considered, the effect of the analyzer onto the incident wave is described by a point spread function (PSF) of finite width (see eqs. 2.42 and 2.45). A generic point of the object, therefore, does not correspond any more to a unique point on the detector plane, but to a certain intensity distribution whose width is determined by the width of the crystal PSF. It is possible to show that the value of the FWHM of the analyzer PSF projected onto the detector plane is on the order of $2p\cdot\cos\theta$, where p is the crystal extinction depth and θ is the angle between the incident beam and the analyzer (Pagot, 2004). This value amounts, in the hard X-rays energy range, to a few micrometers (Authier, 2001).

The effect of the finite resolution of the detector and of the finite size of the source can be considered by convoluting the signal with the point-spread function (PSF) of the detector and with the source distribution function as previously discussed (eq. 2.39).

Fresnel diffraction occurring in the path between the sample and the detector affects the spatial resolution of ABI images. In general, the analyzer-to-detector distance is kept as low as possible in order to reduce the propagation contribution to the signal. On the other hand, this effect has also been demonstrated to be able to produce a signal-to-noise ratio improvement in specific experimental conditions (Coan et al., 2005). The combination of the ABI and PBI has been studied experimentally and theoretically in several published works (Pavlov et al., 2004, Nesterets et al., 2005, Pavlov et al., 2005, Nesterets et al., 2006, Nesterets et al., 2006, Bravin et al., 2007).

2.6 Grating interferometry

Grating interferometry (GIFM), also called grating-based imaging, or X-ray Talbot interferometry, is a relatively new X-ray phase-contrast imaging technique. The physical principles that are at the basis of the GIFM technique have been known since long time: the Talbot effect, i.e. the self imaging of periodic structures under coherent illumination, was discovered more than 170 years ago by H.F. Talbot (Talbot, 1836) and first analytically explained by Lord Rayleigh in 1881 (Rayleigh, 1881). It is a remarkable manifestation of Fresnel diffraction and the basis for useful applications in visible light (Keren and Kafri, 1985, Lohmann and Thomas, 1990, Arrizon and Lopezolazagasti, 1995) and soft X-ray (Ress et al., 1994) optics. The first full observation of the Talbot effect for X-rays is reported by Cloetens et al. (Cloetens et al., 1997) and its first experimental use for imaging by David et al. (David et al., 2002).

The GIFM technique, as we will see in the following, consists in illuminating the imaged object with highly spatially coherent X-rays, and in analyzing the radiation transmitted through the object using a pair of gratings (see figure 2.7). The first is generally a "phase grating" (also referred to as "transmission grating"), which introduces a periodic phase shift onto the beam but negligible absorption. The second, which is an "absorption grating", is placed at a distance where the interference fringes of the first grating give rise to the so-called self-imaging effect.

2.6.1 General GIFM formalism

For the theoretical description of the Talbot effect, we will consider the case of a monochromatic plane wave of wavelength λ, propagating in the z direction and incident on a plane object. We will assume that this object has a complex transmission function $T(y)$ (see eq. 2.3) independent of x and periodic, with period a, in the y direction. An example of such an object is a grating having lines parallel to the x direction and periodic in the y direction. The complex transmission function can be written with a Fourier series as:

$$T(y) = \sum_n b_n \exp\left(i2\pi \frac{ny}{a}\right) \tag{2.55}$$

where b_n is the amplitude of the nth harmonic. Let us assume that the object period a is much bigger than λ (so that the diffracted beams are close to the forward direction and the paraxial approximation holds) and that the illuminating wave has unit amplitude. The wavefield generated behind the periodic object after a propagation distance z can therefore be expressed by using Fresnel diffraction (see eqs. 2.21-2.22) as:

$$\Psi(y,z) = \frac{1}{\sqrt{i\lambda z}} \int T(y') \exp\left[\frac{i\pi}{\lambda z}(y-y')^2\right] dy' \tag{2.56}$$

By inserting eq. 2.55 in eq. 2.56, it can be demonstrated (Guigay, 1971) that the wavefield Ψ is equal to:

$$\Psi(y,z) = \sum_n b_n \exp\left(-i\pi \frac{n^2 z\lambda}{a^2}\right) \exp\left(i2\pi \frac{ny}{a}\right) \tag{2.57}$$

The resulting wavefield, therefore, is not only a periodic function in the y direction but also in the propagation direction z.

Different interesting cases can be considered for particular values of the propagation distance D. When D is an integer multiple of the so-called Talbot distance $D_T = 2a^2/\lambda$, the wavefield Ψ equals the periodic object complex transmission function T:

$$\Psi(y,D) = T(y) \qquad \text{if} \qquad D = 2m\,a^2/\lambda\ , \qquad m = 0,1,2... \tag{2.58}$$

Self-images of the periodic object are therefore generated at these distances. This is the so-called Talbot effect. Fractional Talbot effects appear for the following values of *D*:

$$\Psi\left(y,D\right)=T\left(y+a/2\right) \qquad \text{if} \qquad D=\left(2m+1\right)a^2/\lambda \ , \ m=0,1,2... \tag{2.59}$$

$$\Psi\left(y,D\right)=\frac{1}{\sqrt{2i}}\left[T\left(y\right)+iT\left(y+a/2\right)\right] \quad \text{if} \quad D=\left(m+1/2\right)a^2/\lambda \ , \ m=0,1,2... \tag{2.60}$$

For even fractional Talbot distances (eq. 2.59), therefore, the images obtained are shifted versions of the periodic object self-image. For odd fractional Talbot distances (eq. 2.60), the wavefield is instead expressed as a linear combination of the complex transmission function *T* and of its shifted version.

Let us now consider the case of a pure phase object, for instance a phase grating. The object complex transmission function can therefore be expressed by $T\left(y\right)=\exp\left[i\varphi\left(y\right)\right]$. At distances that are integer multiples of the Talbot distance (eq. 2.58) or at the even fractional Talbot distances (eq. 2.59) no image contrast is observed. At odd fractional Talbot distances, instead, the following expression can be obtained from eq. 2.60 for the intensity in the observation plane:

$$\left|\Psi\left(y,D\right)\right|^2=1+\sin\left[\varphi\left(y\right)-\varphi\left(y+a/2\right)\right] \tag{2.61}$$

At odd fractional Talbot distances, therefore, the phase modulation induced by the periodic structure, which was not measurable in a plane positioned immediately after the object, is converted to a measurable intensity modulation by a simple act of free space propagation. This is a central result that will be used in the following and that is at the basis of the GIFM technique.

Let us suppose that the wave illuminating the phase grating has unit amplitude but is non-plane, and therefore can be expressed by $\exp\left[i\phi\left(x,y\right)\right]$, where the phase ϕ is a function of the spatial coordinates in the plane perpendicular to the optical axis. Note that the distortion of the incident wavefront includes the case of refraction introduced by an object placed before the phase grating. Eq. 2.57, which expresses the wavefield exiting the phase grating after a free-space propagation distance *z*, needs then to be rewritten as (Momose et al., 2003):

$$\Psi\left(x,y,z\right)=\sum_n b_n \exp\left(-i\pi\frac{n^2z\lambda}{a^2}\right)\times\exp\left[i2\pi\frac{n}{a}\left(y-z\Delta\theta_y\left(x,y\right)\right)\right] \tag{2.62}$$

where $\Delta\theta_y$ is the component of the angle between the wave propagation direction and the optical axis in the plane perpendicular to the grating lines (see eq. 2.40). The factor describing the periodicity in the propagation direction is unchanged in eq. 2.62 compared to eq. 2.57. The second factor in eq. 2.62, instead, expresses the fact that the fringes are locally deformed in the *y* direction, in proportion to both $\Delta\theta_y$ and *z*. Eq. 2.61 for the intensity of the wave at the observation plane needs then to be rewritten as:

$$\left|\Psi\left(x,y,D\right)\right|^2 = 1+\sin\left[\varphi\left(y-z\Delta\theta_y\left(x,y\right)\right)-\varphi\left(y-z\Delta\theta_y\left(x,y\right)+a/2\right)\right] \tag{2.63}$$

Typically, phase gratings introducing a phase shift equal to $\pi/2$ or π are used. In the first case, fringes with the same period of the phase grating are generated at odd fractional Talbot distances, while in the second case the fringes period is half this value.

2.6.2 Phase stepping method

The phase grating period is usually equal to a few microns. In order to resolve the interference fringes, therefore, a detector with very high spatial resolution would need to be used. However, such spatial resolution is not achieved by standard detectors, therefore, in general, an alternative method for measuring the intensity fringes is usually employed, the so-called phase stepping method. An absorption grating having the same period of the fringes generated by the phase grating is placed at the considered fractional Talbot distance in front of the detector, and is scanned in the direction perpendicular to the grating lines with respect to the first grating (fig. 2.7(a)).

For each spatial position on the detector plane, the intensity profile obtained by scanning the gratings is given, in the case of perfect spatial coherence, perfect monochromaticity and perfectly rectangular gratings, by a saw-tooth profile in the case of a $\pi/2$ phase grating and by a rectangular profile in the case of a π phase grating. However, due to the limited spatial coherence and monochromaticity of the used X-ray beam, and to the fact that the gratings profiles are not perfectly rectangular, the intensity profile can often be approximated by a sinusoid (fig. 2.7(b)).

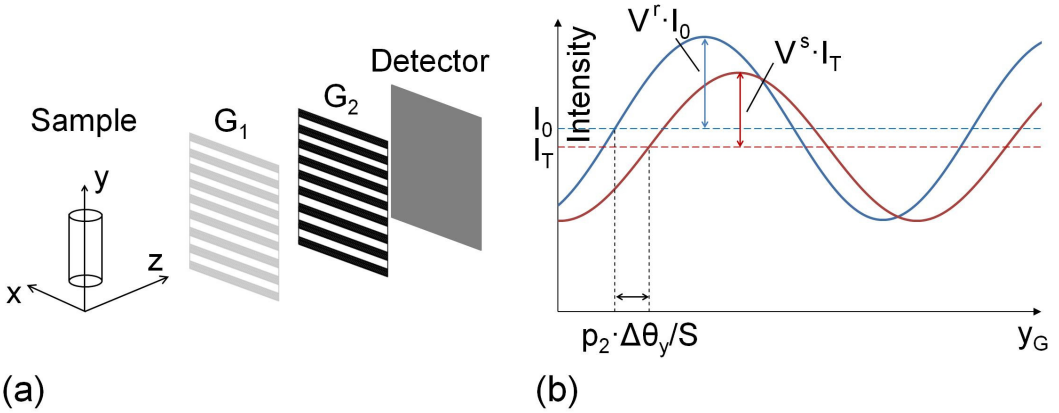

Fig. 2.7 (a) Scheme of the GIFM setup used for this study, with gratings lines parallel to the *x* axis, (b) sinusoidal fringe pattern measured with the phase stepping method. I_0 represents the intensity incident on the object, I_T the transmitted intensity. V^r the fringes visibility in the reference image and V^s the fringes visibility in the sample image.

Let us denote with G_1 and G_2 respectively the phase and the absorption gratings. We will indicate with T_{GR} the average intensity transmission through the gratings and with $S = p_2/d_{Talbot}$ (where p_2 is the period of the absorption grating and d_{Talbot} is the considered fractional Talbot distance) the refraction angle needed to shift the intensity fringes by one period. The intensity

recorded at each point of the detector will be, for a given value of the relative shift y_G between the two gratings (Pfeiffer et al., 2008):

$$I\left(y_G;x,y\right)=T_{GR}\left(x,y\right)I_T\left(x,y\right)\left[1+V\left(x,y\right)\sin\left(\psi\left(x,y\right)+\frac{2\pi}{p_2}y_G+\frac{2\pi}{S}\Delta\theta_y\left(x,y\right)\right)\right]= \quad (2.64)$$
$$=T_{GR}\left(x,y\right)I_TG\left(y_G;\Delta\theta_y;x,y\right)$$

where we have indicated with $I_T(x,y)$ the intensity transmitted through the object, with $\psi(x,y)$ the shift of the sinusoidal fringe profile measured with no object in the beam and with $V(x,y)$ the fringes visibility, which is defined as:

$$V\left(x,y\right)\equiv\frac{I_{\max}\left(x,y\right)-I_{\min}\left(x,y\right)}{I_{\max}\left(x,y\right)+I_{\min}\left(x,y\right)} \quad (2.65)$$

with I_{max} and I_{min} being respectively the maximum and minimum values of the intensity fringes profile. Function G that we have introduced in eq. 2.64 is a function of both the object and the imaging system.

Absorption, refraction and scattering sample information can be retrieved by comparing, for each detector pixel, the sinusoidal intensity profile obtained with the sample in the beam with that obtained after removing the sample. Let us rewrite eq. 2.64 as:

$$I^{r,s}\left(y_G;m,n\right)=a_0^{r,s}\left(m,n\right)+a_1^{r,s}\left(m,n\right)\sin\left(ky_G+\varphi_1^{r,s}\left(m,n\right)\right) \quad (2.66)$$

where the superscripts *r,s* indicate respectively the reference values measured without the sample and the values measured with the sample in the beam, and (m,n) represent the pixel indices in the x and y directions. The coefficients a_0, a_1 and φ_1 can be computed with the use of the fast Fourier transform. The intensity transmission A^2 through the sample (see eqs. 2.3-2.4) is then given by:

$$A^2\left(m,n\right)=a_0^s\left(m,n\right)\Big/a_0^r\left(m,n\right) \quad (2.67)$$

while the refraction angle $\Delta\theta_y$ can be calculated as:

$$\Delta\theta_y\left(m,n\right)=\frac{S}{2\pi}\left[\varphi_1^s\left(m,n\right)-\varphi_1^r\left(m,n\right)\right] \quad (2.68)$$

where the second term also accounts for possible beam wavefront distortions independent of the sample.

The fringes visibility for the reference and sample measurements is given by (cf. eqs. 2.64 and 2.66):

$$V^{r,s}\left(m,n\right)=a_1^{r,s}\left(m,n\right)\Big/a_0^{r,s}\left(m,n\right) \quad (2.69)$$

The ratio between the sample and reference values, $V^s\left(m,n\right)\Big/V^r\left(m,n\right)$, provides an indication of the ultrasmall-angle scattering introduced by the sample (Pfeiffer et al., 2008). For a

homogeneous object providing no USAXS, in fact, the visibility remains unchanged. In the case of a sample characterized by internal sub-pixel structures ranging in the order of hundreds of nanometers up to micrometers, therefore producing USAXS, the fringe visibility will be decreased. A detailed description of the scattering signal and its influence on the visibility can be found in Bech et al. (Bech et al., 2010).

2.6.3 Coherence requirements and spatial resolution

In the previous description of the image formation principles in GIFM, we have considered the case of a strictly monochromatic wave-field radiated by the source. However, it was shown by Momose et al. (Momose et al., 2006) that GIFM is not very sensitive to beam polychromaticity and that GIFM images can be efficiently acquired even with broad energy spectra. Based on simple geometrical considerations, the requirement in terms of temporal coherence for efficient image acquisition was formulated as $\Delta\lambda/\lambda < 1/8$. A more detailed description of the effect of polychromaticity onto the observable image contrast can be found in (Nesterets and Wilkins, 2008).

Spatial coherence requirements are instead rather strict, since GIFM requires a transverse coherence length comparable to the period of the gratings, which is of the order of some microns. In the case of spatially partially coherent radiation illuminating the object, in fact, the interference fringes visibility, and therefore also the technique sensitivity, are reduced. If the degree of coherence is too small, the interference fringes are washed out and the image contrast vanishes. However, Pfeiffer et al. (Pfeiffer et al., 2006) showed that the strict requirements in terms of spatial coherence can be circumvented if an appropriate absorption grating (the so-called source grating) is placed just downstream the source. This grating has the effect of creating a multiplicity of mutually incoherent, but individually coherent sources. A standard X-ray tube can therefore be used for acquiring GIFM images, as experimentally demonstrated by Pfeiffer et al. (Pfeiffer et al., 2006).

A drawback of this last method is represented by the fact that the introduction of the source grating limits the useful flux emitted by the source: not only a limited fraction of the overall surface is exploited, but also the source grating has a limited angular acceptance, meaning that substantial angular filtering is imposed on the photons emitted by the source.

Another present limitation of the GIFM technique is the limited field of view, which is due to the fact that, presently, the maximum size of the produced gratings is in the order of a few centimeters. A scanning through the available field of view therefore needs to be performed when imaging bigger objects. Nevertheless, this is purely a technical limitation that could reasonably be solved in the next years.

Finally, the spatial resolution achievable with the phase stepping method is limited to the gratings period, which is of the order of some microns.

2.7 Overview of the state of the art in cartilage and breast phase-contrast imaging

In the last 15 years, several works have been published on the application of phase-contrast techniques to the imaging of soft biological tissues. The results show that, in agreement with the theoretical predictions, these methods can provide a considerable increase of contrast for such tissues compared to conventional absorption imaging. Here, we will briefly review some of the most relevant studies concerning cartilage and breast imaging.

2.7.1 Phase-contrast imaging of cartilage

The application of phase-contrast techniques to the imaging of cartilage has attracted much interest, due to the difficulty of visualizing this tissue with conventional methods. Most publications have focused on the use of the analyzer-based technique, which has provided until now the most promising results.

Investigations on small excised in-vitro samples have shown that ABI in planar mode may provide a good visualization of the articular cartilage borders and of the collagen fibers structure within it (Majumdar et al., 2004, Muehleman et al., 2004). An example of the images obtained for the cartilage of a femoral head is presented in figure 2.8. In this case, the ABI technique was used in combination with the diffraction-enhanced imaging (DEI) algorithm (described in detail in chapter 4), which allows calculating the maps of the sample absorption and refraction from two images acquired respectively at the positive and negative slopes of the rocking curve. The good visualization obtained in these experimental studies for the tissue structures allowed the detection of degeneration signs like fibrillations at the cartilage edges, cartilage thinning and loss of fibers orientation. Additionally, modifications in the underlying bone tissue related to joint degeneration, like increased bone volume fraction and changes in the subarticular trabecular structure, were also detected (Majumdar et al., 2004). The application of the ABI technique to intact human joints also showed that the articular cartilage borders, as well as tendons, muscles, arteries, may be visible even when superimposed to other joint structures (Muehleman et al., 2006). In this particular study the multiple image radiography (MIR) algorithm, which will be described and analyzed in chapter 4, was used to separate the absorption, refraction and scattering components of the images.

Other publications investigated the possibility of evaluating the integration of titanium implants into bone (Wagner et al., 2006, Coan et al., 2008) both in planar and tomographic mode. The ABI technique proved capable of providing a great level of information concerning bone ingrowth close to the implant. In particular, it was shown that both the re-orientation of the trabecular structures and the merging of bone to the implant could be very well visualized (the latter owing to the fact that the bone ingrowth can considerably weaken the strong refraction signal at the implant edges).

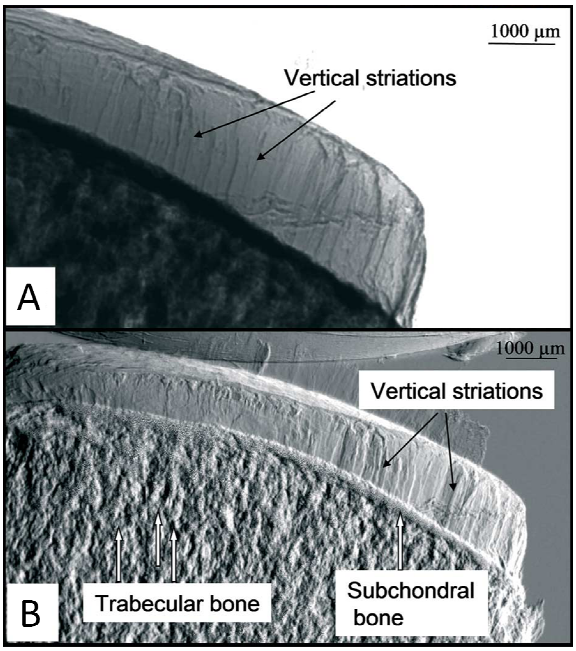

Fig. 2.8. Apparent absorption (A) and refraction (B) images of normal-looking human cartilage of a femoral head (energy 17 keV, pixel size 14 × 14 μm^2). The cartilage vertical striations, as well as their arcing behaviour in the most superficial cartilage layers, are evident. Image taken from (Muehleman et al., 2004).

High-resolution computed tomography of cartilage-bone samples, capable of depicting very fine details of the cartilage internal structure, was recently demonstrated by our group (Coan et al., 2010). Figure 2.9 reports an axial slice and a vertical cut through the volume obtained for a bone-cartilage cylinder with a diameter of about 7 mm, and the comparison with the corresponding histological section. Not only the cartilage borders are very well defined, but also single cartilage cells (chondrocytes) and groups of cartilage cells (chondrons) are clearly visible, with a quality comparable to that of a histological cut. A decrease of homogeneity in cells distribution and in the cells alignment, and a general reduction in cartilage thickness in osteoarthritic samples were found, as well as superficial fibrillations, erosions and small clefts (Coan et al., 2010).

Recently, the first demonstration of ABI acquisitions with an X-ray tube system was reported (Majidi et al., 2009, Parham et al., 2009). Human cadaveric tali, together with a knee and a thumb, were imaged: a good visualization of the tissues structures was obtained, and degeneration signs like ulceration, fissures and loss of cartilage were found. The important drawback linked to the use of a normal X-ray tube consisted in the very long acquisition times. The PBI technique was also recently applied to the imaging of cartilage with a conventional source, a microfocus X-ray tube in this case (Ismail et al., 2010). A good visualization of the cartilage borders in an excised sample was obtained, with an acceptable exposure time (~1 min).

One of the next necessary steps is to verify in-vivo that the same tissues details can be visualized and a diagnosis then performed also in real conditions. The first pilot experiment,

recently published by our group (Coan et al., 2010), opens the way for longitudinal studies directed, for example, to invesitigate the efficacy of pharmacological treatments on osteoarthritis.

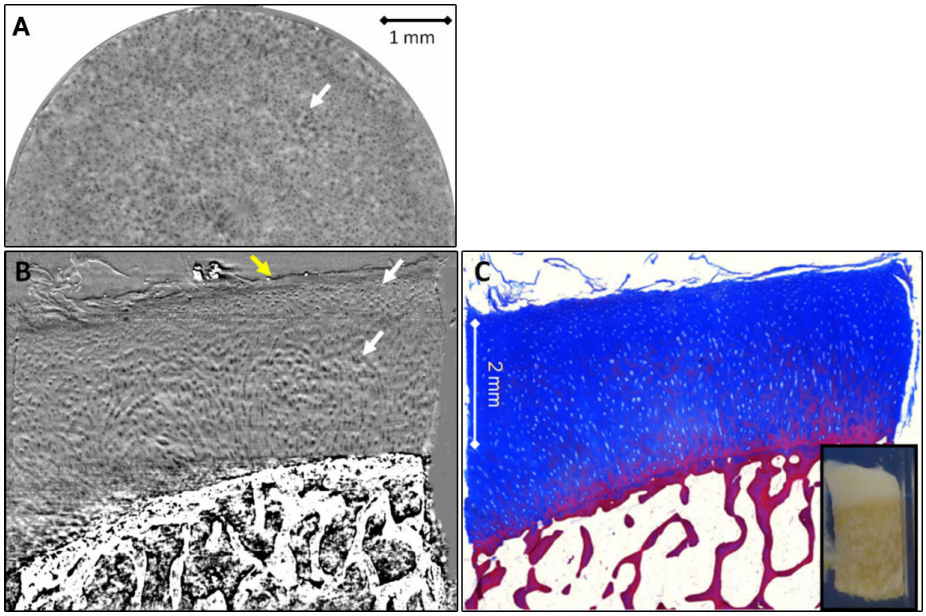

Fig. 2.9. ABI-CT of a normal cartilage sample acquired at the 50% slope position of the analyzer crystal (Si(333) reflection), at an X-ray energy of 26 keV and with a detector pixel size of 8 × 8 μm^2. (A) axial slice in cartilage, (B) vertical cut through the reconstructed CT volume, (C) histological section (Azan staining). In the insert, a picture of the sample is also reported.

2.7.2 Phase-contrast imaging of breast

The applications in mammography have been among the first of synchrotron radiation (Burattini et al., 1995) and of phase-contrast in particular. Concerning this subject, a very good review has been recently published by Keyriläinen and coworkers (Coan et al., 2010). Therefore, we will only mention here the most important results obtained so far for this application.

Almost all phase-contrast imaging studies of the breast have been based on the PBI and ABI techniques. In ABI, the most significant features are due to refraction at the tissue interfaces. In particular, even very thin collagen strands and microcalicifications that are not clearly visible in mammograms are highlighted in AB images. Additionally, beam attenuation is enhanced by extinction (scatter rejection). Small-angle X-ray scattering (SAXS) can be very strong from dissociated (supra)molecular structures, such degraded collagen or invaded collagen. A correlation between changes in the scattering patterns and presence of breast cancer has in fact been demonstrated in several studies (Fernandez M, 2005, Keyriläinen et al., 2008, Sidhu et al., 2008).

Planar AB images of small breast samples showed a better visualization of breast tissues, in particular collagen strands and microcalcifications, with respect to both conventional mammography and digital radiography (Pisano et al., 2000, Keyriläinen et al., 2005). Thanks to the improved contrast, minor tissue changes related to breast cancer could be detected and were

confirmed by histology examination. Furthermore, by changing the position of the analyzer crystal along its rocking curve the observed contrast is also modified and different types of structures can be highlighted. Algorithms for extraction of quantitative information (absorption, refraction and ultrasmall-angle scattering) were also applied to planar images of small breast samples (Hasnah et al., 2002, Wernick et al., 2006, Hasnah et al., 2007). The results indicate that each of these extracted quantitative images may facilitate the visualization of different types of breast tissue structures. These extraction algorithms will be described in detail and analyzed both theoretically and experimentally in chapter 4. Recently, the application of ABI to breast imaging by using an X-ray tube based system was also demonstrated (Faulconer et al., 2009).

Some details may be masked by the superimposed structures in planar images. For this reason, computed tomography for AB imaging of the breast has also been investigated in several publications (Bravin et al., 2007, Keyriläinen et al., 2008, Kao et al., 2009). The high diagnostic value of CT is widely recognized, but its application to the imaging of breast is limited by the large delivered doses. Due to the higher image contrast that they enable to achieve, phase contrast techniques could provide good image quality even with low photon flux. Keyriläinen and coworkers (Keyriläinen et al., 2008) demonstrated that high quality analyzer-based CT images can be obtained with acceptable doses, comparable to those of a normal mammography examination. An example of the resulting images is reported in figure 2.9, where a reconstructed AB axial slice is compared to the corresponding slice obtained with a commercial CT system and to a histological section. The AB image proved superior in contrast and resolution, even if it was acquired with a lower radiation dose. The different fat, glandular and collagen structures seen in the image were confirmed by the histological examination.

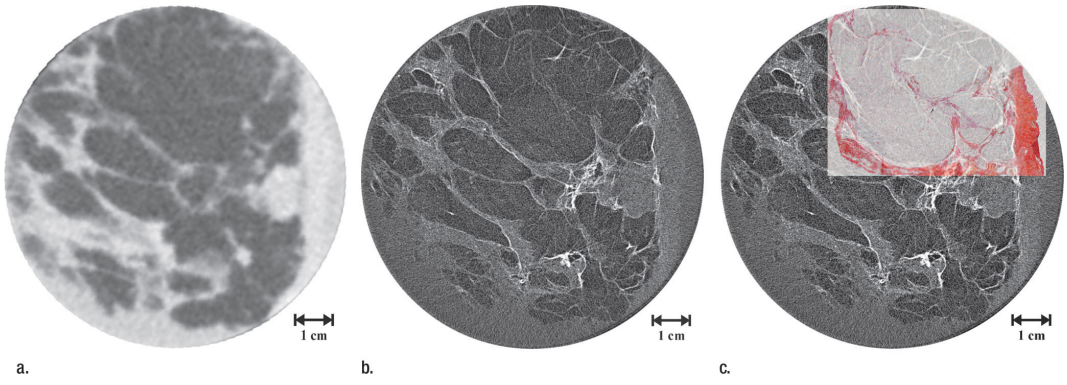

Fig. 2.9. CT images of a human breast tissue specimen with multifocal lobular carcinoma. (a) X-ray tube CT image obtained at 80 kVp and 50 mAs. The mean glandular dose (MGD) is 6.9 mGy. (b) ABI CT "top" image obtained at 30keV. MGD is 1.9 mGy. (c) The same image presented in (b) is shown with the histologic image (Herovici stain) overlapped. Image taken from (Keyriläinen et al., 2008).

Very good results in the imaging of breast have been obtained also with the PBI technique, especially owing to the fact that a considerable fraction of the scattered radiation is rejected (so that the images appear almost scatter-free) and to the edge enhancement due to refraction. Images obtained in both planar (Arfelli et al., 1998, Arfelli et al., 2000) and CT mode (Longo et al., 2003,

Pani et al., 2004) showed improved contrast with respect to the corresponding conventional images. Due to these very promising results, the first phase-contrast clinical trial was started at the SYRMEP beamline of the Elettra synchrotron radiation facility in Trieste (Italy) (Dreossi et al., 2007, Dreossi et al., 2008).

References and links

A. M. Afanas'ev and V. G. Kohn, "Dynamical theory of X-ray diffraction in crystals with defects", Acta Crystallogr. **A27** (1971).

F. Arfelli, M. Assante, V. Bonvicini, A. Bravin, G. Cantatore, E. Castelli, L. Dalla Palma, M. Di Michiel, R. Longo, A. Olivo, S. Pani, D. Pontoni, P. Poropat, M. Prest, A. Rashevsky, G. Tromba, A. Vacchi, E. Vallazza, and F. Zanconati, "Low-dose phase contrast x-ray medical imaging", Phys. Med. Biol. **43** (10), 2845-2852 (1998).

F. Arfelli, V. Bonvicini, A. Bravin, G. Cantatore, E. Castelli, L. Dalla Palma, M. Di Michiel, M. Fabrizioli, R. Longo, R.-H. Menk, A. Olivo, S. Pani, D. Pontoni, P. Poropat, M. Prest, A. Rashevsky, M. Ratti, L. Rigon, G. Tromba, A. Vacchi, E. Vallazza, and F. Zanconati, "Mammography with synchrotron radiation: phase-detection techniques", Radiology **215** (1), 286-293 (2000).

B. D. Arhatari, A. P. Mancuso, A. G. Peele, and K. A. Nugent, "Phase contrast radiography: Image modeling and optimization", Rev. Sci. Instrum. **75** (12), 5271-5276 (2004).

V. Arrizon and E. Lopezolazagasti, "Binary Phase Grating for Array Generation at 1/6 of Talbot Length", J. Opt. Soc. Am. A **12** (4), 801-804 (1995).

A. Authier, *Dynamical theory of X -ray diffraction*, Oxford Press, New York, Vol. 11 (2001).

L. Azaroff, *Elements of X-ray crystallography*, Mc Graw-Hill, New York (1968).

M. Bech, O. Bunk, T. Donath, R. Feidenhans'l, C. David, and F. Pfeiffer, "Quantitative x-ray dark-field computed tomography", Phys. Med. Biol. **55** (10), 5529-5539 (2010).

M. A. Beltran, D. M. Paganin, K. Uesugi, and M. J. Kitchen, "2D and 3D X-ray phase retrieval of multi-material objects using a single defocus distance", Opt. Express **18**(7), 6423-36 (2010).

U. Bonse and M. Hart, "An X-ray interferometer", Appl. Phys. Lett. **6** (8), 155-156 (1965).

M. Born and E. Wolf, *Principles of optics: electromagnetic theory of propagation, interference and diffraction of light,* 7th ed., Cambridge University Press, Cambridge, United Kingdom (1999).

A. Bravin, "Exploiting the X-ray refraction contrast with an analyser: the state of the art", J. Phys. D: Appl. Phys. **36** (10A), A24-A29 (2003).

A. Bravin, J. Keyriläinen, M. Fernandez, S. Fiedler, C. Nemoz, M. L. Karjalainen-Lindsberg, M. Tenhunen, P. Virkkunen, M. Leidenius, K. von Smitten, P. Sipilä, and P. Suortti, "High-resolution CT by diffraction-enhanced x-ray imaging: mapping of breast tissue samples and comparison with their histo-pathology", Phys. Med. Biol. **52** (8), 2197–2211 (2007a).

A. Bravin, V. Mocella, C. Ferrero, P. Coan, S. Fiedler, and W. Thomlison, "A numerical wave-optical approach for the simulation of analyzer-based x-ray imaging", Opt. Express **15** (9), 5641-5648 (2007b).

A. V. Bronnikov, "Reconstruction formulas in phase-contrast tomography", Opt. Commun. **171**(4-6), 239-244 (1999).

E. Burattini, E. Cossu, C. Di Maggio, M. Gambaccini, P. Indovina, M. Marziani, M. Pocek, S. Simeoni, and G. Simonetti, "Mammography with synchrotron radiation", Radiology **195** (1), 239-244 (1995).

V. Bushuev, E. Beliaevskaya, and V. Ingal, "Wave optical description of x-ray phase contrast images of weakly absorbing non crystalline objects", Il Nuovo Cimento **19D**, 513-520 (1997).

V. A. Bushuev, V. N. Ingal, and E. A. Beliaevskaya, "Wave theory of X-ray phase-contrast radiography", Crystallogr. Rep. **43** (4), 538-547 (1998).

E. Castelli, F. Arfelli, D. Dreossi, R. Longo, T. Rokvic, M. A. Cova, E. Quaia, M. Tonutti, F. Zanconati, A. Abrami, V. Chenda, R. H. Menk, E. Quai, G. Tromba, P. Bregant, and F. de Guarrini, "Clinical mammography at the SYRMEP beam line", Nucl. Instrum. Meth. A **572** (1), 237-240 (2007).

C. T. Chantler, K. Olsen, R. A. Dragoset, J. Chang, A. R. Kishore, S. A. Kotochigova, and D. S. Zucker, "X-Ray Form Factor, Attenuation and Scattering Tables (version 2.1): http://physics.nist.gov/ffast", (2005).

D. Chapman, W. Thomlinson, F. Arfelli, N. Gmur, Z. Zhong, R. Menk, R. Johnson, D. Washburn, E. Pisano, and D. Sayers, "Mammography imaging studies using a Laue crystal analyzer", Rev. Sci. Instrum. **67** (9), 1-5 (1996).

D. Chapman, W. Thomlinson, R. E. Johnston, D. Washburn, E. Pisano, N. Gmur, Z. Zhong, R. Menk, F. Arfelli, and D. Sayers, "Diffraction enhanced x-ray imaging", Phys. Med. Biol. **42** (11), 2015-2025. (1997).

P. Cloetens, R. Barrett, J. Baruchel, J. Guigay, and M. Schlenker, "Phase objects in synchrotron radiation hard X-ray imaging", J. Phys. D: Appl. Phys. **29** (1), 133-146 (1996).

P. Cloetens, J. P. Guigay, C. DeMartino, J. Baruchel, and M. Schlenker, "Fractional Talbot imaging of phase gratings with hard x rays", Opt. Letters **22** (14), 1059-1061 (1997).

P. Coan, E. Pagot, S. Fiedler, P. Cloetens, J. Baruchel, and A. Bravin, "Phase-contrast X-ray imaging combining free space propagation and Bragg diffraction", J. Synchrotron Radiat. **12**, 241-245 (2005).

P. Coan, J. Mollenhauer, A. Wagner, C. Muehleman, and A. Bravin, "Analyzer-based imaging technique in tomography of cartilage and metal implants: A study at the ESRF." Eur. J. Radiol. **68S**, S41-S48 (2008).

P. Coan, F. Bamberg, P. C. Diemoz, A. Bravin, K. Timpert, E. Mutzel, J. G. Raya, S. Adam-Neumair, M. F. Reiser, and C. Glaser, "Characterization of osteoarthritic and normal human patella cartilage by computed tomography X-ray phase-contrast imaging: a feasibility study", Invest. Radiol. **45** (7), 437-444 (2010a).

P. Coan, A. Wagner, A. Bravin, P. C. Diemoz, J. Keyriläinen, and J. Mollenhauer, "In vivo x-ray phase contrast analyzer-based imaging for longitudinal osteoarthritis studies in guinea pigs", Phys. Med. Biol. **55** (24), 7649-7662 (2010b).

C. David, B. Nöhammer, H. Solak, and E. Ziegler, "Differential X-ray phase contrast imaging using a shearing interferometer", Appl. Phys. Lett. **81** (17), 3287-3289 (2002).

T. Davis, D. Gao, T. Gureyev, A. Stevenson, and S. Wilkins, "Phase-contrast imaging of weakly absorbing materials using hard X-rays", Nature **373**, 595-598 (1995).

D. Dreossi, A. Bergamaschi, B. Schmitt, E. Vallazza, F. Arfelli, R. Longo, R. H. Menk, L. Rigon, T. Rokvic, C. Venanzi, and E. Castelli, "Clinical mammography at the SYRMEP beam line: Toward the digital detection system", Nucl. Instrum. Meth. A **576** (1), 160-163 (2007).

D. Dreossi, A. Abrami, F. Arfelli, R. Bregant, K. Casarin, V. Chenda, M. A. Cova, R. Longo, R. H. Menk, E. Quai, E. Quaia, L. Rigon, T. Rokvic, D. Sanabor, M. Tonutti, G. Tromba, A. Vascotto, F. Zanconati, and E. Castelli, "The mammography project at the SYRMEP beamline", Eur. J. Radiol. **68** (3), S58-S62 (2008).

L. Faulconer, C. Parham, D. M. Connor, Z. Zhong, E. Kim, D. L. Zeng, C. Livasy, E. Cole, C. Kuzmiak, M. Koomen, D. Pavic, and E. Pisano, "Radiologist Evaluation of an X-ray Tube-Based Diffraction-Enhanced Imaging Prototype Using Full-Thickness Breast Specimens", Acad. Radiol. **16** (11), 1329-1337 (2009).

M. Fernandez, R. Serimaa, M. Torkkeli, M. L. Karjalainen-Lindsberg, M. Leidenius, K. von Smitten, M. Tenhunen, S. Fiedler, A. Bravin, T. M. Weiss, P. Suortti, "Human breast cancer in vitro: matching histo-pathology with small-angle x-ray scattering and diffraction enhanced x-ray imaging." Phys. Med. Biol. **50** (13), 2991-3006 (2005).

M. Fernandez, H. Suhonen, J. Keyrilainen, A. Bravin, S. Fiedler, M. L. Karjalainen-Lindsberg, A. Leidenius, K. von Smitten, and P. Suortti, "USAXS and SAXS from cancer-bearing breast tissue samples", Eur. J. Radiol. **68** (3), S89-S94 (2008).

R. Fitzgerald, "Phase sensitive X-ray imaging", Physics Today **53**, 23 (2000).

E. Förster, K. Goetz, and P. Zaumseil, "Double crystal diffractometry for the characterization of targets for laser fusion experiments", Kristall Technik **15**, 937-945 (1980).

J. P. Guigay, "Fresnel Diffraction by One-Dimensional Periodic Objects, with Application to Structure Determination of Phase Objects", Optica Acta **18** (19), 677-& (1971).

J. P. Guigay, "Fourier-Transform Analysis of Fresnel Diffraction Patterns and in-Line Holograms", Optik **49**, 121-125 (1977).

J. P. Guigay, M. Langer, R. Boistel, and P. Cloetens, "Mixed transfer function and transport of intensity approach for phase retrieval in the Fresnel region", Opt. Lett. **32** (12), 1617-1619 (2007).

T. Gureyev, A. Roberts, and K. Nugent, "Partially coherent fields, the transport-of-intensity equation, and phase uniqueness", J. Opt. Soc. Am. A **12** (9), 1942-1946 (1995).

T. E. Gureyev and S. W. Wilkins, "Regimes of X-ray phase-contrast imaging with perfect crystals", Il Nuovo Cimento **19 D**, 545-552 (1997).

T. E. Gureyev, "Composite techniques for phse retrieval in the Fresnel region", Opt. Commun. **220** (1-3), 49-58 (2003).

T. E. Gureyev, T. J. Davis, A. Pogany, S. C. Mayo, and S. W. Wilkins, "Optical phase retrieval by use of first Bornand Rytov-type approximations", Appl. Optics **43** (12), 2418-2430 (2004).

T. E. Gureyev, Y. I. Nesterets, A. W. Stevenson, P. R. Miller, A. Pogany, and S. W. Wilkins, "Some simple rules for contrast, signal-to-noise and resolution in in-line x-ray phase-contrast imaging", Opt. Express **16**(5), 3223-41 (2008).

M. O. Hasnah, Z. Zhong, O. Oltulu, E. Pisano, R. E. Johnston, D. Sayers, W. Thomlinson, and D. Chapman, "Diffraction enhanced imaging contrast mechanisms in breast cancer specimens", Med. Phys. **29** (10), 2216-2221 (2002).

M. O. Hasnah, Z. Zhong, C. Parham, H. Zhang, and D. Chapman, "Compositional images from the diffraction enhanced Imaging technique", Nucl. Instrum. Meth. A **572** (2), 953-957 (2007).

ICRU, *Tissue Substitutes in Radiation Dosimetry and Measurement*, ICRU Report 44, ICRU Publications, Bethesda MD, USA (1989).

V. Ingal and E. Beliaevskaya, "X-ray plane-wave topography observation of the phase contrast from a non-crystalline object", J. Phys. D: Appl. Phys. **28** (11), 2314-2317 (1995).

E. C. Ismail, W. Kaabar, D. Garrity, O. Gundogdu, O. Bunk, F. Pfeiffer, M. J. Farquharson, and D. A. Bradley, "X-ray phase contrast imaging of the bone-cartilage interface", Appl. Radiat. Isot. **68** (4-5), 767-771 (2010).

J. Jackson, *Classical Electrodynamics*, 3rd edition, Wiley ed., New York, USA (1998).

T. Kao, D. Connor, F. A. Dilmanian, L. Faulconer, T. Liu, C. Parham, E. D. Pisano, and Z. Zhong, "Characterization of diffraction-enhanced imaging contrast in breast cancer", Phys. Med. Biol. **54** (10), 3247-3256 (2009).

E. Keren and O. Kafri, "Diffraction Effects in Moire Deflectometry", J. Opt. Soc. Am. A **2** (2), 111-120 (1985).

J. Keyriläinen, M. Fernández, S. Fiedler, A. Bravin, M. L. Karjalainen-Lindsberg, P. Virkkunen, E. M. Elo, M. Tenhunen, P. Suortti, and W. Thomlinson, "Visualisation of calcifications and thin collagen strands in human breast tumour specimens by the diffraction-enhanced imaging technique: a comparison with conventional mammography and histology", Eur. J. Radiol. **53** (2), 226-237 (2005).

J. Keyriläinen, M. Fernández, M. L. Karjalainen-Lindsberg, P. Virkkunen, M. Leidenius, K. von Smitten, P. Sipilä, S. Fiedler, H. Suhonen, P. Suortti, and A. Bravin, "Towards high-contrast breast CT at low radiation dose", Radiology **249** (1), 321-327 (2008).

J. Keyriläinen, A. Bravin, M. Fernandez, M. Tenhunen, P. Virkkunen, and P. Suortti, "Phase-contrast X-ray imaging of breast", Acta Radiol. **51** (8), 866-884 (2010).

M. J. Kitchen, K. M. Pavlov, K. K. W. Siu, R. H. Menk, G. Tromba, and R. A. Lewis, "Analyser-based phase contrast image reconstruction using geometrical optics", Phys. Med. Biol. **52** (14), 4171-4187 (2007).

M. Langer, P. Cloetens, and F. Peyrin, "Regularization of Phase Retrieval With Phase-Attenuation Duality Prior for 3-D Holotomography", IEEE Trans. Image Process. **19** (9), 2428-2436 (2010).

R. A. Lewis, "Medical phase contrast x-ray imaging: current status and future prospects", Phys. Med. Biol. **49** (16), 3573-3583 (2004).

A. W. Lohmann and J. A. Thomas, "Making an Array Illuminator Based on the Talbot Effect", Appl. Optics **29** (29), 4337-4340 (1990).

R. Longo, S. Pani, F. Arfelli, D. Dreossi, A. Olivo, P. Poropat, E. Quaia, L. Rigon, F. Zanconati, L. Dalla Palma, and E. Castelli, "Morphological breast imaging: tomography and digital mammography with synchrotron radiation", Nucl. Instrum. Meth. A **497** (1), 9-13 (2003).

S. Majumdar, A. Sema-Issever, A. Burghardt, J. Lotz, F. Arfelli, L. Rigon, G. Heitner, and R. H. Menk, "Diffraction enhanced imaging of articular cartilage and comparison with micro computed tomography of the underlying bone structure", Eur. Radiol. **14** (8), 1440-1448 (2004).

S. C. Mayo, P. R. Miller, S. W. Wilkins, T. J. Davis, D. Gao, T. E. Gureyev, D. Paganin, D. J. Parry, A. Pogany, and A. W. Stevenson, "Quantitative X-ray projection microscopy: phase-contrast and multi-spectral imaging", J. Microsc. **207** (2), 79-96 (2002).

A. Momose, T. Takeda, Y. Itai, and K. Hirano, "Phase-contrast X-ray computed tomography for observing biological soft tissues", Nat. Med. **2** (4), 473-475 (1996).

A. Momose, S. Kawamoto, I. Koyama, Y. Hamaishi, K. Takai, and Y. Suzuki, "Demonstration of X-Ray Talbot interferometry", Jpn. J. Appl. Phys. 2 **42** (7B), L866-L868 (2003).

A. Momose, W. Yashiro, Y. Takeda, Y. Suzuki, and T. Hattori, "Phase tomography by X-ray Talbot interferometry for biological imaging", Jpn. J. Appl. Phys. 1 **45** (6A), 5254-5262 (2006).

C. Muehleman, S. Majumdar, A. Issever, F. Arfelli, R. Menk, L. Rigon, G. Heitner, B. Reime, J. Metge, A. Wagner, K. Kuettner, and J. Mollenhauer, "X-ray detection of structural orientation in human articular cartilage", Osteoarthr. Cartilage **12** (2), 97-105 (2004).

C. Muehleman, J. Li, Z. Zhong, J. G. Brankov, and M. N. Wernick, "Multiple-image radiography for human soft tissue", J. Anat. **208** (1), 115-124 (2006).

C. Muehleman, J. Li, D. Connor, C. Parham, E. Pisano, and Z. Zhong, "Diffraction-Enhanced Imaging of Musculoskeletal Tissues Using a Conventional X-Ray Tube", Acad. Radiol. **16** (8), 918-923 (2009).

Y. I. Nesterets, T. E. Gureyev, D. M. Paganin, K. M. Pavlov, and S. W. Wilkins, "Quantitative diffraction-enhanced X-ray imaging of weak objects", J. Phys. D: Appl. Phys. **37** (8), 1262-1274 (2004).

Y. I. Nesterets, T. Gureyev, and S. Wilkins, "Polychromaticity in the combined propagation-based/analyser-based phase-contrast imaging", J. Phys. D: Appl. Phys. **38** (24), 4259-4271 (2005).

Y. I. Nesterets, P. Coan, T. Gureyev, A. Bravin, P. Cloetens, and S. Wilkins, "On qualitative and quantitative analysis in analyser based imaging", Acta Crystallogr. A **62** (4), 296-308 (2006).

Y. I. Nesterets, T. E. Gureyev, K. M. Pavlov, D. M. Paganin, and S. W. Wilkins, "Combined analyser-based and propagation-based phase-contrast imaging of weak objects", Opt. Commun. **259** (1), 19-31 (2006).

Y. I. Nesterets and S. W. Wilkins, "Phase-contrast imaging using a scanning-double-grating configuration", Opt. Express **16** (8), 5849-5867 (2008).

A. Olivo and R. Speller, "Image formation principles in coded-aperture based x-ray phase contrast imaging", Phys. Med. Biol. **53** (22), 6461-6474 (2008).

D. Paganin, S. C. Mayo, T. E. Gureyev, P. R. Miller, and S. W. Wilkins, "Simultaneous phase and amplitude extraction from a single defocused imaged of a homogeneous object", J. Microsc.-Oxford **206**, 33-40 (2002).

D. Paganin, T. Gureyev, K. M. Pavlov, R. A. Lewis, and M. Kitchen, "Phase retrieval using coherent imaging systems with linear transfer functions", Opt. Commun. **234** (1-6), 87-105 (2004).

D. M. Paganin, *Coherent X-ray optics* ,Oxford University Press, Oxford, United Kingdom (2006).

E. Pagot, *Quantitative comparison between two phase-contrast techniques for mammography: diffraction-enhanced imaging (DEI) and phase propagation imaging (PPI)*, PhD Thesis, Université Joseph Fourier, Grenoble, France (2004).

S. Pani, R. Longo, D. Dreossi, F. Montanari, A. Olivo, F. Arfelli, A. Bergamaschi, P. Poropat, L. Rigon, F. Zanconati, L. Dalla Palma, and E. Castelli, "Breast tomography with synchrotron radiation: preliminary results", Phys. Med. Biol. **49** (9), 1739-1754 (2004).

C. Parham, Z. Zhong, D. M. Connor, L. D. Chapman, and E. D. Pisano, "Design and Implementation of a Compact Low-Dose Diffraction Enhanced Medical Imaging System", Acad. Radiol. **16** (8), 911-917 (2009).

K. M. Pavlov, T. E. Gureyev, D. Paganin, Y. I. Nesterets, M. J. Morgan, and R. A. Lewis, "Linear systems with slowly varying transfer functions and their application to x-ray phase-contrast imaging", J. Phys. D: Appl. Phys. **37** (19), 2746–2750 (2004).

K. M. Pavlov, T. E. Gureyev, D. Paganin, Y. I. Nesterets, M. J. Kitchen, K. K. W. Siu, J. E. Gillam, K. Uesugi, Y. Yagi, M. J. Morgan, and R. A. Lewis, "Unification of analyser-based and propagation-based X-ray phase-contrast imaging", Nucl. Instr. Meth. A **548** (1-2), 163-168 (2005).

F. Pfeiffer, T. Weitkamp, O. Bunk, and C. David, "Phase retrieval and differential phase-contrast imaging with low-brilliance X-ray sources", Nat. Phys. **2** (4), 258-261 (2006).

F. Pfeiffer, M. Bech, O. Bunk, P. Kraft, E. F. Eikenberry, C. Brönnimann, C. Grünzweig, and C. David, "Hard-X-ray dark-field imaging using a grating interferometer", Nat. Mater. **7** (2), 134-137 (2008).

E. D. Pisano, R. E. Johnston, D. Chapman, J. Geradts, M. V. Iacocca, C. A. Livasy, D. B. Washburn, D. E. Sayers, Z. Zhong, M. Z. Kiss, and W. C. Thomlinson, "Human breast cancer specimens: diffraction-enhanced imaging with histologic correlation--improved conspicuity of lesion detail compared with digital radiography", Radiology **214** (3), 895-901 (2000).

K. Podurets, V. Somenkov, and S. Shilstein, "Refraction-contrast radiography", Sov. Phys. Tech. Phys. **34** (6), 654-657 (1989).

A. Pogany, D. Gao, and S. Wilkins, "Contrast and resolution in imaging with a microfocus x-ray source", Rev. Sci. Instrum. **68** (7), (1997).

L. Rayleigh, "On copying diffraction-gratings, and on some phenomena connected therewith", Phil. Mag. **11**, 196-205 (1881).

D. Ress, L. B. Dasilva, R. A. London, J. E. Trebes, S. Mrowka, R. J. Procassini, T. W. Barbee, and D. E. Lehr, "Measurement of Laser-Plasma Electron-Density with a Soft-X-Ray Laser Deflectometer", Science **265** (5171), 514-517 (1994).

L. Rigon, Z. Zhong, F. Arfelli, R.-H. Menk, and A. Pillon, "Diffraction Enhanced Imaging Utilizing crystal reflections at Elettra and NSLS", SPIE Medical Imaging **4682**, 255-266 (2002).

S. Sidhu, K. K. W. Siu, G. Falzon, S. Nazaretian, S. A. Hart, J. G. Fox, B. J. Susil, and R. A. Lewis, "X-ray scattering for classifying tissue types associated with breast disease", Med. Phys. **35** (10), 4660-4670 (2008).

A. Snigirev, I. Snigireva, V. Kohn, S. Kuznetsov, and I. Schelokov, "On the possibility of x-ray phase contrast microimaging by coherent high-energy synchrotron radiation", Rev. Sci. Instrum. **66** (12), 5486-5492 (1995).

V. Somenkov, A. Tkalich, and S. Shilshtein, "Refraction contrast in X-ray introscopy", Sov. Phys. Tech. Phys. **36** (11), 1309-1311 (1991).

H. F. Talbot, "Facts relating to optical science. No. IV", Phil. Mag. **9**, 401-407 (1836).

M. R. Teague, "Irradiance Moments - Their Propagation and Use for Unique Retrieval of Phase", J. Opt. Soc. Am. **72** (9), 1199-1209 (1982).

L. D. Turner, B. B. Dhal, J. P. Hayes, A. P. Mancuso, K. A. Nugent, D. Paterson, R. E. Scholten, C. Q. Tran, and A. G. Peele, "X-ray phase imaging: Demonstration of extended conditions with homogeneous objects", Opt. Express **12** (13), 2960-2965 (2004).

A. Wagner, A. Sachse, M. Keller, O. Wagner, M. Aurich, W. D. Wetzel, R. A. Venbrocks, B. \Wiederanders, P. Hortschansky, J. Horn, K. Schmuck, M. Lohmann, B. Reime, J. Metge, F. Arfelli, R. Menk, L. Rigon, C. Muehleman, A. Bravin, P. Coan, and J. Mollenhauer, "Quality evaluation of Titanium Implant Ingrowth into Bone by Diffraction Enhanced Imaging (DEI)", Phys. Med. Biol. **51** (5), (2006).

H. Wen, E. E. Bennett, M. M. Hegedus, and S. Rapacchi, "Fourier X-ray Scattering Radiography Yields Bone Structural Information", Radiology **251** (3), 910-918 (2009).

M. N. Wernick, Y. Yang, I. Mondal, D. Chapman, M. Hasnah, C. Parham, E. Pisano, and Z. Zhong, "Computation of mass-density images from X-ray refraction-angle images", Phys. Med. Biol. **51** (7), 1769-1778 (2006).

S. W. Wilkins, T. E. Gureyev, D. Gao, A. Pogani, and A. W. Stevenson, "Phase-contrast imaging using polychromatic hard X-rays", Nature **384** (6607), 335-338 (1996).

X. Wu and H. Liu, "A general theoretical formalism for X-ray phase contrast imaging", J. X-ray Sci. Technol. **11**(1), 33-42 (2003).

W. H. Zachariasen, *Theory of X-ray diffraction in crystals*, Wiley ed., New York, USA (1945).

Z. Zhong, W. Thomlinson, D. Chapman, and D. Sayers, "Implementation of diffraction-enhanced imaging experiments: at the NSLS and APS", Nucl. Instrum. Meth A **450** (2-3), 556-567 (2000).

3

Experimental implementation and methods

Table of Contents

Abstract: This chapter deals with the practical implementation of the phase-contrast imaging techniques considered in this Thesis. Synchrotron radiation will first be introduced and compared with the radiation provided by other sources, and the characteristics that make it so powerful for phase contrast imaging will be underlined. An overview of the biomedical beamline ID17 and of the other beamlines where the data presented in this Thesis were acquired will be given and the setups for the PBI, ABI and GIFM techniques will be described. Finally, the image acquisition with the Frelon CCD camera will be presented, as well as some general processing methods that have been applied to the recorded images and the quantities used for the analysis of the image quality.

3.1 X-ray sources

Historically, X-rays for imaging and crystallography have usually been produced through the use of Brehmstrahlung and characteristic lines from electrons impinging on a metallic anode (X-ray tubes). Such sources are inexpensive, simple and robust, but provide radiation that is spatially and temporally incoherent at the object position.

The advent of synchrotron radiation sources in the past three to four decades had a revolutionary impact in fields of science and technology extending from material science to biomedical imaging. The main properties of synchrotron radiation that make it such an interesting tool for a variety of different applications are the high brilliance, collimation, and the wide energy range of the produced radiation, which allow for overcoming the typical limitations of the conventional radiation produced with X-ray tubes.

Unfortunately, synchrotron radiation facilities are very large, very expensive and are therefore not suited for routine imaging applications. No alternative has existed until now for experiments that need to operate at various X-ray energies and under particular coherence conditions. The availability of table-top, intense monochromatic sources may fundamentally change the practice of X-ray imaging and can largely extend the application of imaging techniques that are presently confined into synchrotron radiation facilities. Recent developments in this sense are represented by the sources based on the so-called “inverse Compton scattering”.

3.1.1 X-ray tubes

X-ray radiation for medical diagnostics procedures or for research purposes is conventionally produced by X-ray tubes. The basic principles of an X-ray tube have not changed significantly since Röntgen’s discovery of X-rays in 1895. Current applied to a metal cathode produces free electrons which are accelerated by a high voltage towards a metal target (anode). X-rays are produced when the electrons are suddenly decelerated upon collision with the target; these X-rays are commonly called “Brehmsstrahlung”. If the bombarding electrons have sufficient energy, they can knock an electron out of an inner shell of the target metal atoms (ionization process). Then electrons from higher states drop down to fill the vacancy, emitting X-ray photons with precise energies determined by the electron energy levels. These X-rays are called “characteristic X-rays”.

Actually, most of the energy in the electron beam is deposited in the target in the form of heat, and one of the problems faced in designing X-ray tubes is how to limit the heat deposition in the target area and how to remove it. For this reason most of the X-ray tubes make use of a rotating disk as the anode, so that the target area is spread out over the periphery of the disk and the heat deposition problem is less severe.

The shape of the X-ray spectrum produced by the X-ray tube depends on the target material, the voltage applied between the cathode and the anode and the effects of any filters placed in the X-ray beam.

3.1.2 Synchrotron radiation facilities

Synchrotron radiation (SR) is the electromagnetic field generated by relativistic charged particles whose path is bent by a magnetic field. The radiation is emitted tangentially to the curved trajectory of the accelerated particles and occurs in a narrow cone with a natural opening angle equal to $1/\gamma$ ($\gamma = 1/\sqrt{1 - v^2/c^2}$, where v is the electron velocity).

Electrons used in synchrotron radiation facilities are produced in bunches of about 10^{11} particles by means of an electron gun (by heating a cathode) with a frequency up to 10 Hz. After preacceleration using disc-loaded wave guides (Brefeld and Gurtler, 1991) in a linear accelerator (LINAC), electrons are then injected into a first synchrotron accelerator (booster), where their energy is "ramped" to the final energy (figure 3.1). In the first and second generation SR machines, the booster was made to operate as a synchrotron and as a storage ring at the same time. In the new generation of SR facilities, electrons are transferred to a second ring, called "storage ring", where the electron energy is kept constant.

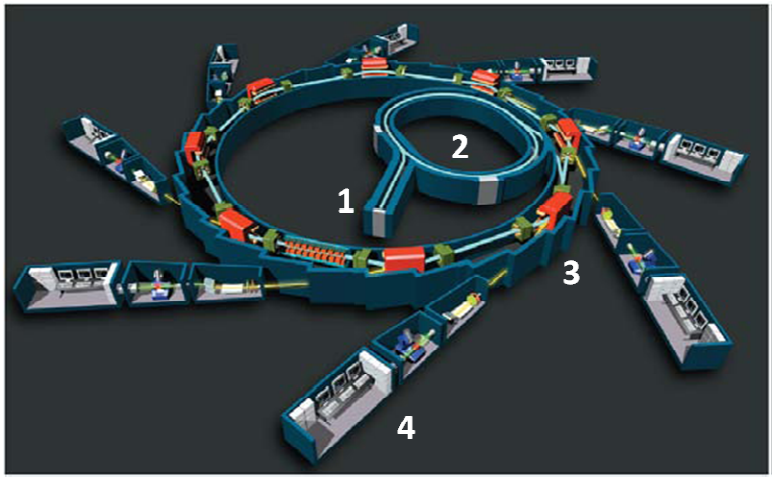

Fig. 3.1. Schematic representation of a third-generation synchrotron radiation facility. 1) Linear accelerator (LINAC), 2) acceleration ring (Booster), 3) storage ring, 4) beamline.

Radiofrequency cavities are used in the booster to accelerate the electrons and in the storage ring to replenish the energy lost by the particles into SR. Magnetic dipoles (bending magnets) are used to define the closed orbit of the particles and, in storage rings, dipoles are also one type of SR light source. Other important components are the quadrupole and sextupole magnets; suitably combined, they provide focusing forces that keep the electron-beam transverse dimensions small. Straight sections are also present, with elements for the injection of the electrons from an accelerator to the other (LINAC-to-booster, booster-to-storage ring).

The electrons run in ultra-high vacuum (less than 10^{-8} mbar) in order to minimize the probability of collisions with residual gas. A closed, continuous high-vacuum chamber extends through the various booster and storage ring elements.

Synchrotron radiation can be extracted from the electrons that circulate in the storage ring in different ways. The already mentioned bending magnets (BM) (fig. 3.2(a)), installed in the curved sections, produce a continuous spectrum of SR. Special insertion devices (ID), which can be either wigglers or undulators, are installed in the straight sections (fig. 3.2(b)). They consist of a sequence of dipole magnets of alternating polarities: the magnetic fields force the electron to oscillate around a straight-line trajectory and the cones of light emitted at each bend superimpose.

- In the case of undulators, the electron beam deflection is less than $1/\gamma$, so that the beams emitted by individual poles can interfere coherently. This leads to a spectrum with strong peaks at a specific energy and its harmonics.
- In the wiggler case, the total divergence is much larger than the natural opening angle of the radiation and no more interference occurs. The final beam emitted by the device is the incoherent sum of the beams emitted at each pole, and the X-ray spectrum exhibits a continuous distribution.

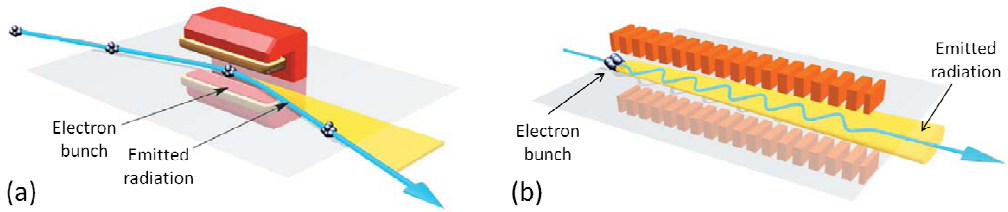

Fig. 3.2. Schematic representation of a bending magnet (a) and of an insertion device (b).

Tangential beam channels (beamlines) starting from the storage ring permit the synchrotron radiation to enter experimental halls. Since many beam channels can be installed all along the ring, and some of them can even be split in more branches by means of mirrors and crystals, a large number of simultaneous experiments are possible.

- Advantages of synchrotron radiation for phase-contrast imaging:

Figure 3.3 shows the different geometries of the beams produced by an X-ray tube and a SR source. X-ray tubes emit radiation over a wide angle and the sample is normally close to the source. One can change the magnification $M = (L + D)/L$ of the image by changing the focal spot – sample distance L or the sample – detector distance D.

The small opening angle of the X-ray beam produced in synchrotron facilities enables to position the sample at large distances from the source, while preserving a high incident intensity. Together with the small size of the source, this is crucial in order to achieve a high degree of spatial coherence, as we saw in chapter 2, which is essential for both the propagation-based imaging (PBI) and grating interferometry (GIFM) techniques. Besides, the small source size and the large source-to-sample distance provide a good geometrical resolution, $R = S \cdot D/L$, since the

beam is almost parallel and the penunmbra typical of conventional imaging with X-ray tubes is thus considerably reduced.

Furthermore, the emitted X-rays are almost parallel at the sample position. This property is particularly important for analyzer-based imaging, due to the very high angular selectivity of the monochromator and analyzer crystals. If the divergence of the initial beam was much larger than the Darwin width of the crystals reflection, in fact, there would be a large loss of intensity in the monochromatization/collimation process.

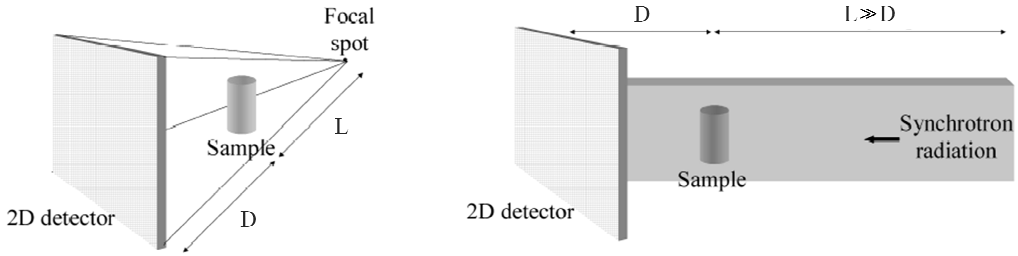

Fig. 3.3. Schemes of the different geometries of irradiation for (a) X-ray tubes and (b) SR imaging.

Figure 3.4 presents the comparison between the X-ray beam spectrum produced by X-ray tubes with that produced by a SR wiggler device. In the first case, the spectrum is given by a continuous Brehmsstrahlung background from where the characteristic X-ray emissions stand out; SR wiggler beams are instead characterized by a continuous emission in a wide energy range which is orders of magnitude more intense than the strongest characteristic lines from X-ray tubes.

The broad energy spectrum and the very high intensity of the SR allow selecting a particular wavelength with a monochromator and, at the same time, maintaining a sufficient photon flux, which would not be possible with radiation delivered by an X-ray tube. Working with quasi-monochromatic radiation is crucial for ABI, while a relatively broad energy range (polychromaticity) is tolerated by the PBI and GIFM techniques.

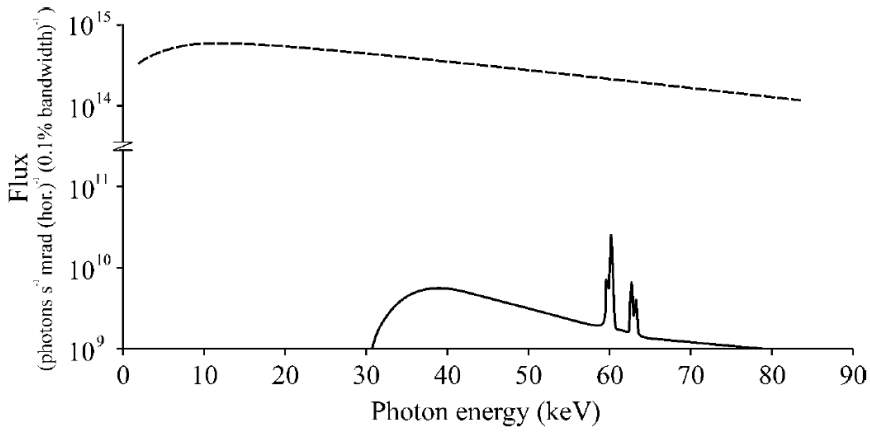

Fig. 3.4. Comparison between a wiggler X-ray spectrum (dashed line) (ESRF, ID17 at 200 mA ring current) and an X-ray tube (110 kVp – 2.5 mm Al filtering at 1 meter from the source).

3.1.3 Inverse Compton scattering sources

There is great interest in developing high brilliance X-ray compact sources capable of delivering highly coherent radiation, which could replace the large and costly synchrotron machines especially for some specific applications (e.g. crystallography, imaging etc…). Delivery of a 2D beam of hard, tunable, high-brightness monochromatic X-rays suitable for rapid medical imaging is a long-sought goal. A device to produce X-rays in a clinical environment has to be relatively compact and capable of delivering an X-ray beam allowing single-shot or fast multi-shot imaging and broadly tunable over the energy range useful for medical diagnostics.

Several groups are simultaneously working in investigating compact light sources. For such machines, most of the proposed solutions are based on the same physical process: inverse Compton (or Thomson) scattering (Huang and Ruth, 1998, Carroll et al., 2003, Dobashi et al., 2005, Kuroda et al., 2007, Oliva et al., 2010). Different methods, anyway, have also been proposed, for example the table-top X-ray free-electron laser (XFEL) (Grüner et al., 2007) and the MIRRORCLE machine, based on a 15 cm radius electron storage ring (energy up to 20 MeV) and on the production of X-rays by Brehmsstrahlung onto a target placed in the electron orbit (Yamada, 2003).

Inverse Compton scattering (ICS) basically consists in the head-on collision of an energetic (20-50 MeV) electron beam with an intense beam of light. Therefore, an ICS machine essentially integrates a laser with a linear or circular accelerator. Both electrons and laser beams are focused to a very small spot size (on the order of 30 μm or smaller) at the point of collision. Light scatters off the electrons, picking up some of their energy and being deflected back out of the interaction zone. The produced X-ray photons propagate along an axis almost collinear with the path of the electron beam (see figure 3.5). By exploiting this process, high-brilliance hard X-ray beams in a narrow energy band can be produced with a laboratory-scale facility. In fact, since the required energy for the electrons is orders of magnitude smaller than that needed for the production of X-rays in SR facilities, the size of the accelerator machine can be scaled down to a few meters.

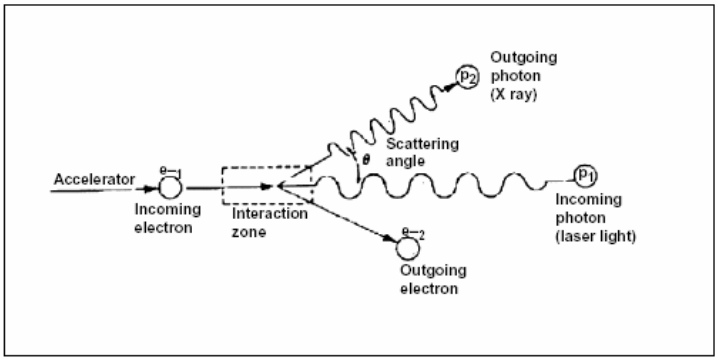

Fig. 3.5. Theory of the inverse Compton scattering process: an electron beam collides with a focused intense infrared beam, resulting in X-rays propagating almost collinearly with the electron beam direction. Image taken from (Carroll et al., 2003).

Very promising works investigating both theoretically and experimentally the possible use of ICS machines for medical imaging applications have been published. De Caro and coworkers (De Caro et al., 2009) and Oliva and coworkers (Oliva et al., 2010) studied theoretically the possibility of propagation-based phase-contrast mammography, while experimental investigations of propagation-based imaging on biological samples were presented in (Ikeura-sekiguchi et al., 2008, Yamada et al., 2009, Oliva et al., 2010). The first experimental feasibility study for the application of grating interferometry with an inverse Compton scattering source was performed by Bech and coworkers (Bech et al., 2009), who used the machine developed by Lyncean Technologies Inc., based on an electron storage ring (http://www.lynceantech.com/sci_tech_cls.html, Huang and Ruth, 1998).

Thanks to their high brightness, short pulses, and a variable bandwidth X-ray beam, compact light sources based on inverse Compton scattering have a high potential to become, in the future, the reference source for clinical programs for the diagnosis and treatment of pathologies in everyday human medical practice.

3.2 The European Synchrotron Radiation Facility (ESRF)

The European Synchrotron Radiation Facility (ESRF) at Grenoble is the most powerful third-generation synchrotron in Europe. It consists of: i) a LINAC that accelerates the electron beam, produced by an electron gun, up to an energy of 200 MeV; ii) a booster of 300 meters of circumference where two radiofrequencies at 10 Hz accelerate the electron bunches up to a maximum energy of 6 GeV; iii) a 844 meters circumference storage ring where the electron bunches turn giving rise to a current that can reach 200 mA.

Fig. 3.6. Aerial view of the European Synchrotron Radiation Facility (ESRF) at Grenoble. On the right side of the picture, the external buildings hosting the two long beamlines ID17 and ID19 are visible.

Forty specialized beamlines are installed by the storage ring. They are designed for research in areas as diverse as engineering, physics, chemistry, crystallography, earth science, biology and medicine, surface and materials science.

The experimental acquisitions performed in the framework of this Thesis have been carried out at the following experimental stations:

- the *biomedical* ID17 beamline (ABI acquisitions)

- the "*topography & tomography*" ID19 beamline (GIFM acquisitions)

- the *optics* BM5 beamline (ABI, GIFM and PBI acquisitions).

In the following section, a general description of the ID17 beamline will be provided, while the main features of the ID19 and BM5 beamlines will be mentioned in section 3.2.2.

3.2.1 Overview of the optics and of the main X-ray properties at the biomedical ID17 beamline

The ID17 beamline is dedicated to preclinical and clinical biomedical research, in particular in the two fields of imaging and radiation therapy. Different kinds of programs are presently being performed: cerebral computed tomography, phase-contrast imaging, bronchography, brain perfusion studies, preclinical Microbeam Radiation Therapy (MRT), Stereotactic Synchrotron Radiation Therapy (SSRT), radiobiological investigations etc…

ID17 is one of the two long ESRF beamlines, together with ID19 (fig. 3.6). One experimental hutch is located at about 40 meters from the source, while a second experimental hutch is hosted in a satellite building, outside the ESRF main experimental hall, at about 150 meters from the source. One of the main reasons that led to the construction of such a long beamline was the requirement of achieving a beam sufficiently large for imaging: the maximum dimensions, in fact, can reach approximately 250 × 10 mm^2 (horizontal × vertical) in the second experimental hutch of ID17 thanks to the X-ray beam divergence and the long distance from the source. In practice, due to the limit in availability of such large X-ray monochromators and imaging detectors, the real beam size is limited to about 150 × 10 mm^2.

The insertion device used for producing the X-ray beam is a multipole wiggler magnet (w150) with adjustable gap (21 poles, period of 15 cm, maximum magnetic field of 1.6 T at the minimum allowed gap – 24.8 mm): the corresponding maximum critical energy is 38.1 keV (unfiltered radiation). Recently, a second wiggler (w125) has been installed, with the aim of further increasing the flux of the produced photon beam. This second wiggler is characterized by 22 poles, a period of 12.5 cm, and a maximum magnetic field of 1.8 T at a gap of 11 mm. The X-ray source size, calculated at a gap of 60 mm for the w150 wiggler, is 132 μm (horizontal) × 24 μm (vertical) as Full Width at Half Maximum (FWHM). The X-ray beam divergence, in the same conditions, is approximately 735 μrad in the horizontal direction and 85 μrad in the vertical one.

As mentioned above, the long source to sample distance (L) and the small dimensions of the source (S) are necessary conditions to obtain a high degree of spatial coherence. The resulting small angular source size as seen from the sample, $\alpha = S/L$, leads to a transversal coherence length l_{coh}^{t} as large as 130 μm in the vertical plane for an X-ray energy of 30 keV.

All optical components were designed and manufactured (polished windows, filters, reductions of small monochromator vibrations etc…) to avoid, as possible, spurious images and/or losses of coherence on the X-ray path, and/or beam inhomogeneities at the sample position.

The general layout of the ID17 beamline is shown in figure 3.7. It consists of:

- a first Optics Hutch (OH1), located just after the front-end at about 26 m from the source, and containing a first set of diaphragms, slits, filters, and shutters for the spectral and geometrical definition of the X-ray beam. A fixed-exit monochromator based on two bent Si crystals in the Laue geometry is also installed in this hutch.
- A first Experimental Hutch (EH1, or MRT hutch), located at 40 m from the source, which is mainly exploited for the Microbeam Radiation Therapy program. In this experimental hutch, it is possible to use either a white beam or a monochromatic one. A sample stage for MRT, a kappa-goniometer for high precision positioning of the sample and a multislit collimator to spatially fractionate the radiation are within the main instruments (Renier et al., 2008). A first control room, where all the beamline and experimental elements are controlled, is located besides this experimental hutch.
- A long tunnel (100 m long) that connects the EH1 with the satellite building located outside the storage ring hall. In this concrete and lead shielded tunnel, the radiation is transported in a vacuum pipe.
- A second Optics Hutch (OH2 or monochromator hutch), where a second set of slits, absorbers, beam monitors and the main monochromators are installed. Two monochromator systems are presently operational: 1) a single crystal monochromator (also called "angiography monochromator") and a double crystal monochromator (called "computed tomography monochromator") for fixed-exit applications. Both systems run in oxygen-free helium filled chambers, at atmospheric pressure. The computed tomography monochromator uses two water-cooled bent Si crystals in Laue geometry producing a monochromatic beam parallel to the incident white beam, with a vertical offset of 40 mm. The central part of the crystals is 1 mm thick, 150 mm wide and 12 mm high, cut with an asymmetry angle of 15°. The X-ray energies that can be selected with this monochromator are in the range 20-140 keV[1]. The hutch contains also a fast shutter and a

[1] A new monochromator, with an energy range of about 30-100 keV, replaced the old one in February 2010. However, all the data from ID17 presented in this Thesis were acquired with the old monochromator.

chopper. The latter, in particular, synchronized with the taper optics Frelon camera, prevents the camera from being exposed during the read out time (see section 3.4).

- A second Experimental Hutch (EH2), where the different experimental setups are installed (including special optical elements, high precision linear or rotating motors for the sample positioning and movement etc…). Most of the experiments are performed in this hutch, including all X-ray imaging data acquisition. A second control room, used to control the beamline and experimental elements, is located close to the hutch.

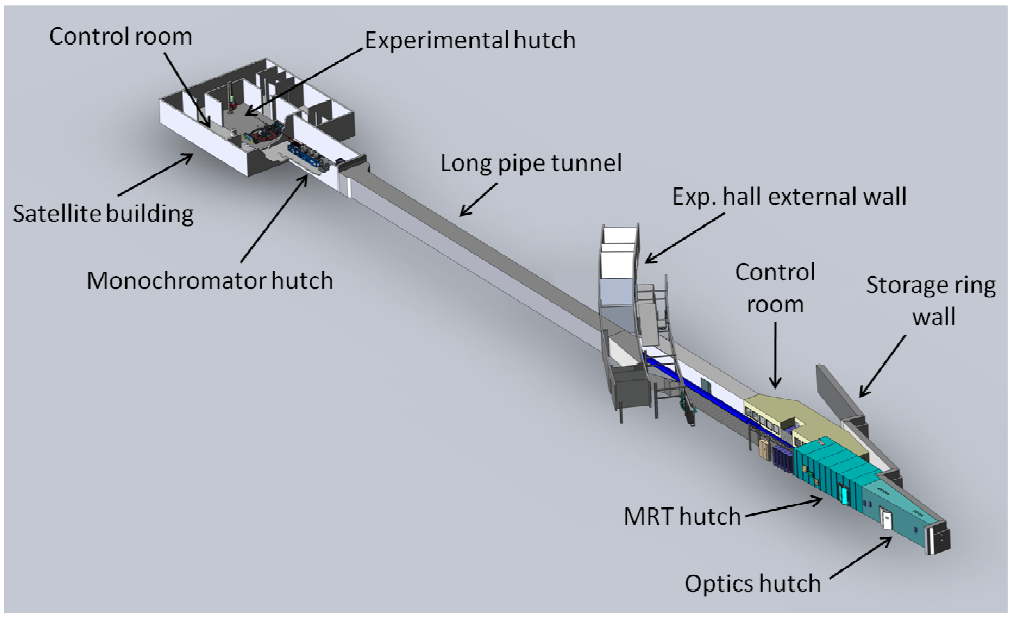

Fig. 3.7. The general layout of the ID17 beamline, from the first optics hutch to the satellite building.

3.2.2 Overview of the topography & tomography ID19 beamline and of the optics BM5 beamline

The ID19 beamline is devoted to research in various fields of X-ray imaging, the main investigation techniques being: topography (Bragg diffraction imaging), high-resolution diffractometry, absorption and phase-contrast radiography or micro-tomography. With ID17, ID19 beamline is one of the two long beamlines at the ESRF: the experimental hutch is located in a separate building outside the ring experimental hall, with a maximum distance from the source of approximately 145 m. The X-ray beam can be produced at ID19 by using either two undulators or, as in most experiments, an 11-pole wiggler (maximum field 1.4 T, period 15 cm, maximum critical energy of 32 keV). X-rays with an energy between 6 and 120 keV can be selected with the double Si(111) monochromator, set in Bragg geometry, or with the multilayer monochromator. Most experiments, however, are performed in the 10-35 keV range. The source size is approximately 120 µm (horizontal) × 30 µm (vertical), while the maximum dimensions of the beam at the sample position are about 45 mm (H) × 15 mm (V).

The BM5 beamline is mainly used as a test and development station for X-ray optical elements, for instrumentation for beam coherence and polarization characterization and for other instrumentation investigations. The X-ray beam is produced by a bending magnet characterized by a magnetic field of 0.82 T, resulting in a critical energy of 19.9 keV. The source size is about 270 µm (H) × 80 µm (V). The double crystal Si(111) monochromator, set in Bragg geometry, or the multilayer monochromator, allow selecting X-ray energies in the range 6-60 keV. In the first case, an energy resolution $\Delta E/E$ of about 10^{-4} can be obtained, while in the case of the multilayer the energy resolution is equal to about 10^{-2}. The first experimental hutch is located at a distance of approximately 30 m from the source, while the second hutch is at about 50 m from the source. A maximum beam size of approximately 120 mm (horizontal) × 6 mm (vertical) can be obtained in this second hutch.

3.3 Experimental setup for the ABI and GIFM techniques

In the following, the ABI setup at ID17 will be described in detail, and the general features of the setup used for the GIFM technique will be provided.

3.3.1 ABI instrumentation at ID17

The ABI setup is located in the experimental hutch, at a distance of about 155 meters from the source. It is schematically shown in figure 3.8, while a photograph is reported in figure 3.9.

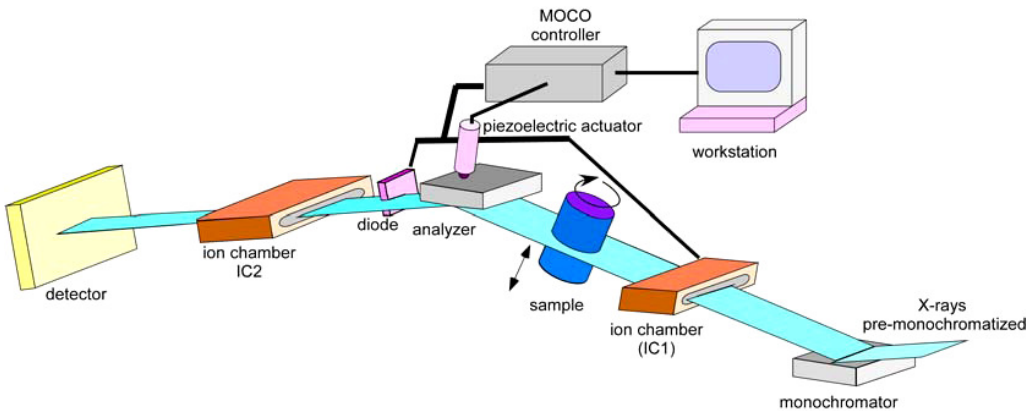

Fig. 3.8. Scheme of the ABI setup at ID17.

The beam coming in the experimental hutch from the Laue double crystal is monochromatized to a narrower bandwidth by a Si(333) Bragg crystal (n°2 in figure 3.9). After passing through the sample (n°4), the beam impinges on a second Si crystal (n°5) that is identical to the first one (and set at the same reflection cut), which is used to filtrate the beam before it reaches the Frelon camera detector (n°8). The ABI crystals are mounted on a granite block (n°1), which efficiently decouples the optics from the floor for increased stability. Two ionization chambers and a diode are used to control the incoming X-ray beam intensity. The first ionization chamber (n°3) is in

front of the sample, while the diode (n°6) and the second ionization chamber (n°7) are placed behind the analyzer.

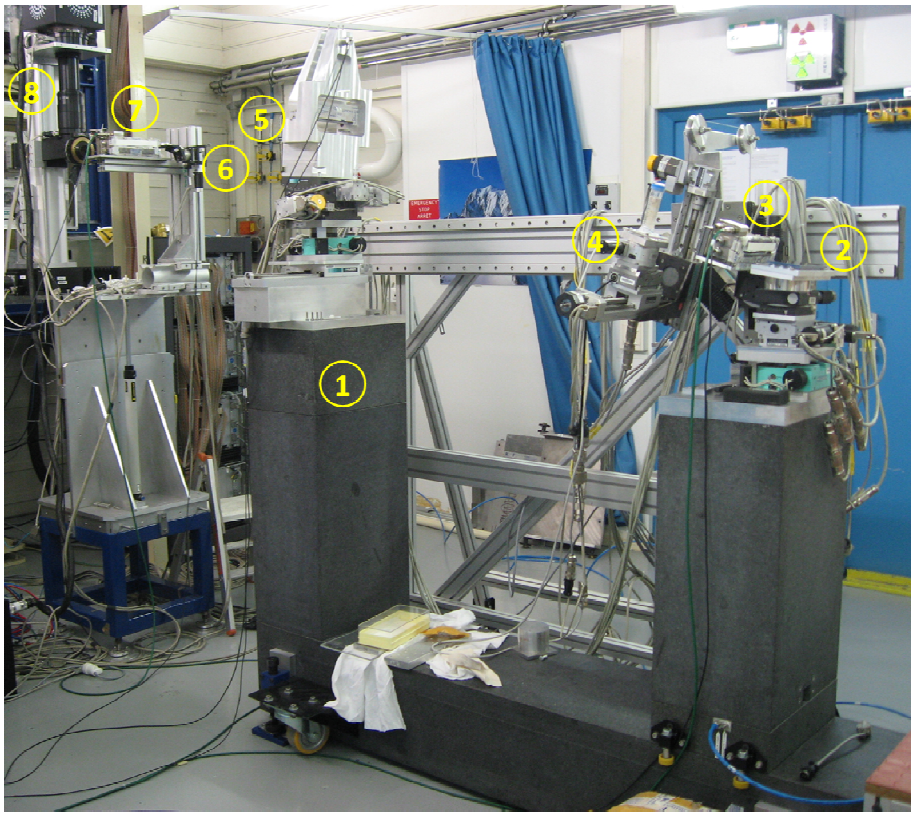

Fig. 3.9. Photograph of the ABI setup at ID17. The following elements are shown: (1) the granite block, (2) the monochromator crystal, (3) the first ionization chamber, (4) the sample stage, (5) the analyzer crystal, (6) the diode, (7) the second ionization chamber, (8) the Frelon camera.

More in detail:

- The monochromator crystal stage, shown in figure 3.10 (n°1), consists of a tower bearing the crystal and mounting on a vertical translation motor and a "theta" and "roll" tilt motors. In particular, "theta" defines the angle in the diffraction plane with respect to the X-rays propagation direction, while "roll" is used to align the angle in a plane perpendicular to the propagation direction. The two tilt motors have a resolution of $0.25 \cdot 10^{-3}$ degrees. The monochromator stage is mounted on one of the two columns of the granite block.
- The sample stage (n°3 in figure 3.10), for both projection and CT imaging, is mechanically decoupled from the granite block, in order not to transmit vibrations from the sample motors to the crystals during motors movements and acquisition scans. The sample stage is anchored to a transverse bar directly fixed on the floor. It consists of:
  - A high resolution vertical translation motor, used for scanning the sample through the laminar SR beam.

- A horizontal translation motor (motion perpendicular to the X-rays direction) to center the sample with respect to the centre of the beam and put it in/out of the beam for reference images acquisitions.
- A rotation stage for tomographic imaging (resolution = 0.01 degrees).
- A "theta" tilt motor for angularly aligning the sample with respect to the X-ray beam direction, in particular to position the whole sample stage perpendicular to X-rays.
- A "roll" tilt motor to align the sample for CT.

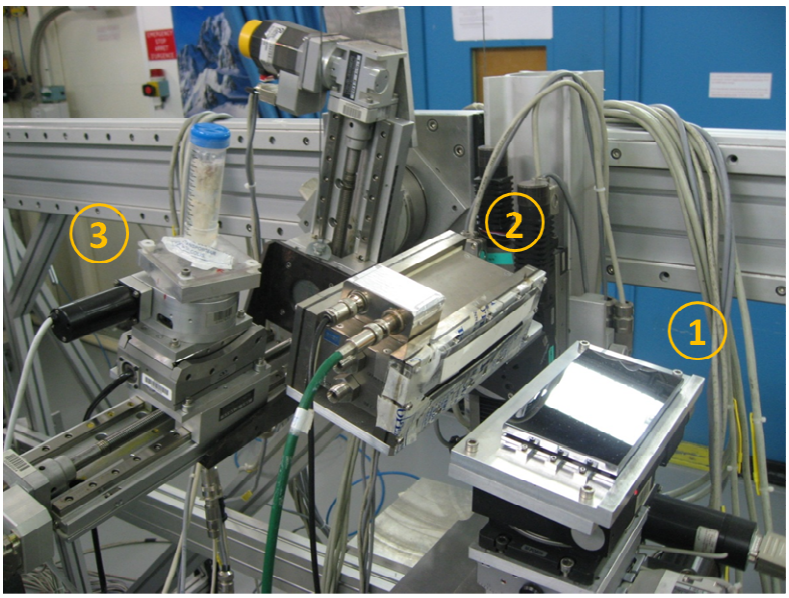

Fig. 3.10. Detail of the ABI setup at ID17: (1) monochromator crystal stage, (2) first ionization chamber, (3) sample stage.

- The analyzer crystal stage is shown in figure 3.11. It is fixed on a 25 cm long arm which is angularly controlled by means of a piezoelectric motor by determining the analyzer tuning (the piezoelectric resolution of 0.02 μrad is limited in the practice by the mechanics so that the final minimum step is about 0.1 μrad). Like for the monochromator, the tower bearing the analyzer crystal is placed on a double cradle ("theta" and "roll" tilts) for alignment and acquisition purposes. The crystal stage is mounted on the second column of the granite block. The two columns of the granite block can be independently moved in the beam direction in order to align the monochromator and the analyzer with the beam.

- Due to the very small angular acceptance of the monochromator and analyzer crystals, the main challenge in this kind of experiment is the insurance of the crystal stability. A monochromator controller (MOCO) is integrated to the ABI setup for this purpose. This device consists of a feedback system that permits to dynamically tune the analyzer piezoelectric actuator in order to keep the ratio between the intensity incident on the analyzer and the diffracted intensity at a given fixed value. The intensity before the analyzer is measured with the first ionization chamber, placed before the sample, while the diffracted

intensity is measured by the diode, which is placed in a portion of the beam outside the footprint of the sample. This system yielded to considerable improvements in terms of the analyzer crystal stability.

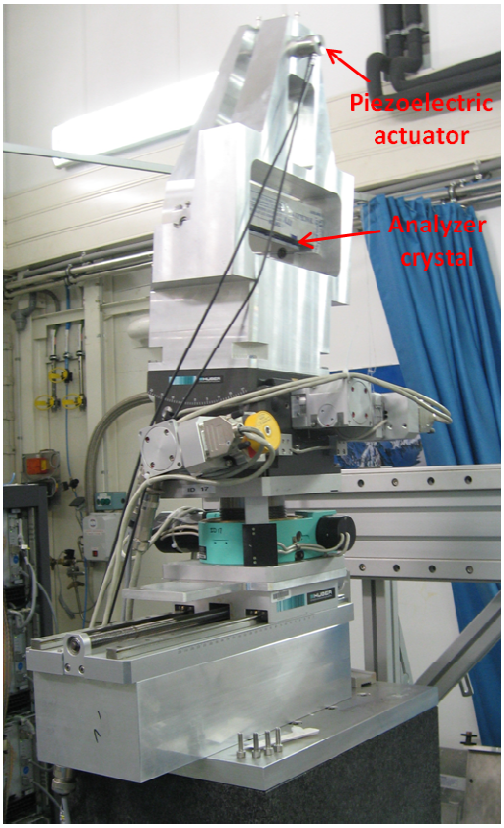

Fig. 3.11. Analyzer crystal stage.

3.3.2 Diffraction gratings for GIFM

A picture of the GIFM setup used at the BM5 beamline is shown in figure 3.12. The phase and the absorption gratings are placed in front of the Frelon camera, at a mutual distance equal to one of the fractional Talbot distances and set with their grating lines in the horizontal direction. The two gratings are mounted on plates that are fixed to a support system based on four parallel rods, which are used to ensure the perpendicularity of the gratings. The whole structure is placed on top of a rotation motor, and of horizontal and vertical translation motors, which are used for alignment purposes. The scanning of the phase grating with respect to the absorption grating is performed by using a high-resolution motor acting in the vertical direction.

The details of the gratings fabrication process are described in (David et al., 2007). A <110> oriented silicon wafer, 280 μm thick and with both sides polished, is used as the substrate for the phase grating. The grating lines are etched into the silicon substrate by using the following process. First, a photo resist pattern (fig. 3.13(a)), produced by photolithography, is transferred into a thin oxide layer (fig. 3.13(b)). The latter serves then as a mask for the anisotropic wet

etching process in a 20% aqueous KOH solution (fig. 3.13(c)). Finally, the oxide masking layer is removed in buffered oxide etch (BOE) (fig. 3.13(d)). In the right part of fig. 3.13, a scanning electron micrograph of the so-produced grating is shown.

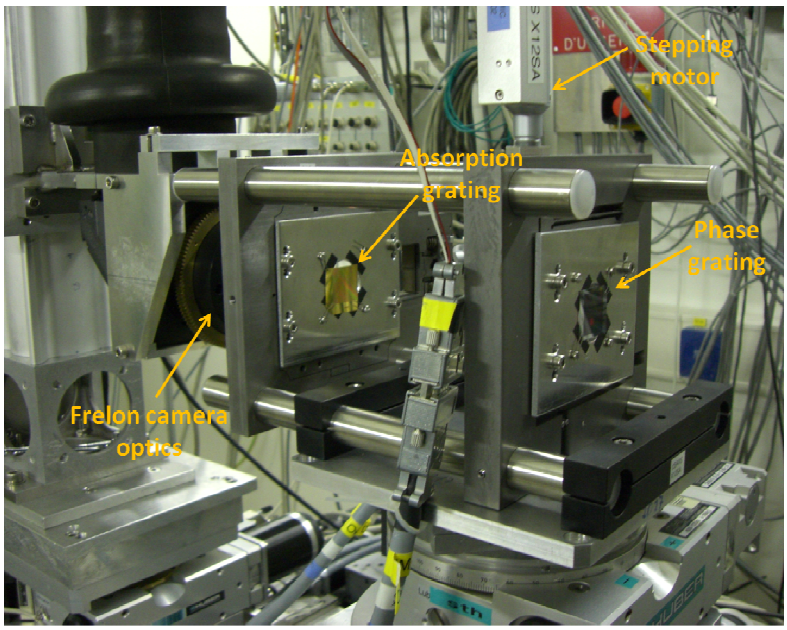

Fig. 3.12. Detail of the GIFM setup used at BM5. The phase and absorption gratings are placed in front of the camera, set with their grating lines horizontal. The phase grating is scanned in the vertical direction thanks to a high-resolution motor.

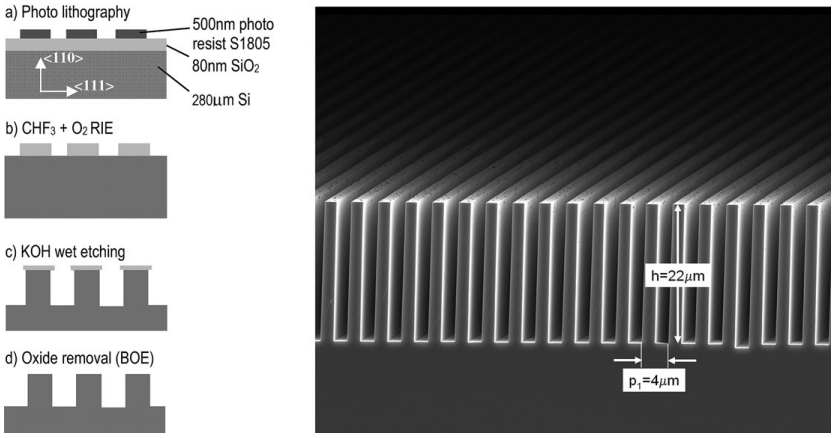

Fig. 3.13. Fabrication process for the silicon phase grating. Image taken from (David et al., 2007).

The fabrication of the absorption grating is schematized in fig. 3.14. A silicon grating with a duty cycle of 0.25, produced by anisotropic wet etching, is used as the starting basis for the process (fig. 3.14(a)). A 15 nm thick adhesive layer of chromium and a 50 nm thick layer of gold are then evaporated onto the grating (fig. 3.14(b)). The grating structures are finally covered with a 1 µm thick layer of gold by electroplating (fig. 3.14(c)). The so-produced gold absorption grating has a period which is half of that of the starting silicon grating.

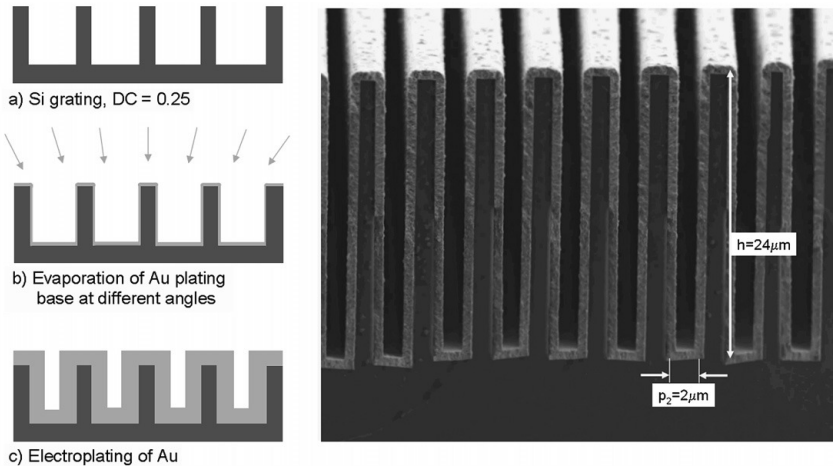

Fig. 3.14. Fabrication process for the gold absorption grating. Image taken from (David et al., 2007).

3.4 Image acquisition

3.4.1 X-ray detectors

The two detector systems used for the measurements performed at the BM5, ID17 and ID19 beamlines will be briefly described in this section.

- Taper optics Frelon camera. This detector system (fig. 3.15) is based on a Fast-Readout Low-Noise (Frelon) CCD camera coupled to a fiber optic taper (Coan et al., 2006). It has been developed at the ESRF for a broad range of applications; its specifications were initially tailored for computed tomography applications in analyzer-based imaging mammography (Bravin et al., 2003). The Frelon taper optics shows an active input surface of 94 × 94 mm^2 where X-rays are converted to visible light by a fluorescent screen; this secondary radiation is then guided by a fiber optic taper with a 3.2:1 reduction ratio and extra-mural absorption (Schott) onto the 2048 × 2048 $pixels^2$ 14 × 14 μm^2 CCD (Atmel Corp, USA). This reduction allows an effective pixel size of about 46 × 46 μm^2 to be achieved.

- High resolution Frelon optics. In order to cope with experiments requiring higher resolution, a Frelon camera coupled to an optical system made of de-magnifying lenses has also been developed. The CCD camera and the electronics are the same as those used for the taper optics Frelon camera. This optical system allows obtaining an effective pixel size of about 7.5 μm, but the available field of view is consequently reduced to 15.3 × 15.3 mm^2.

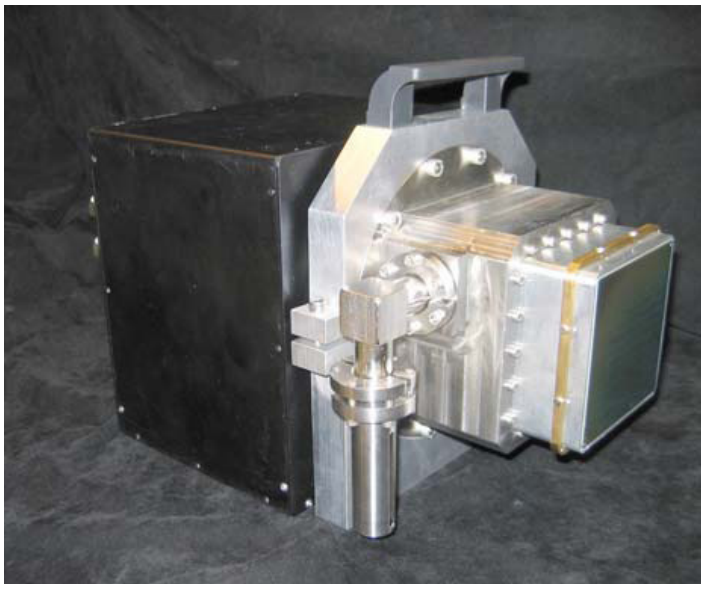

Fig. 3.15. The ID17 taper optics Frelon camera.

Thanks to a careful design of the electronics and to a Peltier-type cooling of the CCD (standard operation at -18 °C), both readout and dark signal levels are kept low. At the same time, a maximum readout speed of 20 Mpixels/s through four outputs provides the possibility of high frame rate imaging (4.2 frames/s) in full size image mode without binning. The gain is constant and it is 23 electrons/ADU (analog-to-digital unit); the maximum analog-to-digital readout of 2^{14} bits corresponds to $3 \cdot 10^4$ electrons whatever the binning applied.

The fluorescent screens can be easily exchanged in order to optimize the X-ray conversion with the different experimental applications and the selected energy. The taper optics and the high-resolution Frelon cameras can be coupled to powder phosphor screens (Gd_2O_2S:Tb, 5g/cm^3 density) of 40 μm, 100 and 200 μm thicknesses. The thin screen favors the spatial resolution at the expenses of absorption efficiency, whereas the thicker screen provides the opposite compromise. Both screens consist of an active phosphor layer deposited on a thin plastic film substrate, the active layer being in direct contact with the fiberoptic taper input surface.

3.4.2 Modalities of image acquisition

The imaging modalities employed for the acquisition of the images presented in this Thesis are the projection mode and the tomographic mode. In both cases, the acquisition procedure is determined by the laminar shape of the SR X-ray beam.

1. **The projection mode** consists of a vertical scan of the sample through the laminar beam. Depending on the detector operating mode, the sample movement, synchronized with the detector acquisition, can be continuous or discrete (in the latter case the sequence is: movement, acquisition, movement etc.). In these two cases, the movement speed or the step, respectively, is regulated so that the height of each acquired object frame is equal to an

integer multiple of the pixel size. The object images are then reconstructed by combining (piling up) the acquired object frames.

Whitefield images (images of the beam when no object is present) and darknoise images (obtained without illuminating the detector) are also acquired in order to normalize the object images, as described in section 3.5.2.

In the PBI and ABI techniques several images are often recorded respectively at different sample-detector distances and different analyzer orientations, in order to apply the algorithms for the extraction of quantitative sample information (see chapters 2 and 4), or simply to compare the contrast in the different conditions. In these cases, the procedure described above for the image acquisition is repeated for each of the considered experimental configurations. In the case of the GIFM technique, instead, the vertical scanning of the sample and that of the gratings (employed in the so-called phase stepping method) are inverted. For each vertical position of the sample, in fact, one of the gratings is scanned with respect to the other and an object frame is acquired at each grating step.

2. **The CT acquisition** consists in a vertical scan combined with a sample rotation. For each vertical step, a rotation of the sample over 180 or 360 degrees is performed, which is synchronized with the detector acquisition and can be either discrete or continuous. An arbitrary number of projections at different angular orientations of the sample can then be acquired. Each sample slice, corresponding to a given height within the sample, is then reconstructed from the corresponding sinogram with the use of a direct filtered backprojection algorithm (Kak and Slaney, 1988). We implemented the reconstruction using the program PyHST (Python High Speed Tomography), which is being developed and maintained by the Scientific Software Group (SciSoft) of the ESRF. This software is based on the HST program originally written in Fortran by A. Hammersley (http://www.esrf.eu/computing/scientific/HST/HST_REF/hst.html).

   The acquisition can be made in two modes. In **full mode** the rotating sample must be fully included in the Field Of View (FOV) of the detector so that the side pixels record only the background outside the object. The **half mode** is used for samples wider than the detector. In half mode, it is possible to enlarge the FOV up to a factor of 2 by displacing laterally the centre of rotation. The acquisition is made over 360 degrees: each point of the object will be in the FOV for at least 180 degrees within the tomography rotation. The second half of the sonogram, acquired between 180 and 360 degrees, is then reversed and "glued" to the 0-180 degrees sinogram; in this way a complete 0-180 degrees sinogram of up to twice the FOV is available for reconstruction.

   When different positions on the analyzer rocking curve (for ABI) and different sample-detector distances (for PBI) are considered, the procedure described above needs to be repeated for each of the considered configuration acquisitions. Differently, in GIFM a grating scanning is performed at each vertical position and for each rotation angle considered.

3.5 Image processing

In this section we will present some of the general image processing methods that have been used in this Thesis, which are strictly linked to the image acquisition modalities introduced in the previous section.

3.5.1 Correction of taper deformations

Each raw image acquired by using the Frelon camera coupled to the 46 μm optics must be corrected for the image deformations arising from the fiber-optics taper and from the coupling of the taper with the CCD.

By using images of a periodic object (a grid), it was possible to quantitatively calculate pixel-by-pixel the distortion introduced by the camera and to calculate the corrections to be applied (C. Nemoz, ID17 team, private communication).

In figure 3.16(A) an image of a grid (holes distance: 2.5 mm) is shown as acquired with the Frelon camera and also overlapped to its expected shape (smaller points). As a result, a two-dimensional correction matrix (of same dimensions as the raw image) has been written. Each element of the matrix contains the shifts to be applied to each image pixel in both horizontal and vertical directions in order to obtain the undistorted image of the object. The corrected image of the grid is presented in fig. 3.16(B). The taper-correction procedure has been implemented in the IDL software routinely used at ID17 for the image processing.

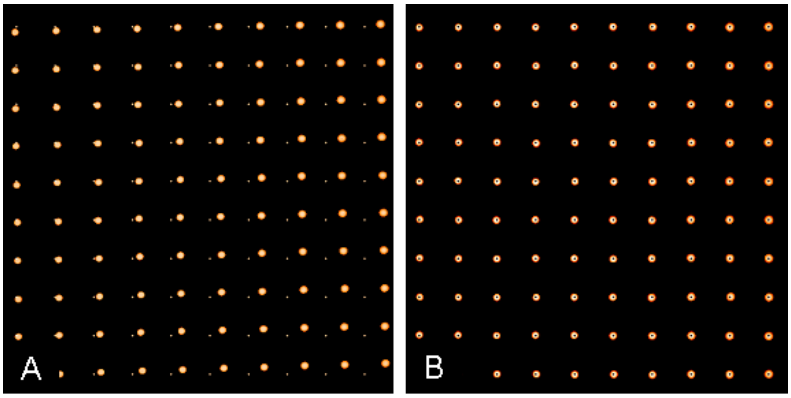

Fig. 3.16. (A) Image of a grid overlapped with its expected shape. The displacement of each hole from its theoretical position is due to the imperfections of the camera optics. (B) The corrected image.

3.5.2 Image normalization

A number of image normalization techniques can be used in order to correct the unavoidable artefacts arising from the image acquisition. Only those used in this Thesis, however, will be here reviewed.

In general the acquired images (after correction for the taper distortion, if the fiber-optics taper is used) appear non-uniform not only in correspondence of the imaged object but also outside it. These inhomogeneities can have different origins, in particular:

1. the temporal instability of the incident X-ray beam
   Causes: machine current decreased with time, vibrations or thermal drift of optical elements (filters, crystals) along the X-ray path etc…
2. the spatial inhomogeneity of the incident X-ray beam
   Causes: intrinsic inhomogeneity of the X-ray beam from the wiggler, defects or deformations of optical elements etc…
3. the detector response inhomogeneities
   Causes: electronic noise (dark current), pixels with different gain etc…

The darknoise/whitefield normalization is applied in order to eliminate or at least reduce these contributions to the image. As we saw in the previous section, together with the object frames also the darknoise and whitefield images are always acquired. The **darknoise image** is recorded without illuminating the detector. The signal consists only of the electronic noise of the detection chain, which is of additive type. The **whitefield image** is registered in the same conditions as the raw image to normalize but without the sample in the X-ray beam. Whitefield images are usually acquired before or after the object scanning in the case of fast acquisitions (in planar mode, for instance), whereas they are collected also at regular intervals within the object acquisition in the case of longer scans (for instance in computed tomography mode). The normalization process can be schematized as:

$$normalized\ image = \frac{raw\ image - darknoise}{whitefield - darknoise} \tag{3.1}$$

where the subtraction and the division operations are performed on a pixel-by-pixel basis. Note that in some of the algorithms for extraction of quantitative information (for instance the phase stepping method for GIFM described in chapter 2) the whitefield normalization is incorporated in the algorithm itself, and therefore eq. 3.1 is not explicitly applied.

Despite of the darknoise/whitefield normalization, residual artefacts are often visible when the corrected object frames are piled up to form the object image (see fig. 3.17(a)). These are due, in particular, to instabilities in the spatial position of the beam and to variations of the beam intensity that occur over short times and are therefore not accounted for by the previous correction. An additional normalization is then often necessary.

These inhomogeneities are visible in general as streak artefacts perpendicular to the direction of the object scanning (fig. 3.17(a)). In many cases, normalizing the image by selecting bands of pixels on the image itself (in regions not covered by the sample) can partially solve the problem. In the image of figure 3.17(a), a 50 pixels wide vertical band has been used to this end. For each row, the average value over the 50 pixels in the band was calculated: each column of the image was then divided, on a pixel-by-pixel basis, by the so-computed column vector. In the example of figure 3.17, most of the streak artefacts have been compensated for and are not visible anymore in the corrected image shown in figure 3.17(b).

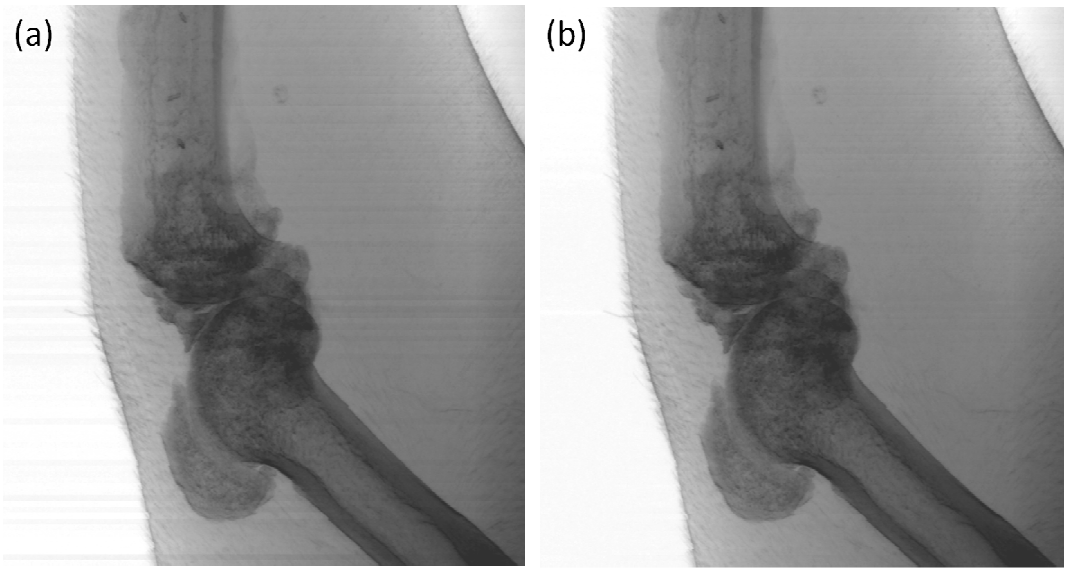

Fig. 3.17. ABI planar image of the knee of a guinea pig: (a) uncorrected image, (b) image corrected for the horizontal streak artefacts.

3.5.3 Correction of artefacts in CT imaging

Residual artefacts that are not eliminated by the darknoise/whitefield normalization can produce effects also on the subsequent tomographic reconstruction, when CT is considered. Ring artefacts on the reconstructed axial slices, which are generated by line artefacts in the sinograms, are a typical example of such effects (see figure 3.18(a), for instance). They potentially originate from dead detector pixels, defects in the optical elements, spatial instabilities of the beam etc…

The algorithm that was used to correct the ring artefacts in the images presented in this Thesis consists of the following steps:

- Median filtering of each reconstructed slice. The kernel needs to be wider than the size of the ring artefacts, so that the rings are almost completely eliminated by this operation. The filtered image is then subtracted from the original slice: in this way, only the high object frequencies and the ring artefacts remain in the resulting image.

- The obtained image is then transformed to polar coordinates (where the values on the *x* axis represent the distance from the rotation axis and the values on the *y* axis the rotation angle). The ring artefacts show up in this image as lines parallel to the *y* direction. A convolution with a Gaussian filter is then performed, along this latter direction, for each column of the image. By doing so, the image components corresponding to the slice ring artefacts are not eliminated (because they are almost constant over a column), while the high object frequencies mainly cancel out.
- The resulting image is then transformed back to normal spatial coordinates. A slice containing only the ring artefacts is therefore obtained. The latter is then subtracted from the original slice in order to eliminate or at least reduce the ring artefacts contribution.

In the actual application of this algorithm, the values of several parameters need to be adjusted and optimized for the considered images: parameters controlling the width (in pixels) of the median and Gaussian filtering, a subtraction factor controlling the strength of the subtraction of the "ring artefacts" slice from the original image, thresholds for better differentiating the rings from the object etc…

An example of the application of the described ring correction algorithm is reported in figures 3.18(a,b). In fig. 3.18(a), a detail of a reconstructed slice in a region with a carcinoma solid tumour is reported. Some ring artefacts are evident in the image. In fig. 3.18(b), the corresponding region after the application of the ring correction algorithm is shown. The rings have almost disappeared, without a degradation of the image resolution.

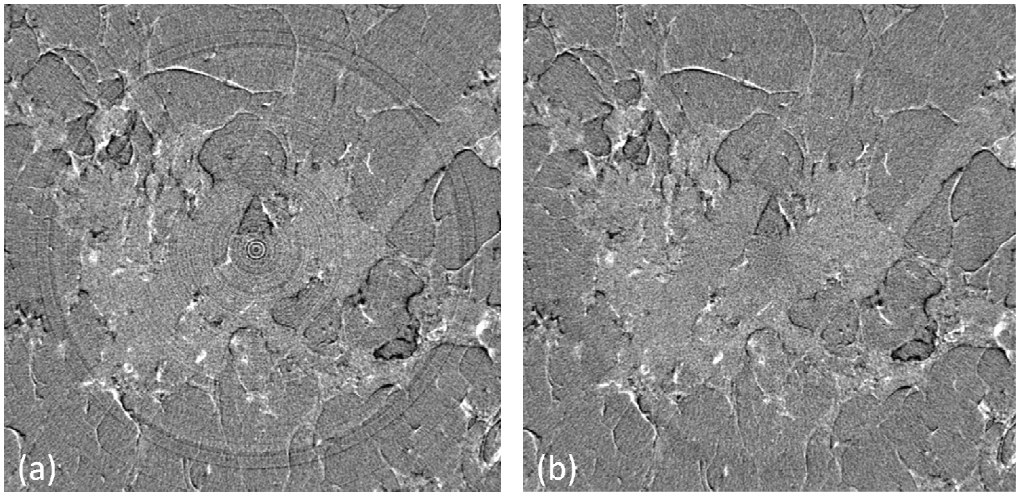

Fig. 3.18. (a) Detail of an ABI reconstructed slice (in a region close to the centre of rotation) of a human breast sample affected by carcinoma: the solid tumour is visible at the centre of the image, as well as ring artefacts. (b) The same detail in the corrected slice, where the ring artefacts have almost disappeared.

3.5.4 Distributed computation for fast image reconstruction

Distributed (or parallel) computing can be a particularly useful tool when the computation times required by a given application are long. Parallelization consists in splitting up the calculations into many independent processes and in running them in parallel on different PCs, or CPUs (central processor units), or GPUs (graphical processor units) etc…

An efficient parallelization depends on the implemented algorithm, which needs to be divisible into many independent parallel processes in order to take advantage of the distributed computation. Several examples of calculations that can be easily parallelized can be found in the field of image processing: a pixel-by-pixel calculation (each image pixel is processed independently of the others), tomography reconstruction (each slice is reconstructed independently of the others), calculations involving a processing of many images independently of the others etc… The latter case is that encountered in chapter 5 of this Thesis, where a distributed computation was performed.

Furthermore, an obvious requirement for an efficient parallelization is that the data transfer time (i.e. the time needed to transfer the information for example from one processor to the other) must be much shorter than the effective computation time.

Distributed computations can be performed at the ESRF by using Condor®, a high-throughput computer software framework developed at the University of Wisconsin-Madison (Thain et al., 2005). With the use of Condor, the different processes into which the calculation has been divided can be sent to the ESRF machines cluster, where they are independently computed. To this end, the algorithm to be repeatedly implemented on the different machines (written in Matlab, in the specific case examined in chapter 5) needs to be compiled before it can be used.

3.6 Contrast, signal-to-noise ratio and figure of merit

In these last sections of the chapter, we will introduce some quantities that can be used for the assessment of the quality of the obtained images. In particular, the contrast, the signal-to-noise ratio and the figure of merit will be defined in the standard case of area contrast (section 3.6.1) and in the case, specific to phase contrast, of an edge signal (section 3.6.2).

3.6.1 Area contrast case

The area contrast of an object detail with respect to the surrounding region (considered as background) is defined as (Evans, 1981):

$$C_{area} \equiv \frac{I_{obj} - I_{back}}{I_{back}} \tag{3.2}$$

where I_{obj} and I_{back} are the mean intensity values of a given area respectively in the object and in the background.

The signal-to-noise ratio (SNR) in the area case is defined as:

$$SNR_{area} \equiv \frac{I_{obj} - I_{back}}{\sqrt{std^2\left(I_{obj}\right) + std^2\left(I_{back}\right)}} = \frac{\sqrt{A}\left(I_{obj} - I_{back}\right)}{\sqrt{\sigma_{obj}^2 + \sigma_{back}^2}} \tag{3.3}$$

where $std(I_{obj})$ and $std(I_{back})$ are the standard deviations on the mean values I_{obj} and I_{back} calculated over a number of pixels A, and σ_{obj} and σ_{back} are the standard deviations associated to each pixel value in the detail and in the background.

It should be noted that, according to these definitions, the area contrast and area SNR can be either positive or negative. We can therefore account for intensity values that are larger in the detail compared to the background or the opposite. In conventional X-ray imaging, where the intensity incident on the detector is determined only by the differences in absorption, a positive (negative) contrast corresponds to a detail less (more) absorbing than the surrounding region.

The area SNR is dependent on the incoming flux. More precisely, it is proportional to the square root of the number of incident photons, if we assume the noise to be determined only by the statistical (white) Poisson noise. Therefore, if images acquired with different fluxes need to be compared, the SNR does not represent an appropriate parameter. To measure the quality of an image independently of the delivered dose used to obtain the image, it is necessary to consider another quantity, independent of the number of photons or equivalently of the dose. For this reason the following Figure of Merit (FoM) is defined (Pani, 1996, Arfelli et al., 1998):

$$FoM \equiv \frac{SNR}{D} \tag{3.4}$$

which is in principle independent of the number of photons because the dose, D, is directly proportional to the X-ray flux for a given sample and energy (Webb, 1988).

3.6.2 Edge contrast case

The signal generated by a detail, when phase-contrast techniques are used, has a different shape compared to the absorption case. As we saw in chapter 2, in fact, the signal is in general produced by a combination of absorption, scattering and refraction effects. The refraction component, in particular, is localized at the object edges, where the value of the refractive index decrement changes. Therefore, quantities for analysis of the image quality corresponding to those introduced above in the case of area signal need to be defined also in the edge signal case.

In analogy with eq. 3.2, the contrast can be defined as (Snigirev et al., 1995):

$$C_{edge} \equiv \frac{I_{\max} - I_{\min}}{I_{back}} \tag{3.5}$$

where I_{back} is the intensity outside the detail, and I_{max} and I_{min} are respectively the maximum and minimum of a mean intensity profile across the edge, calculated over a certain number of columns

of pixels. Note that when the edge is characterized by only one positive (or negative) peak, I_{min} (or I_{max}) is considered equal to the background value.

The SNR in the edge case can be defined as (Coan et al., 2005, Pagot et al., 2005):

$$SNR_{edge} \equiv \frac{I_{\max} - I_{\min}}{\sqrt{2} \cdot std\left(I_{back}\right)} = \frac{\sqrt{A}\left(I_{\max} - I_{\min}\right)}{\sqrt{2} \cdot \sigma_{back}} \tag{3.6}$$

where $std(I_{back})$ is the standard deviation on the mean value I_{back}, calculated by considering the same number of pixels A over which I_{max} and I_{min} are computed, and σ_{back} is the standard deviation of each pixel outside the object. The associated FoM can be defined by using eq. 3.4 as in the area contrast case and the definition of the edge SNR given in eq. 3.6.

References and links

F. Arfelli, V. Bonvicini, A. Bravin, G. Cantatore, E. Castelli, L. Dalla Palma, M. Di Michiel, R. Longo, A. Olivo, S. Pani, D. Pontoni, P. Poropat, M. Prest, A. Rashevsky, G. Tromba, and A. Vacchi, "Mammography of a phantom and breast tissue with synchrotron radiation and a linear-array silicon detector", Radiology **208** (3), 709-715 (1998).

M. Bech, O. Bunk, C. David, R. Ruth, J. Rifkin, R. Loewen, R. Feidenhans, and F. Pfeiffer, "Hard X-ray phase-contrast imaging with the compact light source based on inverse Compton scattering", J. Synchrotron Radiat. **16** (1), 43-47 (2009).

A. Bravin, S. Fiedler, P. Coan, J.-C. Labiche, C. Ponchut, A. Peterzol, and W. Thomlinson, "Comparison between a position sensitive germanium detector and a taper optics CCD "FRELON" camera for Diffraction Enhanced Imaging", Nucl. Instr. Meth. A **510** (1-2), 35-40 (2003).

W. Brefeld and P. Gurtler, "Synchrotron Radiation Sources", in *Handbook on Synchrotron Radiation*, S. Ebashi, M. Koch, and E. Rubenstein, eds., Elsevier Sience Publishers, Amsterdam, Netherlands (1991), pp. 269-296.

F. E. Carroll, M. H. Mendenhall, R. H. Traeger, C. Brau, and J. W. Waters, "Pulsed, tunable monochromatic X-ray beams from a compact source: New opportunities", Am. J. Roentgenol. **181** (5), (2003).

P. Coan, E. Pagot, S. Fiedler, P. Cloetens, J. Baruchel, and A. Bravin, "Phase-contrast X-ray imaging combining free space propagation and Bragg diffraction", J. Synchrotron Radiat. **12** (2), 241-245 (2005).

P. Coan, A. Peterzol, S. Fiedler, C. Ponchut, J. C. Labiche, and A. Bravin, "Evaluation of imaging performance of a taper optics CCD 'FReLoN' camera designed for medical imaging", J. Synchrotron Radiat. **13** (3), 260-270 (2006).

C. David, J. Bruder, T. Rohbeck, C. Grunzweig, C. Kottler, A. Diaz, O. Bunk, and F. Pfeiffer, "Fabrication of diffraction gratings for hard X-ray phase contrast imaging", Microelectron. Eng. **84** (5-8), 1172-1177 (2007).

L. De Caro, C. Giannini, R. Bellotti, and S. Tangaro, "A theoretical study on phase-contrast mammography with Thomson-scattering x-ray sources", Med. Phys. **36** (10), 4644-4653 (2009).

K. Dobashi, A. Fukasawa, M. Uesaka, H. Iijima, T. Imai, F. Sakamoto, F. Ebina, J. Urakawa, M. Akemoto, T. Higo, and H. Hayano, "Design of compact monochromatic tunable hard X-ray source based on X-band linac", Jpn. J. appl. Phys. 1 **44** (4A), 1999-2005 (2005).

A. L. Evans, *The evaluation of medical images*, Adam Hilger Ltd, Bristol, United Kingdom (1981).

F. Grüner, S. Becker, U. Schramm, T. Eichner, M. Fuchs, R. Weingartner, D. Habs, J. Meyer-ter-Vehn, M. Geissler, M. Ferrario, L. Serafini, B. Van der Geer, H. Backe, W. Lauth, and S. Reiche, "Design considerations for table-top, laser-based VUV and X-ray free electron lasers", Appl. Phys. B - Lasers O. **86** (3), 431-435 (2007).

Z. Huang and R. D. Ruth, "Laser-electron storage ring", Phys. Rev. Lett. **80** (5), 976-980 (1998).

H. Ikeura-sekiguchi, R. Kuroda, M. Yasumoto, H. Toyokawa, M. Koike, K. Yamada, F. Sakai, K. Mori, K. Maruyama, H. Oka, and T. Kimata, "In-line phase-contrast imaging of a biological specimen using a compact laser-Compton scattering-based x-ray source", Appl. Phys. Lett. **92** (13), 131107 (2008).

A. C. Kak and M. Slaney, *Principles of Computerized Tomographic Imaging* , IEEE Press, New York, USA (1988).

R. Kuroda, H. Toyokawa, N. Sei, M. Yasumoto, H. Ogawa, M. Koike, K. Yamada, T. Nakajyoo, F. Saka, and T. Yanagida, "Injector study for compact hard X-ray source via laser Compton scattering", International J. Mod. Phys. B **21** (3), 488-496 (2007).

P. Oliva, A. Bacci, U. Bottigli, M. Carpinelli, P. Delogu, M. Ferrario, D. Giulietti, B. Golosio, V. Petrillo, L. Serafini, P. Tomassini, C. Vaccarezza, C. Vicario, and A. Stefanini, "Start-to-end simulation of a Thomson source for mammography", Nucl. Instrum. Meth. A **615** (1), 93-99 (2010a).

P. Oliva, M. Carpinelli, B. Golosio, P. Delogu, M. Endrizzi, J. Park, I. Pogorelsky, V. Yakimenko, O. Williams, and J. Rosenzweig, "Quantitative evaluation of single-shot inline phase contrast imaging using an inverse Compton x-ray source", Appl. Phys. Lett. **97** (13), 134104 (2010b).

E. Pagot, S. Fiedler, P. Cloetens, A. Bravin, P. Coan, K. Fezzaa, J. Baruchel, and J. Härtwig, "Quantitative comparison between two-phase contrast techniques: Diffraction Enhanced Imaging and Phase Propagation Imaging", Phys. Med. Biol. **50** (4), 709-724 (2005).

S. Pani, *La qualità dell'immagine in relazione alla dose assorbita in mammografia diagnostica con luce di sincrotrone*, Tesi di Laurea in Fisica, Trieste, Italia (1996).

M. Renier, T. Brochard, C. Nemoz, H. Requardt, E. Brauer, F. Esteve, J. Balosso, P. Suortti, J. Baruchel, H. Elleaume, G. Berruyer, P. Berkvens, and A. Bravin, "The radiotherapy clinical trials projects at the ESRF: Technical aspects", Eur. J. Radiol. **68** (3), S147-S150 (2008).

A. Snigirev, I. Snigireva, V. Kohn, S. Kuznetsov, and I. Schelokov, "On the possibility of x-ray phase contrast microimaging by coherent high-energy synchrotron radiation", Rev. Sci. Instrum. **66** (12), 5486-5492 (1995).

D. Thain, T. Tannenbaum, and M. Livny, "Distributed Computing in Practice: The Condor Experience", Concurrency and computation: Practice and Experience **17**, 323-356 (2005).

S. Webb, "The physics of medical imaging", F. Mould ed., Iop, Avon, United Kingdom (1988).

H. Yamada, "Novel X-ray source based on a tabletop synchrotron and its unique features", Nucl. Instrum. Meth. B **199**, 509-516 (2003).

K. Yamada, R. Kuroda, H. Toyakawa, H. Ikeura-sekiguchi, M. Yasumoto, M. Koike, F. Sakai, K. Mori, H. Mori, N. Fukuyama, and E. Sato, "A trial for fine and low-dose imaging of biological specimens using quasi-monochromatic laser-Compton X-rays", Nucl. Instrum. Meth. A **608** (1), S7-S10 (2009).

4

Extraction of quantitative information from analyzer-based projection images

Table of Contents

Abstract: Many mathematical methods have been so far proposed in order to separate absorption, refraction and ultra-small angle scattering information in phase-contrast analyzer-based images. In this chapter a comprehensive quantitative comparison between five of the most widely used extraction algorithms based on the geometrical optics approximation is presented: the diffraction-enhanced imaging (DEI), the extended diffraction-enhanced imaging (E-DEI), the generalized diffraction-enhanced (G-DEI), the multiple-image radiography (MIR) and the Gaussian curve fitting (GCF). The algorithms are theoretically analyzed in terms of their validity conditions and experimentally compared by using geometrical phantoms providing various amounts of absorption, refraction and scattering. The application of the various extraction algorithms to images of a human bone-cartilage sample is also presented and discussed.

4.1 Introduction

The theoretical basis and the requirements concerning the experimental setup of the analyzer-based imaging (ABI) technique have been extensively discussed in chapters 2 and 3. In the present chapter, we will focus on the contrast mechanisms that contribute to the image formation and on the algorithms so far proposed to separate and quantify them.

As we saw in chapter 2, the analyzer crystal acts as an angular filter of the radiation transmitted through the object, since only the X-rays travelling in a narrow angle window close to the Bragg condition are diffracted onto the detector. Before being detected, furthermore, the beam is modulated (according to equation 2.53, in the geometrical optics approximation) by the angular-dependent rocking curve (RC) of the analyzer crystal. The full-width at half maximum (FWHM) of the RC is typically of the order of a few microradians.

A deflection of the beam of a few microradians arising from the refraction inside the object will therefore transform, thanks to the modulation given by the RC, into a change of the intensity recorded on the detector. The beam attenuation due to the absorption inside the object will instead decrease the recorded intensity, which is proportional to the transmission through the object (equation 2.53). Besides absorption and refraction, also X-ray scattering plays an important role in the generation of the image contrast. Scattering originates by very tiny object internal structures that are not resolved by the detector, being smaller than the pixel size. Ultrasmall-angle scattering (USAXS), which is due to structures ranging in the order of magnitude of hundreds of nanometers up to micrometers and which occurs at angles of several microradians, partially falls within the acceptance of the analyzer crystal and has the effect of broadening the measured RC, as we will see in detail in section 4.2.3. Diffuse scattering in the milliradian range, originating from object internal structures at the nanometer scale, is instead rejected and gives rise to what is called extinction contrast. Another important effect of the angular selectivity is the rejection of the Compton-scattered photons which eliminates the additional background due to scattering encountered in conventional X-ray tube CT.

The contrast in the recorded AB images is therefore given by a mixture of absorption, refraction, USAXS and small-angle X-ray scattering rejection (the latter three effects having the same physical nature as demonstrated by Davis (Davis, 1994)). The information contained in the images is thus very rich but the image interpretation can be in some cases ambiguous due to the signals superposition. In order to both effectively separate the different physical effects and accurately quantify them, several mathematical methods have been so far proposed. They allow calculating the corresponding physical parameters by means of combining two or more images acquired at different positions on the analyzer RC.

Most of the proposed methods are based on the geometrical optics (GO) approximation, introduced in chapter 2, which imposes some restrictions on the imaged object. This approximation, in fact, is strictly valid only if the phase of the wave incident on the crystal analyzer is a slowly varying function on the length scale of the extinction length of the crystal, which has been shown to

be equivalent to the condition $N_T >> 1$, where N_T is the so-called Takagi number (Pavlov et al., 2004, Nesterets et al., 2006).

Other methods based on different approximations have also been developed. The method proposed by Nesterets et al. (Nesterets et al., 2004) is based on the so-called weak object (WO) approximation, which requires that the phase shifts introduced by the object are weak. Another method introduced in literature (Paganin et al., 2004) is, instead, based on the linear transfer function (LTF) approximation, which requires that the transfer function of the imaging system can be linearized in the Fourier space. The application of these last two methods, however, requires the knowledge of the imaging system PSF (point spread function), which is a complex function that needs specific measurements and calculations. Furthermore, additional terms to the expression of the imaging system PSF need to be considered if the incoming beam is not perfectly parallel and monochromatic (Nesterets et al., 2005), which is usually the case in common experimental conditions. Under the GO approximation, instead, just the knowledge of the imaging system RC, which can be easily measured, is needed.

The different GO algorithms have been widely applied to extract quantitative information from ABI images in different application fields, and particularly in biological tissues imaging. A comprehensive and systematic quantitative comparison of the most used GO extraction algorithms is not available in the literature to the best of our knowledge. In particular, no complete quantitative comparison of the different methods in terms of their accuracy in the presence of variable amounts of refraction and scattering has been performed. This is an aspect of crucial importance especially in biological and medical imaging. The choice of the algorithm to use may significantly influence the image quality and the accuracy of the extracted information, and therefore, ultimately, the image interpretation. Moreover, biological samples may differ greatly in the amount of absorption, refraction and scattering they produce. It is thus important to assess the performance of each algorithm under different experimental conditions simulating the cases that can be encountered with biological tissues. The final goal of the present study is to identify which algorithm could be the most suitable for a particular biological application.

In the present chapter, a theoretical and experimental comparison of the main GO algorithms is presented. Different experimental conditions characterized by various amounts of absorption, refraction and scattering are considered. The quantitative comparison is performed by using simple geometrical phantoms consisting of plastic materials (exhibiting absorption and refraction) and of paper (exhibiting absorption and scattering). The same algorithms are then applied to a human bone-cartilage sample, as a challenging example in biomedical imaging.

The chapter is organized in the following way. In section 4.2 the various GO algorithms are introduced and discussed, with particular attention paid to their underlying assumptions and applicability range. In section 4.3, the experimental parameters and the computational implementation of the algorithms as well as the geometrical phantoms and the human bone-cartilage sample that have been used in the experiments are described. In section 4.4, results

obtained by applying the various algorithms to experimental images of the considered samples are shown and discussed. Conclusions are given in section 4.5.

4.2 Algorithms for quantitative analysis of AB images

4.2.1 Diffraction-enhanced imaging (DEI)

The simplest extraction method is the diffraction-enhanced imaging (DEI) algorithm, developed by Chapman et al. (Chapman et al., 1997). It is based on linearizing the imaging system RC recorded without the sample at the two slopes, where its second derivative is equal to zero. With the object in the beam, equation 2.53 can then be rewritten, respectively for the 'low' (L) and 'high' (H) slopes of the RC, for each image pixel, as:

$$I_{L,H} = I_T\left(R\left(\theta_{L,H}\right) + \frac{dR}{d\theta}\left(\theta_{L,H}\right)\Delta\theta_y \right) \tag{4.1}$$

Equations 4.1 represent a linear system with two unknown quantities, I_T and $\Delta\theta_y$. Therefore, if two images of the sample are acquired, with the analyzer positioned at the 'low' and at the 'high' slopes of the RC, equations 4.1 can be solved analytically on a pixel-by-pixel basis in order to calculate the transmission and the refraction angle images:

$$I_T = \frac{I_L \frac{dR}{d\theta}\left(\theta_H\right) - I_H \frac{dR}{d\theta}\left(\theta_L\right)}{R\left(\theta_L\right)\frac{dR}{d\theta}\left(\theta_H\right) - R\left(\theta_H\right)\frac{dR}{d\theta}\left(\theta_L\right)} \tag{4.2}$$

$$\Delta\theta_y = \frac{I_H R\left(\theta_L\right) - I_L R\left(\theta_H\right)}{I_L \frac{dR}{d\theta}\left(\theta_H\right) - I_H \frac{dR}{d\theta}\left(\theta_L\right)} \tag{4.3}$$

The image of I_T will henceforth be referred to as the "absorption image" for consistency with the terminology used in most publications. However, we have to keep in mind that, strictly speaking, this is the image of the intensity transmitted through the sample (with bright pixels corresponding to low absorption values and dark pixels to high absorption values).

Since only two input images are needed under this approach, DEI has the advantage that both the dose deposited to the sample and the acquisition time may be reduced compared to other methods requiring a larger number of images. However, the assumptions concerning the sample are quite restrictive. The linear approximation of the RC at the two slopes is valid only if the refraction angles are small compared to the RC FWHM. Additionally, this method does not take into account the USAXS produced by the object, which has the effect of broadening the observed RC compared to the reference RC used in the calculations, as we will see in section 4.2.3.

The presence of scattering, characteristic of many biological tissues, and large refraction angles (of the order of the RC FWHM or bigger), typically encountered at the boundaries between

different materials/objects, can therefore lead to incorrect results (Pagot et al., 2003, Rigon et al., 2003, Wernick et al., 2003, Huang et al., 2007, Hu et al., 2008).

4.2.2 Extended DEI (E-DEI)

In order to overcome the intrinsic limitations of the DEI algorithm, other analytical algorithms have been proposed that allow for separation of the absorption and refraction contributions by using two input images without imposing a Taylor approximation to the RC (Maksimenko, 2007, Hu et al., 2008). These methods are usually referred to as extended-DEI (E-DEI) algorithms.

Here, the approach proposed by Hu et al. will be followed (Hu et al., 2008). In this case, the 'reference' imaging system RC, measured without the sample, is fitted by a Gaussian function. It is assumed that, once the object is in the beam, its effect on the measured RC will consist only in a shift of the RC centre (due to refraction), and in a decrease in intensity (due to absorption), but not in a change in the RC shape. In particular, no RC broadening due to USAXS is considered. Therefore, if two images are taken at different angular positions of the analyzer, $\theta_{L,H}$, the following expression for the intensity recorded after the analyzer can be written for each image pixel:

$$I_{L,H} = I_T A \exp\left[-\frac{(\Delta\theta_y + \theta_{L,H})^2}{2\sigma^2}\right] \tag{4.4}$$

where A is the 'reference' RC peak value and σ is its standard deviation. The values of I_T and $\Delta\theta_y$ can then be analytically calculated, on a pixel by pixel basis, by using the following expressions obtained from equations 4.4:

$$\Delta\theta_y = \frac{2\sigma^2 \log\left(I_L / I_H\right) + \theta_L^2 - \theta_H^2}{2\left(\theta_H - \theta_L\right)} \tag{4.5}$$

$$I_T = \frac{I_L}{A} \exp\left[\frac{\left(\theta_L + \Delta\theta_y\right)^2}{2\sigma^2}\right] \tag{4.6}$$

Since this method does not impose any restrictions on the values of the refraction angles (provided that the GO conditions are still fulfilled (Pavlov et al., 2004, Nesterets et al., 2006)) the range of refraction angles that can be calculated is wider than in the case of the DEI algorithm. Furthermore, the two images do not need to be acquired exactly at the two slopes of the RC but can be chosen anywhere along it. However, also in this case the RC broadening due to USAXS is not accounted for, which may lead to errors in the calculated absorption and refraction images in case of highly scattering samples.

4.2.3 Generalized DEI (G-DEI)

Since the amount of scattering introduced by the sample is in many cases not negligible (notably, for many biological tissues), different algorithms have been developed in order to separate the USAXS contribution from the other contrast mechanisms and quantify it. The aim is double. On one hand, the effect of USAXS, if not accounted for appropriately, can lead to artefacts in the calculated absorption and refraction images. On the other hand, USAXS represents an additional contrast mechanism that can potentially provide important information on the sub-pixel sample structure, enabling, for instance, to distinguish different biological tissues.

We will adopt in the following the approach independently proposed by Rigon and coworkers and Chou and coworkers (Chou et al., 2007, Rigon et al., 2007) to model the effect of USAXS onto the acquired ABI images. It has to be noted that a similar approach had already been introduced by Rigon et al. (2003) which, however, only took into account the scattering contribution but not the beam refraction.

Until now we have assumed that, for each small region of the object corresponding to one detector pixel, all the photons are deviated at a well-defined refraction angle. However, this hypothesis is not verified anymore if we consider an object that contains structures smaller than the pixel size (for instance, at the sub-micrometer or micrometer scale). In this case, photons collected by the same detector pixel may have experienced different refraction angles inside the object. We can describe this effect by considering, for each pixel, an average refraction angle $\Delta\theta_y(x,y)$ (in the vertical direction) and by using a probability density function $f(\Delta\theta_S;x,y)$ to describe the distribution of the scattering angles around this mean value. We define this function such that its first three moments are:

$$\int f(\Delta\theta_S;x,y)d(\Delta\theta_S)=1 \tag{4.7a}$$

$$\int \Delta\theta_S f(\Delta\theta_S;x,y)d(\Delta\theta_S)=0 \tag{4.7b}$$

$$\int (\Delta\theta_S)^2 f(\Delta\theta_S;x,y)d(\Delta\theta_S)=\sigma^2_{\Delta\theta_S}(x,y) \tag{4.7c}$$

Therefore, the probability density function is normalized to 1 (equation 4.7a), is centred around 0 (equation 4.7b) and has a width $\sigma_{\Delta\theta_S}$ (standard deviation of the scattering angles distribution) (equation 4.7c).

The intensity collected by each detector pixel when the analyzer is set at a generic angle θ_{AN} can thus be obtained by integrating over all the scattering angles (Chou et al., 2007, Rigon et al., 2007):

$$I(\theta_{AN};x,y)=I_T(x,y)\int R(\theta_{AN}+\Delta\theta_y(x,y)+\Delta\theta_S)f(\Delta\theta_S;x,y)\,d(\Delta\theta_S) \tag{4.8}$$

From equation 4.8, we see that the effect of USAXS is a broadening of the measured RC when the object is in the beam with respect to the imaging system RC measured without the object, and that this broadening depends on the width of the scattering angle distribution. Equation 2.53, which was derived in the geometrical optics approximation under the assumption that a well-defined refraction angle is associated to each detector pixel, can be obtained as a special case of equation 4.8 where $f\left(\Delta\theta_s; x, y\right) = \delta\left(\Delta\theta_s = 0\right)$ and $\delta\left(\Delta\theta_s = 0\right)$ is a Dirac delta function centered on $\Delta\theta_s = 0$.

The method proposed by Rigon 2007 and Chou 2007 is based on assuming that the refraction and the scattering angles are small compared with the RC FWHM, so that the expression of *R* in equation 4.8 can be replaced by its second-order Taylor approximation. Using equations 4.7, the following expression can be obtained:

$$I = I_T\left[R\left(\theta_{AN}\right) + \frac{\partial R}{\partial\theta}\left(\theta_{AN}\right)\Delta\theta_y + \frac{1}{2}\frac{\partial^2 R}{\partial\theta^2}(\theta_{AN})\Delta\theta_y{}^2 + \frac{1}{2}\frac{\partial^2 R}{\partial\theta^2}(\theta_{AN})\sigma^2_{\Delta\theta_s}\right] \tag{4.9}$$

where we have omitted the spatial variables (*x*,*y*). If three images are acquired at three arbitrary analyzer angular positions θ_i (i=1,2,3), absorption, refraction and scattering can then be analytically calculated for each pixel:

$$I_T = \frac{\sum_{i,j,k=1}^{3}\varepsilon_{ijk} I_i \dot{R}_j \ddot{R}_k}{\sum_{i,j,k=1}^{3}\varepsilon_{ijk} R_i \dot{R}_j \ddot{R}_k} \tag{4.10a}$$

$$\Delta\theta_y = -\frac{\sum_{i,j,k=1}^{3}\varepsilon_{ijk} I_i R_j \ddot{R}_k}{\sum_{i,j,k=1}^{3}\varepsilon_{ijk} I_i \dot{R}_j \ddot{R}_k} \tag{4.10b}$$

$$\sigma^2_{\Delta\theta_S} = \frac{2\sum_{i,j,k=1}^{3}\varepsilon_{ijk} I_i R_j \dot{R}_k}{\sum_{i,j,k=1}^{3}\varepsilon_{ijk} I_i \dot{R}_j \ddot{R}_k} - \Delta\theta_y^2 \tag{4.10c}$$

where $\varepsilon_{i,j,k}$ is the totally antisymmetric tensor and where we have indicated with R_i, $\dot{R}_i$ and $\ddot{R}_i$ respectively the RC and its first and second derivatives at the position θ_i. Since the second-order Taylor expansion is a good approximation of the RC just for small angular deviations, the accuracy of this algorithm is limited to values of $\sigma_{\Delta\theta S}$ and $\Delta\theta_y$ that are small compared to the FWHM of the RC.

4.2.4 Multiple image radiography (MIR)

Pagot et al. (Pagot et al., 2003) and Wernick et al. (Wernick et al., 2003) independently developed two statistical methods which allow for reconstructing the RC on a pixel-by-pixel basis, by conveniently combining several images at different positions along the RC.

Here the approach of Pagot et al. (Pagot et al., 2003) will be followed. The method consists in taking two series of N (N ≥ 3) images at different positions of the crystal analyzer with and without the sample, respectively. The 'reference' RC (acquired without the sample) and the 'object' RC (acquired with the sample) are then compared. If it is assumed that for each pixel the angular distribution of the diffracted intensity is the convolution of the object angular spectrum with the imaging system RC (equation 4.8), then the refraction, integrated absorption and scattering images can be computed from the zeroth-, first- and second-order moments, $M_i = \sum_{j=1..N} \left(\theta_j\right)^i \cdot R\left(\theta_j\right)$, (i=0,1,2), of the 'reference' and 'object' RCs. The zeroth-order moment M_0 is equal to the integrated intensity, the first-order moment provides the centre of mass $\theta_y = M_1 / M_0$ and the second-order moment gives the standard deviation $\sigma = \left(M_2 / M_0 - \theta_y^2\right)^{1/2}$.

The integrated absorption image is calculated as the ratio of the integrated intensities of the 'object' and 'reference' RCs:

$$I_T = M_{0,obj} / M_{0,ref} \tag{4.11}$$

Since the effect of refraction is a shift of the 'object' RC with respect to the 'reference' one, the refraction image is computed as the angular displacement of the centre of mass:

$$\Delta\theta_y = \theta_{y,obj} - \theta_{y,ref} \tag{4.12}$$

Since the effect of USAXS is a broadening of the 'object' RC with respect to the 'reference' one, USAXS is instead calculated as the 'object' RC standard deviation deconvolved from the 'reference' one:

$$\sigma_{\Delta\theta_S} = \sqrt{\sigma_{obj}^2 - \sigma_{ref}^2} \tag{4.13}$$

An additional maximum absorption image can be calculated as the ratio of the 'object' RC maximum with respect to the 'reference' one:

$$I_m = \max(R_{obj}) / \max(R_{ref}) \tag{4.14}$$

Whereas the integrated absorption image computes the area under the measured RC, the maximum absorption computes the value of the measured RC peak.

Similarly to the G-DEI algorithm, the MIR method has the advantage that the USAXS contribution is explicitly taken into account. In addition, it is in principle very stable with respect to noise, since many images are combined in order to calculate the different parameters. A notable

drawback of this method is that, since many images need to be acquired, both the dose to the sample and the acquisition time are increased.

4.2.5 Limitations of MIR

As Huang et al. pointed out (Huang et al., 2007), large refraction angles can be underestimated in the MIR algorithm. Under this approach, in fact, the refraction angle is calculated as the shift of the 'object' RC centroid relative to the 'reference' RC centroid. Theoretically, the centre of the 'object' RC and its centroid are equal only if the sampling along the RC is continuous and made on an infinite range. Since the number of sampling points is limited in the experiment, the centroid and centre values may differ. It can actually be shown that, in particular for large refraction angles, the calculated values always underestimate the actual ones.

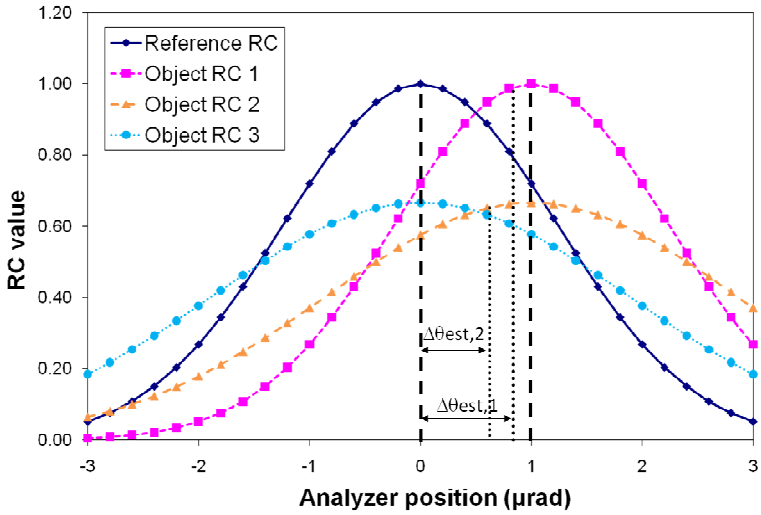

Fig. 4.1. Example of the finite sampling of a 'reference' RC ($FWHM_{ref}$ = 2.94 μrad), a first 'object' RC characterized by refraction ($\Delta\theta_y$ = 1 μrad), a second 'object' RC characterized by refraction and USAXS ($\Delta\theta_y$ = 1 μrad, $FWHM_{obj}$ = 1.5 $FWHM_{ref}$) and a third 'object' RC characterized by USAXS only ($FWHM_{obj}$ = 1.5 $FWHM_{ref}$). The refraction angles calculated with the MIR algorithm respectively for the first 'object' RC (absence of scattering) and the second 'object' RC (presence of scattering) are $\Delta\theta_{est,1}$ = 0.88 μrad and $\Delta\theta_{est,2}$ = 0.62 μrad.

The situation is schematically presented in figure 4.1. Let suppose that the 'reference' RC is a Gaussian function with a FWHM of 2.94 μrad (this corresponds to the FWHM measured in our experiment, as described in section 4.3) and that two different 'object' RCs are considered: a first one characterized by a shift of the centre of 1 μrad, simulating a refraction effect, and a second one characterized by the same centre shift plus a broadening, simulating USAXS. For the latter 'object' RC, the $FWHM_{obj}$ is 1.5 times the $FWHM_{ref}$. Let further suppose that the 'reference' and 'object' RCs are sampled with 31 analyzer positions ranging from -3 to +3 μrad with a 0.2 μrad step.

When applying the MIR method to retrieve the refraction angle in the case of the first 'object' RC (case of pure refraction), a $\Delta\theta_y$ = 0.88 μrad is calculated instead of the expected value of 1

μrad. The calculated value is smaller than the actual one and this is due to the fact that the 'object' RC is no longer symmetrically sampled with respect to its centre (peak) since the curve is shifted.

What no publication has pointed out yet, to the best of our knowledge, is that this smoothing effect is even enhanced when, besides a large refraction angle, we are in the presence of considerable scattering. In the case of the second 'object' RC, in fact, where large refraction and a large amount of USAXS mix up, the MIR method gives an even lower calculated refraction angle, $\Delta\theta_y$ = 0.62 μrad, than in the previous case. This means that, under this approach, large amounts of USAXS can increase the inaccuracy of the refraction angle estimate.

Similarly, we can show that under the conditions of high refraction and/or high USAXS, also the extracted USAXS signal can be underestimated. Let consider two different 'object' RCs: a first one characterized by broadening (with a $FWHM_{obj}$ that is 1.5 times the $FWHM_{ref}$) simulating USAXS ('object' RC 3 in figure 4.1) and a second one characterized by the same broadening and a centre shift of 1 μrad simulating refraction ('object' RC 2 in figure 4.1). The value for the width of the USAXS distribution calculated in the first case with the MIR algorithm, $USAXS_{est,3} = 0.89\,\mu rad$, considerably underestimates the expected value, $USAXS_{th} = \sqrt{\sigma_{obj}^2 - \sigma_{ref}^2} = 1.40\,\mu rad$. In the second case, where refraction is also present, not only the USAXS contribution is underestimated, but the calculated standard deviation of the 'object' RC is even lower than that of the 'reference' RC, leading to an evidently incongruous value of $USAXS_{est,2} = \sqrt{-0.17}\,\mu rad$. These incorrect results can be explained by the fact that, due to the limited range of sampling, the contribution of the tails is heavily underestimated when the RC is broadened by scattering and even more in the presence of additional refraction, since in this case one of the two sides of the RC is considerably cut.

Additionally, we can show that also the estimated values for absorption are affected by high levels of scattering and large refraction angles. Considering the 'object' RCs in figure 4.1, in fact, by applying the MIR algorithm we obtain the following values for the transmission: I_T = 0.97 for 'object' RC 1 (refraction), I_T = 0.91 for 'object' RC 3 (scattering) and I_T = 0.87 for 'object' RC 2 refraction and scattering). We remind that no absorption was considered for simulating the 'object' RCs, therefore a transmission value different from the unity is an artefact only due to the influence of refraction and scattering values in the calculation.

Furthermore, if the sampling range and/or the number of sampling points are decreased compared with the experimental conditions considered above, the inaccuracies in the calculation of refraction, scattering and absorption are expected to become even more important.

4.2.6 Gaussian curve fitting (GCF)

An alternative approach which allows for overcoming these problems, the so-called Gaussian curve fitting (GCF) algorithm, has been proposed by Nesterets et al. (Nesterets et al., 2006). This method consists in fitting, pixel-by-pixel, a Gaussian function to the 'reference' and 'object' RCs.

Under this approach, for each pixel the sampled 'reference' and 'object' RCs are fitted with the following Gaussian expression:

$$I_{ref,obj} = A_{ref,obj} \exp\left[-\frac{(\theta_{y\,ref,obj} + \theta_{AN})^2}{2\sigma^2_{ref,obj}} \right] \tag{4.15}$$

By analogy to the MIR case, the peak value A, the centre $\Delta\theta_y$ and the standard deviation σ of the 'reference' and 'object' RCs are then used to calculate the sample refraction angle, maximum absorption, integrated absorption and USAXS as:

$$\Delta\theta_y = \theta_{y,obj} - \theta_{y,ref} \tag{4.16a}$$

$$I_{\mathrm{m}} = A_{obj} / A_{ref} \tag{4.16b}$$

$$I_T = A_{obj}\sigma_{obj} / A_{ref}\sigma_{ref} \tag{4.16c}$$

$$\sigma_{\Delta\theta_S} = \sqrt{\sigma^2_{obj} - \sigma^2_{ref}} \tag{4.16d}$$

The quantities obtained with the GCF algorithm correspond to those calculated using the MIR algorithm, but they are expected to provide more accurate estimates of the different parameters since they are exempt from the above-described limitations.

An important drawback of this method is that it is computationally very intensive, since the fitting procedure has to be repeated for each pixel. For example, for an image of $10^3 \times 10^3$ pixels^2, the fitting calculation is repeated 10^6 times and this leads to much longer computation times compared to those needed with the other algorithms.

4.2.7 Methods for phase image calculation

As we saw in detail in chapter 2, refraction of the beam occurs at the boundaries between materials with different refractive index decrement δ; the refraction angle at a specific object position (x,y) is proportional to the wave phase gradient at that point (equation 2.40). Therefore, if the refraction angle at each image point is known, the phase values can in principle be calculated by inverting equation 2.40:

$$\phi(x,y) = -\frac{2\pi}{\lambda}\int_{y_0}^{y} dy' \Delta\theta_y\left(x,y'\right) + \phi\left(x, y = y_0\right) \tag{4.17}$$

where an integration of the refraction angle map has to be performed in the refraction-gradient direction and where $\phi(x, y = y_0)$ is a boundary condition representing the values of the phase shift on a reference line perpendicular to the integration direction.

Because of the finite size of the pixels dimensions, in the real experimental conditions only a discrete representation of the refraction angle is available, and therefore a discrete version of equation 4.17 needs to be used (Hasnah et al., 2005):

$$\phi(m,n) = -\frac{2\pi}{\lambda} \sum_{n'=n_0}^{n} p_y \Delta\theta_y (m,n') + \phi(m, n = n_0) \tag{4.18}$$

where (m,n) represent the pixel indexes in the x and y directions respectively and where p_y is the pixel size in the y direction. If the refraction angle map is calculated with one of the above extraction algorithms, an object phase map can therefore be obtained, provided that the boundary phase values $\phi(x, y = y_0)$ are known a priori. The simplest case occurs if the reference edge is made of a homogeneous material, so that the $\phi(x, y = y_0)$ values are independent of x, and in particular if the chosen reference edge is in air, so that $\phi(y = y_0)$ is equal to zero. Equation 4.18 can be easily computationally implemented by using the following recursive expression:

$$\phi(m,n) = \phi(m,n-1) - \frac{2\pi}{\lambda} p_y \Delta\theta_y (m,n-1) \tag{4.19}$$

where each image row n is calculated from the $n-1$ row by adding to it a quantity proportional to the refraction angle at $n-1$.

Calculating such a phase image can be very advantageous for different reasons. First of all, the phase shift is directly related (equation 2.8) to the refractive index δ and the latter can be calculated if the object thickness is known. Additionally, unlike the refraction signal that inherently occurs at the edges, the phase signal provides an area contrast and is therefore visually more similar to the absorption one. For this reason its interpretation may be easier in some cases, for example when the imaged object is characterized by a complex structure or for medical doctors not familiar with the appearance of a refraction image.

However, as pointed out in Wernick et al. (Wernick et al., 2006), a simple application of equation 4.18 produces significant artefacts even in the presence of low levels of noise. The integration in equation 4.18, in fact, introduces streak artefacts in the integration direction: these are due to the fact that the pixel noise and all other refraction angle calculations artefacts propagate over the whole image, as we will see on experimental images in section 4.4.1.

An alternative approach, based on a constrained least-squares algorithm, was proposed by Wernick et al. (Wernick et al., 2006). Following this approach, let us denote the refraction angle map $\Delta\theta_y(m,n)$ and the phase map $\phi(m,n)$ with the matrices $\Delta\Theta$ and Φ, respectively. Equation 2.40 can then be expressed as:

$$\Delta\Theta = D \cdot \Phi \tag{4.20}$$

where D is a matrix representing a difference operator acting along the vertical axis (y) of the image. In particular, D has the effect of performing circular convolution with the kernel:

$$d = -\frac{\lambda}{2\pi}\begin{pmatrix} 1 \\ -1 \end{pmatrix} \tag{4.21}$$

Assuming that the noise in $\Delta\Theta$ is Gaussian-distributed, it is appropriate to use a constrained least-squares (CLS) method to solve the equation 4.20. For this purpose, the following CLS objective function can be introduced:

$$J(\varphi) = \left\|\Delta\Theta - D \cdot \Phi\right\|^2 + \gamma \left\|Q \cdot \Phi\right\|^2 \tag{4.22}$$

where γ is a regularization parameter and Q is a matrix that has the effect of performing a two-dimensional convolution with the one-dimensional Laplacian kernel (Rosenfeld and Kak, 1982):

$$q = \begin{pmatrix} -1 & 2 & -1 \end{pmatrix} \tag{4.23}$$

The first term on the right-hand side of equation 4.22 represents the analytical solution term, while the second is a regularization term that has the objective of reducing the phase image streak artefacts by penalizing solutions with large variations in the direction orthogonal to the refraction-gradient direction. The regularization parameter defines the weight of the regularization with respect to the analytical solution and can be varied according to the image noise (higher levels of noise, for instance, will require larger values of γ). The solution of the objective function minimization is given by (Jain, 1988):

$$\hat{\Phi} = \arg\min_{\Phi} J(\Phi) = \left(D^T D + \gamma Q^T Q\right)^{-1} D^T \Delta\Theta \tag{4.24}$$

An additional analytical method, which we will call the "averaged integration method", with the aim of reducing the effect of the streak artefacts in the phase image calculation, has been developed in the framework of this Thesis. Let us consider again equation 4.19, which is used to solve equation 2.40 for the phase in the discrete case. Assuming that the expected phase image does not present rapid variations in the direction orthogonal to the integration direction, the observed high-frequency variations in this direction can be attributed mainly to the effect of the image noise. In order to reduce them, the following expression can be used to replace the equation 4.19:

$$\phi(m,n) = \left[\phi(m,n-1) - \frac{2\pi}{\lambda} p_y \Delta\theta_y(m,n-1)\right] * c \tag{4.25}$$

where the symbol "*" denotes convolution and c is a vector that can be defined, for instance, as $c = \begin{pmatrix} -1 & -2 & 6 & -2 & -1 \end{pmatrix}$, and whose aim is to smooth the rapid variations along the direction orthogonal to the integration direction. Note that the convolution operation for a generic row n is

performed before the next row $n+1$ is calculated, and therefore the application of equation 4.25 is very different from a convolution applied to a whole phase image previously calculated using equation 4.19.

4.3 Experimental methods

4.3.1 Experimental parameters

The experiment was performed at the ID17 biomedical beamline. X-rays with an energy of 26 keV (energy resolution $\Delta E/E \sim 2 \cdot 10^{-4}$) were selected with the fixed-exit Laue-Laue Si(111) double-crystal monochromator. A Si(333) additional crystal monochromator and a Si(333) crystal analyzer were used to monochromatize the incoming beam and to analyze the refracted beam after the sample, respectively. The measured analyzer RC width (as FWHM) at the considered energy was 2.94 μrad.

Images have been recorded with the FReLoN CCD camera (Coan et al., 2006) coupled with the 8 μm optics.

4.3.2 Plastics phantoms

In order to perform a quantitative comparison between the different extraction algorithms, simple geometrical phantoms giving rise to either refraction or scattering signals were used.

The first phantom consisted of two cylindrical nylon wires of diameters of 350 μm and 200 μm, respectively (figure 4.2(a)). They can be considered as pure phase objects, since their absorption contrast is almost negligible at the used energy. Instead, they show a very high refraction signal especially at the edges, where the refraction angles become very large. The values of the real and imaginary parts of the complex index of refraction are, for nylon at 26 keV: $\delta = 3.50 \times 10^{-7}$; $\beta = 1.29 \times 10^{-10}$ (Henke et al., 1993). The absorption contrast is about 1.2% for the 350 μm diameter wire and about 0.7% for the 200 μm diameter wire.

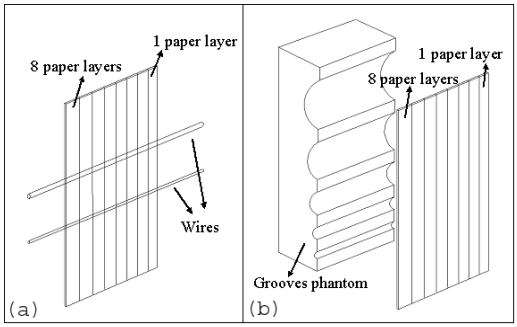

Fig. 4.2. Sketches of the phantoms used in the experiment: 200 μm and 350 μm diameter nylon wires with overlapped paper layers (a), and Lucite grooves phantom with overlapped paper layers (b).

The second phantom is a Lucite parallelepiped of section 40 × 40 mm^2 and thickness 2.9 mm, in which five almost cylindrically-shaped grooves (holes) of different radius are made (figure 4.2(b)). The section of the holes can be well approximated by a part of circumference. Unlike the polymer wires, this phantom produces both refraction and absorption. The refraction angles at the edges of the grooves are smaller than in the case of the wires, since in this case the object thickness varies more slowly at the edges. The characteristics of the grooves phantom are summarized in table 4.1.

The third phantom is made of eight partially overlapping layers of newspaper. Paper is known to produce a large quantity of scattering and has been used for this scope in various publications concerning ABI extraction algorithms (Oltulu et al., 2003, Wernick et al., 2003). Paper thickness ranges from 40±5 μm, in the region where just one layer of paper is present, to 320±5 μm, where all the eight layers of paper overlap. The wires and the grooves phantoms were imaged superimposed to the newspaper layers, in order to produce a variety of combinations of absorption, refraction and ultra-small angle X-ray scattering on the same image, as schematically presented in figures 4.2(a) and 4.2(b).

Images of the wires were acquired at 9 different positions along the RC, respectively at the peak (100%, "top" position), ±75%, ±50%, ±30% and ±15% (positions relative to the maximum RC intensity). Images of the grooves phantom were acquired at 7 positions along the RC, respectively at the peak, ±50%, ±30% and ±15%.

Groove number	Depth (μm)	Width (μm)	Absorption contrast
1	300	825	1.1 %
2	590	1800	2.2 %
3	790	2475	2.9 %
4	1140	3525	4.3 %
5	1440	4125	5.4 %

Table 4.1. Some physical parameters of the groove phantom. The absorption contrast is calculated at the groove centre with respect to the maximum thickness of the groove phantom. For Lucite at 26 keV, $\delta = 3.94 \times 10^{-7}$; $\beta = 1.39 \times 10^{-10}$ (Henke et al., 1993).

4.3.3 Biological sample

As a biological sample, a cylinder-shaped healthy cartilage-on-bone sample with a diameter of 7 mm was used. The sample was extracted from the lateral facet of a human patella using a shell auger. The cylinder was trimmed to a total height of 12 mm including the complete cartilage tissue and about 6 mm of subchondral bone.

During the images acquisition the sample was placed in a cylindrical container and was dipped into a saline solution. Images of the sample were acquired at 5 different positions on the RC, ±50%, ±15% and 100%, respectively.

4.3.4 Computational implementation

MATLAB (The MathWorks, Inc.) was used for the image analysis using the different extraction algorithms. Calculations were performed on a Dual-Core AMD Opteron 2218 Processor (64-bit, 2.6 GHz).

Concerning the GCF method, the pixel-by-pixel fitting of equation 4.15 was done with a built-in MATLAB function, which uses a trust-region algorithm to iteratively solve a non-linear least-squares problem (Branch et al., 1999). This fitting routine required initial estimates of the parameters to be calculated: the RC peak value A, centre $\Delta\theta_y$ and standard deviation σ obtained from the MIR method were used for this purpose.

DEI, E-DEI, G-DEI and MIR algorithms run fast on the used PC: the calculation time for any of these three methods, applied for example to a $10^3 \times 10^3$ pixels^2 image, was a few seconds only. The GCF method, instead, requires much longer computation time. In fact, about 10 hours were needed to process the same image size.

4.4 Results and discussion

4.4.1 Plastics phantoms planar images

The absorption, refraction and USAXS angle distribution images obtained by applying the different ABI algorithms to the images of the 350 μm diameter wire are reported in figures 4.3, 4.4 and 4.5 respectively. For DEI and E-DEI algorithms, only the AB images at the positions ±50% on the RC were used. These two images and the additional "top" one were used for the G-DEI algorithm, while all images at the 9 different RC positions were used for the MIR and GCF algorithms. Concerning the DEI and E-DEI methods, only the absorption and the refraction angle images are presented since no USAXS image is calculated. Concerning the MIR and the GCF absorption images, only the integrated absorption is shown in figure 4.3.

The paper layers are clearly visible in the absorption images. Also the nylon wire can be clearly seen but mainly because of the artefacts at the edges. In these regions the refraction angles are very large and this fact leads to the violation of the GO assumptions. Strong artefacts are therefore visible on the absorption images, in which the signal intensity itself is quite low.

In the calculated USAXS images (figure 4.4), the different paper layers, which give different amounts of scattering, and the nylon wire edges are again clearly visualized. The strong USAXS signal generated at the edges of the wire is due to the very strong variations of the refraction angles, which may considerably increase the range of refracted X-rays falling within a single pixel. This leads to a broadening of the observed RC.

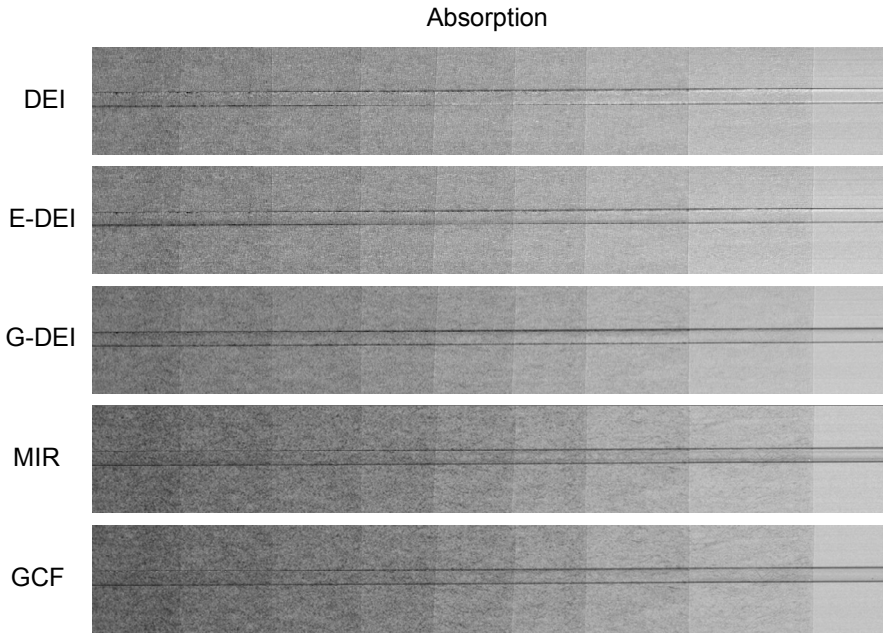

Fig. 4.3. Calculated absorption images of the 350 µm diameter nylon wire overlapped to the newspaper layers. The latters are progressively increased from right to left: no paper layers are present on the right side, 8 paper layers are present on the left side.

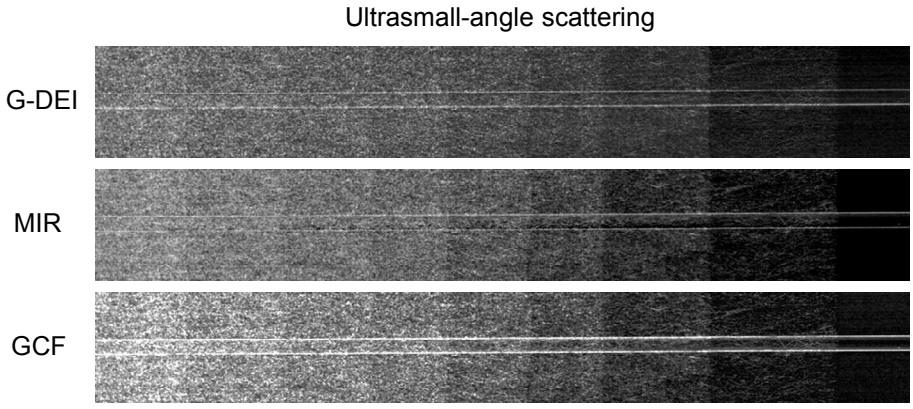

Fig. 4.4. Calculated USAXS images of the 350 µm diameter nylon wire overlapped to the newspaper layers. The latters are progressively increased from right to left: no paper layers are present on the right side, 8 paper layers are present on the left side.

In the refraction images (figure 4.5) just the nylon wire is visible, while the paper does not produce any visible signal. Profiles of the refraction angle across the wire have been considered for the different algorithms and the corresponding phase profiles have been calculated by simple integration. The latter are reported in figures 4.6(a) and 4.6(b), respectively in the case in which scattering can be neglected (no paper) and in the case in which scattering is maximum (8 layers). The calculated profiles are obtained by taking the average value over 30 horizontal pixels in order to reduce the contribution of noise. In figures 4.6(a) and 4.6(b) also the theoretical profile for the phase is shown, which can be calculated using the real part δ of the complex refractive index for nylon and the known pixel-by-pixel cross-section thickness of the wire (Wilkins et al., 1996).

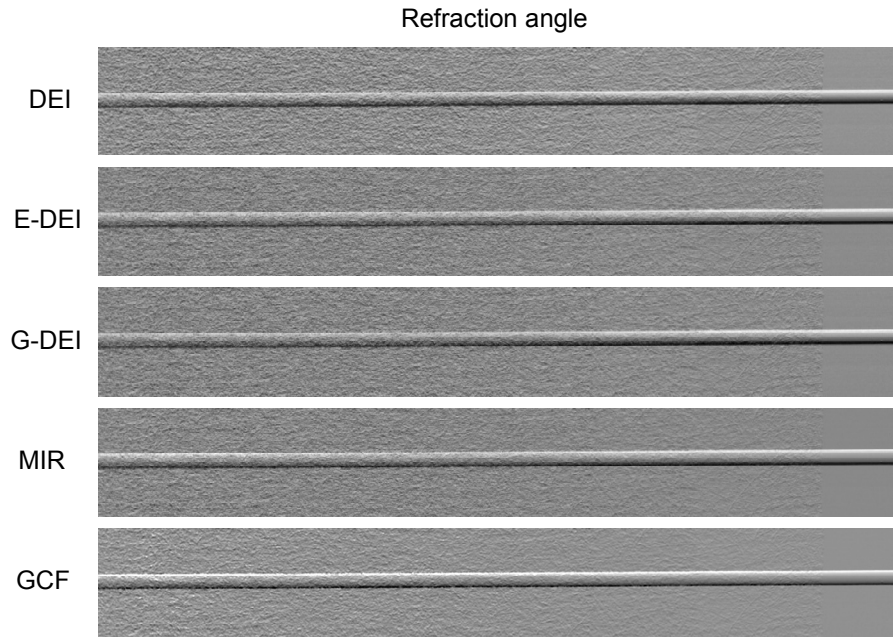

Fig. 4.5. Calculated refraction angle images of the 350 µm diameter nylon wire overlapped to the newspaper layers. The latters are progressively increased from right to left: no paper layers are present on the right side, 8 paper layers are present on the left side.

In the absence of scattering (figure 4.6(a)), it can be seen that for large refraction angles (comparable with the FWHM of the RC), like those given by the nylon wire, the agreement between the theoretical and the calculated values strongly depends on the used extraction algorithm. The best agreement (13% difference in the centre of the wire) is obtained when the experimental RC is fitted pixel-by-pixel to a Gaussian function (GCF method). Calculated values are most inaccurate in the case of the DEI algorithm, which is based on the linear approximation of the RC and fails when the refraction angles become comparable with the RC FWHM. The G-DEI algorithm, based on a second-order Taylor approximation that is strictly valid only if the refraction angles are very small, also significantly differ with respect to the theoretical values. The discrepancies between the GCF and the MIR algorithms are due to the fact that, for large refraction angles and when the number of the sampling points on the RC is limited, the calculated centroid of the sampled 'object' RC underestimates the actual centre of the 'object' RC. This last result perfectly agrees with the theoretical considerations presented in Section 4.2.5.

The difference between the algorithms is even more pronounced when high scattering is superimposed to the refraction signal (figure 4.6(b)). Both the DEI and E-DEI methods, which do not take into account the scattering, show the highest discrepancy compared to the theoretical values. Refraction angles are highly underestimated also in the case of the G-DEI and MIR algorithms. In the first case the difference can be explained by the fact that the second-order Taylor approximation fails when the refraction angle or the scattering distribution (or both) are not small compared to the RC FWHM. In the latter case, the discrepancy is due to the difference between the calculated centroid of the sampled 'object' RC and the peak position. As discussed in

Section 4.2.5, such a difference increases when, additionally to the large refraction angles, the large scattering contribution broadens the measured RC. The GCF algorithm maintains also in this case a good agreement with the theoretical values. The comparison of the various algorithms presented in figures 4.6(a) and 4.6(b) shows that, under conditions of large refraction angles (~ RC FWHM) and especially when, besides refraction, also the amount of scattering is important, the GCF method can provide much more accurate results than the other methods considered here.

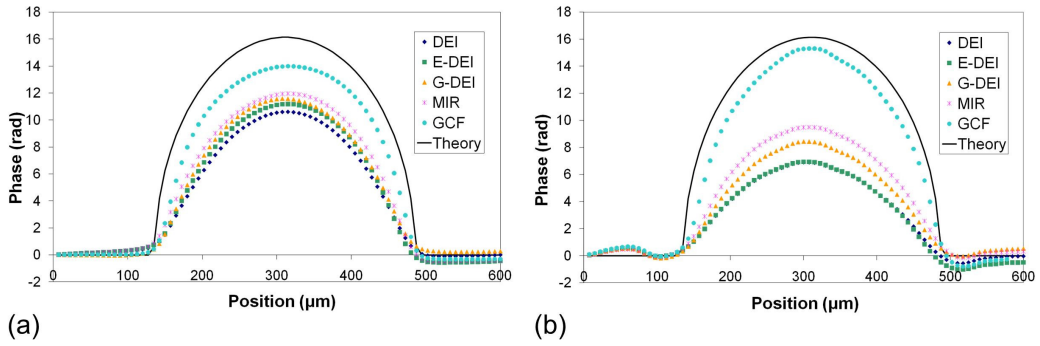

Fig. 4.6. Calculated phase profiles for the 350 μm diameter wire, when (a) no overlapping paper layers are present and when (b) 8 overlapping paper layers are present. The results extracted by DEI, E-DEI, G-DEI, MIR and GCF algorithms are compared with the theoretical profile. The plotted values are obtained by taking the average over 30 horizontal pixels.

In figure 4.7(a) the values of the phase at the centre of the wire, calculated with the different ABI algorithms, are plotted versus the number of paper layers superimposed to the sample. The aim is to compare the accuracy of the refraction angle calculation when scattering progressively increases. The theoretical estimation of the phase value is therefore reported as well. The graph in figure 4.7(a) shows that the more the scattering increases the more the difference between the algorithms becomes pronounced. The values calculated with the GCF algorithm show no evident variations while the values calculated with the other methods present a decreasing magnitude as the layers of paper increase. A drop of 42% of the phase for the DEI algorithm, of 44% for the E-DEI, of 31% for the G-DEI algorithm and of 25% for MIR is calculated by comparing the case of no scattering (x = 0) and the case of 8 layers of paper (x = 8) superimposed to the wire. As expected, the percentage decrement is higher in the case of the algorithms that do not take the X-ray scattering into account (DEI and E-DEI) than in the case of algorithms that explicitly consider it (G-DEI and MIR).

In figure 4.7(b) the calculated phase values for the second nylon wire with a 200 μm diameter are reported. As in the previous case, the values obtained at the centre of the wire are plotted with respect to the number of overlapping paper layers, for each of the considered algorithms. The theoretical estimation of the phase value is also reported for comparison. When the amount of scattering increases, a behaviour similar to the one encountered for the 350 μm diameter nylon wire can be observed. The percentage decrease in the phase values, when passing from the condition with no scattering (x = 0) to the condition with the highest amount of scattering (x = 8),

is even slightly increased in the case of the 200 µm diameter wire, with a drop of 48% for the DEI algorithm, of 51% for the E-DEI, of 41% for the G-DEI and of 34% for the MIR. No decrease is observed for the GCF algorithm.

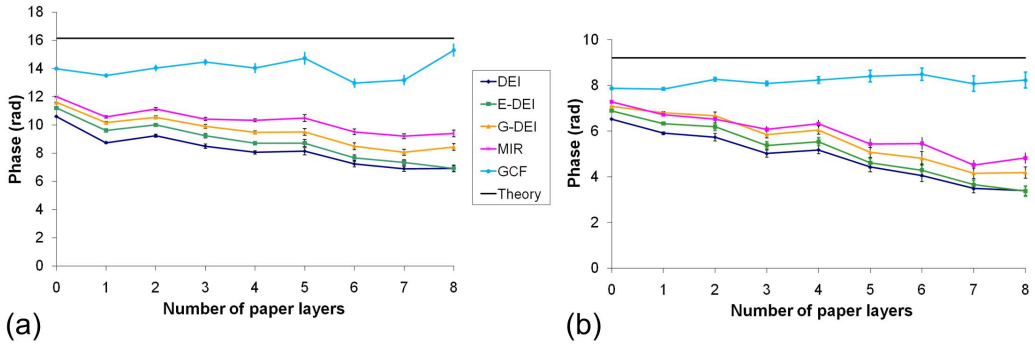

Fig. 4.7. Extracted phase values (a) at the centre of the 350 µm diameter wire and (b) at the centre of the 200 µm diameter wire, plotted with respect to the number of overlapping paper layers. Results obtained with the DEI, E-DEI, G-DEI, MIR and GCF algorithms are shown. The plotted values are obtained by taking the average over 30 horizontal pixels; the error bars represent the standard deviation of the mean. The theoretical value is also shown for comparison.

The fluctuations of the plotted values of the phase corresponding to different layers of paper may be attributed not simply to the image noise but also to the inhomogeneity of the paper itself. Besides microscopic unresolved structures that mainly generate a scattering signal, the paper contains internal structures of dimensions bigger than the pixel size which determine a real measurable phase signal.

Entire phase images of the nylon wires were also calculated by applying all the three methods presented in section 4.2.7. Representative results for the 350 µm diameter wire, obtained from the refraction angle image calculated by the GCF algorithm, are shown in figure 4.8. The phase image that is calculated by pure integration of the refraction angle image (equation 4.19) is reported in figure 4.8(a). The vertical streak artefacts due to the image noise are clearly visible. They appear smoothed, instead, in the phase image obtained by applying the averaged integration method according to equation 4.25 (figure 4.8(b)). Phase images obtained by using the CLS method (equation 4.24) with different values of the regularization parameter, $\gamma = 10^{-5}$, $\gamma = 10^{-4}$, $\gamma = 10^{-3}$, are reported respectively in figures 4.8(c,d,e). The vertical streak artefacts are progressively eliminated when the value of the regularization parameter is increased, because solutions characterized by large variations in the horizontal direction are more penalized for large values of γ. However, some horizontal artefacts become visible in the proximity of the nylon wire in figure 4.8(d) and more evidently in figure 4.8(e). A black region appears close to the wire and the phase values are strongly underestimated, since in these cases the regularization term in equation 4.24 is given high importance at the expense of the analytical term. Therefore, when precise quantitative values need to be obtained, the pure integration and the averaged integration algorithms seem to be a more appropriate choice than the CLS algorithm.

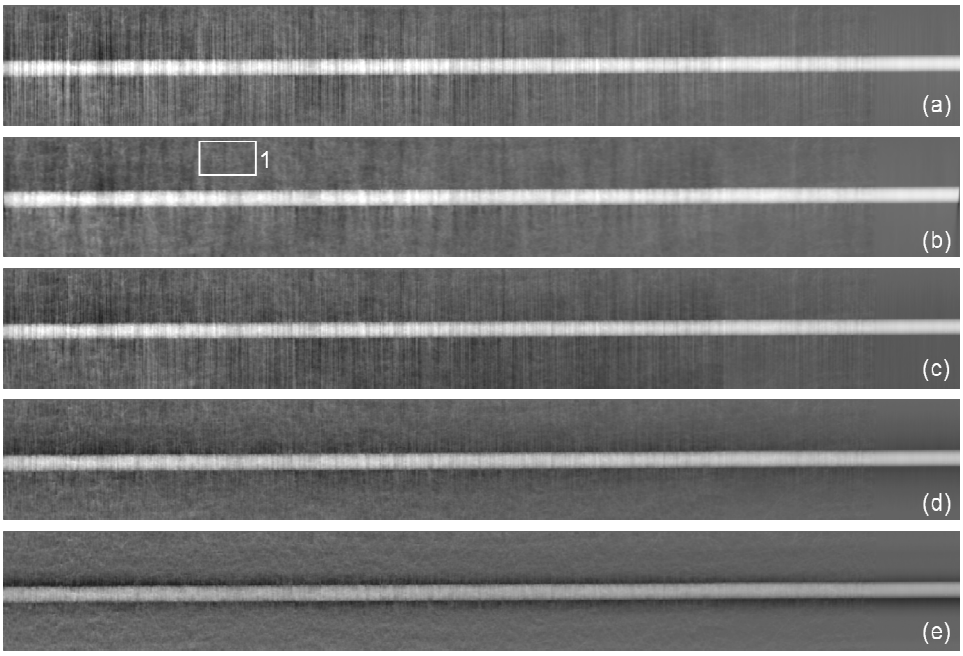

Fig. 4.8. Phase images calculated from the GCF refraction angle image of the 350 µm diameter nylon wire. Paper layers are superimposed to the wire, progressively increasing from right (no paper layers) to left (8 paper layers). (a) is obtained by pure integration, (b) is obtained with the averaged integration method, (c,d,e) are calculated with the CLS method respectively with the following values for the regularization parameter: $\gamma = 10^{-5}$, $\gamma = 10^{-4}$, $\gamma = 10^{-3}$. Expanded views of region 1 for images (a,b,c,d) are reported in figure 4.9.

Additional considerations can be done if we look closely to these images in a region where only the paper is present. Figures 4.9(a,b,c,d) show an expanded view of region 1 from figures 4.8(b,c,d,e), respectively. The results show that the best visualization for the paper fibrous structure is achieved in the CLS phase image calculated with a value of $\gamma = 10^{-3}$ (figure 4.9(d)). Evident vertical stripes are present in the CLS images calculated with $\gamma = 10^{-5}$ (figure 4.9(b)) and $\gamma = 10^{-4}$ (figure 4.9(c)), while the suppression of these stripes is obtained in the averaged integration method (figure 4.9(a)) at the expense of the spatial resolution. These results suggest that the choice of the most suited algorithm for calculating the phase image and, in the case of the CLS method, the choice of the parameter γ, also depend on the dimensions of the details that need to be visualized or studied.

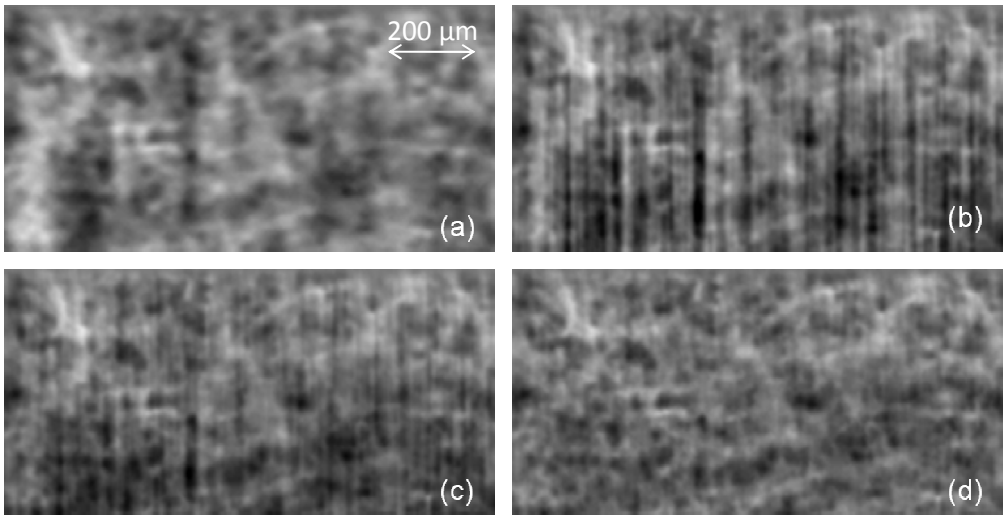

Fig. 4.9. Expanded views of the phase images in a region where only paper is present (region 1 in figure 4.8(b)). (a,b,c,d) correspond to figures 4.8(b,c,d,e) respectively.

The ABI extraction algorithms were also applied to images of the grooves phantom superimposed to the newspaper layers. The phase profiles for the biggest groove (groove 5), obtained by a simple integration of the refraction angle profiles calculated for each of the considered extraction algorithms, are reported in figures 4.10(a) and 4.10(b), respectively in the case in which scattering can be neglected (no paper) and in the case in which scattering is maximum (8 layers). They are obtained by taking the average value over 30 horizontal pixels in order to reduce the contribution of noise. The theoretical phase profile is also shown for comparison. While in the absence of scattering the differences among the various algorithms and between these and the theory are tiny, in the presence of high levels of scattering the obtained phase profiles differ considerably and in some cases greatly underestimate the theoretical one.

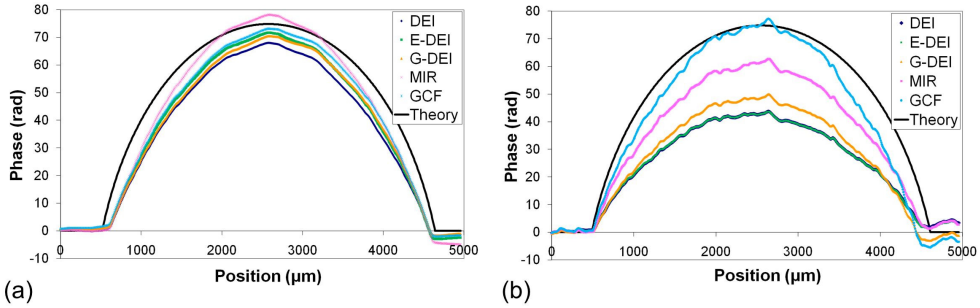

Fig. 4.10. Calculated phase profiles for the groove 5, when (a) no overlapping paper layers are present and when (b) 8 overlapping paper layers are present. The results extracted by DEI, E-DEI, G-DEI, MIR and GCF algorithms are compared with the theoretical profile. The plotted values are obtained by taking the average over 30 horizontal pixels

Results for the phase values calculated at the centre of the groove versus the number of overlapping paper layers are shown and compared to the calculated theoretical values in figure 4.11. In the case in which no scattering is superimposed to the phantom, all the algorithms show a

good agreement with the theory. The refraction angles introduced by the groove are not very large (even at the edges) compared to the RC FWHM, and therefore the validity conditions of the different algorithms are never strongly violated. As soon as the fraction of scattered X-rays increases, the differences between the various algorithms become more marked. In cases of large scattering, the refraction and the scattering signals cannot be completely separated.

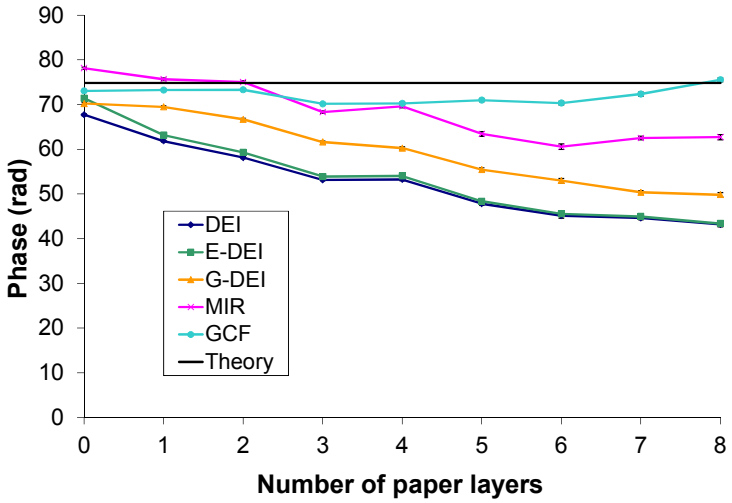

Fig. 4.11. Extracted phase values at the centre of groove 5 plotted with respect to the number of overlapping paper layers. Results obtained with the DEI, E-DEI, G-DEI, MIR and GCF algorithms are shown. The plotted values are obtained by taking the average over 30 horizontal pixels; the error bars represent the standard deviation of the mean. The theoretical value is also shown for comparison.

The percentage decrement between the calculated phase values under conditions of no scattering (x = 0) and the values calculated under conditions of maximum scattering (x = 8) is more important for those algorithms that do not consider scattering (40% in DEI, 44% in E-DEI) than for the other ones (29% in G-DEI method, 20% in MIR), as already seen in the case of the wires phantom. Results obtained with the MIR method are particularly interesting in this case. They show that the broadening of the measured RC due to high levels of scattering induces an underestimation of the refraction angle even when the latter is not extremely large.

Unlike the nylon wires, the grooves phantom shows non-negligible absorption and may allow therefore for an analysis of efficiency of the different algorithms in separating the absorption component from the other contrast contributions. The calculated profiles of the absorption signal for the biggest groove (# 5) are compared in figure 4.12 with the theoretical profile. The experimental curves have been calculated by averaging 30 horizontal pixels in order to improve statistics. For the MIR and GCF algorithms, only the integrated absorption is considered. Theoretical absorption values have been calculated from the imaginary component β of the complex index of refraction (Raven et al., 1996). The extracted profiles for absorption look more affected by noise and artefacts than the phase ones because of the very low contrast (5.4 %) of the absorption signal. The image noise can be of statistical nature or due to spatial inhomogeneities and temporal instability of the X-ray beam.

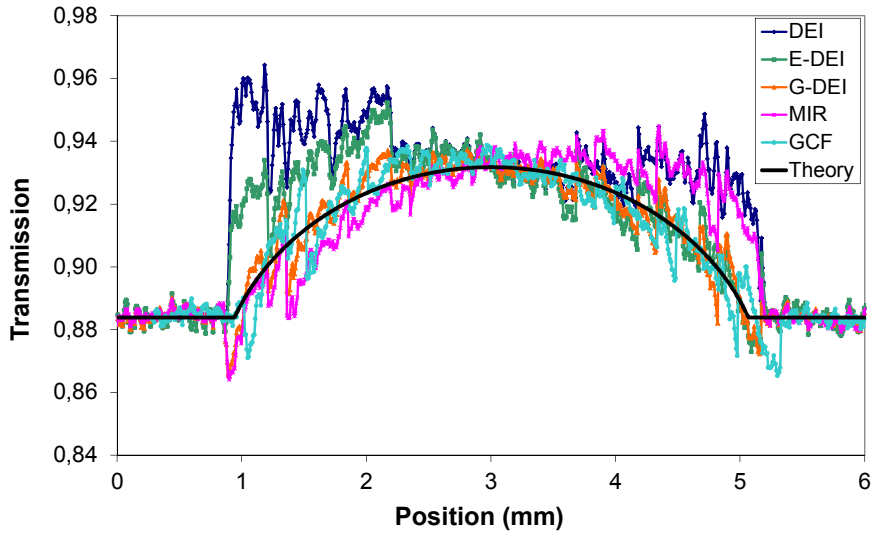

Fig. 4.12. Cross-sections of absorption images of groove 5 (depth 1.44 mm). Values extracted by the DEI, E-DEI, G-DEI, MIR and GCF algorithms are compared with the theoretical profile.

The DEI algorithm is the one that exhibits the highest artefacts at the two edges, since the validity conditions on which it is based (very low refraction angle) are violated in these regions. A similar behaviour and an additional asymmetry between the two edges appear also in the plots of the E-DEI and MIR algorithms. The reason has to be probably attributed to the fact that the actual positions of the crystal analyzer during acquisition were slightly different from the nominal ones. As a consequence, some systematic errors can be present in the calculation of the absorption. Apart from noise and artefacts, the agreement between the theory and the extracted values in the points where the refraction signal is absent (or low) is very good.

In figure 4.13 the profile of the USAXS signal through the papers, as calculated with the G-DEI, MIR and GCF algorithms, is reported. The plotted profiles are the result of the average over 100 vertical pixels. No theoretical value is displayed since no modeling of the paper structure has been attempted. The results for the MIR and the G-DEI algorithms are very similar while the GCF, especially for high levels of scattering, leads to sensibly higher values. These results suggest the presence of some saturation effect in both the MIR and G-DEI methods (but not in the GCF). This effect can be attributed to the limitations of these algorithms, pointed out in sections 4.2.3 and 4.2.5, in experimental conditions characterized by large scattering angles. In the case of the G-DEI algorithm, the second-order Taylor approximation that is introduced is accurate only if the scattering angles are small compared to the RC FWHM. In the MIR algorithm, as demonstrated by simple simulations (section 4.2.5), large scattering angles are underestimated due of the limited number of sampling points and to the limited sampling range.

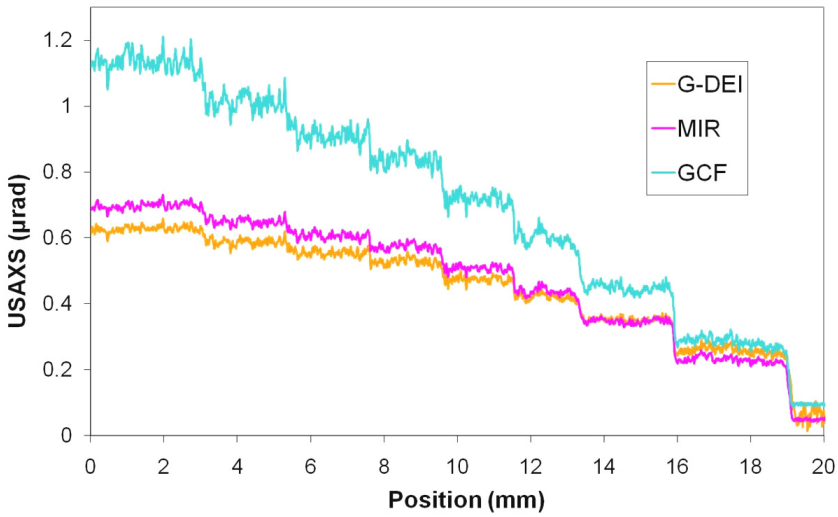

Fig. 4.13. USAXS profiles from a horizontal line across images in figure 4.4. The results from G-DEI algorithm, MIR algorithm and GCF algorithm are shown.

4.4.2 Bone-cartilage planar images

Extraction algorithms were also applied to ABI images of a human bone-cartilage sample. In figure 4.14 the maximum absorption (a), the integrated absorption (b), the refraction angle (c) and the USAXS (d) images obtained by using the MIR algorithm are reported as an example. In figure 4.14(e) an expanded view of a cartilage region in the refraction angle image (figure 4.14(c)) is also shown.

In all the images the bone and cartilage parts of the sample can be distinguished. Because of the particular and different elemental composition and structure of the two tissues, the bone presents very intense signal for all contrast contributions (absorption, USAXS and refraction) with respect to the cartilage.

Nevertheless, in the refraction image (Figure 4.14(c)) and in the expanded view in figure 4.14(e), it is noteworthy the depiction of details inside the cartilage tissue that are instead completely invisible in the other calculated images. The refraction from these fine cartilage structures, which are compatible with the cells (chondrocytes), the groups of cells (chondrons), and the collagen fibers present in the tissue, produces sufficient contrast and well represents the different architecture of the tissue along its height (from the bone-cartilage interface up to the surface) (Muehleman et al., 2004, Coan et al., 2010).

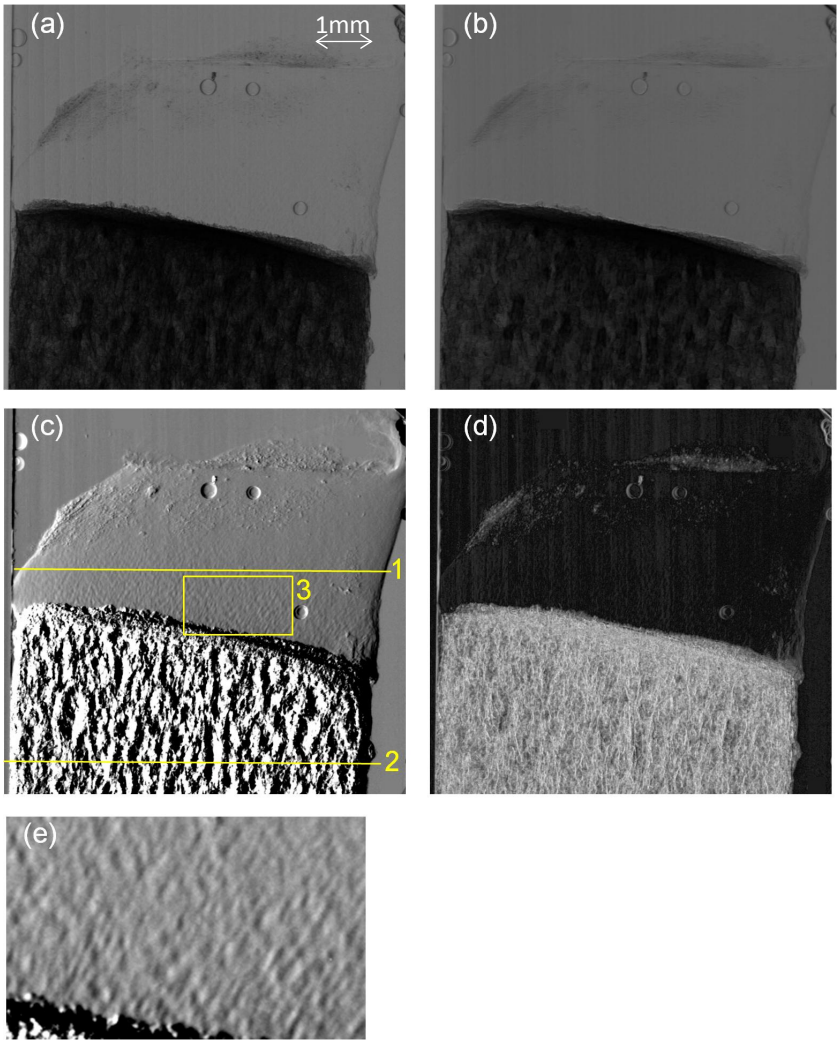

Fig. 4.14. Images calculated by applying MIR algorithm to the human bone-cartilage sample: (a) maximum absorption, (b) integrated absorption, (c) refraction angle and (d) USAXS images. An expanded view of region 3 in (c) is shown in (e).

Horizontal profiles in the cartilage and in the bone were obtained from the refraction angle images calculated using the DEI, MIR and GCF algorithms and are reported in figures 4.15 and 4.16. Two important characteristics are clearly visible in the profile of the cartilage: a fine amplitude oscillation at high frequency and a low frequency decrease from the left to the right side. The fine amplitude oscillations likely represent the signal given by the chondrocytes cells embedded in the cartilage matrix. The approximate estimated dimensions of these structures from the profile, about 35-50 μm, are in fact compatible with the common dimensions of chondrocytes. The overall refraction angle variation visible in the plot is instead given by the cylindrical shape of the sample.

A careful comparison of the signal amplitude obtained with the different algorithms shows that the MIR and GCF lead to very similar values, while with the DEI algorithm the refraction angles are underestimated, especially at the borders (see the left and right sides of the cartilage profiles). This is in agreement with the results obtained for the plastics phantoms, and is due to the

fact that the linearization of the RC introduced in the DEI method is accurate only if the refraction angles are very small, as already discussed.

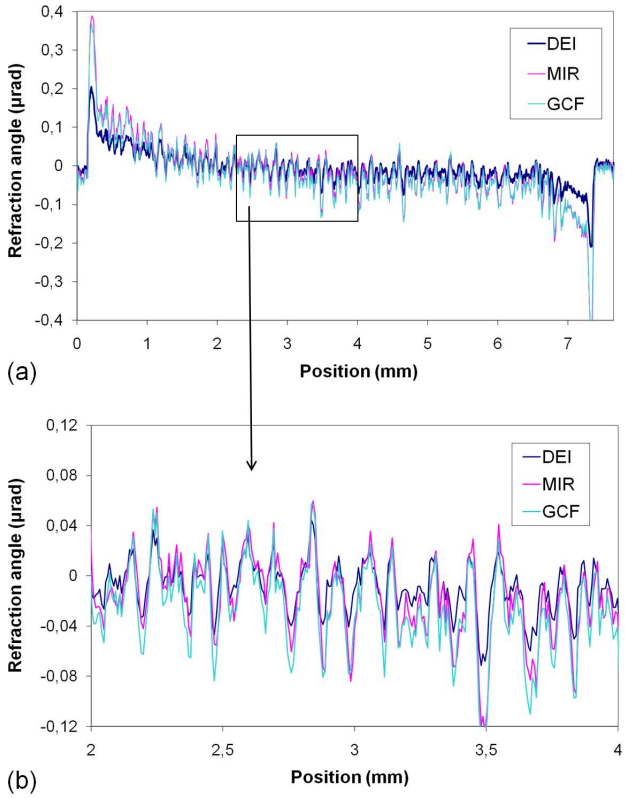

Fig. 4.15. Comparison of cartilage refraction angle values extracted by the DEI, MIR and GCF algorithms. Profiles over line 1 in figure 4.14(c) are reported in (a), an expanded view is shown in (b).

The horizontal profile in the bone shows a very different scenario. The refraction angles, here originating by the trabecular structure of the bone, are characterized by very high amplitude compared with angles produced in the cartilage. In particular, values extracted using the GCF algorithm are in some cases bigger than 7 µrad, which is considerably higher than the FWHM of the experimental RC (about 2.94 µrad). It is clear that in this situation the validity conditions of the DEI algorithm are strongly violated and the algorithm fails. Also the MIR algorithm underestimates the refraction signal with respect to the GCF algorithm. As seen theoretically in section 4.2.5 and experimentally on phantoms in section, this is due to the inaccuracy of the estimation of the actual RC centre when calculating the RC centroid. The error increases when the refraction angles are large compared to the angles sampling range.

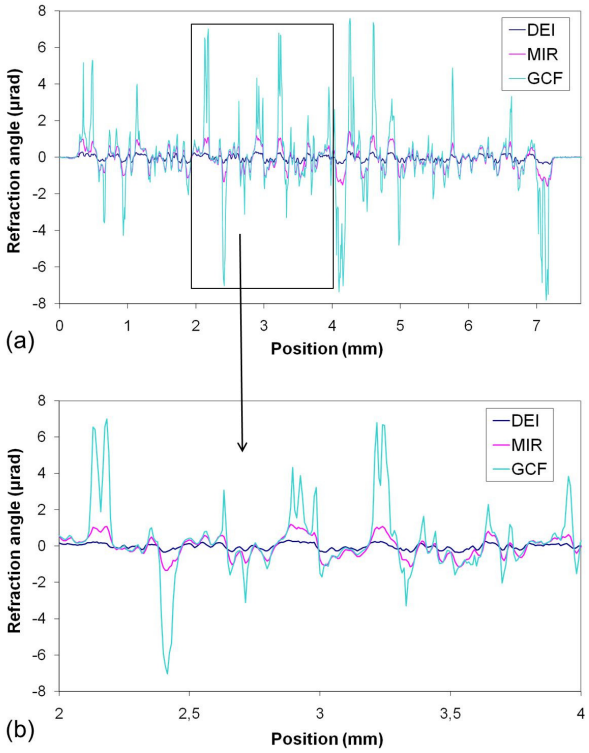

Fig. 4.16. Comparison of bone refraction angle values extracted by the DEI, MIR and GCF algorithms. Profiles over line 2 in figure 4.14(c) are reported in (a), an expanded view is shown in (b).

4.5 Conclusions

Results show that in the presence of low refraction and low USAXS the five algorithms studied here are all in good agreement with the theory. When the refraction angles are larger, the discrepancies among the methods also increase. For refraction angles of the order of the RC FWHM, only the GCF algorithm is in good agreement with the theoretical estimations. This effect is still more pronounced when, besides large refraction angles, considerable scattering is also present: the algorithms (DEI and E-DEI) that do not take USAXS into account show the worst agreement with the theory, while the GCF method gives the most accurate results.

The calculated absorption images show strong artefacts at the edges of samples, where the refraction angles are large and thus the validity conditions of the GO approximation are violated. The agreement with the theoretical values is instead good in the regions where the refraction angles are less important.

The USAXS signal from the newspaper layers has been extracted for the G-DEI, MIR and GCF methods. Both G-DEI and MIR methods underestimate the signal compared to the GCF algorithm, especially when the USAXS contribution is important. This saturation effect, similar to the one encountered in the refraction angle calculation, is in agreement with the theoretical considerations done in sections 4.2.3 and 4.2.5.

Three methods for calculating the phase images from the refraction angle images have been applied. The strong streak artefacts arising in the pure integration method can be reduced by the averaged integration method (but with a certain loss in the spatial resolution) and especially by the CLS method, if large values for the regularization parameter are used (but with a certain loss of quantitative information).

It has been shown that the calculated images in the case of biological samples are able to provide important information concerning tissues structure. In the specific case of the sample used in this work, the bone and cartilage are clearly discriminated and the internal structure of cartilage is visible as well. This may represent an important result for an improved diagnosis of diseases affecting the cartilage, like osteoarthritis.

The refraction angle images show that the differences between the algorithms are reduced when considering the cartilage tissue, where the refraction angles are relatively small. The discrepancies are important on the bone tissue, where the refraction angles are very large compared to the RC FWHM. The signal provided by the GCF algorithm is here much higher than that given by the DEI and MIR algorithms. These results are in agreement with the theoretical considerations and with the results obtained for the plastics phantoms.

The analysis and the comparison of the different algorithms, under variable conditions of refraction and scattering, clearly identify the GCF method as the one having the best agreement with the theory. This result is confirmed also when refraction and scattering contributions are very important.

A drawback of this method is that it is computationally intensive compared to the other ABI extraction methods, since a fitting of equation 4.15 has to be performed for each image pixel. It will be shown in chapter 5, however, that the large computational time needed by the fitting routine can be sensibly reduced if distributed processing on computer clusters is used. This is an important point especially for the application of this method in the tomography mode, where a large number of projection images need to be processed, as we will see in chapter 5.

The high accuracy of the GCF algorithm in calculating the refraction signal with respect to the other considered extraction methods (also in the presence of high scattering) makes this algorithm of great interest for different kinds of applications especially where the quantitative accuracy of the results is essential. The use of the GCF method for the separation of the different contrast contributions (refraction, absorption and scattering) from phase contrast AB images of clinical samples may help in the detection of those structures and pathologies that are otherwise difficult to visualize by improving the obtainable image contrast.

In the next chapter, it will be shown how the three dimensional representation of the absorption, refraction and scattering contributions can also be obtained, if the extraction algorithms here considered in the planar case are applied in the computed tomography mode. This can be very interesting for example in biological or medical imaging since, as we will see, an even more precise sample characterization can be obtained.

References and links

M. A. Branch, T. F. Coleman, and Y. Y. Li, "A subspace, interior, and conjugate gradient method for large-scale bound-constrained minimization problems", Siam J. Sci. Comput. **21** (1), 1-23 (1999).

D. Chapman, W. Thomlinson, R. Johnston, D. Washburn, E. Pisano, N. Gmur, Z. Zhong, R. Menk, F. Arfelli, and D. Sayers, "Diffraction enhanced x-ray imaging", Phys. Med. Biol. **42** (11), 2015-2025 (1997).

C. Y. Chou, M. A. Anastasio, J. G. Brankov, M. N. Wernick, E. M. Brey, D. M. Connor, and Z. Zhong, "An extended diffraction-enhanced imaging method for implementing multiple-image radiography", Phys. Med. Biol. **52** (7), 1923-1945 (2007).

P. Coan, A. Peterzol, S. Fiedler, C. Ponchut, J. C. Labiche, and A. Bravin, "Evaluation of imaging performance of a taper optics CCD 'FReLoN' camera designed for medical imaging", J. Synchrotron Radiat. **13** (13), 260-270 (2006).

P. Coan, F. Bamberg, P. C. Diemoz, A. Bravin, K. Timpert, E. Mutzel, J. G. Raya, S. Adam-Neumair, M. F. Reiser, and C. Glaser, "Characterization of osteoarthritic and normal human patella cartilage by computed tomography X-ray phase-contrast imaging: a feasibility study", Invest. Radiol. **45** (7), 437-444 (2010).

T. J. Davis, "A unified treatment of small-angle X-ray scattering, X-ray refraction and absorption using the Rytov approximation", Acta Crystallogr. A **50** (6), 686-690 (1994).

M. O. Hasnah, C. Parham, E. D. Pisano, Z. Zhong, O. Oltulu, and D. Chapman, "Mass density images from the diffraction enhanced imaging technique", Med. Phys. **32** (2), 549-552 (2005).

B. Henke, E. Gullikson, and J. Davis, "X-Ray Interactions: photoabsorption, scattering, transmission and reflection at E= 50-30000 eV, Z= 1-92", Atomic Data Nuclear Data Tables 54, 181-342 (http://henke.lbl.gov/optical_constants/) (1993).

C. H. Hu, L. Zhang, H. Li, and S. Q. Luo, "Comparison of refraction information extraction methods in diffraction enhanced imaging", Opt. Express **16** (21), 16704-16710 (2008).

Z. F. Huang, K. J. Kang, and Y. G. Yang, "Extraction methods of phase information for X-ray diffraction enhanced imaging", Nucl. Instrum. Meth. A **579** (1), 218-222 (2007).

A. K. Jain, *Fundamentals of digital image processing*, Prentice-Hall, Inc., Upper Saddle River, NJ, USA (1988).

A. Maksimenko, "Nonlinear extension of the x-ray diffraction enhanced imaging", Appl. Phys. Lett. **90** (15), 154106 (2007).

C. Muehleman, S. Majumdar, A. Issever, F. Arfelli, R. Menk, L. Rigon, G. Heitner, B. Reime, J. Metge, A. Wagner, K. Kuettner, and J. Mollenhauer, "X-ray detection of structural orientation in human articular cartilage", Osteoarthr. Cartilage **12** (2), 97-105 (2004).

Y. I. Nesterets, T. E. Gureyev, D. M. Paganin, K. M. Pavlov, and S. W. Wilkins, "Quantitative diffraction-enhanced X-ray imaging of weak objects", J. Phys. D: Appl. Phys. **37** (8), 1262-1274 (2004).

Y. I. Nesterets, T. Gureyev, and S. Wilkins, "Polychromaticity in the combined propagation-based/analyser-based phase-contrast imaging", J. Phys. D: Appl. Phys. **38** (24), 4259-4271 (2005).

Y. I. Nesterets, P. Coan, T. Gureyev, A. Bravin, P. Cloetens, and S. Wilkins, "On qualitative and quantitative analysis in analyser based imaging", Acta Crystallogr. A **62** (4), 296-308 (2006).

O. Oltulu, Z. Zhong, M. Hasnah, M. N. Wernick, and D. Chapman, "Extraction of extinction, refraction and absorption properties in diffraction enhanced imaging", J. Phys. D: Appl. Phys. **36** (17), 2152–2156 (2003).

D. Paganin, T. Gureyev, K. M. Pavlov, R. A. Lewis, and M. Kitchen, "Phase retrieval using coherent imaging systems with linear transfer functions", Opt. Commun. **234** (1-6), 87-105 (2004).

E. Pagot, P. Cloetens, S. Fiedler, A. Bravin, P. Coan, J. Baruchel, J. Härtwig, and W. Thomlinson, "A method to extract quantitative information in analyser-based X-ray phase contrast imaging", Appl. Phys. Lett. **82** (20), 3421-3423 (2003).

K. M. Pavlov, T. E. Gureyev, D. Paganin, Y. I. Nesterets, M. J. Morgan, and R. A. Lewis, "Linear systems with slowly varying transfer functions and their application to x-ray phase-contrast imaging", J. Phys. D: Appl. Phys. **37** (19), 2746–2750 (2004).

C. Raven, A. Snigirev, and I. Snigireva, "Phase-contrast microtomography with coherent high-energy synchrotron X rays", Appl. Phys. Lett. **69** (13), 1826-1828 (1996).

L. Rigon, H. Besch, F. Arfelli, R. Menk, G. Heitner, and H. Plothow-Besch, "A new DEI algorithm capable of investigating sub-pixel structures", J. Phys. D: Appl. Phys. **36** (10A), A107-A112 (2003).

L. Rigon, F. Arfelli, and R. H. Menk, "Three-image diffraction enhanced imaging algorithm to extract absorption, refraction, and ultrasmall-angle scattering", Appl. Phys. Lett. **90** (11), 114102 (2007).

A. Rosenfeld and A. C. Kak, *Digital picture processing,* 2nd edition, Academic Press, Inc., Orlando, FL, USA (1982).

M. N. Wernick, O. Wirjadi, D. Chapman, Z. Zhong, N. P. Galatsanos, Y. Yang, J. G. Brankov, O. Oltulu, M. A. Anastasio, and C. Muehleman, "Multiple-image radiography", Phys. Med. Biol. **48** (23), 3875-3895 (2003).

M. N. Wernick, Y. Yang, I. Mondal, D. Chapman, M. Hasnah, C. Parham, E. Pisano, and Z. Zhong, "Computation of mass-density images from X-ray refraction-angle images", Phys. Med. Biol. **51** (7), 1769-1778 (2006).

S. W. Wilkins, T. E. Gureyev, D. Gao, A. Pogani, and A. W. Stevenson, "Phase-contrast imaging using polychromatic hard X-rays", Nature **384** (6607), 335-338 (1996).

5

Quantitative analysis of analyzer-based computed tomography images

Table of Contents

Abstract: In this chapter we present a quantitative comparison, in the case of the computed tomography (CT) modality, of five extraction algorithms based on the geometrical optics approximation: the diffraction-enhanced imaging (DEI), the extended diffraction-enhanced imaging (E-DEI), the generalized diffraction-enhanced imaging (G-DEI), the multiple-image radiography (MIR) and the Gaussian curve fitting (GCF). The extraction algorithms are applied to analyzer-based CT images of both plastics phantoms and a bone-cartilage sample: quantitative sample information, namely the linear attenuation coefficient and the refractive index decrement, is derived and the results for the different algorithms are compared with the values predicted from theory. Furthermore, an additional method for CT reconstruction needing only a single set of angular projections is demonstrated and applied to analyzer-based CT images of a bone-cartilage sample and a breast mastectomy.

5.1 Introduction

In chapter 4, the application of different extraction algorithms to planar images of phantoms and of a biological sample was presented. The validity conditions for each of the methods were discussed in details: the methods accuracy and the consequences of the violation of their validity conditions were analyzed by comparing the experimental results with those predicted by theory.

The topic of the present chapter is the application and comparison of the same algorithms in the case of the computed tomography acquisition geometry. As shown in various publications (Dilmanian et al., 2000, Maksimenko et al., 2005, Zhu et al., 2005, Brankov et al., 2006, Huang et al., 2006, Huang et al., 2007, Rigon et al., 2008), in fact, ABI extraction algorithms can also be applied to CT images, as we will explain in the following. The coupling of a phase contrast tomography acquisition and of the considered extraction algorithms can be advantageous for many imaging applications, for example in materials science or medical imaging, since quantitative information about the absorption, refraction and ultrasmall-angle scattering object properties can be derived for each point of the three-dimensional (3D) object volume. By using extraction algorithms applied to ABI CT images we will show in particular, for both phantoms and biological tissues, that the total linear attenuation coefficient and the refractive index decrement can be calculated respectively from the extracted absorption and refraction images. Since the refractive index decrement depends on the tissue composition and density, the value of this parameter can be very useful for characterizing the object geometry and composition for example in materials science studies or for detecting pathological tissue changes in medical imaging. Besides, this information is particularly important especially when the tissues show very small absorption differences, which is usually the case for elements of low atomic number Z like the ones composing the human soft tissues, since in this case the refraction signal is able to provide much higher contrast (see section 2.2 in chapter 2).

In addition to these quantitative ABI-CT extraction algorithms, we will describe in details in this chapter a method to reconstruct the object volume by directly applying the filtered-backprojection algorithm to only one single set of angular projections acquired with a fixed position of the analyzer crystal. Under this approach, the absorption and refraction contributions are not separated but, as we will show, the resulting values are given by a linear combination of these two effects. The validity conditions of this method will be discussed in details.

The chapter is organized in the following way. In sections 5.2 and 5.3 the theoretical background for the application of CT extraction algorithms and the theoretical demonstration of the reconstruction method requiring a single set of angular projections are respectively described. In section 5.4 the experimental configuration and parameters as well as the considered samples are illustrated, while in section 5.5 the experimental results are presented and discussed. Concluding remarks are given in section 5.6.

5.2 Application of extraction algorithms to CT

Two different ABI-CT acquisition geometries have been considered in the literature: a) the sample rotation axis is parallel to the rotation axis of the analyzer (Maksimenko et al., 2005, Zhu et al., 2005) and b) the sample rotation axis is perpendicular to both the beam direction and the rotation axis of the analyzer (figure 5.1) (Dilmanian et al., 2000, Brankov et al., 2006, Rigon et al., 2008). Here we will focus on the latter geometry, where the refraction direction to which the analyzer is sensitive and the sample rotation axis are parallel. A more detailed comparison between the two different configurations can be found in section 6.1 of this Thesis and in the work of Nesterets et al. (Nesterets et al., 2006).

Let us follow the approach of Brankov et al. (Brankov et al., 2006) and consider the two coordinate systems in figure 5.1. The system (x,y,z) represents the sample reference frame and it is fixed. The rotated system (x_r,y,z_r), with $x_r = x\cos\varphi + z\sin\varphi$ and $z_r = z\cos\varphi - x\sin\varphi$, instead describes the beam-detector coordinate system, which is rotating around the y-axis. The beam propagates along z_r and the rotation axis of the analyzer crystal is parallel to x_r. In the CT method, projection images of the sample need to be acquired at different tomographic view angles φ around the sample (see section 1.1.2 in chapter 1). In the case of ABI-CT, these acquisitions have to be repeated for each considered position of the analyzer crystal along its RC. As a result, an angular projections dataset (over 360° or 180°) is acquired for each analyzer position.

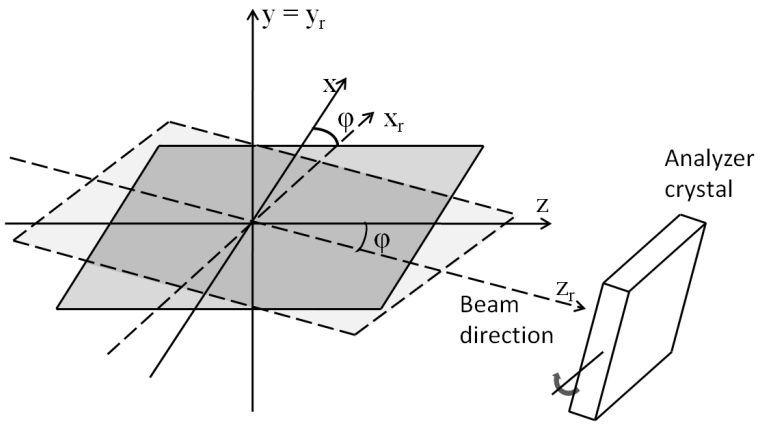

Fig. 5.1. Scheme of the considered tomographic acquisition geometry. (x,y,z) represents the coordinate system of the sample, which is considered to be fixed, while (x_r,y,z_r) represents the beam-detector coordinate system, which is supposed to rotate around the y axis. The beam propagates along z_r and yz_r represents the diffraction plane. The rotation axis of the analyzer crystal is parallel to x_r.

It can be demonstrated (Brankov et al., 2006) that, if the extraction algorithms are applied to the projection images acquired for the different analyzer positions at a given angular view φ, the derived absorption, refraction and USAXS images can be expressed in the form of line integrals. If we indicate with $L_\varphi(x_r,y)$ the path of the beam traversing the object before being detected at the position (x_r,y) on the detector, we can express, like in conventional absorption CT, the logarithm of the transmission through the sample at the view angle φ, as (see equation 1.3 in chapter 1):

$$-\ln\left[\frac{I_T(x_r,y,\varphi)}{I_0(x_r,y)}\right]=\int_{L_\varphi(x_r,y)}\mu(x_r,y,z_r)dz_r \tag{5.1}$$

where $I_0(x_r,y)$ indicates the intensity of the beam before the sample, $I_T(x_r,y,\varphi)$ the transmitted intensity and $\mu(x_r,y,z_r)$ the total linear attenuation coefficient.

The extracted refraction angle image at the view angle φ can be expressed as the line integral of the gradient, in the vertical direction y, of the refractive index decrement δ (cf. eqs. 2.8 and 2.40 in chapter 2):

$$\Delta\theta_y(x_r,y,\varphi)=\int_{L_\varphi(x_r,y)}\frac{\partial\delta}{\partial y}(x_r,y,z_r)dz_r \tag{5.2}$$

A similar expression can also be found for the USAXS contribution. Let us consider the probability density function $f_\varphi(\Delta\theta_S;\, x,y_r)$ introduced in chapter 4 (section 4.2.3) to describe the distribution of the scattering angles. Note that $f_\varphi(\Delta\theta_S;\, x,y_r)$ represents the object angular response function due to scattering at the view angle φ. Let us also indicate with $f'(\Delta\theta_S;x,y_r,z_r)$ the object local angular response function, which represents the corresponding quantity for an infinitesimal region in the object at location (x,y_r,z_r). We will indicate the second central moment of $f_\varphi(\Delta\theta_S;x,y_r)$ with $\sigma^2_{\Delta\theta_S}$, like in chapter 4 (see equation 4.7(c)). Note that this is the square of the quantity represented in the USAXS image.

We denote instead the second central moment of $f'(\Delta\theta_S;\, x,y_r,z_r)$ as:

$$M_l(x_r,y,z_r)=\int\left(\Delta\theta_S\right)^2 f'(\Delta\theta_S;x_r,y,z_r)d\left(\Delta\theta_S\right) \tag{5.3}$$

As it was demonstrated by Brankov et al. (Brankov et al., 2006) and by Rigon et al. (Rigon et al., 2008), these quantities are related by the following expression:

$$\sigma^2_{\Delta\theta_S}(x_r,y,\varphi)=\int_{L_\varphi(x_r,y)}M_l(x_r,y,z_r)dz_r \tag{5.4}$$

Equations 5.1, 5.2 and 5.4 are formally identical to the line integral encountered in conventional absorption CT. Therefore, if images of the transmission, of the refraction angle and of the USAXS are calculated at the different view angles φ, then the three-dimensional (3D) distributions of μ, $\partial\delta/\partial y$ and M_l can be respectively obtained by applying reconstruction algorithms, like the filtered back-projection (FBP) algorithm, as in conventional parallel-beam CT.

5.2.1 Calculation of the refractive index decrement

Starting from the 3D distribution of $\partial\delta/\partial y$, which can be calculated from the refraction angular projection images as we saw in the previous section, the quantitative value of the refractive index decrement δ can be in principle calculated. One possibility, in analogy to the projection case, where the 2D phase image was calculated from the refraction angle image, is to integrate the $\partial\delta/\partial y$ values in the refraction gradient direction with one of the methods we saw in chapter 4, section

4.2.7: pure integration method, averaged integration method and CLS method. Similarly to the projection case, the values of δ over a reference surface perpendicular to the integration direction need to be known a priori.

A second possibility to calculate δ, proposed by Dilmanian et al. (Dilmanian et al., 2000) and requiring the refraction gradient values on one single axial slice, is described in the following. Let us consider a boundary between two homogeneous objects/materials with different refractive index decrements δ_1 and δ_2. $\partial\delta/\partial y$ is zero at all points except at the interface between the two materials, and the refraction axial slice values will be, in the case of infinitely small pixel size and spatial resolution, equal to:

$$\frac{\partial \delta}{\partial y}(l) = (\delta_2 - \delta_1)\, tg(\alpha)\, \delta(l - l_0) \tag{5.5}$$

where α is the inclination of the interface with respect to the vertical direction, which can be easily calculated from the reconstructed volume, $\delta(l-l_0)$ is a Dirac delta function and l_0 is the spatial location of the interface. For a finite detector pixel size p_y in the vertical direction, however, the width Δl of the refraction signal profile is given by:

$$\Delta l = p_y\, tg(\alpha) \tag{5.6}$$

and can be further broadened by the imaging system point spread function. Equation 5.5 thus needs to be rewritten in a more general form as:

$$\int_{l_0-\frac{\Delta l}{2}}^{l_0+\frac{\Delta l}{2}} \frac{\partial \delta}{\partial y}(l)\, dl = (\delta_2 - \delta_1) \cdot tg(\alpha) \tag{5.7}$$

If the refraction index decrement of one of the two materials, let us say δ_1, is known, the corresponding value δ_2 for the second material can then be estimated by integrating the refraction signal over a horizontal line crossing the boundary between the two materials and using the following equation:

$$\delta_2 = \delta_1 + \frac{1}{tg(\alpha)} \int_{l_0-\frac{\Delta l}{2}}^{l_0+\frac{\Delta l}{2}} \frac{\partial \delta}{\partial y}(l)\, dl \tag{5.8}$$

5.3 CT direct reconstruction method

In section 5.2 we have seen how the absorption, refraction and scattering 3D maps can be separately reconstructed, using as input the corresponding calculated angular projections sets. In many published experimental works (for instance Dilmanian et al., 2000, Bravin et al., 2007, Keyriläinen et al., 2008, Coan et al., 2010), however, tomographic axial slices have been

reconstructed by applying directly the FBP algorithm to the projection data acquired at one single analyzer crystal position, without prior separation of the different contrast mechanisms. Here, we will present a theoretical justification for the direct application of the FBP algorithm and we will discuss its validity conditions.

If we consider, in analogy with conventional absorption CT, the logarithm of the ratio between the intensities impinging on the detector with and without the sample, we obtain, if the scattering contribution is neglected, the following quantity (see eq. 2.53):

$$-\ln\frac{I(x_r,y,\varphi)}{I_0(x_r,y,\varphi)R(\theta_{AN})}=\left[\int_{L_\varphi(x_r,y)}dz_r\mu(x_r,y,z_r)\right]-\ln\frac{R\left[\theta_{AN}+\Delta\theta_y(x_r,y,\varphi)\right]}{R(\theta_{AN})} \tag{5.9}$$

where the first term on the right side of equation 5.9 is the usual Radon transform encountered in conventional CT but the second term, due to the refraction inside the object and to the angular selectivity of the analyzer crystal, is not expressed as a line integral. Therefore, the application of the FBP algorithm to the raw angular projections acquired in the ABI technique is not justified in general. We will, in the following, demonstrate that this operation is mathematically correct under certain conditions and derive what is the physical quantity that can be reconstructed in this case.

If the analyzer is set at one of the two slopes of the rocking curve where the RC second derivative is approximately equal to zero, and if the refraction angles are small compared to the RC FWHM, the second term on the right side of equation 5.9 can be approximated with its first-order Taylor expansion around $\Delta\theta_y = 0$:

$$\begin{aligned}\ln\frac{R\left[\theta_{AN}+\Delta\theta_y(x_r,y,\varphi)\right]}{R(\theta_{AN})}&\approx\ln\left[1+\frac{1}{R(\theta_{AN})}\frac{\partial R}{\partial\theta}(\theta_{AN})\Delta\theta_y(x_r,y,\varphi)\right]\approx\\ &\approx\frac{1}{R(\theta_{AN})}\frac{\partial R}{\partial\theta}(\theta_{AN})\Delta\theta_y(x_r,y,\varphi)=K(\theta_{AN})\Delta\theta_y(x_r,y,\varphi)\end{aligned} \tag{5.10}$$

where the quantity $K(\theta_{AN})$ depends only on the chosen analyzer position and can then be considered as a constant. By using equation 5.10 and by expressing $\Delta\theta_y$ as a function of δ through equation 5.2, we can rewrite equation 5.9 as:

$$-\ln\frac{I(x_r,y,\varphi)}{I_0(x_r,y,\varphi)R(\theta_{AN})}\approx\int_{L_\varphi(x_r,y)}dz_r\left[\mu(x_r,y,z_r)-K(\theta_{AN})\frac{\partial\delta}{\partial y}(x_r,y,z_r)\right] \tag{5.11}$$

Under the conditions stated above, we have expressed the logarithm of the ratio between the intensities impinging on the detector with and without the sample in the form of a line integral: the direct application of the FBP algorithm for the axial slices reconstruction is therefore mathematically correct under this approximation. Furthermore, we can observe that the quantity reconstructed for each object point by applying the FBP algorithm to equation 5.11 is:

$$f(x,y,z)=\mu(x,y,z)-K(\theta_{AN})\frac{\partial\delta}{\partial y}(x,y,z) \tag{5.12}$$

The reconstructed values are therefore expressed, point by point, as a linear combination of the absorption coefficient and of the vertical gradient of the refractive index decrement. The signal provided by the first quantity is typically the dominant one on the inside of homogeneous object structures, while refraction gives the highest signal at the structures edges. Special cases of eq. 5.12 occur when either the absorption or the refraction signals are absent. In the latter case, the second term on the right side of eq. 5.12 vanishes, and the equation therefore reduces to the well-known result for conventional absorption CT (cf. eq. 1.2). In the case, instead, in which refraction is present but absorption is negligible, the reconstructed quantity is given only by the second term on the right side of equation 5.12: the quantitative values for the vertical gradient of δ can then be calculated in this case.

In the previous demonstration, we have assumed that the analyzer crystal is set at one of the RC slopes. This choice presents two important advantages. The second derivative of the RC is equal to zero, so the first-order Taylor approximation adopted in equation 5.10 is valid for a relatively large range of refraction angles. Additionally, the RC first derivative, and therefore also the coefficient K, are maximized at these points (see equation 5.10), leading to a maximization of the sensitivity to refraction in the reconstructed values (see equation 5.12). Other positions on the RC may be considered besides the positive and negative RC slopes, but as a direct consequence the refraction angles interval of validity will be more limited and the sensitivity to refraction will be decreased.

Equation 5.11 was obtained under the assumption that scattering is negligible. However, if the scattering angles are sufficiently small, so that $\Delta\theta_y + \Delta\theta_S$ is much smaller than the RC FWHM, the approximation is still valid. If we consider the first order approximation of the RC, in fact, scattering positive and negative contributions cancel out.

Finally, it is interesting to remark the analogy between the approximations that we have made in this section in order to obtain equation 5.11 and the DEI extraction method, because in both cases the RC is linearized at its slope, in the hypothesis that the refraction (and scattering) angles are small. We therefore expect the validity conditions and the consequences of their violation to be similar in the two considered methods.

5.4 Experimental methods

5.4.1 Experimental configuration

The experiment was performed at the ID17 biomedical beamline (ID17). The beam exiting from the fixed-exit Laue-Laue Si(111) double-crystal monochromator was further monochromatized by an additional Si(333) crystal and analyzed, after the sample, by a Si(333) crystal analyzer.

Experiments have been conducted at two different X-rays energies, 25 keV and 70 keV (energy resolution $\Delta E/E \sim 2 \cdot 10^{-4}$). The measured analyzer RC width (as FWHM) was 3.16 μrad (25 keV) and 1.17 μrad (70 keV). Images have been recorded with the FReLoN CCD camera coupled with the 8 μm optics in the case of the 25 keV beam and with the 46 μm optics at 70 keV.

5.4.2 Plastics phantoms for CT

Various phantoms were used in order to compare extraction algorithms in conditions of different amounts of absorption, refraction and scattering. A 8 mm thick Lucite bar, adjusted with an inclination of 11° with respect to the vertical direction, was imaged together with three cone-shaped polypropylene containers filled with different media: ethanol, water with 30 μm diameter glass micro-bubbles, and air (figure 5.2). The containers axes were vertical and the inclination of the containers walls with respect to the vertical direction was about 8°. The values of the mass density, total linear attenuation coefficient, and complex refractive index (imaginary part β and real part δ) of the materials constituting the phantoms are listed in table 5.1, for 70 keV (http://www.esrf.fr/computing/scientific/dabax/, , Chantler et al., 2005).

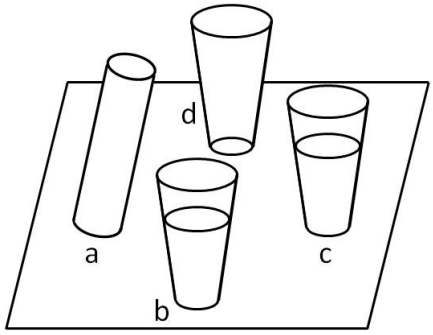

Fig. 5.2. Sketch of the custom-made phantom. The plexiglass bar has an inclination with respect to the vertical direction of about 11° (a), the three cone-shaped polypropylene containers have walls with an inclination of about 8° with respect to the vertical direction and are filled respectively with ethanol (b), water with 30 μm diameter glass micro-bubbles (c) and air (d).

Tomographic images of the phantoms were acquired at 70 keV and with a detector pixel size of 46 μm. Two thousand angular projections over 360° were recorded at four different positions of the analyzer along its RC: -60%, -80%, +90% and +60% relative intensity positions.

	ρ ($g \cdot cm^{-3}$)	μ_{total} (cm^{-1})	β ($\cdot 10^{-11}$)	δ ($\cdot 10^{-8}$)
Lucite	1.190	2.20	3.11	5.44
Polypropylene	0.855	1.63	2.30	4.13
Ethanol	0.789	1.53	2.15	3.77

Table 5.1. Mass density, total linear attenuation coefficient, imaginary and real parts of the complex index of refraction for Lucite, polypropylene and ethanol at 70 keV.

5.4.3 Bone-cartilage and breast samples

The first biological sample considered in this study was a cartilage-on-bone cylinder with a diameter of approximately 8 mm, extracted from a human patella of a 70-years-old male donor. The sample was placed in a cylindrical plastic container and dipped into a 10% formalin solution. Tomographies were acquired at 25 keV and with a detector pixel size of 8 μm, at five different positions along the analyzer RC: ±30% and ±50% relative intensity positions and peak position. For each considered crystal orientation, 1000 angular projections were recorded over 360°.

The second biological sample was a human breast, which was entirely surgically removed (operation called mastectomy) from a patient affected by an invasive ductal carcinoma. The specimen was formalin fixed and placed in a 15 cm diameter plastic container. The considered X-ray energy was 70 keV. The Frelon camera in combination with the 46 μm optics was used in this case: the 2×2 binning of the detector pixels led to an effective pixel size of 92 μm. A single CT scan was performed with the analyzer crystal positioned at the +60% position along its rocking curve. Two thousands angular projections were acquired over 360° in half-acquisition geometry.

5.4.4 Computational implementation

The ABI-CT extraction algorithms were implemented in MATLAB (The MathWorks, Inc.). The computer processor used for the calculations was a Dual-Core AMD Opteron™ 2218 Processor (64-bit, 2.6 GHz).

The pixel-by-pixel fitting of the RC expression in the CT-GCF method was performed with a MATLAB built-in function, which uses a trust-region algorithm to iteratively solve a non-linear least-squares problem (Branch et al., 1999). The values determined with the MIR method (the RC peak value, the RC centre position and the RC standard deviation) were used as the initial estimates for the parameters to be determined.

The DEI, E-DEI, G-DEI and MIR algorithms are characterized by short processing times (for example, a few seconds for a $10^3 \times 10^3$ $pixels^2$ image on the used PC), while computation times in the case of the GCF algorithm are much longer. For example, as it was already mentioned in chapter 4, the time needed to process one single $10^3 \times 10^3$ $pixels^2$ projection image was about 10 hours. In order to reach reasonable computation times when applying GCF algorithm to CT, where a large number of angular projection images need to be processed, the calculation was parallelized on the ESRF computer cluster using Condor®, a high-throughput computer software framework developed at the University of Wisconsin-Madison (Thain et al., 2005).

By using the 50-PC-cluster, the needed computation time can be reduced by a roughly equivalent factor of about 50 (for example, for a $10^3 \times 10^3$ pixels^2 image, the processing time is 12 minutes instead of 10 hours). As a result, the processing of the whole set of angular projections of the bone-cartilage sample (1000 angular projections, 190 × 1640 pixels^2 per projection) lasted less than three days.

5.5 Results and discussion

5.5.1 CT reconstruction of plastics phantoms with ABI extraction algorithms

The DEI, E-DEI, G-DEI, MIR and GCF algorithms have been applied to the phantoms angular projections. Images acquired at -60% and +60% relative intensity positions along the RC were used in the DEI and E-DEI algorithms. For the G-DEI algorithm also the acquisition at +90% relative intensity position was considered, while MIR and GCF used all four images acquired along the RC. Tomographic slices for the different contrast contributions were obtained by applying the standard FBP algorithm to the calculated angular projections. In the case of the DEI and E-DEI algorithms, only absorption and refraction images can be calculated, while the G-DEI, MIR and GCF algorithms provide also USAXS images.

CT images obtained using the MIR algorithm, depicting respectively maximum absorption, integrated absorption, refraction and USAXS, are shown in figure 5.3.

The maximum and integrated absorption images are very similar. The Lucite bar, the polypropylene containers and the scattering micro-bubbles are clearly discernible from the background. The difference in contrast between the ethanol and its container is small, because ethanol has an absorption coefficient that is quite similar to the polypropylene one (see table 5.1). The glass micro-bubbles show a much higher absorption signal than the polypropylene container. This may be due both to the higher absorption of the glass micro-bubbles and to an extinction effect arising from the high scattering that they originate. Some artefacts that are caused by refraction contamination are present at the edges of the different objects. They can be attributed in part to the fact that the geometrical optics approximation fails in the case of relatively large refraction angles (as already discussed in chapters 2 and 4) and in part to the uncertainty in the determination of the exact analyzer crystal positions along the RC at which the images were taken.

In the refraction images, the Lucite bar and polypropylene containers walls give strong signals, since they are inclined with respect to the vertical direction and therefore introduce strong refraction. In particular, the Lucite bar and the polypropylene containers give positive or negative signals depending on the sign of the refractive index decrement gradient. Furthermore, it can be noted that the refraction signal observable in the inner part of the polypropylene containers is lower in the case of the container filled with ethanol than in the case of the one left unfilled, in accordance with the lower difference in the refractive indexes of polypropylene and ethanol.

In the USAXS images both the scattering glass micro-bubbles and the edges of the different objects give a strong signal. This behavior was already observed in the projection case (see chapter 4, section 4.4.1) and may be attributed to the strong variations of the refraction angles, which may considerably increase the range of refracted X-rays falling within a single pixel. This leads to a broadening of the observed RC. In the Lucite bar USAXS image, the signal is stronger at the left and right edges than at the top and bottom edges since the refraction angles (and therefore their variations) are larger at those positions. For the same reasons the USAXS signal for the container filled with ethanol is higher at the container outer edge than at the inner one. From the extracted images it is also possible to see that materials like Lucite, polypropylene and ethanol do not produce any detectable scattering signal.

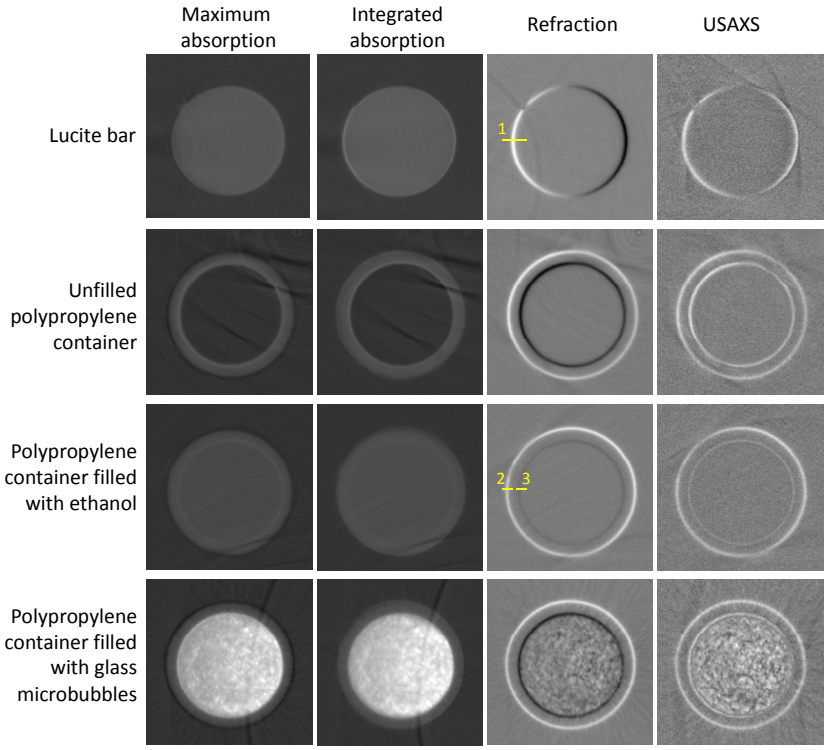

Fig. 5.3. Images of maximum absorption, integrated absorption, refraction and USAXS calculated with the MIR algorithm respectively for the Lucite inclined bar, the unfilled polypropylene container, the polypropylene container filled with ethanol and the polypropylene container filled with water and glass micro-bubbles. Lines 1-3 in the refraction images, across the air-Lucite, air-polypropylene and polypropylene-ethanol borders, respectively, are considered in the following for the calculation of the objects refractive index decrements.

A quantitative comparison of the absorption signals obtained with the different algorithms was then performed. If the extinction effect due to scattering can be neglected, the extracted absorption images (the integrated absorption images in the case of the MIR and GCF methods) depict, pixel-by-pixel, the values of the total linear attenuation coefficient in the object. The Lucite, polypropylene and ethanol total linear attenuation coefficients were estimated by calculating the average value over the whole volume of the corresponding phantom. Results are shown in table 5.2, where also the theoretical values for the total linear attenuation coefficients at 70 keV are

reported. Calculated standard deviations of the pixel values distribution in the considered regions, as well as in a background region (outside the object), are reported in table 5.3.

	Calculated values ($\cdot 10^{-1}$ cm^{-1})					Theoretical values ($\cdot 10^{-1}$ cm^{-1})
	DEI	E-DEI	G-DEI	MIR	GCF	
μ_{Lucite}	2.19	2.21	2.20	2.20	2.20	2.20
$\mu_{polypropylene}$	1.58	1.64	1.69	1.65	1.65	1.63
$\mu_{ethanol}$	1.53	1.54	1.56	1.54	1.54	1.53

Table 5.2. Total linear attenuation coefficients for Lucite, polypropylene and ethanol at 70 keV: comparison of calculated and theoretical values. The calculated values have been obtained as the average values over the whole considered object, respectively the Lucite bar, the polypropylene container and the ethanol contained in it.

It can be noticed that the agreement between the theoretical and the calculated values is very good for all the considered algorithms, the difference being always lower than 5% and in most cases lower than 1%.

	Calculated values ($\cdot 10^{-1}$ cm^{-1})				
	DEI	E-DEI	G-DEI	MIR	GCF
σ_{Lucite}	0.11	0.10	0.13	0.07	0.08
$\sigma_{polypropylene}$	0.17	0.12	0.24	0.08	0.09
$\sigma_{ethanol}$	0.14	0.12	0.20	0.11	0.12
$\sigma_{background}$	0.10	0.13	0.11	0.06	0.07

Table 5.3. Standard deviations of the absorption image pixel values in Lucite, polypropylene, ethanol and in the background region where no object is present.

The standard deviation values show that the contribution of noise changes depending on the algorithm. This behaviour can be partially explained by the fact that the number of input images is different for the various cases. A higher number of input images corresponds to a higher counts statistics and an expected lower relative contribution of noise. However, this does not explain the fact that the noise in G-DEI is higher than in DEI and E-DEI, and that the noise in GCF is higher than in MIR. This suggests that some algorithms may be inherently noisier than the others.

The refractive index decrement for Lucite was calculated by applying equation 5.8, considering a line crossing the edge between the air and the Lucite bar (line 1 in figure 5.3) and the refractive index decrement of air equal to zero. In order to reduce the effect of noise, this calculation was repeated for ten adjacent horizontal lines and the results were averaged. $\delta_{polypropylene}$ was obtained in an analogous way (considering line 2 in figure 5.3) while $\delta_{ethanol}$ was obtained considering a line crossing the edge between ethanol and the container (line 3 in figure 5.3) and using the previously calculated $\delta_{polypropylene}$. The refractive index decrements calculated respectively with DEI, E-DEI, G-DEI, MIR and GCF, as well as the theoretical values at 70 keV, are presented in table 5.4. The reported uncertainties were calculated by propagating the statistical error on the integral expression in equation 5.8 and the uncertainty in the determination of $tg(\alpha)$. The statistical error on the first quantity was estimated as the standard deviation of its mean value, obtained as

average over 10 different lines, and was found experimentally to be lower in percentage than the error on *tg(α)*. Therefore the errors reported in table 5.4 are mainly due to an uncertainty in the determination of α and not to intrinsic noise levels of the different algorithms. The same calculations for δ_{Lucite}, $\delta_{polypropylene}$ and $\delta_{ethanol}$ have also been carried out considering the right edges of the phantoms instead of the left ones (figure 5.3). The obtained values are very similar to those for the left edges and are not reported.

	Calculated values ($\cdot 10^{-8}$)					Theoretical values ($\cdot 10^{-8}$)
	DEI	E-DEI	G-DEI	MIR	GCF	
δ_{Lucite}	3.7±0.2	4.2±0.2	4.1±0.2	4.6±0.2	4.9±0.2	5.4
$\delta_{polypropylene}$	3.3±0.2	3.8±0.2	3.8±0.2	4.0±0.2	4.1±0.3	4.1
$\delta_{ethanol}$	3.0±0.2	3.2±0.2	3.3±0.2	3.4±0.2	3.5±0.3	3.8

Table 5.4. Refractive index decrements for Lucite, polypropylene and ethanol at 70 keV: comparison of calculated and theoretical values. The calculated values have been obtained using equation 5.8.

The results for the different algorithms differ greatly. The discrepancies among the different calculated values and between some of these and the theory, which are much larger than the estimated uncertainties, suggest the presence of additional systematic errors. In fact, as it was pointed out in chapter 4 for the projection case, the calculated refraction signals tend to underestimate the real values when the refraction angles are large, as it is usually the case at the edges of two objects with different refraction indexes. This is attributed to the fact that the validity conditions of both the geometrical optics approximation and of the individual algorithms can be violated in these cases. The highest difference between calculated values and the theory is provided by DEI, which is the simplest algorithm, based on a linear approximation of the RC at its two (positive and negative) slopes. This approximation is only valid for small refraction angles and leads to an important underestimation of the calculated refraction angles when these are large (Hu et al., 2008). The best agreement with the theory is provided by the MIR and the GCF algorithms, which are also those using the highest number of input images (four, in this case). The GCF method, in particular, in which a Gaussian fit of the measured object RC is performed, provides more accurate results than MIR, especially when the refraction angles are very large, as in the case of the Lucite bar. This is in agreement with previous results obtained, in projection mode, by Huang et al. (Huang et al. 2007a) and with the results presented in chapter 4. As expected, the difference between the theoretical and the calculated values is higher in percentage for the Lucite than for the polypropylene, since in the first case the difference in the refractive index decrements at the edge (and then the refraction angle) is higher. Both the geometrical optics and the algorithms validity conditions may be more strongly violated in this condition.

5.5.2 CT reconstruction of bone-cartilage sample with ABI extraction algorithms

ABI-CT algorithms were applied to the images of the human bone-cartilage sample. All the five CT acquisitions at the five analyzer positions along the RC were used by the MIR and GCF algorithms. The peak and the images at ±50% relative intensity positions were considered for the G-DEI algorithm while only the images at ±50% positions were considered for the DEI and E-DEI algorithms.

Examples of reconstructed tomographic images of integrated absorption and refraction calculated by using the CT-GCF method are reported in figure 5.4, for regions of interest inside the bone (a,b) and the cartilage (c,d). The grayscale level has been adequately adjusted for bone and cartilage, respectively.

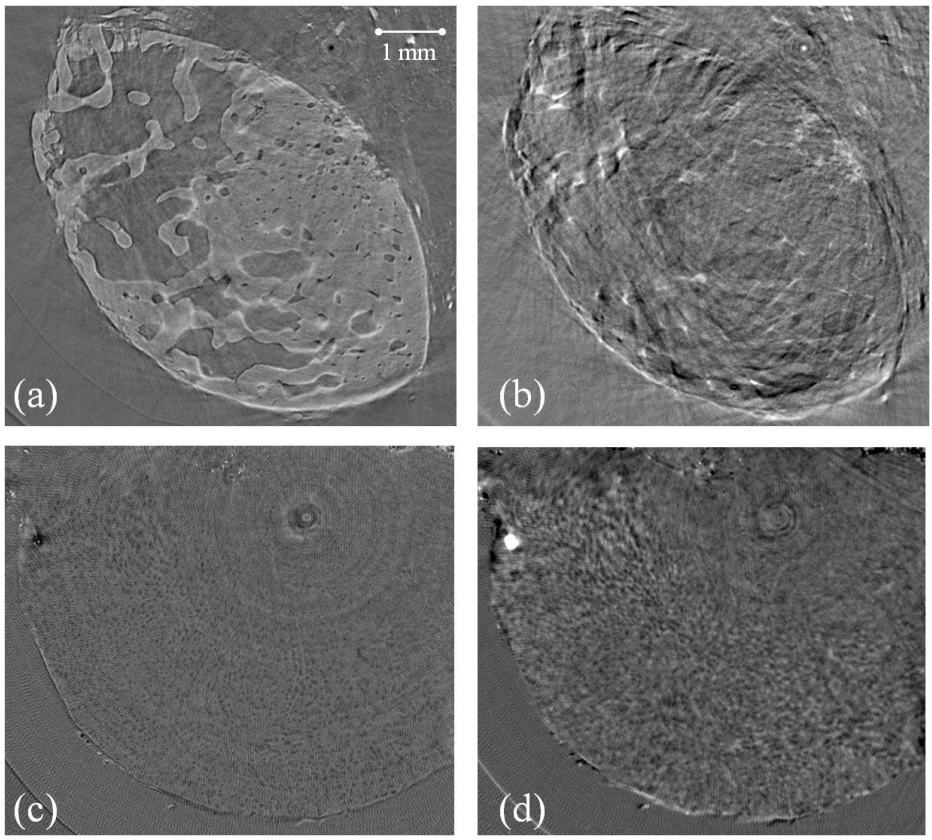

Fig. 5.4. Axial slices of the bone-cartilage sample extracted with the CT-GCF algorithm: integrated absorption (a) and refraction (b) in subchondral bone close to bone-cartilage interface, integrated absorption (c) and refraction (d) in the radial cartilage close to bone-cartilage interface.

The trabecular structure in the subchondral bone (figure 5.4(a)) is very well depicted in the absorption image. The refraction image (figure 5.4(b)), instead, presents many streak artefacts. These can be attributed to the very large refraction angles encountered at the interface between the cartilage and the subchondral bone, where both tissues with high and low atomic number Z are present. It must be pointed out, however, that the experimental parameters (such as the energy and the crystals reflection order) are not optimized for bone, already well visible in the extracted

absorption image, but for enhancing the refraction signal in the cartilage. The image interpretation is also complicated by the fact that here the contrast does not depend on the refractive index itself but on its vertical gradient.

Small oval-shaped structures that can be identified as cartilage cells (chondrocytes) and groups of cartilage cells (chondrons) (see chapter 1, section 1.1.1) appear in the absorption image (figure 5.4(c)) as black spots, which indicate that they are characterized by a slightly lower total linear attenuation coefficient with respect to the cartilage matrix. The resulting contrast for the chondrocytes and chondrons, however, is higher in the refraction image (figure 5.4(d)) than in the absorption one.

In figure 5.5, reconstructed vertical slices of the integrated absorption (a) and refraction (b) are shown. Expanded views in regions 1 (figure 5.5(a)) and 2 (figure 5.5(b)) inside the cartilage are reported in figures 5.5(c) and 5.5(d), respectively. The absorption image depicts very well the bone structure since bone has a total linear attenuation coefficient which is much higher than both the soft tissue and the formalin solution surrounding the sample. The cartilage, instead, is poorly discernible from the liquid due to very similar absorption characteristics, and also the cartilage structure is not well depicted. In the refraction image, the contrast is highly enhanced: the cartilage borders as well as the cartilage internal structure are clearly visualized. The chondrocytes and chondrons are visible as oval structures with typical black (down) and white (up) refraction contrast (Coan et al., 2010). The contrast is greatly increased with respect to that obtained in the absorption images. The characteristic black-white contrast of the chondrocytes, which has an opposed direction if compared for example with the one at the cartilage-formalin solution interface, indicates that the cartilage chondrocytes have a lower value for the refractive index decrement δ than the cartilage matrix.

Images of the refractive index decrement have also been calculated from the refraction image by using the CLS method and the averaged integration method. Expanded views in the cartilage (same region shown in figures 5.5(c) and 5.5(d)) are reported in figures 5.5(e) and 5.5(f) respectively.

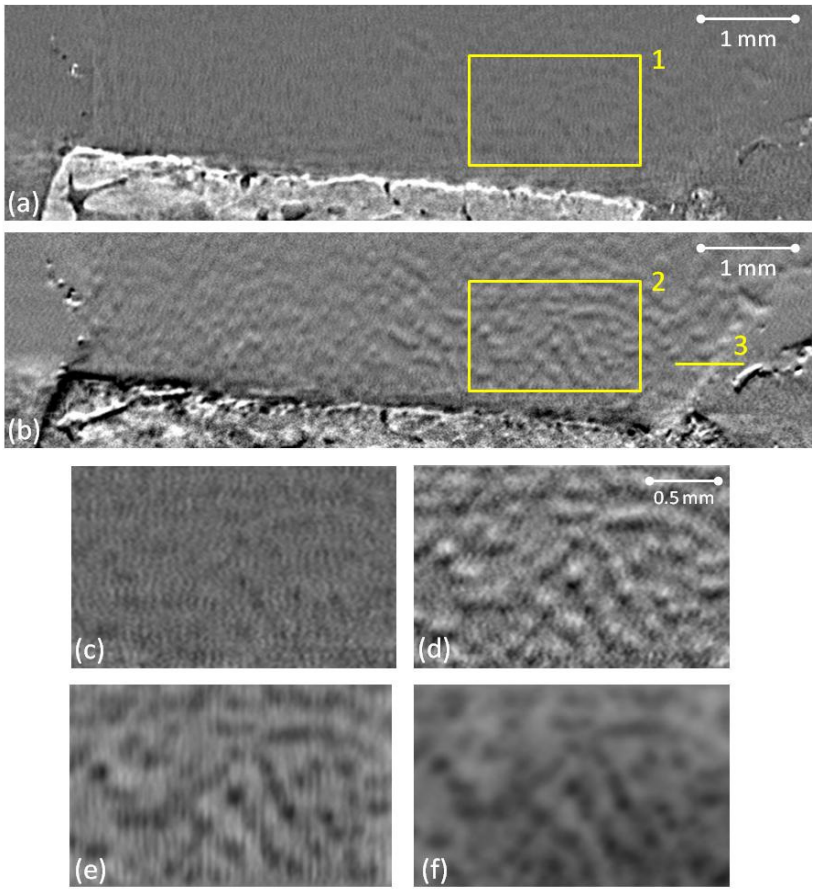

Fig. 5.5. Integrated absorption (a) and refraction (b) vertical slices of the bone-cartilage sample, extracted using the GCF algorithm. Zooms in regions 1 and 2 are shown respectively in (c) and (d): refraction image shows a greatly improved contrast in cartilage compared to integrated absorption image. Images of the refractive index decrement δ, calculated from the refraction image with the CLS method and with the averaged integration method, are also reported for the same cartilage region in (e) and (f) respectively. Line 3 in (b), across the formalin solution-cartilage interface, is considered in the following for the calculation of the cartilage matrix refractive index decrement.

Vertical profiles over one chondrocyte cell of the refraction gradient and refractive index signals are reported in figures 5.6(a,b). Results obtained with the various ABI-CT algorithms have been plotted. The refraction gradient profile values (figure 5.6(a)) have been averaged over four horizontal pixels. The profile in figure 5.6(b) has been calculated by integrating the corresponding refraction gradient profile in figure 5.6(a). Therefore, the quantity plotted in the *y*-axis represents the difference between the refractive index decrement of the cartilage matrix, $\delta_{cartilage}$, and that of a chondrocyte cell, $\delta_{chondrocyte}$.

Similarly to the results obtained in chapter 4 in the projection mode, the MIR and especially GCF methods provide the highest signal while DEI, because of its smaller refraction angle interval of validity, gives the lowest signal. The smooth shape of the calculated profiles for the chondrocyte refractive index signal (figure 5.6(b)) can be attributed both to the point spread function of the imaging system and to an inhomogeneity of the chondrocyte cell itself.

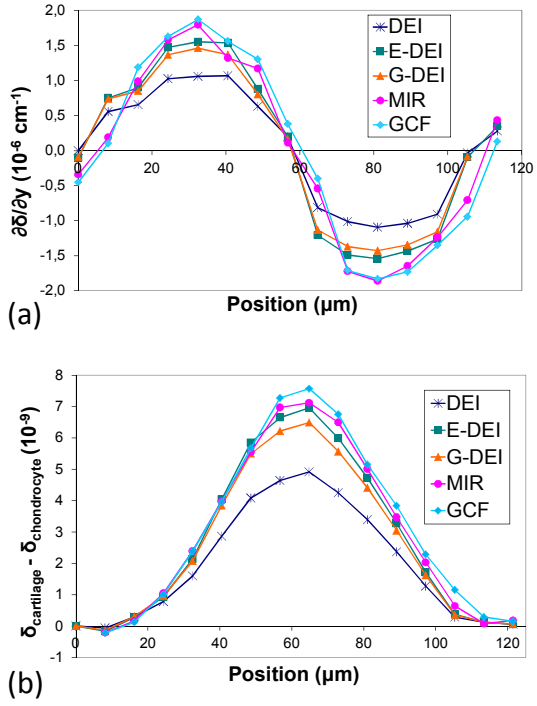

Fig. 5.6. Vertical intensity profiles over one chondrocyte: refraction gradient (a) and refractive index decrement (b). The latter was obtained by integrating the refraction gradient profile. Plotted profile values are an average over 4 horizontal pixels.

The calculated refraction images can be used for a quantitative estimation of the refractive index decrements for both the cartilage matrix and the chondrocytes. In order to estimate $\delta_{cartilage}$, horizontal line 3 in figure 5.5(b), crossing the formalin solution–cartilage interface, was considered, and equation 5.8 was applied. The value of $\delta_{formalin} = (3.71 \pm 0.18) \cdot 10^{-7}$ can be calculated by considering formalin solution elemental composition and the δ values for the composing elements at 25 keV (Henke et al., 1993). In order to reduce the effect of noise, the calculation of the integral in equation 5.8 was done by averaging ten adjacent horizontal lines. The values of $\delta_{cartilage}$ - $\delta_{formalin}$ and of $\delta_{cartilage}$ obtained using the refraction images from the different extraction algorithms are presented in table 5.5; the reported errors for $\delta_{cartilage}$ are mainly due to the uncertainty on $\delta_{formalin}$ and to the uncertainty in the determination of the inclination α of the cartilage border with respect to the vertical direction. We can see that the percentage differences among the δ values obtained from the various algorithms for cartilage (table 5.5) are much smaller than the corresponding differences for phantoms (table 5.4). This can be explained by the fact that in the case of the cartilage the reference material considered in equation 5.8 was not air but formalin, which has a refractive index decrement similar to that of the sample material. $\delta_{cartilage}$ was in this case calculated as the sum of two quantities, $\delta_{formalin}$ and $\delta_{cartilage}$ - $\delta_{formalin}$, and only the latter, which is small compared to the first one, is dependent on the considered algorithm (table 5.5). The results for the refractive index decrement of cartilage are in excellent agreement with the reference value of $\delta_{cartilage} = (4.0 \pm 0.2) \cdot 10^{-7}$ that can be calculated by considering the average

elemental composition of cartilage (ICRU, 1989) and the values of δ for the composing elements at 25 keV (Henke et al., 1993).

The difference between the cartilage matrix and the chondrocytes refractive index decrements, as we showed, can be estimated by integrating the vertical refraction gradient profile over a chondrocyte, as in figure 5.6(b). The peak value of the calculated refractive index decrement profile was considered and the results obtained for ten different chondrocytes were averaged. The calculated values are reported in table 5.5, for each of the considered algorithms. The indicated errors have been estimated as the standard deviation of the mean value over ten different chondrocytes.

The absolute values of $\delta_{chondrocytes}$ can finally be calculated from the values of $\delta_{cartilage}$ and $\delta_{cartilage}$ - $\delta_{chondrocytes}$, and are reported in table 5.5 as well.

	$\delta_{cartilage}$ - $\delta_{formalin}$ ($\cdot 10^{-7}$)	$\delta_{cartilage}$ ($\cdot 10^{-7}$)	$\delta_{cartilage}$ - $\delta_{chondrocytes}$ ($\cdot 10^{-7}$)	$\delta_{chondrocytes}$ ($\cdot 10^{-7}$)
DEI	0.20 ± 0.04	3.91 ± 0.19	0.058 ± 0.004	3.85 ± 0.19
E-DEI	0.25 ± 0.04	3.96 ± 0.19	0.071 ± 0.005	3.89 ± 0.19
G-DEI	0.23 ± 0.04	3.94 ± 0.19	0.066 ± 0.005	3.88 ± 0.19
MIR	0.25 ± 0.04	3.96 ± 0.19	0.081 ± 0.006	3.88 ± 0.19
GCF	0.26 ± 0.04	3.97 ± 0.19	0.085 ± 0.006	3.88 ± 0.19

Table 5.5. Refractive index decrements at 25 keV of the cartilage matrix and of the cartilage chondrocytes, calculated using different extraction algorithms.

5.5.3 CT direct reconstruction of two biological samples

The CT direct reconstruction method was tested on CT acquisitions of both the bone-cartilage and the breast samples. In the case of the human bone-cartilage sample, the FBP algorithm was directly applied to the angular projections recorded with the analyzer crystal set at the +50% position of its RC. Examples of the reconstructed axial slices in a bone region and in a cartilage region close to the bone-cartilage interface are shown in figures 5.7(a) and 5.7(b) respectively. A transversal cut through the reconstructed volume is reported in figure 5.7(c), while an expanded view of region 1 in cartilage is reported in figure 5.7(d).

In figure 5.7(a) the structure of the trabecular bone is very well visualized. The bone tissue is characterized by much stronger absorption than the bone marrow present in the bone cavities and consequently appears brighter in the image. In addition to the area contrast due to absorption, however, as predicted by equation 5.12, a black and white signal due to refraction is visible at the bone edges. The large variations of the refractive index decrement in these regions, in fact, give rise to a refraction signal that is white or black according to the positive or negative vertical gradient of the refractive index decrement. This can be better understood by looking at the vertical cut shown in figure 5.7(c), where the black signal at the top of the bone and the white signal at the bottom of the bone are well visible (see for example the signals indicated by the two yellow arrows).

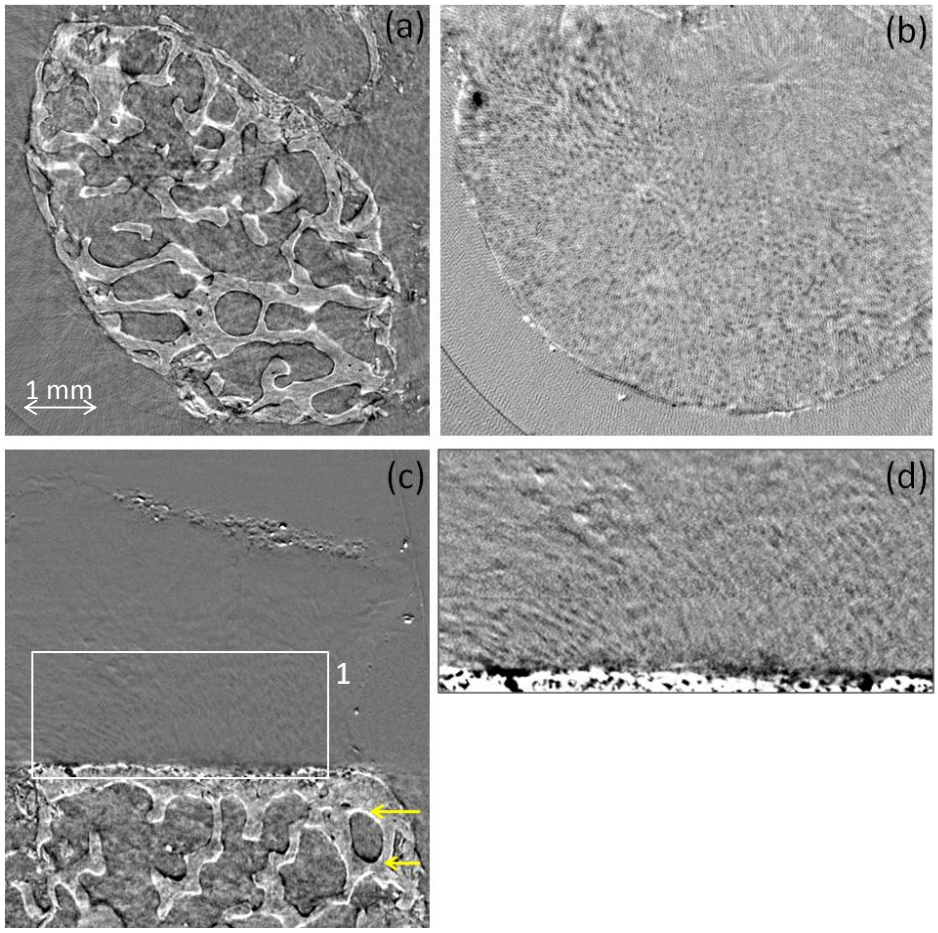

Fig. 5.7. Slices of the bone-cartilage sample reconstructed by directly applying the FBP algorithm to the +50% acquisition: (a) axial slice in trabecular bone, (b) axial slice in a cartilage region close to the bone-cartilage interface, (c) transversal cut of the reconstructed volume, (d) expanded view of region 1 in (c). Note that the grayscale level has been adequately adjusted for bone (a,c) and cartilage (b,d), respectively.

Since in the cartilage the differences in absorption are very small, as we saw in section 5.5.2, the signal in this region is provided almost entirely by the refraction occurring at the cartilage-formalin solution interface and at the edges between the cartilage matrix and the chondrocytes/chondrons. As it was previously calculated (see table 5.5), these structures have in fact a refractive index decrement lower than the cartilage matrix. In the axial slices (figure 5.7(b)) they are visualized as white or black oval shaped structures, while in the vertical slices (figures 5.7(c,d)) the black (bottom) and white (top) contrast already observed in figure 5.5(b) for chondrocytes and chondrons is obtained. As expected (see section 1.1.1 chapter 1), a vertical or oblique alignment of these structures can be observed.

The CT direct reconstruction method was also applied to the angular projections of the breast sample with invasive ductal carcinoma, acquired at the +60% analyzer position. A reconstructed axial slice is presented in figure 5.8(a). On the bottom of the image the big solid tumour, indicated by the symbol "#", is well visualized. Furthermore, many other structures in the breast are also

visible. The homogeneous grey zones (one is indicated by the symbol "+") represent regions of fat tissue. Since fat is characterized by lower X-ray absorption compared to the glandular, connective and tumour tissues, it appears darker in the image. The black and white lines in figure 5.8(a) are generated by refraction at the edges between the fat and the glandular or connective tissues regions, according to eq. 5.12, since these tissues differ not only in the value of the absorption coefficient but also in that of the refractive index decrement. One thin strand of collagen tissue is indicated by the arrow in fig. 5.8(a): on one side, the interface with fat appears white while on the other side black, depending on the sign of the vertical gradient of the refractive index decrement.

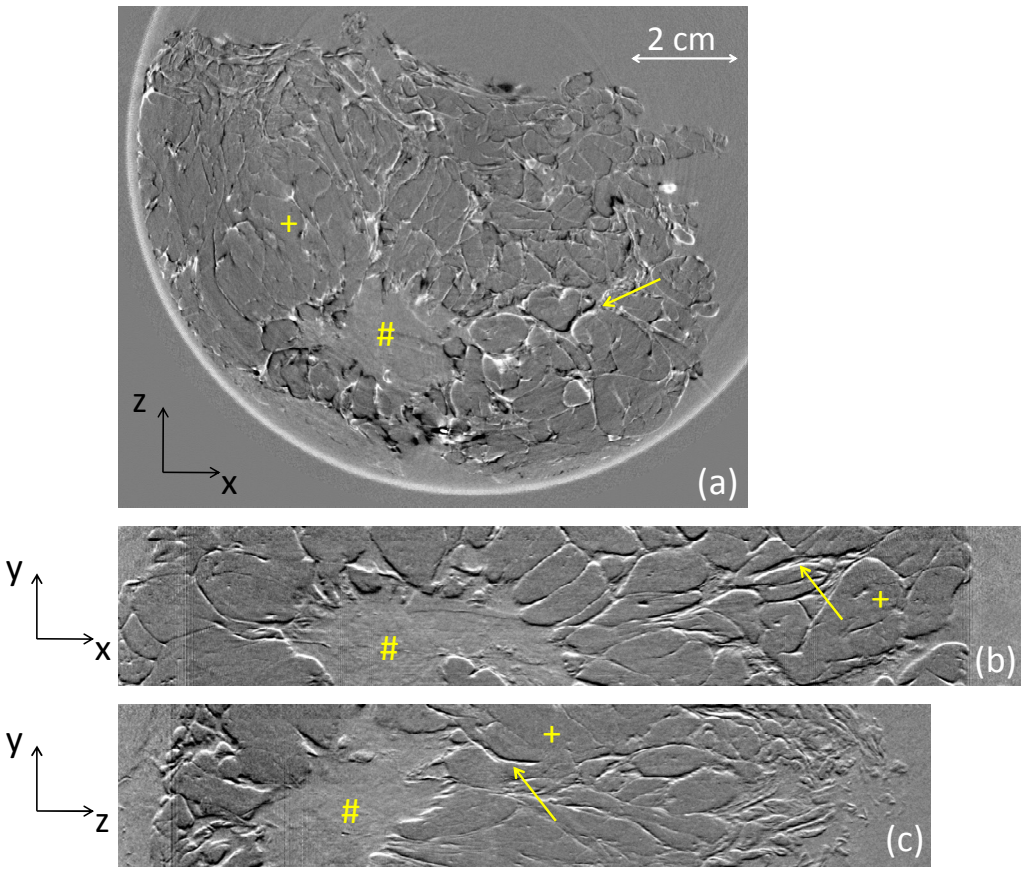

Fig. 5.8. Slices of the breast sample reconstructed by directly applying the FBP algorithm to the +60% acquisition: (a) axial slice, (b) transversal cut of the volume in the *x* direction, (c) transversal cut of the volume in the *z* direction. The symbol "#" indicates the tumour, while the "+" indicates fat regions and the arrow the interface between the fat and collagen fibers tissues.

Despite the big amount of information present in the axial slice, however, its interpretation and the understanding of the tissues geometry are not always straightforward. In figures 5.8(b,c), two vertical cuts of the reconstructed volume in two perpendicular directions are shown. As we see from these images, the determination of the tissues geometry is easier in this case. This is mostly due to the fact that the refraction signal, responsible for the signal produced at the edges, depends on the vertical variations of the refractive index decrement. The tumour is indicated by the sign "#" in the images, while homogeneous fat regions are denote by the "+" sign. The arrows indicates

collagen fibres: in this case, the behaviour of the refraction signal, white and black respectively on the top and on the bottom of the fat tissue, can be better appreciated. As it is evident from figures 5.8(a,b,c), this type of signal considerably enhances the visualization of the different structures if compared to absorption alone, allowing, in particular, a very precise definition of the structures edges.

5.6 Conclusions

We have compared different ABI-CT extraction algorithms based on the geometrical optics approximation: diffraction-enhanced imaging (DEI), extended diffraction-enhanced imaging (E-DEI), generalized diffraction-enhanced imaging (G-DEI), multiple-image radiography (MIR) and Gaussian curve fitting (GCF).

The application of the GCF algorithm in CT requires very large computational times. It was shown that reasonable execution times can be achieved by parallelizing the process with Condor® (Thain et al., 2005) on the ESRF computer cluster (for example less than three days for the processing of the bone-cartilage CT presented in this chapter). It is expected that these times can be still sensibly reduced by using parallel processing on multi-core CPUs or GPUs, or by writing a dedicated fitting routine in a programming language different from MATLAB, for example C or Fortran.

The CT extraction algorithms have first been applied to CT images of phantoms. The extracted absorption, refraction and USAXS images all provide a good visualization of the corresponding physical properties. The absorption images contain some small artefacts at the objects edges, where the refraction angles are large, which can be attributed both to a violation of the validity conditions of geometrical optics approximation, and to an uncertainty concerning the actual analyzer position during the image acquisition.

The quantitative comparison of the CT extraction algorithms with the expected theoretical values shows that all the methods are able to estimate with good accuracy the values for the total linear attenuation coefficient. The refractive index decrements for the different materials can be calculated from the extracted refraction images. The results obtained with the various algorithms differ substantially and generally underestimate the theoretical values. DEI, which is the simplest method based on a linear approximation of the RC at its two slopes, presents the highest discrepancy with respect to the theoretically predicted values. As expected, the best agreement is instead provided by MIR and especially by GCF, since in principle in the latter case there is no restriction on the amplitude of the refraction angles that can be calculated (provided that the validity conditions of the geometrical optics approximation are not violated). It has to be noted that in both the MIR and GCF methods a larger number of images acquired at different positions of the crystal RC are needed, leading to an increase in the dose to the sample and in the acquisition time. These results are in agreement with those reported in chapter 4 for planar images.

Extraction algorithms have been applied to a cylindrical cartilage-on-bone sample. The calculated absorption images are particularly accurate in depicting the bone trabecular structure, but provide low contrast in the cartilage. In the refraction images, instead, the cartilage microstructure is very well visualized and the cells (the chondrocytes) and groups of cells (chondrons) can be easily identified.

We have also shown that very informative images representing the refractive index decrement can be calculated from the refraction images, and that refractive index decrements of both the cartilage matrix and the chondrocytes can be estimated by using the different extraction algorithms. Furthermore, the obtained values for $\delta_{cartilage}$ are in very good agreement with the value that can be expected by considering the average elemental composition of cartilage. This quantitative analysis of the cartilage properties may be applied for improving the characterization of healthy and osteoarthritic cartilage tissues.

Additionally, a method for object volume reconstruction that requires only one set of angular projections acquired at a single analyzer position has been demonstrated and its validity conditions have been discussed. The method does not allow for separating the absorption, refraction and scattering signals. The resulting values, in fact, are given by a linear combination of the total linear attenuation coefficient and of the vertical gradient of the refractive index decrement, while the USAXS component does not contribute to the image contrast at a first approximation. From a mathematical point of view, the application of this reconstruction method is correct only if the refraction and scattering angles are small compared to the RC FWHM, so that the RC can be approximated with a first-order Taylor expansion. As we saw, this condition is best satisfied when the analyzer crystal position is chosen at one of the two RC slopes, where the second derivative of the RC is equal to zero. Besides, since the first RC derivative is maximized at its two slopes, the sensitivity of the method is highest at these positions. This last point will be analyzed in more detail in chapter 7. It is interesting to note that the approximations on which this method is based are very similar to the basic assumptions of the DEI extraction algorithm.

This method was applied to images of two biological samples: a human bone-cartilage cylinder and a breast mastectomy. In the resulting images very important details concerning the structure of these two specimens are visible. In the bone-cartilage sample, the bone trabecular structure is very well represented and the cartilage cells distribution and orientation can be appreciated. In the breast specimen not only the tumor is clearly visualized, but also the glandular and collagen strands structure. The correct visualization of these details is crucial for enabling the medical doctor to differentiate healthy and diseased (for example osteoarthritic) tissues in bone-cartilage imaging and to detect malignancies, even at early stages, in the imaging of breast.

We will see in the next chapter that a similar approach can be successfully implemented also in the case of the grating interferometry technique.

References and links

M. A. Branch, T. F. Coleman, and Y. Y. Li, "A subspace, interior, and conjugate gradient method for large-scale bound-constrained minimization problems", Siam J. Sci. Comput. **21** (1), 1-23 (1999).

J. G. Brankov, M. N. Wernick, Y. Y. Yang, J. Li, C. Muehleman, Z. Zhong, and M. A. Anastasio, "Computed tomography implementation of multiple-image radiography", Med. Phys. **33** (2), 278-289 (2006).

A. Bravin, J. Keyriläinen, M. Fernandez, S. Fiedler, C. Nemoz, M. L. Karjalainen-Lindsberg, M. Tenhunen, P. Virkkunen, M. Leidenius, K. von Smitten, P. Sipilä, and P. Suortti, "High-resolution CT by diffraction-enhanced x-ray imaging: mapping of breast tissue samples and comparison with their histo-pathology", Phys. Med. Biol. **52** (8), 2197–2211 (2007).

C. T. Chantler, K. Olsen, R. A. Dragoset, J. Chang, A. R. Kishore, S. A. Kotochigova, and D. S. Zucker, "X-Ray Form Factor, Attenuation and Scattering Tables" (version 2.1): http://physics.nist.gov/ffast (2005).

P. Coan, F. Bamberg, P. C. Diemoz, A. Bravin, K. Timpert, E. Mutzel, J. G. Raya, S. Adam-Neumair, M. F. Reiser, and C. Glaser, "Characterization of osteoarthritic and normal human patella cartilage by computed tomography X-ray phase-contrast imaging: a feasibility study", Invest. Radiol. **45** (7), 437-444 (2010).

F. Dilmanian, Z. Zhong, B. Ren, X. Wu, L. Chapman, I. Orion, and W. Thomlinson, "Computed tomography of x-ray index of refraction using the diffraction enhanced imaging method." Phys. Med. Biol. **45** (4), 933-946 (2000).

B. Henke, E. Gullikson, and J. Davis, "X-Ray Interactions: photoabsorption, scattering, transmission and reflection at E= 50-30000 eV, Z= 1-92", Atomic Data Nuclear Data Tables **54**, 181-342 **(**http://henke.lbl.gov/optical_constants/) (1993).

C. H. Hu, L. Zhang, H. Li, and S. Q. Luo, "Comparison of refraction information extraction methods in diffraction enhanced imaging", Opt. Express **16** (21), 16704-16710 (2008).

Z. F. Huang, K. J. Kang, Z. Li, P. P. Zhu, Q. X. Yuan, W. X. Huang, J. Y. Wang, D. Zhang, and A. M. Yu, "Direct computed tomographic reconstruction for directional-derivative projections of computed tomography of diffraction enhanced imaging", Appl. Phys. Lett. **89** (4), 041124 (2006).

Z. F. Huang, K. J. Kang, P. P. Zhu, W. X. Huang, Q. X. Yuan, and J. Y. Wang, "Strategy of extraction methods and reconstruction algorithms in computed tomography of diffraction enhanced imaging", Phys. Med. Biol. **52** (1), 1-12 (2007).

ICRU, *Tissue Substitutes in Radiation Dosimetry and Measurement*, ICRU Report 44, ICRU Publications, Bethesda MD, USA (1989).

J. Keyriläinen, M. Fernández, M. L. Karjalainen-Lindsberg, P. Virkkunen, M. Leidenius, K. von Smitten, P. Sipilä, S. Fiedler, H. Suhonen, P. Suortti, and A. Bravin, "Towards high-contrast breast CT at low radiation dose", Radiology **249** (1), 321-327 (2008).

A. Maksimenko, M. Ando, S. Hiroshi, and T. Yuasa, "Computed tomographic reconstruction based on x-ray refraction contrast", Appl. Phys. Lett. **86** (12), 124105 (2005).

Y. I. Nesterets, T. E. Gureyev, and S. W. Wilkins, "General reconstruction formulas for analyzer-based computed tomography", Appl. Phys. Lett. **89**(26) (2006).

L. Rigon, A. Astolfo, F. Arfelli, and R. H. Menk, "Generalized diffraction enhanced imaging: Application to tomography", Eur. J. Radiol. **68** (3), S3-S7 (2008).

D. Thain, T. Tannenbaum, and M. Livny, "Distributed Computing in Practice: The Condor Experience", Concurrency and computation: Practice and Experience **17**, 323-356 (2005).

P. P. Zhu, J. Y. Wang, Q. X. Yuan, W. X. Huang, H. Shu, B. Gao, T. D. Hu, and Z. Y. Wu, "Computed tomography algorithm based on diffraction-enhanced imaging setup", Appl. Phys. Lett. **87** (26) (2005).

6

CT reconstruction methods for GIFM images

Table of Contents

Abstract: In this chapter, the implementation of computed tomography (CT) in the grating interferometry technique is discussed. The application of the usual phase stepping method to CT is first described. A new simplified acquisition and processing method is then presented, which eliminates the need to scan the gratings, thus allowing for a faster CT acquisition. A theoretical foundation is provided and the validity conditions are discussed. The method is applied to experimental images of a test sample made of known materials and of a human bone-cartilage sample. The here proposed approach might be highly interesting in many fields where a reduced imaging acquisition time is requested and/or where the radiation dose delivered to the sample has to be kept low, such as, for example, in in-vivo imaging.

6.1 Phase stepping method: application to CT

The so-called phase stepping method is usually employed in grating interferometry (GIFM), as we saw in chapter 2, in order to separate the different contributions to the image contrast, namely the beam absorption, the refraction angle and the scattering introduced by the sample. Under this approach, the scanning of one grating and the acquisition of several images ($n \geq 3$), one for each step of the grating scan, are required.

The application of GIFM to CT has been already demonstrated (Weitkamp et al., 2005) and employed in several published works (see, for instance, Pfeiffer et al., 2007, Herzen et al., 2009, McDonald et al., 2009, Momose et al., 2009, Bech et al., 2010) and can be advantageous for many imaging applications, because the 3D maps of the absorption, refraction and scattering signals can be calculated. Similarly to analyzer-based imaging, two possible configurations for CT exist: 1) the sample rotation axis is perpendicular to the gratings lines (fig. 6.1(a)), 2) the sample rotation axis is parallel to the gratings lines. In the first configuration the refraction gradient sensitivity direction is therefore parallel to the rotation axis, while in the latter the two directions are perpendicular. Most of the publications concerning the application of GIFM to CT (for instance Weitkamp et al., 2005, Pfeiffer et al., 2007, Herzen et al., 2009, Bech et al., 2010) have focused on this latter geometry. As we will see, the absorption component is reconstructed in the same way in the two cases, while refraction signal requires different reconstruction methods. The tomographic reconstruction of the scattering contribution (Bech et al., 2010) will not be considered in this work.

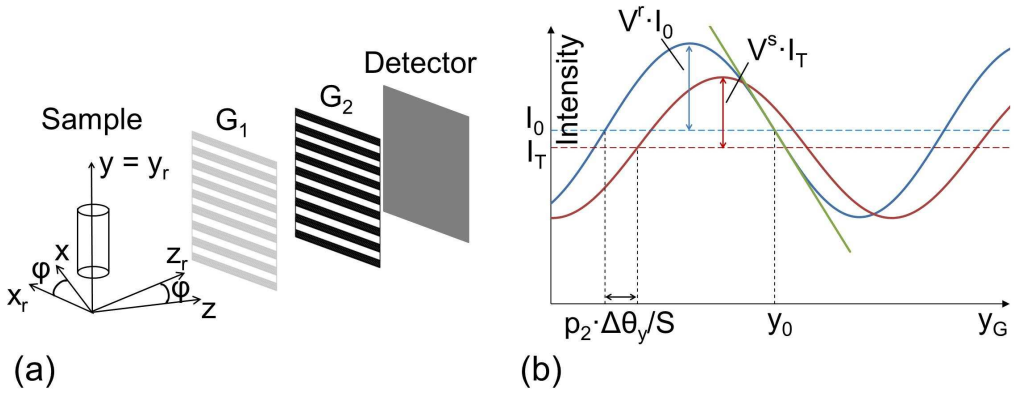

Fig. 6.1. (a) Scheme of the GIFM setup used for this study, with gratings lines perpendicular to the sample rotation axis. (b) Sinusoidal fringe pattern measured with the phase stepping method, the linear approximation of the curve around the point y_0 is indicated. V^r represents the fringes visibility in the reference image, V^s the fringes visibility in the sample image, I_0 the intensity incident on the object and I_T the transmitted intensity.

The first configuration is presented in fig. 6.1(a). The grating lines of the phase shifting grating G_1 and of the absorption grating G_2 are horizontal, while the rotation axis of the sample is vertical. The coordinates system (x_r,y,z_r) of the X-ray beam, the gratings and the detector is rotated with respect to the sample reference frame (x,y,z) by an angle φ around the CT axis y. The beam propagates along z_r and the gratings lines are parallel to x_r. In this geometry the gratings are

therefore sensitive to the component of the refraction angle that is parallel to the y axis. Note that this geometry corresponds to the case considered in chapter 5 for analyzer-based imaging CT.

Let us indicate with $L_\varphi(x_r,y)$ the path that the beam travels along through the object before being detected at the position (x_r,y) on the detector, for a certain viewing angle φ. As already seen in chapter 5, it is possible to show that the logarithm of the transmitted intensity I_T and the vertical component of the refraction angle $\Delta\theta_R$ can be expressed as line projections respectively of the total linear attenuation coefficient (μ):

$$p\left(x_r,y,\varphi\right)=-\ln\left[I_T\left(x_r,y,\varphi\right)/I_0\left(x_r,y,\varphi\right)\right]=\int_{L_\varphi(x_r,y)}dz_r\,\mu\left(x_r,y,z_r\right) \tag{6.1}$$

and of the gradient of the refractive index decrement (δ):

$$\Delta\theta_y\left(x_r,y,\varphi\right)=\int_{L_\varphi(x_r,y)}dz_r\,\frac{\partial\delta}{\partial y}\left(x_r,y,z_r\right) \tag{6.2}$$

Note that in the considered configuration the first derivative of δ is calculated with respect to the tomographic axis y, and is therefore rotation invariant. The value of the total linear attenuation coefficient for each point (x,z) of each axial plane $y = cost$ in the sample can be reconstructed, as in conventional absorption CT (Kak and Slaney, 1988), by applying the filtered backprojection algorithm:

$$\mu\left(x,y,z\right)=\int_0^\pi d\varphi\,\mathcal{F}^{-1}\left[P\left(\omega,y,\varphi\right)R\left(\omega\right)\right] \tag{6.3}$$

where P is the Fourier transform with respect to x_r of the function p defined in equation 6.1 and $\mathcal{F}^{-1}$ denotes the inverse Fourier transform. R is the so-called ramp filter, which has the form $R\left(\omega\right)=\left|\omega\right|$ (see fig. 6.2(a)).

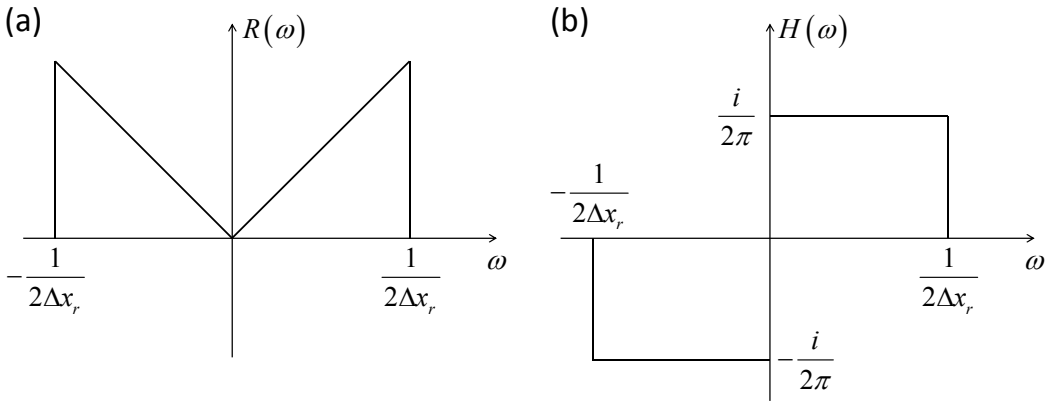

Fig. 6.2. Filter functions considered in the text for the backprojection of line integrals: (a) usual ramp filter, (b) Hilbert filter.

The first derivative of the refractive index decrement, being invariant for rotation with respect to the tomographic axis y, can also be reconstructed by using the FBP algorithm:

$$\frac{\partial \delta}{\partial y}(x,y,z) = \int_0^{\pi} d\varphi \, \mathcal{F}^{-1}\left[\Theta_y(\omega, y, \varphi) R(\omega)\right] \tag{6.4}$$

where Θ_y denotes the Fourier transform with respect to x_r of $\Delta\theta_y$.

In the second CT configuration here considered, instead, the gratings lines of G_1 and G_2, as well as the rotation axis of the sample, are vertical. As in the previous case, the system of coordinates (x_r,y,z_r) of the X-ray beam, the gratings and the detector is rotated with respect to the sample reference frame (x,y,z) by an angle φ around the CT axis y. When this CT geometry is employed, the logarithm of the transmitted intensity I_T can still be expressed by eq. 6.1, while for the refraction component the following modified equation needs to be considered, since the gratings are now sensitive to the component of the refraction angle parallel to the x_r axis:

$$\Delta\theta_{x_r}(x_r, y, \varphi) = \int_{L_\varphi(x_r, y)} dz_r \frac{\partial \delta}{\partial x_r}(x_r, y, z_r) \tag{6.5}$$

The FBP algorithm cannot be directly applied to eq. 6.5 to reconstruct, for each point of the object volume, the value of the first derivative of δ, as in this case the quantity in the line integral is not any more invariant with respect to rotation around the tomographic axis y. As shown for instance by Faris et al. (Faris and Byer, 1988) for visible light tomography, by Huang et al. (Huang et al., 2006) for analyzer-based imaging and by Pfeiffer et al. (Pfeiffer et al., 2007) in the case of X-ray grating interferometry, however, the problem can be solved by modifying the filter function considered by the FBP algorithm. In particular, it can be shown that the refractive index decrement can be reconstructed by making use of the following convolution backprojection integral:

$$\delta(x,y,z) = \int_0^{\pi} d\varphi \, \mathcal{F}^{-1}\left[\Theta_x(\omega, y, \varphi) H(\omega)\right] \tag{6.6}$$

where Θ_x indicates the Fourier transform with respect to x_r of $\Delta\theta_x$ and where the imaginary filter function $H(\omega) \equiv 1/2\pi i \, \mathrm{sgn}(\omega)$, with $sgn(\omega)$ being the sign function, is used (see fig. 6.2(b)). Note that this type of filtering corresponds to a Hilbert transform in real space. An important difference with the previous geometry is that in this case the value of δ, instead of its first derivative, is obtained. This implies that the vertical integration required to retrieve δ from its first derivative in the CT configuration considered in fig. 6.1(a) is no longer necessary and thus that the problem of streak artefacts discussed in chapters 4 and 5 can be avoided. An additional advantage of this configuration is the fact that this modified filter no longer amplifies high-frequency noise, unlike the classical ramp filter.

In both the above considered cases, the so-called phase stepping method is employed. This means that the scan of one grating, and the acquisition of several images (one for each scan step),

have to be repeated for each viewing angle. This leads to a high number of collected images, long integral acquisition time and considerable dose delivered to the sample. Other methods that do not require scanning of the gratings exist (Momose et al., 2009, Wen et al., 2009), but have the disadvantage of a much reduced spatial resolution. For this reason, in the present chapter we propose and test a method that, by sacrificing the separation of the absorption and refraction components, enables to simplify the acquisition by requiring only a single image per projection angle.

6.2 CT direct reconstruction method

Let us consider, for this scope, the configuration shown in fig. 6.1(a), in which G_1 and G_2 have the gratings lines oriented in the horizontal direction, and the rotation axis of the sample is vertical.

Let us denote by T_{GR} the average intensity transmission through the gratings and by $S = p_2/d_{Talbot}$ (where p_2 is the period of G_2 and d_{Talbot} is the considered fractional Talbot distance) the angle corresponding to one grating period. If we indicate with $\psi(x_r,y)$ the shift of the sinusoidal fringe profile measured with no object in the beam and with y_G the relative position of the two gratings, the beam intensity at each point of the detector is (Pfeiffer et al., 2008):

$$I\left(y_G;x_r,y\right)=T_{GR}(x_r,y)I_T\left(x_r,y\right)\left[1+V\left(x_r,y\right)\sin\left(\psi\left(x_r,y\right)+\frac{2\pi}{p_2}y_G+\frac{2\pi}{S}\Delta\theta_y\left(x_r,y\right)\right)\right]= \quad (6.7)$$
$$=T_{GR}(x_r,y)I_T\left(x_r,y\right)G\left(y_G;\Delta\theta_y;x_r,y\right)$$

where $G\left(y_G;\Delta\theta_y;x_r,y\right)$ is a function of both the object and the imaging system.

We will assume here that the scattering introduced by the object is negligible, so that the visibility map $V(x_r,y)$ is the same when recorded with or without the object. It is worthwhile to note that $V(x_r,y)$ and $\psi(x_r,y)$ can be easily measured from phase stepping scans acquired before inserting the object in the beam. We will further assume that V and ψ are spatially homogeneous, so that their dependence on x_r and y can be neglected. The spatial homogeneity of V is generally easily satisfied in grating interferometry experimental setups, since the fringes visibility ultimately depends on the beam spatial coherence and on the thickness of the second grating, both of which can be reasonably assumed to be constant. The condition on the homogeneity of ψ is less trivial, since it amounts to assuming no residual Moiré fringes are present on the images. In particular, in order to avoid these fringes, the two gratings need to be perfectly aligned with each others with their lines parallel. Additionally, the period of the second grating needs to match that of the first grating, the beam divergence and the distance between the two gratings.

In analogy with conventional absorption CT, we consider the logarithm of the ratio between the intensities impinging on the detector with and without the sample (i.e. the logarithm of the image intensity after whitefield normalization):

$$-\ln\frac{I(x_r,y,\varphi)}{I_0(x_r,y,\varphi)T_{GR}(x_r,y)G(y_G;\Delta\theta_y=0)}=\int_{L_\varphi(x_r,y)}dz_r\mu(x_r,y,z_r)-\ln\frac{G(y_G;\Delta\theta_y)}{G(y_G;\Delta\theta_y=0)} \quad (6.8)$$

The first term on the right side of eq. 6.8 is the usual Radon transform encountered in conventional CT. Since this term has the form of a line integral, the values of $\mu(x,y,z)$ can be reconstructed by applying conventional algorithms like FBP, as described above (eq. 6.3). In the case of GIFM there is an additional term depending on the refraction, which does not have the form of a line integral. However, if the working point y_G is chosen such that $\psi+2\pi y_G/p_2=n\pi$ (n=0,1,2..), where $\ddot{G}=0$ and $\dot{G}$ is maximum (see point y_0 in fig. 6.1(b)), and in the hypothesis that $\Delta\theta_y << S/4$, then we can apply the first-order Taylor expansion around $\Delta\theta_y$=0:

$$\ln\frac{G(y_G;\Delta\theta_y)}{G(y_G;\Delta\theta_y=0)}\approx\frac{\dot{G}(y_G;\Delta\theta_y=0)}{G(y_G;\Delta\theta_y=0)}\Delta\theta_y(x_r,y,\varphi)=K(y_G)\cdot\int_{L_\varphi(x_r,y)}dz_r\frac{\partial\delta}{\partial y}(x_r,y,z_r) \quad (6.9)$$

where we have expressed $\Delta\theta_y$ as a function of δ and where the quantity $K(y_G)$ depends only on the chosen gratings position and is therefore a constant in our case. By inserting eq. 6.9 in eq. 6.8 and applying the FBP algorithm, the following quantity can be reconstructed for each point of the object:

$$f(x,y,z)=\mu(x,y,z)-K(y_G)\cdot\frac{\partial\delta}{\partial y}(x,y,z) \quad (6.10)$$

The value calculated for each point of the object is therefore given by a linear combination of μ and of the vertical gradient of δ.

This expression was obtained under the assumption that scattering is negligible. However, if the scattering angles are sufficiently small, so that $\Delta\theta_y+\Delta\theta_{Scatt}<<S/4$, the approximation is still valid. If we consider the first order approximation of the function G, in fact, scattering positive and negative contributions cancel out.

The choice of the working point y_G in the linear region of the intensity function G presents two advantages. The first derivative $\dot{G}$ is maximized: this implies that the highest sensitivity to refraction can be achieved at this point since the coefficient K in eq. 6.10 is also maximized. Besides, since the second derivative $\ddot{G}$ is equal to zero, the interval of validity of the first-order Taylor approximation for G is relatively large. Other positions along the intensity function may be used, but this would inevitably lead to a reduction of the refraction sensitivity and to more stringent requirements on the values of the refraction angles introduced by the object.

6.3 Experimental methods

The experimental verification was carried out at the ID19 beamline using a monochromatic X-ray beam ($\Delta E/E \approx 10^{-4}$) of 32 keV. A silicon π-shifting grating (G_1), with period p_1=4.787 μm and thickness t_1=45 μm, and a gold absorption grating (G_2) with period p_2=2.4 μm and thickness t_2=50 μm, were used, in the geometry of fig. 6.1(a). The distance between G_1 and G_2 was 37 cm (5^{th} fractional Talbot distance for the energy used); the sample-to-detector distance was 55 cm. The images were recorded by the FReLoN CCD camera with the 8 μm optics. In these experimental conditions a visibility of 32%, homogeneous over the whole field of view, was obtained.

The first sample, a phantom made of objects of known composition and geometry, consisted of two hollow polypropylene cylinders, with an outer diameter of 2.3 mm and a wall thickness of 0.4 mm, inclined by approximately 11° with respect to the vertical axis and containing, respectively, ethanol and a 10% formalin solution in water. The second sample was a bone-cartilage cylinder with a diameter of approximately 8 mm, extracted from a human patella. The specimen was placed in a cylindrical plastic container and dipped into a 10% formalin solution. CT scans of both samples were performed with the gratings kept fixed at a relative position y_0, as in fig. 6.1(b). Eight hundred angular projections over 360° were recorded for imaging the plastic phantom and 1600 for the bone-cartilage sample. For comparison, an additional phase stepping CT acquisition was carried out for the plastic phantom at three gratings positions over one period, with the same angular sampling and the same exposure time for each raw projection image as in the previous case. A 2x2 binning of the detector pixels was used for the scans of the plastic phantom, leading to an effective pixel size of 16 μm.

6.4 Results and discussion

The 3D distributions of absorption and refraction have been reconstructed for the test phantom by using the phase stepping method. The combined absorption-refraction distribution (according to eq. 6.10) has been obtained by directly applying the FBP algorithm to the angular projections acquired at one fixed position of the gratings. An example of the resulting absorption, refraction and combined CT images obtained for the same slice within the sample are reported respectively in figs. 6.3(a), 6.3(b) and 6.3(c) for the cylinder containing ethanol and in figs. 6.3(d), 6.3(e) and 6.3(f) for that containing the formalin solution.

In the absorption images, the difference in intensity between the plastic cylinder and the liquid is more pronounced for formalin than for ethanol because the linear attenuation coefficients for the liquid and for the plastic container differ more in the first case (μ_{pol} = 0.23 cm^{-1}, μ_{form} = 0.35 cm^{-1}, μ_{eth} = 0.24 cm^{-1}). Edge enhancement due to propagation-based ("inline") phase contrast is also observable in the absorption images, due to the finite propagation distance between the sample and the detector (Weitkamp et al., 2005). In the refraction images a signal is produced at the interfaces between materials. It is interesting to remark that the black-white contrast is reversed for the

polypropylene-formalin boundary (fig. 6.3(e)) with respect to the polypropylene-ethanol boundary (fig. 6.3(b)), because the difference in the δ values has opposite signs in the two cases (δ_{pol} = $2.0 \cdot 10^{-7}$, $\delta_{form} = 2.3 \cdot 10^{-7}$, $\delta_{eth} = 1.8 \cdot 10^{-7}$). In figs. 6.3(c) and 6.3(f), as expected from the theory, the absorption and refraction signals visible in the previous images are combined in the same image and the variations of μ and δ can be qualitatively evaluated.

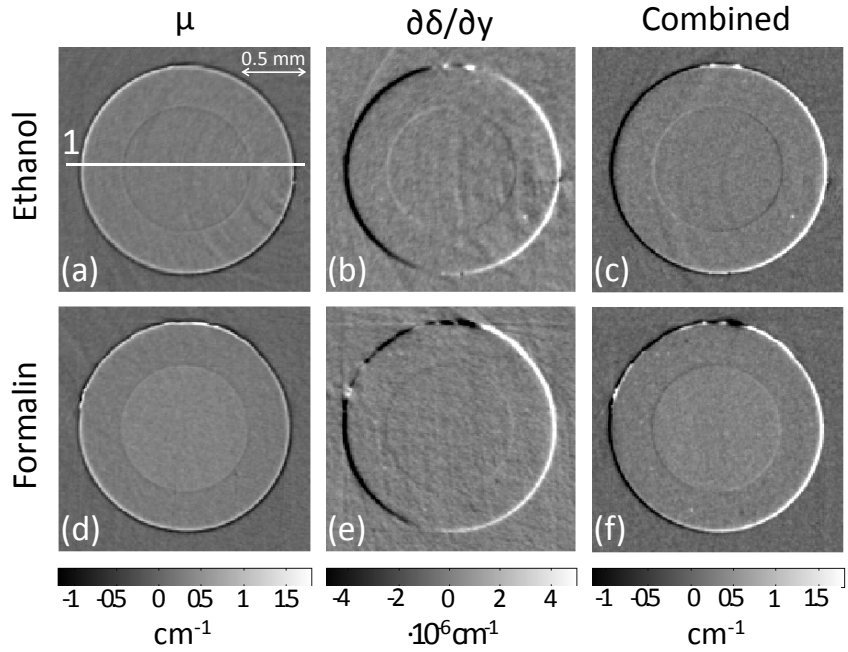

Fig. 6.3. Reconstructed axial slices for the two cylinders containing ethanol (a,b,c) and formalin (d,e,f): absorption (a,d) and refraction (b,e) images obtained with phase stepping method and combined absorption-refraction images (c,f) obtained for one fixed position of the gratings.

For a quantitative comparison, the profiles over a horizontal line across the cylinders in figs. 6.3(a,b,c) have been considered; the profiles for absorption, refraction and combined absorption-refraction signals are reported in fig. 6.4(a). In fig. 6.4(b) the profile for combined absorption-refraction is compared to that obtained using eq. 6.10. The latter has been calculated using the absorption and refraction profiles reconstructed from the phase stepping method and the theoretical value for the coefficient K, estimated to be $K(y_0) \approx -3.1 \cdot 10^5$ in our experimental conditions. An excellent agreement between the absorption and the combined absorption-refraction images in the regions where refraction is absent (i.e. far from the interfaces) is obtained (fig. 6.4(a)). Furthermore, the combined absorption-refraction profile is very close to that expected from eq. 6.10 (fig. 6.4(b)), both in regions where absorption is the only signal and in regions where refraction is predominant, like at the boundaries between the different materials.

The signal-to-noise ratio (SNR) (defined as the ratio between the pixels average value and their standard deviation) has been calculated in regions of interest (ROI) within the different materials. SNR is about 1.51-1.68 times higher in the absorption image than in the combined image. This result is close to the expected value of $\sqrt{3} \approx 1.73$ that can be estimated considering that

in the phase stepping acquisition the irradiation time was three times larger. To evaluate the statistical errors in the refraction signal, for each (negative and positive) refraction peak of the two cylinders, the area under the peak has been calculated for ten adjacent horizontal lines. The obtained SNR values (defined as the ratio between the average integral values over the ten lines and their standard deviation) are only 1.04 to 1.41 times higher in the refraction image than those for the combined image, despite of the much shorter exposure time in the latter case. This result suggests that the here presented method may be more robust to noise than the phase stepping method.

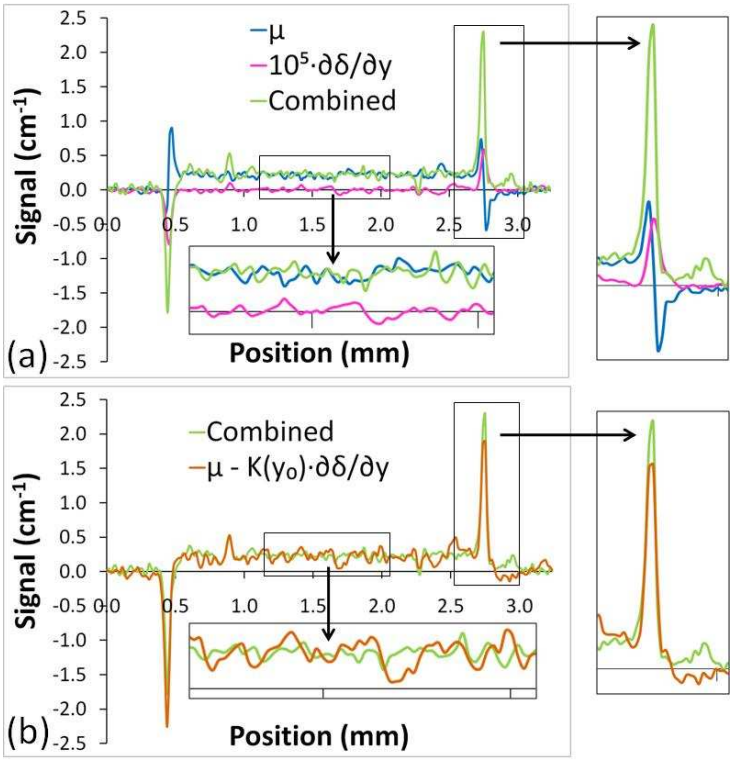

Fig. 6.4. Profiles across the cylinder containing ethanol (line 1 in fig. 6.3(a)). In (a), the absorption and refraction profiles extracted with phase stepping method are reported (the latter multiplied by 10^5 for visualization purposes), together with the absorption-refraction combined profile obtained from a single gratings position. In (b), the absorption-refraction combined profile is compared to that theoretically expected from eq. 6.10 (see text).

In fig. 6.5 the bone-cartilage sample reconstructed from the CT acquisition with a fixed position of the gratings is presented. Fig. 6.5(a) shows an axial slice in a region of bone close to the bone-cartilage interface, while fig. 6.5(b) shows a slice in the cartilage tissue. The grayscale level has been adequately adjusted for bone and cartilage, respectively. In fig. 6.5(a) the trabecular structure of the subchondral bone is very well depicted, while in fig. 6.5(b) single cartilage cells (chondrocytes) and clusters of them (chondrons) are visible as black and white spots within the cartilage matrix. A cut in the transversal direction of the reconstructed object volume is reported in fig. 6.5(c); fig. 6.5(d) shows a zoom within the cartilage. Both the internal structure of the bone

and the contours of the cartilage tissue are clearly identifiable on the top and bottom regions of fig. 6.5(c), respectively. It is evident from the image that the signal in the bone is given by a combination of absorption of the bulk and of refraction at the edges of the trabecular meshwork, in agreement with what predicted by equation 6.10. Concerning cartilage, the signal is mainly given by the refraction occurring at the boundaries between the tissue and the surrounding liquid, because the difference in absorption between the two materials is very small. A closer inspection to the cartilage reveals also that small spherical structures, identified as chondrocytes and chondrons, are visible. They show a reversed black-white contrast if compared to the cartilage-liquid interface, since they are characterized by a refractive index decrement lower than the surrounding cartilage matrix, as calculated in chapter 5 with the ABI technique. Note, however, that the energy of 32 keV used in these acquisitions is not optimized to reveal these details.

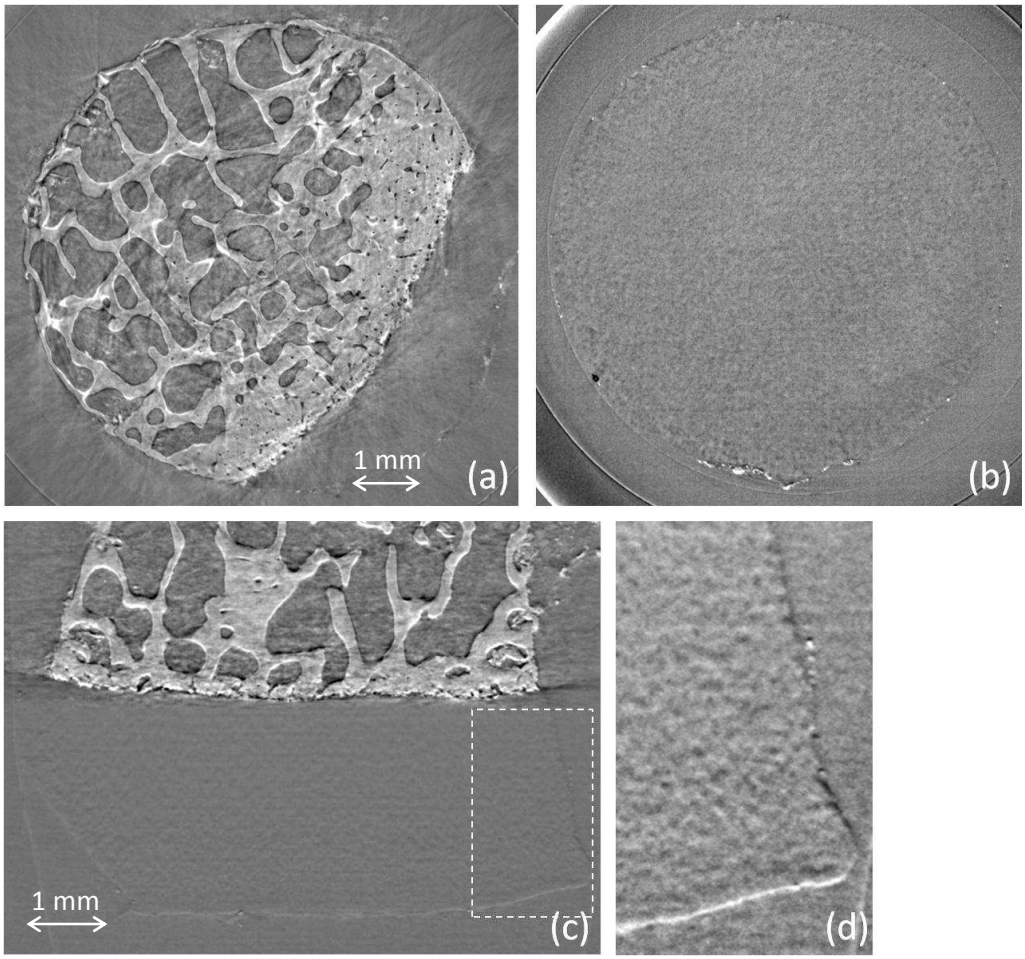

Fig. 6.5. Images of a human bone-cartilage sample calculated by using the combined absorption-refraction reconstruction: (a) CT axial slice in bone close to the interface with cartilage, (b) CT axial slice in cartilage, (c) vertical plane in the reconstructed volume showing the bone (top) and the cartilage tissues (bottom), (d) expanded view of the previous image in a cartilage tissue region. The grayscale level has been adjusted differently for bone (a,c) and cartilage (b,d), respectively.

6.5 Conclusions

A simplified method for CT data acquisition and reconstruction in grating interferometry has been proposed in this chapter. This technique needs only one raw image per viewing angle and does not require any motion of the gratings, which can remain in a fixed position with respect to each other and the rest of the setup. The procedure does not allow obtaining separate maps of the absorption and refraction of the sample, respectively, but produces images in which the contrast is generated by a combination of the two effects. However, this mixed signal contains more information than the absorption or refraction image alone and, from a diagnostic point of view, it may be advantageous. Important benefits arise from the fact that this method eliminates the need for moving the gratings during acquisition of a tomography scan. In particular, a greater stability of the setup can be obtained and also a reduction in the total acquisition time, because of the reduced number of image frames and the removal of the dead times due to gratings movement. In any potential future in-vivo application of grating interferometric tomography, shorter acquisition time will result in reduced motion artefacts. Additionally, the analysis of the signal-to-noise ratio (SNR) obtained in the reconstructed images suggests that the method may be more robust to noise than the phase stepping, and thus may allow reducing the delivered radiation dose. A more detailed study, however, will be needed to thoroughly investigate this point.

We demonstrated the feasibility of the method for both a simple test phantom and a complex biological sample. Furthermore, the results show not only a good quality of the reconstructed images, but also very good agreement with what predicted by theory. We therefore believe that the here-proposed method has the potential to find applications in many fields, in particular in possible future medical applications of X-ray grating interferometry, seen its advantages with respect to the usual phase stepping method.

Finally, it is noteworthy to remark the analogy between working within the linear region of the intensity function G in grating interferometry and acquiring images with the analyzer-based imaging technique within the linear-slope region at approximately 50% the peak height of the rocking curve. The same linear dependence on absorption and refraction is in fact encountered at these positions. As a result, the method here proposed for the direct reconstruction of GIFM CT data has essentially the same validity conditions and the same advantages of the corresponding method described in chapter 5 for ABI. Note that the precise range of validity for the refraction angle will be determined in ABI by the width of the RC (dependent, among others, on the crystal material and on the chosen reflection and energy) and in GIFM by the fringes period (dependent, among others, on the second grating period and on the chosen Talbot fractional distance and energy). The analogy between the signal in ABI and GIFM will be exploited and analyzed in more detail in the next chapter, where a comparison of the two above techniques, together with the propagation-based imaging (PBI) technique, will be presented.

References and links

M. Bech, O. Bunk, T. Donath, R. Feidenhans'l, C. David, and F. Pfeiffer, "Quantitative x-ray dark-field computed tomography", Phys. Med. Biol. **55** (18), 5529-5539 (2010).

G. W. Faris and R. L. Byer, "3-Dimensional Beam-Deflection Optical Tomography of a Supersonic Jet", Appl. Optics **27** (24), 5202-5212 (1988).

J. Herzen, T. Donath, F. Pfeiffer, O. Bunk, C. Padeste, F. Beckmann, A. Schreyer, and C. David, "Quantitative phase-contrast tomography of a liquid phantom using a conventional x-ray tube source", Opt. Express **17** (12), 10010-10018 (2009).

Z. F. Huang, K. J. Kang, Z. Li, P. P. Zhu, Q. X. Yuan, W. X. Huang, J. Y. Wang, D. Zhang, and A. M. Yu, "Direct computed tomographic reconstruction for directional-derivative projections of computed tomography of diffraction enhanced imaging", Appl. Phys. Lett. **89** (4), 041124 (2006).

A. C. Kak and M. Slaney, *Principles of Computerized Tomographic Imaging*, IEEE Press, New York, USA (1988).

S. A. McDonald, F. Marone, C. Hintermüller, G. Mikuljan, C. David, F. Pfeiffer, and M. Stampanoni, "Advanced phase-contrast imaging using a grating interferometer", J. Synchrotron Radiat. **16**, 562-572 (2009).

A. Momose, W. Yashiro, H. Maikusa, and Y. Takeda, "High-speed X-ray phase imaging and X-ray phase tomography with Talbot interferometer and white synchrotron radiation", Opt. Express **17** (15), 12540-12545 (2009).

F. Pfeiffer, C. Kottler, O. Bunk, and C. David, "Hard X-ray phase tomography with low-brilliance sources", Phys. Rev. Lett. **98** (10) (2007).

F. Pfeiffer, M. Bech, O. Bunk, P. Kraft, E. F. Eikenberry, C. Brönnimann, C. Grünzweig, and C. David, "Hard-X-ray dark-field imaging using a grating interferometer", Nat. Mat. **7** (2), 134-137 (2008).

T. Weitkamp, A. Diaz, C. David, F. Pfeiffer, M. Stampanoni, P. Cloetens, and E. Ziegler, "X-ray phase imaging with a grating interferometer", Opt. Express **13** (16), 6296-6304 (2005).

H. Wen, E. E. Bennett, M. M. Hegedus, and S. Rapacchi, "Fourier X-ray Scattering Radiography Yields Bone Structural Information", Radiology **251** (3), 910-918 (2009).

7

Comparison of three phase-contrast imaging techniques

Table of Contents

Abstract: The present chapter is dedicated to a comparison of three phase-contrast techniques: propagation-based imaging (PBI), analyzer-based imaging (ABI) and grating interferometry (GIFM). A theoretical comparison of the signal, in terms of signal-to-noise ratio, figure of merit and sensitivity, is first presented. Experimental images of plastics phantoms, recorded with different values of the acquisition parameters, are then analyzed and the results are compared with the theoretical predictions. Finally, extraction algorithms are applied to images acquired respectively with the PBI, ABI and GIFM techniques and the results are discussed.

7.1 Introduction

The theoretical foundations that form the basis of the propagation-based imaging (PBI), analyzer-based imaging (ABI) and grating interferometry (GIFM) techniques have been the object of chapter 2. The requirements of the methods in terms of spatial and temporal coherence and the needed experimental setup have also been discussed in details in chapters 2 and 3. As we have seen, ABI needs high X-ray temporal coherence (i.e. high beam monochromaticity) and a highly parallel beam, while PBI and GIFM are characterized by more strict requirements concerning the beam spatial coherence. As it was mentioned, however, the requirement on the high spatial coherence in GIFM can be circumvented if an appropriately shaped third (absorption) grating is placed downstream the source, creating an array of individually coherent, but mutually incoherent beams (Pfeiffer et al., 2006).

However, these techniques differ not only for the needed experimental setup and beam coherence requirements but also for the nature and amplitude of the provided image signal. Pagot et al. (Pagot et al., 2005) already presented an interesting comparison of the PBI and ABI techniques. However, a comprehensive theoretical and experimental comparison of the PBI, ABI and GIFM techniques is still missing in the literature. This will be the object of this chapter. In particular we will investigate, for each of the considered techniques, the nature of the image signal and its dependency upon the various acquisition parameters. We will then compare the amplitude of the signal provided by the different techniques on the same test objects. The peculiarities of each technique and the analogies among them will be discussed.

The chapter is organized in the following way. In section 7.2, general expressions for the signal-to-noise ratio and figure of merit are derived from the expression of the intensity in the various techniques. Approximated formulas are then obtained under the assumption of small refraction angles, and the sensitivities of the different techniques are compared. In section 7.3 the experimental parameters and the imaged test phantoms are described. The raw images acquired with different experimental parameters are analyzed and quantitative images are computed by applying extraction algorithms in section 7.4; the results are discussed and compared with the theory. Conclusions are provided in section 7.5.

7.2 Signal-to-noise ratio (SNR) and figure of merit (FOM)

The definitions of the signal-to-noise ratio (SNR) and of the figure-of-merit (FOM) for area contrast signals have been formulated in chapter 3 (section 3.6). The extension of these definitions to the edge signals characteristic of phase-contrast techniques has also been discussed.

We will consider here the case of an object/detail immersed in a homogeneous background. Let us assume the detector to be able to detect all photons incident on it (the extension of the following results for an arbitrary detector efficiency different from 100%, however, is straightforward) and that the photons impinging on each detector pixel can be described by the

Poisson statistics. Let us further assume that the noise is dominated by statistical (white) noise, and that other possible noise sources like, for example, beam inhomogeneities and aberrations arising from non-ideal optics components are negligible compared to it. We expect, however, that these hypotheses will not be verified for very low or very high photon counts. For very low counts, in fact, the dark noise of the detector cannot be neglected and becomes the dominant noise source. Such a situation can be obtained, for example, when in the ABI technique the analyzer is set at the far tails of its rocking curve, where the value of the reflectivity is very low. If the photon counts are increased to very high values, instead, the statistical fluctuations are supposed to become very small and the beam inhomogeneities due to the optics cannot be anymore neglected. It is worth mentioning that potential future medical applications of phase-contrast will likely be photon-limited in order to minimize the radiation dose delivered to the sample.

Under the hypothesis of Poisson statistics, the standard deviation of the counts in each detector pixel (corresponding to a position within the object or in the background) is equal to the square root of the number of counts itself:

$$\sigma(x,y) = \sqrt{I(x,y)} \tag{7.1}$$

where (x,y) denotes the considered position on the detector, $I(x,y)$ the average number of photons on the detector pixel and $\sigma(x,y)$ the standard deviation of this value. Note that in the following the spatial variables (x,y) will be omitted for simplicity of the resulting equations.

Since the radiation dose absorbed by the sample is proportional to the intensity of the beam incident on it (Webb, 1988), we can express it as follows:

$$D = K_{dose} I_0 \tag{7.2}$$

where I_0 indicates the beam intensity before the sample and K_{dose} is a constant that depends in a complicated way on both the imaging system (X-rays energy, irradiation geometry..) and the object (shape, dimensions, composition..). Note that in general K_{dose} cannot be calculated analytically but only through Monte Carlo simulations.

Equations 3.6 and 3.4 formulated in chapter 3 for SNR and FOM in the "edge signal" case can therefore be rewritten as:

$$SNR = \frac{\sqrt{A}\left(I_{\max} - I_{\min}\right)}{\sqrt{2I_{back}}} \tag{7.3}$$

$$FOM = \frac{\sqrt{A}\left(I_{\max} - I_{\min}\right)}{\sqrt{2K_{dose} I_0 I_{back}}} \tag{7.4}$$

where $I_{\min}$ and $I_{\max}$ are the number of photons incident on a detector pixel in the regions of the edge of minimum and maximum intensity respectively, I_{back} is the number of photons on a detector pixel in the background (out of the detail/object), and A is the number of pixels in each of

the three considered regions. In the case of area contrast, instead, like in conventional absorption imaging, eqs. 3.3 and 3.4 need to be considered. Under the same assumptions for the noise that we have done above, they can be rewritten as:

$$SNR = \frac{\sqrt{A}\left(I_{obj} - I_{back}\right)}{\sqrt{I_{obj} + I_{back}}} \tag{7.5}$$

$$FOM = \frac{\sqrt{A}\left(I_{obj} - I_{back}\right)}{\sqrt{K_{dose} I_0 \left(I_{obj} + I_{back}\right)}} \tag{7.6}$$

where I_{obj} and I_{back} denote respectively the intensities for a pixel within the object and for a pixel in the background.

In the following, we will use eqs. 7.3-7.6 to derive analytical formulas for the SNR and the FOM in both the conventional absorption and phase-contrast techniques. In the latter case, the absorption and refraction signals will be considered separately for simplicity, keeping in mind, however, that in general the contrast will be provided by a combination of both signals.

7.2.1 SNR and FOM in absorption imaging

In conventional absorption imaging, the intensity impinging on the detector depends only on the absorption of the sample. If the object absorption is small, the expression for intensity can be approximated as follows:

$$I = I_0 \exp\left(-\int dz\mu\right) \approx I_0 \left(1 - \int dz\mu\right) \tag{7.7}$$

where μ denotes the value of the linear attenuation coefficient and z is the direction of the beam passing through the object. By inserting eq. 7.7 in eqs. 7.5 and 7.6, the SNR and FOM can be expressed as:

$$SNR_{ABS} \approx \frac{\sqrt{AI_0}\left(\int dz\mu_{back} - \int dz\mu_{obj}\right)}{\sqrt{2 - \int dz\mu_{obj} - \int dz\mu_{back}}} \tag{7.8}$$

$$FOM_{ABS} \approx \frac{\sqrt{A}\left(\int dz\mu_{back} - \int dz\mu_{obj}\right)}{\sqrt{K_{dose}\left(2 - \int dz\mu_{obj} - \int dz\mu_{back}\right)}} \tag{7.9}$$

It is worth mentioning, however, that both equations do not take into account the effect of the scattered X-rays, which can blur the detected signal and can introduce additional noise in the image.

7.2.2 SNR and FOM in propagation-based imaging

We will first consider the case of an object showing negligible absorption. Let us assume the sample-to-detector distance D to be small and the phase to be a slowly varying function. As we have shown in chapter 2, this is equivalent to the assumption of large Fresnel numbers N_F in the near-field diffraction regime. We can then safely write the following expression for the intensity on the detector (transport of intensity equation (TIE) for slowly varying absorption):

$$I \approx I_0 \left(1 - \frac{\lambda D}{2\pi} \nabla_{\perp}^2 \phi \right) \tag{7.10}$$

where $\nabla_{\perp}^2 \phi$ indicates the Laplacian of the phase in the (x,y) plane perpendicular to the propagation direction. Under the assumption we have made of large Fresnel numbers N_F, the expressions for SNR and FOM (eqs. 7.3 and 7.4) can then be rewritten for PBI as:

$$SNR_{PBI} = -\frac{\lambda D \sqrt{A I_0}}{2\pi\sqrt{2}} \left(\nabla_{\max}^2 \phi - \nabla_{\min}^2 \phi \right) \tag{7.11}$$

$$FOM_{PBI} = -\frac{\lambda D \sqrt{A}}{2\pi\sqrt{2K_{dose}}} \left(\nabla_{\max}^2 \phi - \nabla_{\min}^2 \phi \right) \tag{7.12}$$

In this regime, both SNR and FOM are therefore proportional to the difference between the values of the Laplacian of the phase at the two sides of the object/detail edge, and to the propagation distance. They are therefore improved when the distance between the sample and the detector is increased, provided that the validity conditions for TIE are still valid. Furthermore, since the phase is inversely proportional to the energy (see section 2.2), we can observe that the SNR is proportional to $1/E^2$. The dependence of the FOM upon the energy is instead more complex and cannot be univocally determined, since the coefficient K_{dose} is dependent both on E and on the sample geometry and composition, and the two dependences are correlated.

It is worth mentioning that, in the derivation of eqs. 7.11 and 7.12, the influence of the finite spatial resolution of the imaging system on the edge signal has not been considered. Partial spatial coherence of the incoming beam (determined by the finite angular source size) and finite spatial resolution of the detector, both encountered to a certain extent in experimental setups, have in fact the effect of blurring the image signal. The intensity measured on the detector is therefore given by the convolution of the ideal intensity distribution with the PSF of the imaging system (see eq. 2.39 in chapter 2 and Gureyev et al., 2008 for a detailed discussion). Eqs. 7.11 and 7.12 need then to be rewritten as:

$$SNR_{PBI,conv} = -\frac{\lambda D \sqrt{A I_0}}{2\pi\sqrt{2}} \left[\max\left(\nabla^2 \phi * PSF_{PBI} \right) - \min\left(\nabla^2 \phi * PSF_{PBI} \right) \right] \tag{7.13}$$

$$FOM_{PBI,conv} = -\frac{\lambda D\sqrt{A}}{2\pi\sqrt{2K_{dose}}}\left[\max\left(\nabla^2\phi * PSF_{PBI}\right) - \min\left(\nabla^2\phi * PSF_{PBI}\right)\right] \tag{7.14}$$

Since both maximum and minimum intensity values across the edge are smoothed by the imaging system PSF, the measured SNR and FOM will be reduced with respect to the ideal case represented by eqs. 7.11-7.12.

Let us now consider the contribution of the absorption contrast to the image signal. By considering the transport of intensity equation for slowly varying absorption (eq. 7.10), we observe that the dependence of the intensity incident on the detector upon the object absorption is very simple, since the intensity is proportional to the local beam transmission. In the (fictitious) case in which the object showed no refraction, the image signal would be very similar to that obtained in the pure absorption case, and eqs. 7.8 and 7.9 for SNR and FOM are therefore valid. An important difference, arising from the propagation distance D between the sample and the detector is, however, that the blurring due to scattering, typical of conventional absorption imaging, can be largely reduced since X-rays scattered at a sufficiently large angle will not reach the detector.

7.2.3 SNR and FOM in analyzer-based imaging

Let us consider that the beam incident on the object has been monochromatized by both a double-crystal main monochromator and a second monochromator placed just before the object. The beam exiting the sample is then filtrated by an analyzer crystal before being recorded on the detector.

Let us further suppose that the distance between the sample and the detector is not sufficient to give rise to propagation ("inline") phase contrast, and that the object/detail absorption is negligible. The intensity for each detector pixel can then be expressed, in the geometrical optics approximation, by (cf. eq. 2.53 in chapter 2):

$$I\left(\theta_{AN}, \Delta\theta_y\right) = I_0 R\left(\theta_{AN} + \Delta\theta_y\right) \tag{7.15}$$

where I_0 is the value of the intensity incident on the sample and R is the so-called rocking curve (RC), whose expression is given by (cf. eq. 2.54):

$$R\left(\theta\right) = \frac{\int_{\theta} d\theta' R_1^2\left(\theta'\right) R_2\left(\theta'\right) R_3\left(\theta - \theta'\right)}{\int_{\theta} d\theta' R_1^2\left(\theta'\right) R_2\left(\theta'\right)} \tag{7.16}$$

where R_1, R_2 and R_3 denote respectively the reflectivity curves of each of the two crystals of the main monochromator, of the second monochromator and of the analyzer. The analyzer crystal is detuned by an angle θ_{AN} with respect to the Bragg condition for diffraction and the beam direction is locally deviated of a refraction angle $\Delta\theta_R$ by the sample. $\Delta\theta_y$ indicates the component of the refraction angle in the diffraction plane (see eq. 2.40 in chapter 2).

By inserting eq. 7.15 in eqs. 7.3 and 7.4, the following expressions for SNR and FOM can be obtained:

$$SNR_{ABI} = \frac{\sqrt{AI_0}\left[R\left(\theta_{AN}+\Delta\theta_y\right)-R\left(\theta_{AN}\right)\right]}{\sqrt{2R\left(\theta_{AN}\right)}} \tag{7.17}$$

$$FOM_{ABI} = \frac{\sqrt{A}\left[R\left(\theta_{AN}+\Delta\theta_y\right)-R\left(\theta_{AN}\right)\right]}{\sqrt{2K_{dose}R\left(\theta_{AN}\right)}} \tag{7.18}$$

The SNR is proportional to both the square root of the beam intensity I_0 and the square root of the number of pixels A. This means that its value is increased with increased photon flux and when the detail over which the signal is calculated is large. The FOM, as expected, is instead independent of the beam intensity I_0.

Equations 7.17 and 7.18 can be further simplified if we assume that the refraction angles are small compared to the RC FWHM. In this case, the RC can in fact be expressed with good accuracy by a first–order Taylor expansion (note that this is the same approximation considered in the DEI extraction algorithm). The following approximate expressions for SNR and FOM can then be obtained:

$$SNR_{ABI} \approx \frac{\sqrt{AI_0}}{\sqrt{2}}\frac{R'\left(\theta_{AN}\right)}{\sqrt{R\left(\theta_{AN}\right)}}\Delta\theta_y \tag{7.19}$$

$$FOM_{ABI} \approx \frac{\sqrt{A}}{\sqrt{2K_{dose}}}\frac{R'\left(\theta_{AN}\right)}{\sqrt{R\left(\theta_{AN}\right)}}\Delta\theta_y \tag{7.20}$$

Under these hypotheses, both the SNR and FOM are now proportional to the value of the refraction angle. The factor $R'(\theta_{AN})\Big/\sqrt{R(\theta_{AN})}$ that appears in both equations depends strongly on the chosen analyzer position. It is thus very important to study the dependence of the SNR and FOM on the position of the analyzer along its RC, in order to determine at which working points the highest sensitivity can be achieved in a particular experimental setup.

The profiles of the imaging system rocking curve, of its first derivative, and of the quantity $R'(\theta_{AN})\Big/\sqrt{R(\theta_{AN})}$ have been calculated with XOP (X-ray Oriented Programs) (http://www.esrf.fr/computing/scientific/dabax/), in the case of an X-ray energy of 26 keV (which corresponds to the energy employed in our experiment) and with Si(111) reflection used by both the crystals of the monochromators and of the analyzer. The profiles are reported in figures 7.1(a,b,c). As we can see, the first derivative of the imaging system RC (fig. 7.1(b)) assumes values that are almost constant along the two RC slopes for a relatively large range of angles, and reaches its maximum at around ±10 μrad (close to the end of the two slopes, where the rocking curve is approximately the 10% of its peak value). The $R'(\theta_{AN})/\sqrt{R(\theta_{AN})}$ function, instead, is not

constant at the RC slopes but it is strongly peaked around ±10 μrad (fig. 7.1(c)). This implies that, for refraction angles sufficiently small for the linear approximation of the RC to hold, the sensitivity is maximized at these points.

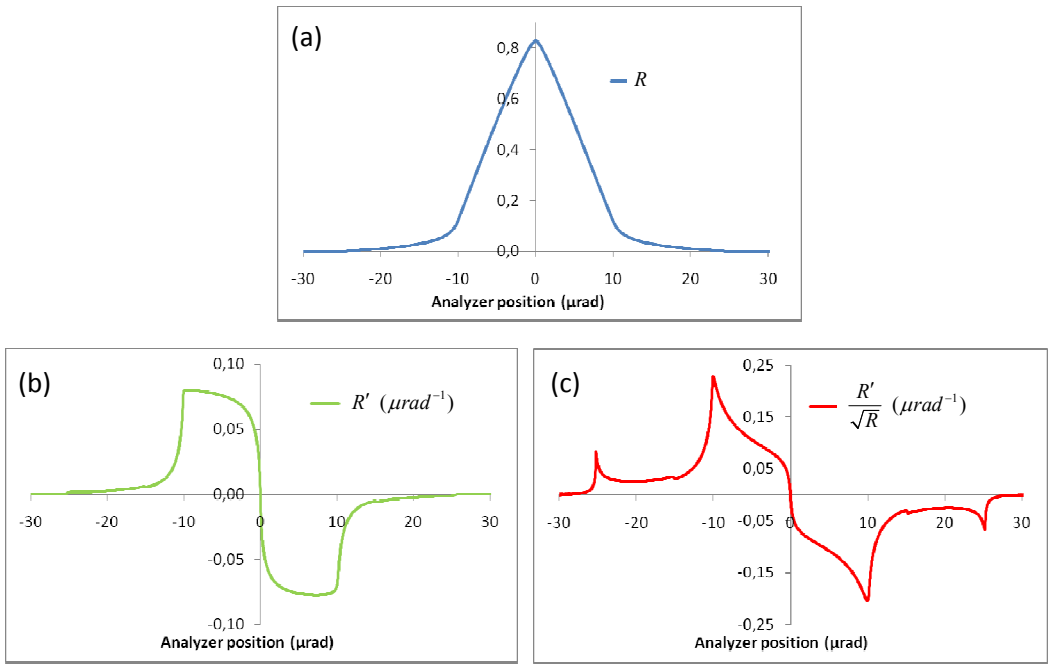

Fig. 7.1. (a) Profile of the theoretical imaging system RC for double main monochromator, second monochromator and analyzer in Si(111) reflection geometry, (b) profile of its first derivative, and (c) ratio between the first derivative and the square root of the RC. All quantities have been calculated with XOP (http://www.esrf.fr/computing/scientific/dabax/) for an X-ray energy of 26 keV.

The SNR goes to zero for high (positive or negative) values of the analyzer angle and also at the top of the rocking curve. This is obviously an effect of the linear approximation of the RC, which is not accurate at this point, where the first derivative is equal to zero and the second derivative is large. It is worth mentioning that at this position the following second-order Taylor expansions would be a much more accurate estimation of the SNR and FOM:

$$SNR_{ABI,top} \approx \frac{\sqrt{AI_0}}{2\sqrt{2}} \frac{R''(\theta_{AN})}{\sqrt{R(\theta_{AN})}} (\Delta\theta_y)^2 \tag{7.21}$$

$$FOM_{ABI,top} \approx \frac{\sqrt{A}}{2\sqrt{2K_{dose}}} \frac{R''(\theta_{AN})}{\sqrt{R(\theta_{AN})}} (\Delta\theta_y)^2 \tag{7.22}$$

From the previous equations we see that, at these points, both quantities are not anymore proportional to the refraction angle $\Delta\theta_y$ but instead to its squared value and to the second derivative of the rocking curve.

It is important to remark that the hypothesis at the basis of equations 7.19 and 7.20 (i.e. that the statistical white noise is the dominant source of noise) is not valid, as already mentioned, when the number of X-rays reaching the detector is too small, because the effect of the detector dark

noise will be predominant. Note that if a single photon counting detector was used the dark noise could be very low; however, since in our experimental setup we are using CCD cameras, its contribution is important for low photon counts. The extrapolation of the value of $R'(\theta_{AN})/\sqrt{R(\theta_{AN})}$ for large analyzer angles (for example θ_{AN} > 20 μrad), therefore, is of no interest for our purposes.

Profiles corresponding to the ones presented in figures 7.1(a,b,c) are reported in figures 7.2(a,b,c) for the case where the considered reflection is the Si(111) for the double main monochromator and the Si(333) for the second monochromator and the analyzer. As in the previous case, the considered energy was 26 keV and the functions were calculated with XOP. We can observe that the obtained RC is much narrower in this case and, as a consequence, increased sensitivity can be achieved. The RC first derivative values, in fact, are increased compared to the Si(111) case and this leads to higher values for the quantity $R'(\theta_{AN})/\sqrt{R(\theta_{AN})}$. This means that, in the case of very small refraction angles, the maximum SNR is achieved in this second configuration.

The dependence of the SNR upon the photon energy can be derived from eq. 7.19, considering that: i) the Darwin width of the crystal is inversely proportional to the energy, and therefore the rocking curve first derivative is approximately proportional to E; (ii) the refraction angle goes as $1/E^2$ (see section 2.2). It follows then that the SNR is inversely proportional to E.

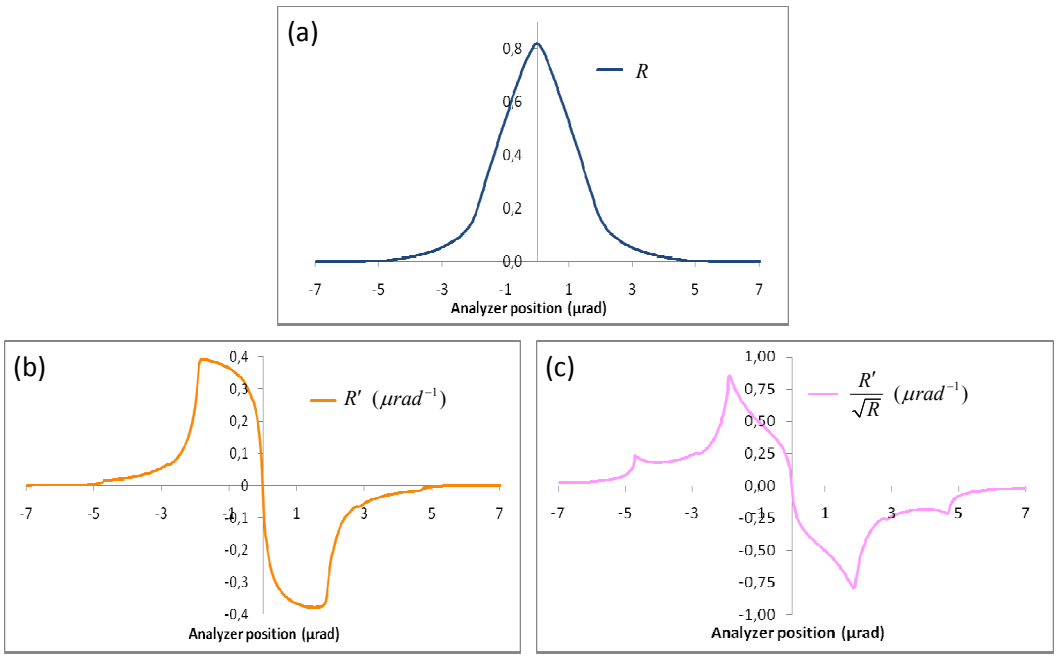

Fig. 7.2. (a) Profile of the theoretical imaging system RC for double main monochromator in Si(111) reflection geometry, and both second monochromator and analyzer in Si(333) reflection geometry; (b) profile of the RC first derivative, and (c) ratio between the first derivative and the square root of the RC. All quantities have been calculated with XOP (http://www.esrf.fr/computing/scientific/dabax/) for an X-ray energy of 26 keV.

For sake of completeness, we wish to remark that, analogously to the corresponding expressions for SNR and FOM derived in the PBI case (eqs. 7.11-7.12), eqs. 7.19 and 7.20 do not consider the effect of the finite spatial resolution of the imaging system on the edge signal. In this latter case, in fact, the measured intensity is given by a convolution of the ideal image intensity and the imaging system PSF. The expressions for SNR and FOM (eqs. 7.19-7.20) need to be rewritten as:

$$SNR_{ABI,conv} = \frac{\sqrt{AI_0}}{\sqrt{2}} \frac{R'(\theta_{AN})}{\sqrt{R(\theta_{AN})}} \left(\Delta\theta_y * PSF_{ABI}\right) \tag{7.23}$$

$$SNR_{ABI,conv} = \frac{\sqrt{A}}{\sqrt{2K_{dose}}} \frac{R'(\theta_{AN})}{\sqrt{R(\theta_{AN})}} \left(\Delta\theta_y * PSF_{ABI}\right) \tag{7.24}$$

where the imaging system point spread function in the case of ABI can be expressed as $PSF_{ABI} = \left(2\pi\sigma_{ABI}^2\right)^{-1} \exp\left[-\left(x^2+y^2\right)/\left(2\sigma_{ABI}^2\right)\right]$, with $\sigma_{ABI} = \left(d/L\right)\sigma_{src}^2 + \sigma_{det}^2 + \sigma_{an}^2$. σ_{src} and σ_{det} indicate the standard deviations of the source intensity distribution and of the detector PSF, respectively, d is the sample-to-detector distance, L is the source-to-sample distance and σ_{an} is the width of the analyzer crystal PSF projected onto the detector (see chapter 2, section 2.5.4). For typical ABI setups, the sample-to-detector distance is usually small and the loss in resolution due to the finite angular source size, $\left(d/L\right)\sigma_{src}^2$, can then be neglected. An additional source of image blurring with respect to PBI is provided by the PSF of the analyzer crystal placed between the sample and the detector, as discussed in section 2.5.4 of chapter 2. This contribution can amount, in the hard X-rays range, to a few micrometers.

Let us finally briefly discuss the contribution of the absorption contrast to the SNR in ABI images. As we can see from the expression of the intensity in the geometrical optics approximation (eq. 2.53), its dependence upon the absorption signal is trivial. The intensity at a particular position on the detector is in fact proportional to the local transmission of the object. For an object showing negligible refraction and scattering, the image contrast would then be similar to the contrast obtained in conventional absorption imaging, with the important difference that in this case the number of photons on the detector, and therefore the SNR and FOM values, are reduced by the filtration introduced by the analyzer crystal. Eqs. 7.8 and 7.9 need then to be rewritten as:

$$SNR_{ABI,abs} = \sqrt{R(\theta_{AN})} \frac{\sqrt{AI_0}\left(\int dz\mu_{back} - \int dz\mu_{obj}\right)}{\sqrt{2 - \int dz\mu_{obj} - \int dz\mu_{back}}} \tag{7.25}$$

$$FOM_{ABI,abs} = \sqrt{R(\theta_{AN})} \frac{\sqrt{A}\left(\int dz\mu_{back} - \int dz\mu_{obj}\right)}{\sqrt{K_{dose}\left(2 - \int dz\mu_{obj} - \int dz\mu_{back}\right)}} \tag{7.26}$$

Another important difference with respect to conventional absorption imaging is that all the Compton scattered and small-angle scattered X-rays will be rejected by the analyzer, eliminating the blurring due to scattering typical of conventional absorption imaging.

7.2.4 SNR and FOM in grating interferometry

If we assume the object/detail absorption to be negligible, the intensity for each detector pixel is given by (see eq. 2.64 in chapter 2):

$$I\left(y_G\right) = T_{GR} I_0 \left[1 + V \sin\left(\psi + \frac{2\pi}{p_2} y_G + \frac{2\pi}{S}\Delta\theta_y\right)\right] = T_{GR} I_0 G\left(y_G; \Delta\theta_y\right) \tag{7.27}$$

T_{GR} is the average intensity transmission through the gratings, V is the fringes visibility and ψ the shift of the sinusoidal fringe profile measured with no object in the beam. $S = p_2 / d_{Talbot}$ (where p_2 is the period of the second grating G_2 and d_{Talbot} is the here considered fractional Talbot distance) represents the angle corresponding to one grating period, while y_{GR} is the relative position of the two gratings in the direction y perpendicular to both the optical axis and the grating lines (see fig. 6.1). Finally, $\Delta\theta_y$ is the component of the refraction angle in the plane perpendicular to the grating lines (see fig. 6.1).

By combining equation 7.27 with equations 7.3 and 7.4, the following expressions for SNR and FOM are obtained:

$$SNR_{GIFM} = \frac{\sqrt{A T_{GR} I_0}\left[G\left(y_G; \Delta\theta_y\right) - G\left(y_G; \Delta\theta_y = 0\right)\right]}{\sqrt{2G\left(y_G; \Delta\theta_y = 0\right)}} \tag{7.28}$$

$$FOM_{GIFM} = \frac{\sqrt{A T_{GR}}\left[G\left(y_G; \Delta\theta_y\right) - G\left(y_G; \Delta\theta_y = 0\right)\right]}{\sqrt{K_{dose} 2G\left(y_G; \Delta\theta_y = 0\right)}} \tag{7.29}$$

The SNR, as expected, is proportional to the square root of the beam intensity I_0 and of the considered number of pixels A. The FOM, instead, is independent of the beam intensity I_0. The dependence of SNR and FOM on the refraction angle $\Delta\theta_y$ (through the intensity function G) is not trivial in the general case.

In order to simplify equations 7.28 and 7.29, let us suppose that the refraction angle $\Delta\theta_y$ is much smaller than $S/4$. The function G can therefore be approximated linearly around $\Delta\theta_y=0$. Note that this is the same approximation that was at the basis of the GIFM CT reconstruction method presented in chapter 6. In this hypothesis, the following approximate expressions for SNR and FOM can then be obtained:

$$SNR_{GIFM} \approx \frac{\sqrt{AT_{GR}I_0}G'\left(y_G;\Delta\theta_y=0\right)}{\sqrt{2G\left(y_G;\Delta\theta_y=0\right)}}\Delta\theta_y = \sqrt{2}\pi\sqrt{AT_{GR}I_0}\frac{Vd_{Talbot}}{p_2}\frac{\cos\left(\psi+\frac{2\pi}{p_2}y_G\right)}{\sqrt{1+V\sin\left(\psi+\frac{2\pi}{p_2}y_G\right)}}\Delta\theta_y \tag{7.30}$$

$$FOM_{GIFM} \approx \frac{\sqrt{AT_{GR}}G'\left(y_G;\Delta\theta_y=0\right)}{\sqrt{2K_{dose}G\left(y_G;\Delta\theta_y=0\right)}}\Delta\theta_y = \sqrt{2}\pi\frac{\sqrt{AT_{GR}}}{\sqrt{K_{dose}}}\frac{Vd_{Talbot}}{p_2}\frac{\cos\left(\psi+\frac{2\pi}{p_2}y_G\right)}{\sqrt{1+V\sin\left(\psi+\frac{2\pi}{p_2}y_G\right)}}\Delta\theta_y \tag{7.31}$$

SNR and FOM are now directly proportional to the refraction angle $\Delta\theta_y$, as in the case of ABI. This also implies that, if all the other parameters are unchanged, the SNR is inversely proportional to the square of the energy, i.e. $SNR \propto 1/E^2$. Furthermore, the SNR and FOM are also inversely proportional to $S = p_2 / d_{Talbot}$, which is the angle corresponding to one fringes period. This is not surprising, since, if this angle is reduced, the sensitivity of the method is also expected to be increased. Since in the practice the beam will never be perfectly coherent (but only partially coherent), the visibility V will in general decrease with increasing distances d_{Talbot}. The optimal distance d_{Talbot} is therefore, in general, a function of the degree of coherence of the beam.

The SNR and FOM are dependent, through the function G and its first derivative, on the relative gratings position y_G. Theoretically, the highest values can be achieved when the quantity:

$$f = \frac{\sqrt{1+V\sin\left(\psi+\frac{2\pi}{p_2}y_G\right)}}{\left|\cos\left(\psi+\frac{2\pi}{p_2}y_G\right)\right|} \tag{7.32}$$

is minimized (cf. eqs. 7.30 and 7.31). It is easy to verify that the expression in eq. 7.32 is minimized when

$$\sin\left(\psi+\frac{2\pi}{p_2}y_G\right) = -\frac{1}{V}\left(1-\sqrt{1-V^2}\right) \tag{7.33}$$

and that in this case the function f is equal to:

$$f_{MIN} = \frac{V}{\sqrt{2}}\frac{\sqrt[4]{1-V^2}}{\sqrt{V^2-1+\sqrt{1-V^2}}} \tag{7.34}$$

The maximum obtainable values for SNR and FOM are therefore:

$$SNR_{GIFM,\max} = 2\pi\sqrt{AT_{GR}I_0}\frac{d_{Talbot}}{p_2}\frac{\sqrt{V^2-1+\sqrt{1-V^2}}}{\sqrt[4]{1-V^2}}\Delta\theta_y \tag{7.35}$$

$$FOM_{GIFM,\max} = 2\pi \frac{\sqrt{AT_{GR}}}{\sqrt{K_{dose}}} \frac{d_{Talbot}}{p_2} \frac{\sqrt{V^2 - 1 + \sqrt{1 - V^2}}}{\sqrt[4]{1 - V^2}} \Delta\theta_y \tag{7.36}$$

The progress of the SNR as a function of the relative gratings position y_G is plotted in figure 7.3(b) over one fringes period. As a reference, the corresponding intensity values along the fringes profile are plotted in figure 7.3(a), and the different positions on the curve are indicated. The points $x = 0$ and $x = \pi$ represent the positions in the middle of the positive and negative slopes, respectively, (which correspond to the positions already considered in the CT method presented in chapter 6), while the points $x = -\pi/2$ and $x = +\pi/2$ indicate respectively the bottom and the top of the fringes profile (figure 7.3(a)).

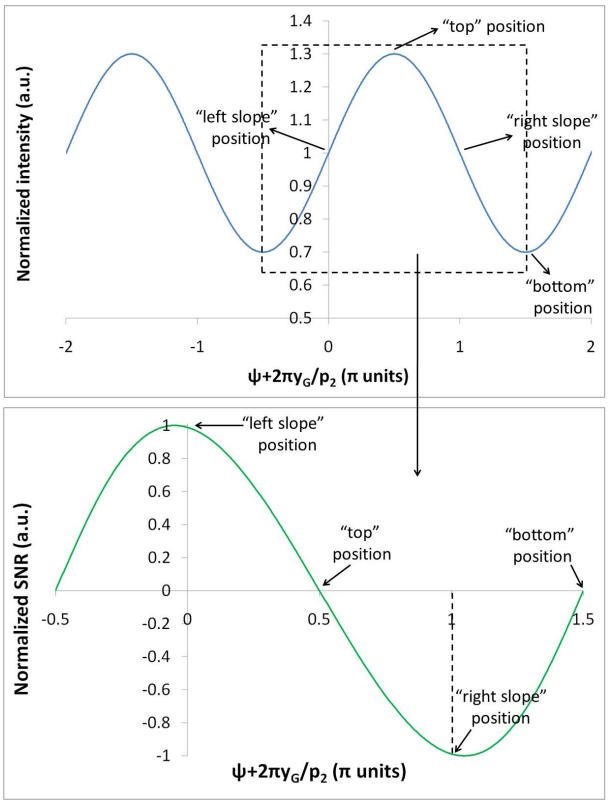

Fig. 7.3. (a) Intensity profile as a function of the gratings relative displacement, for a visibility of 30%, (b) Normalized SNR values calculated by using eq. 7.30 in the range [–π/2, 3/2π] for the quantity $\psi+2\pi y_G/p_2$. The different positions on the fringes profile are indicated.

As it was calculated above, the highest theoretical SNR is achieved at a point that is slightly detuned from the half slope. The positions where the SNR is minimized, instead, are the bottom and the top of the function G. At these positions a linear approximation of the intensity function gives a value of zero for the SNR, because the first derivative of G vanishes. Note however that in this case, since the first derivative is equal to zero and the second derivative is maximized, the following second-order Taylor approximations would yield much more correct estimates compared to the linear approximation:

$$SNR_{GIFM,top\ and\ bottom} \approx \frac{\sqrt{AT_{GR}I_0}G''\left(y_G;\Delta\theta_y=0\right)}{2\sqrt{2G(y_G;\Delta\theta_y=0)}}\left(\Delta\theta_y\right)^2 \tag{7.37}$$

$$FOM_{GIFM,top\ and\ bottom} \approx \frac{\sqrt{AT_{GR}}G''\left(y_G;\Delta\theta_y=0\right)}{2\sqrt{2K_{dose}G(y_G;\Delta\theta_y=0)}}\left(\Delta\theta_y\right)^2 \tag{7.38}$$

It is interesting to remark that in this case the SNR and FOM are not anymore proportional to the refraction angle but to its squared value. We will come back to this point in section 7.4 when we will present the analysis of the experimental images of the test phantoms used in this study.

It is worth pointing out that, similarly to the corresponding expressions for SNR and FOM in the PBI and ABI cases (eqs. 7.11-7.12 and eqs. 7.19-7.20), eqs. 7.30-7.31 were obtained neglecting the effect of a finite imaging system PSF. Since the intensity measured on the detector is given by a convolution between the ideal intensity and the PSF of the imaging system, eqs. 7.30-7.31 can be rewritten more precisely as:

$$SNR_{GIFM,conv} \approx \frac{\sqrt{AT_{GR}I_0}G'\left(y_G;\Delta\theta_y=0\right)}{\sqrt{2G\left(y_G;\Delta\theta_y=0\right)}}\left(\Delta\theta_y * PSF_{GIFM}\right) \tag{7.39}$$

$$FOM_{GIFM,conv} \approx \frac{\sqrt{AT_{GR}}G'\left(y_G;\Delta\theta_y=0\right)}{\sqrt{2K_{dose}G\left(y_G;\Delta\theta_y=0\right)}}\left(\Delta\theta_y * PSF_{GIFM}\right) \tag{7.40}$$

where the point spread function in the case of the GIFM technique can be expressed as $PSF_{GIFM}=\left(2\pi\sigma_{GIFM}^2\right)^{-1}\exp\left[-\left(x^2+y^2\right)/\left(2\sigma_{GIFM}^2\right)\right]$, with $\sigma_{GIFM}=\left(d/L\right)\sigma_{src}^2+\sigma_{det}^2$. The first term, with σ_{src} being the standard deviation of the source intensity distribution, d the sample-to-detector distance and L the source-to-sample distance, represents the effect of blurring due to the finite angular source size; the second term accounts for the finite spatial resolution of the detector σ_{det}.

Finally, let us consider the SNR and FOM related to the absorption signal in the GIFM technique. As for ABI, if the object does not introduce any refraction or scattering onto the beam the recorded image contrast is the same as the one that would be obtained without the gratings. The SNR and FOM are instead reduced, because part of the beam that passes through the object will be absorbed by the gratings before reaching the detector. Furthermore, the beam intensity transmission, and therefore the SNR and FOM, depend also on the considered working point on the fringes period. We can in fact write, for small values of absorption (cf. eqs. 7.8 and 7.9):

$$SNR_{GIFM,abs} \approx \sqrt{T_{GR}G\left(y_G\right)}\frac{\sqrt{AI_0}\left(\int dz\mu_{back}-\int dz\mu_{obj}\right)}{\sqrt{2-\int dz\mu_{obj}-\int dz\mu_{back}}} \tag{7.41}$$

$$FOM_{GIFM,abs} \approx \sqrt{T_{GR} G(y_G)} \frac{\sqrt{A}\left(\int dz\,\mu_{back} - \int dz\,\mu_{obj}\right)}{\sqrt{K_{dose}\left(2 - \int dz\,\mu_{obj} - \int dz\,\mu_{back}\right)}} \tag{7.42}$$

7.2.5 Sensitivity in PBI, ABI and GIFM

In this section, by using the expressions obtained above for the signal-to-noise ratio, we want to briefly compare the sensitivity in the three phase-contrast techniques considered in this work: PBI, ABI and GIFM.

As it was seen (eq. 7.11), the SNR in PBI is, at a first approximation (for small propagation distances and small beam curvature), proportional to the Laplacian of the phase (or, more correctly, to the difference between the values of the Laplacian of the phase at the two sides of the object/detail edge). In ABI and GIFM, instead, the SNR is at first approximation (for small refraction angles) proportional to the component of the refraction angle on the diffraction plane (for ABI) and on the plane perpendicular to the grating lines (for GIFM). The signal in the images acquired with the ABI and GIFM techniques is therefore sensitive to a different physical quantity compared to that obtained with PBI (although the two quantities, the Laplacian of the phase and the one-directional phase derivative, are interconnected). A very well-known advantage of PBI deriving from the above signal dependency is that this technique is sensitive to phase perturbations in the two directions, while ABI and GIFM are one-dimensional. This means that, in the latter techniques, phase variations perpendicular to the refraction sensitivity direction do not in principle produce any detectable signal. Another relevant difference is that, since PBI signal depends on the Laplacian of the phase and not on its first derivative, this technique is more sensitive to high object frequencies, while ABI and GIFM are more sensitive to lower frequencies, as shown by Pagot et al. (Pagot et al., 2005).

As we have already mentioned in chapter 2, the contribution of "inline" phase-contrast is often observable in images acquired with the ABI and GIFM techniques, because of the finite sample-detector distance. Rather than being considered an artefact, this additional contrast mechanism can also be accentuated by deliberately increasing the propagation distance in both ABI and GIFM setups, in order to improve the image contrast. Theoretical and experimental analysis of the signal in the combined PBI-ABI technique can be found in the works of Pavlov et al (Pavlov et al., 2004, Pavlov et al., 2005), Coan et al. (Coan et al., 2005) and Nesterets et al. (Nesterets et al., 2005).

We will turn now to a quantitative comparison of the sensitivity in ABI and GIFM techniques, and in particular to the estimation of the smallest refraction angle detectable by the two techniques. Let us consider an object detail providing negligible absorption and very low refraction signal. Under these assumptions, it is possible to use eqs. 7.19 and 7.30 for describing the SNR. Similarly to the case of conventional absorption imaging, the object detail will be visible if the value of the SNR associated to it will be large enough (in modulus) to allow distinguishing the detail from the background. We can thus write, for instance in the case of ABI:

$$\left|SNR\right| = \frac{\sqrt{AI_0}}{\sqrt{2}} \frac{\left|R'\left(\theta_{AN}\right)\right|}{\sqrt{R\left(\theta_{AN}\right)}} \left|\Delta\theta_y\right| \geq K_{SNR} \tag{7.43}$$

where K_{SNR} is an arbitrary threshold. By inverting eq. 7.43, we obtain:

$$\left|\Delta\theta_y\right| \geq \left(\Delta\theta_y\right)_{MIN,ABI} = \frac{\sqrt{2}K_{SNR}}{\sqrt{AI_0}} \frac{\sqrt{R\left(\theta_{AN}\right)}}{\left|R'\left(\theta_{AN}\right)\right|} \tag{7.44}$$

The absolute value of the refraction angle has to be larger than a certain minimum value in order for the detail to be visible. Note that this minimum value is not fixed for a given setup but is inversely proportional to the square root of the beam intensity incident onto the object. This is not surprising since the image noise is directly related to the number of photon counts. For a fixed photon flux, when the exposure time is increased smaller features in the object will therefore become visible.

Analogously, for GIFM we obtain:

$$\left|\Delta\theta_y\right| \geq \left(\Delta\theta_y\right)_{MIN,GIFM} = \frac{\sqrt{2}K_{SNR}}{\sqrt{AT_{GR}I_0}} \frac{\sqrt{G\left(y_G;\Delta\theta_y=0\right)}}{\left|G'\left(y_G;\Delta\theta_y=0\right)\right|} \tag{7.45}$$

If we now consider the same detail in the ABI and GIFM techniques, and we assume the intensity of the beam incident onto the object to be the same in the two cases, in order to deliver the same radiation dose to the sample, the ratio of the smallest detectable refraction angles in GIFM and ABI is given by:

$$\frac{\left(\Delta\theta_y\right)_{MIN,GIFM}}{\left(\Delta\theta_y\right)_{MIN,ABI}} = \frac{\sqrt{G\left(y_G;\Delta\theta_y=0\right)}}{\sqrt{T_{GR}}\left|G'\left(y_G;\Delta\theta_y=0\right)\right|} \frac{\left|R'\left(\theta_{AN}\right)\right|}{\sqrt{R\left(\theta_{AN}\right)}} \tag{7.46}$$

for a generic working point respectively on the intensity function G and on the rocking curve. By considering only the positions where the sensitivity is maximized in each of the two techniques, we can write (cf. eq. 7.35):

$$\frac{\left(\Delta\theta_y\right)_{MIN,GIFM}}{\left(\Delta\theta_y\right)_{MIN,ABI}} = \frac{1}{2\sqrt{2}\pi\sqrt{T_{GR}}} \frac{p_2}{d_{Talbot}} \frac{\sqrt[4]{1-V^2}}{\sqrt{V^2-1+\sqrt{1-V^2}}} \frac{\left|R'\left(\theta_{AN,MAX}\right)\right|}{\sqrt{R\left(\theta_{AN,MAX}\right)}} \tag{7.47}$$

where $\theta_{AN,MAX}$ indicates the analyzer position corresponding to the highest value of the SNR. In section 7.3, where we will present the experimental setups, we will calculate the ratio of the smallest detectable refraction angles in GIFM and ABI techniques for the parameters used in our experimental implementation. We only mention here the fact that this ratio depends on the particular used parameters. Among others, important parameters are: the energy, the crystals material and chosen reflection in ABI, the energy, the visibility, the period of the second grating

and the Talbot distance in GIFM. In particular, it is interesting to remark that, since in ABI the first derivative of the RC is proportional to the energy (see section 7.2.3), the ABI technique is favoured with respect to GIFM when the energy is increased (cf. eq. 7.47).

In analogy to the approach that we have adopted for ABI and GIFM, we can write in the case of PBI the smallest value for the Laplacian of the phase that can be detected for a particular setup configuration and beam intensity:

$$\left|\nabla^2_{\max}\phi - \nabla^2_{\min}\phi\right| \geq \frac{2\sqrt{2}\pi}{\lambda D\sqrt{AI_0}} K_{SNR} \tag{7.48}$$

In this case the most relevant parameters to be considered are the propagation distance and the energy.

7.3 Experimental methods

The experimental verification was carried out at the BM5 beamline. X-rays with an energy of 26 keV (energy resolution $\Delta E/E \approx 10^{-4}$) were selected with the fixed-exit Bragg-Bragg double-crystal monochromator. The three different setups required by PBI, ABI and GIFM techniques were mounted in turn, in order to image the same test objects in similar acquisition conditions. In all cases the images were recorded with the Frelon CCD camera. The effective pixel size at the sample position was about 7.5 μm.

The considered test objects have been already described in chapter 4. The first phantom consisted of two horizontal nylon wires with diameters of 200 μm and 350 μm, respectively, and of a vertical nylon wire with a diameter of 350 μm. The values of the real and imaginary parts of the complex refractive index for nylon at 26 keV are: $\delta = 3.50 \times 10^{-7}$; $\beta = 1.29 \times 10^{-10}$. The beam attenuation at the centre of the two types of wires is therefore very low, respectively 0.7% and 1.2%, while the corresponding phase shifts are respectively 9.2 rad and 16.1 rad.

The second phantom was a Lucite parallelepiped of section 40 × 40 mm^2 and thickness 2.9 mm, in which five almost cylindrically shaped grooves (holes) of different radius are made. The section of the holes can be well approximated by a part of circumference. Only the smallest groove (300 μm deep and 825 μm wide) has been considered: like the polymer wires, this groove produces very low absorption contrast (1.1%) but a phase shift of 15.6 rad with respect to the full thickness of the Lucite parallelepiped. The refraction angles at the groove edges are instead smaller than in the case of the wires, since in this case the object thickness varies more slowly at the edges. The phantom was imaged with the grooves oriented in the horizontal direction.

In the case of PBI, three sample-detector distances were considered: 7 cm (almost pure absorption), 57 cm, 150 cm. When acquiring images with the ABI and GIFM techniques, the distance between the sample and the detector was set to 57 cm. Ideally, in order to avoid the contribution from “inline” phase-contrast, the propagation distance should be zero. However, this

is not possible due to ABI and GIFM setups constraints. The propagation distance was chosen to be the same in the two methods in order to work with similar acquisition conditions.

In ABI, two Si(333) crystals were employed respectively to further monochromatize the incoming beam and to analyze the beam exiting the object. The rotation axis of the crystals was perpendicular to both the optic axis and the vertical direction (see figure 5.1). The phantoms were imaged at the following positions of the analyzer along the RC: ±15%, ±50% and top positions for the nylon wires, ±15%, ±50% and +90% positions for the groove.

In the GIFM acquisitions, a silicon π-shifting grating (G_1), with period p_1=3.99 μm and thickness t_1=34 μm, and a gold absorption grating (G_2) with period p_2=2.00 μm were used. The exact thickness of the gold lines in G_2 is not known, but it can be safely assumed that it corresponds to an absorption of at least 90% for 26 keV X-rays. The two gratings were set with their lines oriented horizontally, so that the refraction sensitivity direction is vertical like in the case of ABI. The average intensity transmission through both gratings was calculated theoretically to be about 50%. G_1 and G_2 were set at a mutual distance of 125 mm (3rd fractional Talbot distance for X-rays of 26 keV). The periods p_1 and p_2 (designed in order to account for the beam divergence), together with the distance from the source (~50 m) dictate in fact a spacing between the gratings of about 125 mm. The measured fringes visibility was 34% in these experimental conditions. Phase-stepping acquisitions were performed by considering 9 equispaced gratings positions along one fringe period.

In these experimental conditions, the theoretically estimated ratio between the smallest detectable refraction angles in GIFM and ABI is, according to equation 7.47, $\left(\Delta\theta_y\right)_{GIFM,MIN} \Big/ \left(\Delta\theta_y\right)_{ABI,MIN} = 9.0$. This means that, with the considered setup, the highest theoretical sensitivity to small refraction angles achieved in ABI is 9 times that obtainable in GIFM, for the same dose delivered to the sample. It is important to remark that a more similar value for the two sensitivities would be obtained by using in ABI a Si(111) reflection for both the second monochromator and the analyzer. The theoretical ratio between the smallest detectable refraction angles in GIFM and ABI would in fact be, in this case, $\left(\Delta\theta_y\right)_{GIFM,MIN} \Big/ \left(\Delta\theta_y\right)_{ABI,MIN} = 2.6$. Rather than trying to achieve the most similar sensitivities in the two techniques, we optimized each of them in order to have the largest sensitivity obtainable with the available X-rays source.

The dose estimation was performed by using a calibrated ionization chamber (PTW semiflex 31002, PTW Freiburg, Germany) that is scanned through the X-ray beam. The measured values for the skin dose in air are reported in table 7.1 for the various acquisitions.

	Measured skin dose in air (mGy)									
	PBI			ABI						GIFM
	7 cm	57 cm	150 cm	-15%	-50%	top	+90%	+50%	+15%	
Nylon wires	93.6	49.7	73.1	62.5	36.8	26.4		37.2	80.2	183.0
Groove #1	89.6	56.3	72.5	76.6	35.6		25.6	39.5	76.6	79.6

Table 7.1. Measured values of the skin dose rate in air for the images acquisition.

7.4 Results and discussion

7.4.1 Experimental images

All the acquired raw images have been normalized by using the corresponding whitefield and darkfield images. Expanded views of the horizontal 350 μm diameter wire and of the small groove in small regions of interest are reported in figure 7.4 in the case of PBI, for the three considered sample-detector distances. The chosen grayscale is the same for the three distances, but is different for the two considered objects. The images of the 200 μm diameter wire have been omitted since they are very similar to those obtained for the bigger wire.

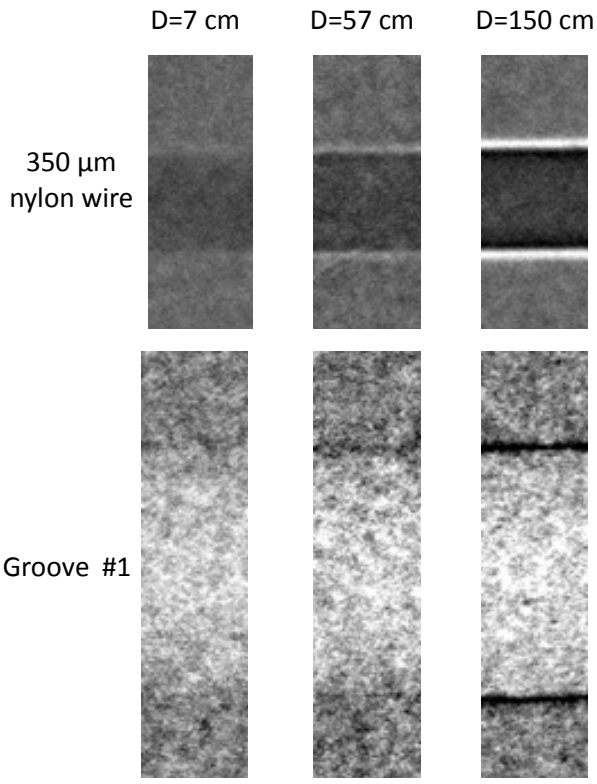

Fig. 7.4. Acquired PB images at three different sample-detector distances: expanded views in small regions of interest in the 350 μm diameter nylon wire and in the small groove.

When the propagation distance increases, the visualization of the object is improved because the magnitude of the interference fringes becomes higher. This is in agreement with what predicted by theory (eq. 7.10) in the case of propagation distances that are sufficiently small to assume near-field diffraction regime. Interestingly, if we compare the two objects, we see that not only the absorption contrast is reversed for the wire and for the groove, but also the resulting phase contrast. The edges show in fact positive (white) or negative (black) signal according to the negative or positive values of the Laplacian of the phase at these points (cf. eqs. 7.10-7.11).

In order to quantitatively estimate the signal produced by the object edges in the different images, we calculated the signal to noise ratio following the definition provided in chapter 3 for an edge signal (eq. 3.6). The maximum and minimum values for the intensity at the edges were calculated, by averaging each of them over a region A of 30 horizontal pixels. The average of several values of the background intensity, each one being the mean of the pixel counts over a different area A, and the related standard deviation, were also computed. Repeated calculations of the SNR based on eq. 3.6 were done in different regions of the image: the estimate for the SNR was obtained from the average of these values while the associated uncertainty was obtained from their standard deviation. Finally, the corresponding FOM was calculated by using the measured skin doses in air reported in table 7.1.

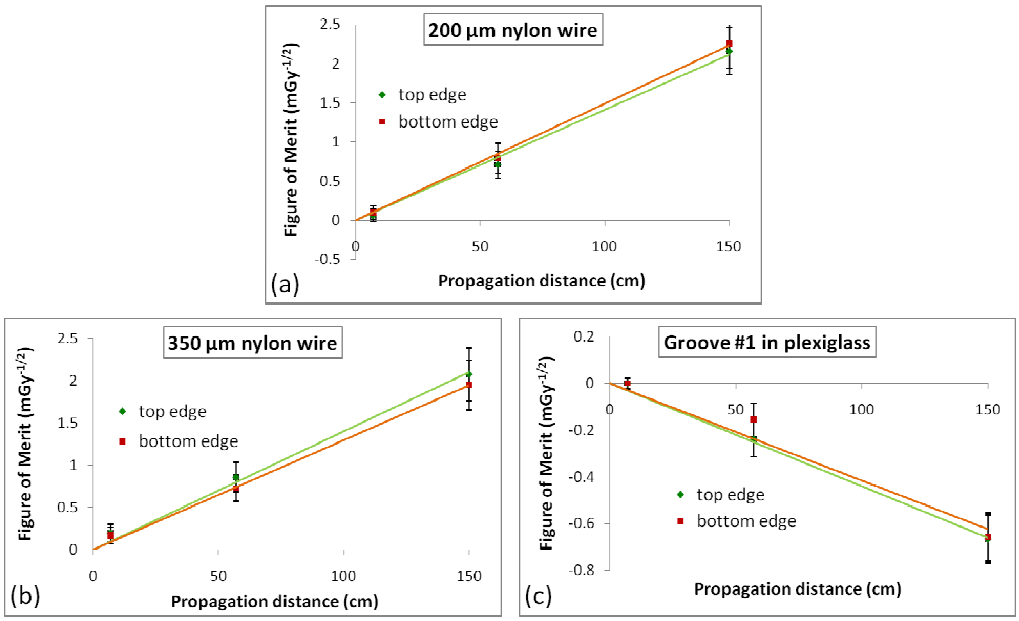

Fig. 7.5. Calculated values of the figure of merit (FOM) of the PBI edge signal for three different objects: (a) the 200 µm diameter nylon wire, (b) the 350 µm diameter nylon wire, (c) the small groove (groove #1). Both values at the top and bottom edges are reported.

Results are plot in figure 7.5(a,b,c), for the top and bottom edges of the 200 µm diameter wire (fig. 7.5(a)), of the 350 µm diameter wire (fig. 7.5(b)) and of the small groove (fig. 7.5(c)). We can see that the increase in the FOM with the propagation distance is linear for all the considered objects, in agreement with eq. 7.12 for the FOM, which was derived under the assumption of near-

field diffraction regime. In the case of the groove the FOM assumes negative values, since the edge signals are negative. The largest FOM values in modulus are observed for the thinnest wire, while the smallest values are obtained for the groove.

Images of the same test objects acquired with the ABI technique are presented in figure 7.6, for five different positions of the analyzer along the rocking curve. The grayscale level has been adjusted independently for each of the images in order to optimize the objects visualization. All images, with exception of the "top position" one, show opposite contrast at the two edges since, unlike in the PBI technique, the signal is at first approximation proportional to the refraction angle, which has opposite signs at the two edges. At the "top position", instead, as we have seen (eq. 7.21), the signal is proportional to the square of the refraction angle, which has the same value at the two object sides. The X-rays undergoing refraction at the two edges of the object are therefore attenuated in the same way by the analyzer, as expected. The refraction contrast is also reversed when the considered side of the rocking curve is changed, since its first derivatives have opposite signs, and in the two different objects, since the X-rays are refracted in opposite directions.

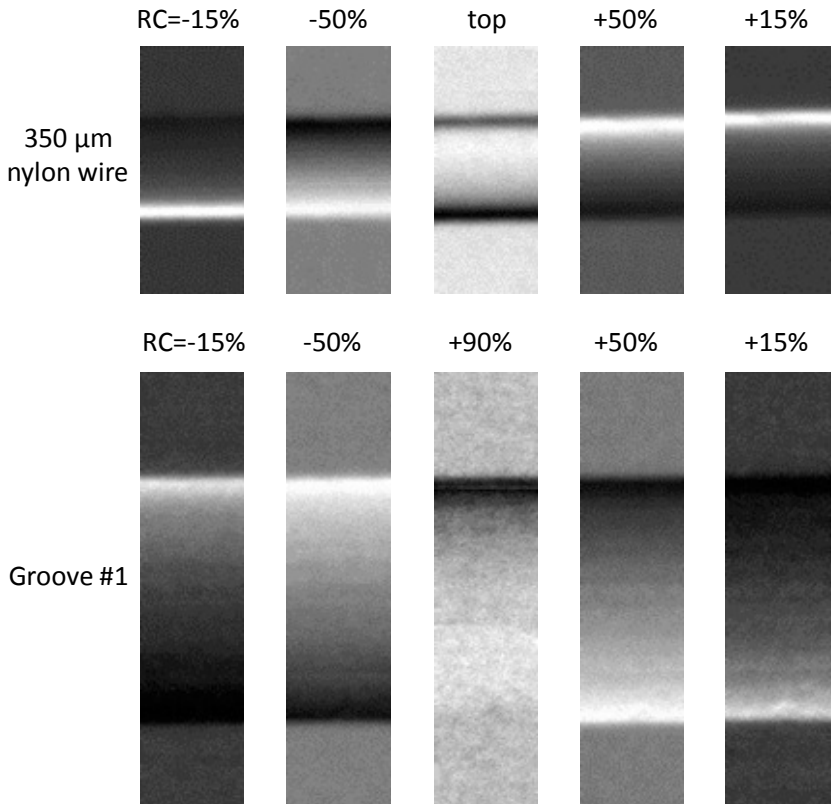

Fig. 7.6. Acquired AB images at 5 different orientations of the analyzer crystal: expanded views in small regions of interest in the 350 µm diameter nylon wire and in the small groove.

In ABI, contrary to the case of PBI, we see that the objects absorption can hardly be evaluated from the raw unprocessed images, since the refraction signal is both very strong and more extended compared to that obtained in PBI. This is directly related to the signal dependence on the

first derivative of the phase (different from zero almost everywhere in the considered objects) rather than on the Laplacian of the phase (which has large values only on the very edges).

The calculation of the FOM was carried out like in the case of PBI for the 200 µm and 350 µm wires and the small groove, and for both the bottom and top objects edges (figure 7.7). The results for the three objects are very similar, apart from the fact that the sign of the FOM values is reversed in the case of the groove, since the refraction angles have opposite directions. In all the three cases the highest FOM is achieved at the two positive and negative RC slopes, in agreement with what foreseen by the theory (cf. eq. 7.20 and fig. 7.2(c)). The values are instead minimized at the top position and at the tails of the RC, where the RC first derivative is small. Note that the positive values of the FOM are in general slightly larger in modulus than the negative ones, differently from what foreseen theoretically. This effect can be attributed to the fact that, when the refraction angles are large, like at the edges of the considered objects, the linear approximation of the RC is not very accurate. In this case, in fact, the variations in the intensity for positive or negative displacements on the RC are not the same, but are bigger when moving to angles corresponding to larger values on the RC.

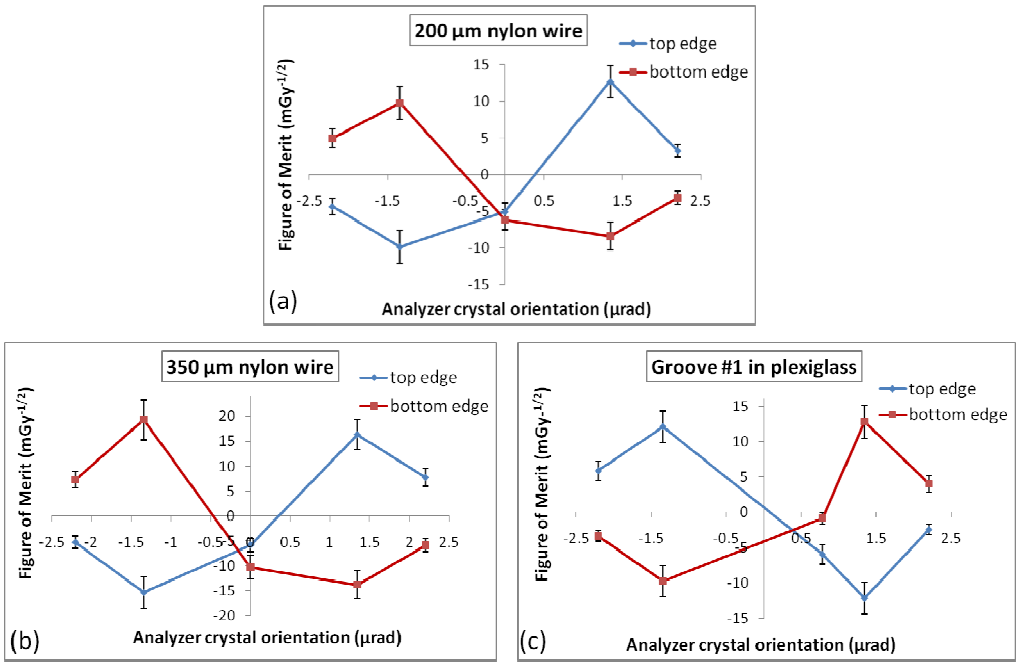

Fig. 7.7 Calculated values of the figure of merit (FOM) of the ABI edge signal for three different objects: (a) the 200 µm diameter nylon wire, (b) the 350 µm diameter nylon wire, (c) the small groove (groove #1). Both values at the top and bottom edges are reported.

Differently from the results obtained in PBI, where the largest FOM was obtained for the 200 µm nylon wire, in ABI the FOM shows the highest values in the case of the 350 µm nylon wire, while smaller values are obtained for the thinner wire and for the groove. This underlines the fact, already mentioned, that the two methods are sensitive in a different way to different object frequencies, and in particular that the PBI technique reaches its highest sensitivity for higher

frequencies than ABI does. We also remark that, as it is already evident from the images, the FOM provided by ABI is in all cases considerably larger than the one obtained in PBI.

The images of the horizontal 350 μm nylon wire and of the groove acquired with the GIFM technique are reported in figure 7.8, for various relative positions of the gratings along one fringe period. The grayscale level has been adjusted independently for each image in order to optimize the objects visualization. Note that, for each of the two presented objects, the first and the last image have been recorded at exactly one period displacement (p_2=1.92 μm) and, as foreseen, no difference can be observed between them. The 9 images show a variety of different contrasts, depending on the corresponding position on the intensity curve G and in particular on the first and second derivatives of G. Images similar to those obtained at the RC slopes with the ABI technique can be observed (x_G=0.24 μm and x_G=1.2 μm for the nylon wire and x_G= 0.72 μm and x_G=1.68 μm for the groove) at positions corresponding to the slopes of the intensity function G (figure 7.3(a)). Like for ABI, also in this case the contrast is reversed when moving from one slope to the other one since the first derivative of G has opposite signs at these points. Images acquired at the "top position" of the function G (figure 7.3(a)) show a contrast similar to that obtained at the "top position" of the RC (images at x_G=0.72 μm and x_G=0.96 μm for the nylon wire and the image at x_G= 0.24 μm for the groove), since in this case the refracted X-rays are preferentially attenuated with respect to those that were not deviated. Interestingly, in the case of GIFM an image showing a new kind of contrast compared to ABI is obtained, corresponding to the "bottom position" on the intensity function G (for instance, image at x_G=1.68 μm for the nylon wire). In this case the X-rays refracted in both directions give rise to positive intensity variations in the image compared to the undeviated X-rays, as foreseen from the intensity curve in figure 7.3(a). The "bottom position" image is also visible in the case of the groove (x_G=1.2 μm) but the white GIFM refraction signal is here superposed to the black "inline" contrast due to the finite sample-detector distance. Note that the various positions on the fringe period are shifted for the groove with respect to the wire because of a long term drift of the gratings and because the two series of images were acquired at different times (Δt ~ few hours).

Also in the case of GIFM the calculation of the FOM was performed for the 200 μm and 350 μm wires and the small groove, and for both the bottom and top objects edges. The results are presented in figure 7.9. The experimental FOM profiles resemble those obtained theoretically by using a linear approximation for the intensity function G (see eq. 7.31 and figure 7.3(b)). Unlike in the theoretical case, however, the experimental FOM values never go to zero because at both the "top" and "bottom" positions, where the first derivative of the function G vanishes, the linear approximation is inaccurate. In this case the equation for the FOM derived from a second-order Taylor expansion of the intensity function (eq. 7.38) is expected to provide a better estimate.

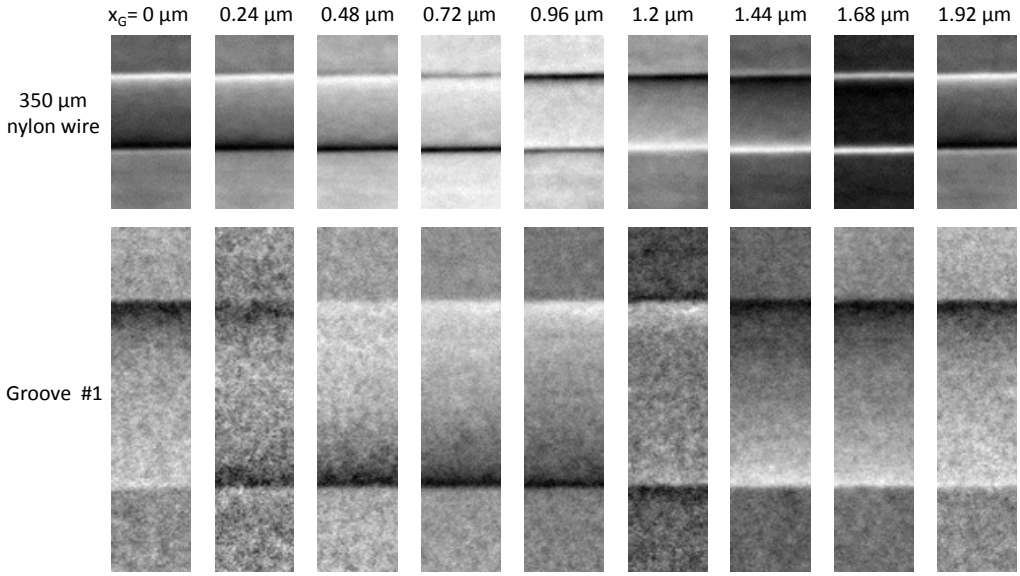

Fig. 7.8. Acquired GIFM images at 9 different relative positions of the two gratings along one fringe period: expanded views in small regions of interest in the 350 µm diameter nylon wire and in the small groove.

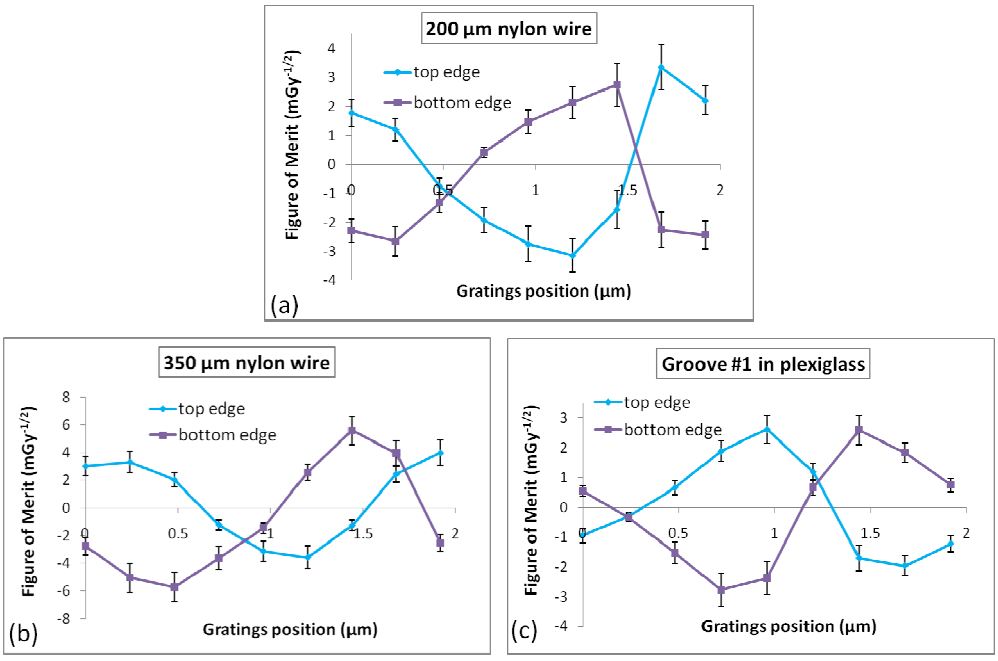

Fig. 7.9. Calculated values of the figure of merit (FOM) of the GIFM edge signal for three different objects: (a) the 200 µm diameter nylon wire, (b) the 350 µm diameter nylon wire, (c) the small groove (groove #1). Both values at the top and bottom edges are reported.

Like in the ABI case, the largest FOM values are obtained for the thickest wire, while the thinner wire and the groove provide smaller values. This is not surprising since the two techniques are expected to be sensitive to the same physical quantity (the one-directional first derivative of the phase shift, at a first approximation) contrary to the PBI technique (which is sensitive at a first approximation to the Laplacian of the phase). Therefore the objects that give the largest signals for

ABI are expected to provide the largest signals also for GIFM. By comparing the amplitude of the FOM values in the different techniques, we see that the values computed in GIFM are larger than those obtained from PB images but 3 to 5 times smaller than those obtained in ABI. By using eq. 7.47, we had previously calculated (see section 7.3) the maximum sensitivity to small refraction angles to be theoretically 9 times larger in ABI than in GIFM in our experimental conditions. The values obtained in the two techniques, instead, present lower differences. This can be attributed to two reasons: 1) the refraction angles at the edges of the considered objects are not small, thus the linear approximations of the RC and of the function G used to derive eq. 7.47 are not completely accurate in this case; 2) the images, especially the AB ones, have not been acquired at exactly the points of highest theoretical sensitivity, and, as we saw (fig. 7.2(c)), the curve of the theoretical ABI sensitivity is rather steep close to the maximum position.

As discussed in section 7.2, it is important to remark that the obtained results are also dependent, especially in the case of PBI, on the beam spatial coherence and on the spatial resolution of the used detector. The measured intensity can in fact be expressed as a convolution between the ideal intensity and the imaging system PSF (see eqs. 7.11, 7.19 and 7.39 respectively for the PBI, ABI and GIFM techniques). This smoothing due to the PSF is expected to affect the PBI signal to a higher degree with respect to the ABI and GIFM ones for two main reasons: a) the PBI edge signal, due its dependence upon the phase Laplacian, is narrower and b) the contiguous positive and negative peaks present in PBI tend to cancel each others (while this effect is not encountered in ABI and GIFM, where only one isolated peak is present). This means for example that, if a smaller pixel size had been used, the SNR values in the case of PBI could have been much higher, while this would have presumably affected ABI and GIFM to a much lesser degree.

The images of the vertical 350 μm wire are reported in figure 7.10. In the case of PBI the images at the three propagation distances, respectively 7 cm (fig. 7.10(a)), 57 cm (fig. 7.10(b)) and 150 cm (fig. 7.10(c)), are presented. In the cases of ABI and GIFM, only the images respectively at the -50% slope position on the RC (fig. 7.10(d)) and at x_G=0 μm (fig. 7.10(e)) are reported. The sample-detector distance was equal to 57 cm in this case. The grayscale level has been adjusted in the same way for all the shown images.

Since the wire edges are now parallel to the refraction sensitivity direction for both ABI and GIFM, the typical refraction contrast obtained in figs. 7.6 and 7.8 is not observed here for the images acquired with these two techniques (figs. 7.10(d,e)). The signal is instead determined by both the wire absorption and the "inline" phase-contrast due to the propagation distance between the sample and the detector. The PB images appear very similar to those obtained with the horizontal wire, because this technique is sensitive to phase variations in both directions (note that the signals in the two directions do not have necessarily the same amplitude because of the possible differences in the spatial coherence in the two directions, determining a different fringe visibility). The ABI and GIFM images (figs. 7.10(d,e)) and the PB image acquired at a distance of 57 cm (fig. 7.10(b)) look similar, as expected. The noise contribution, however, is not the same in the different cases because of two main reasons: 1) the doses used for the images acquisition are

different (see table 7.1); 2) the beam is attenuated after the sample by the presence of the analyzer (in ABI) and of the two gratings (in GIFM): the counts are therefore decreased and the noise relative contribution increased. Note that this second effect has been considered in eqs. 7.25 and 7.41 for the theoretical estimation of the absorption signal-to-noise ratio respectively in ABI and GIFM.

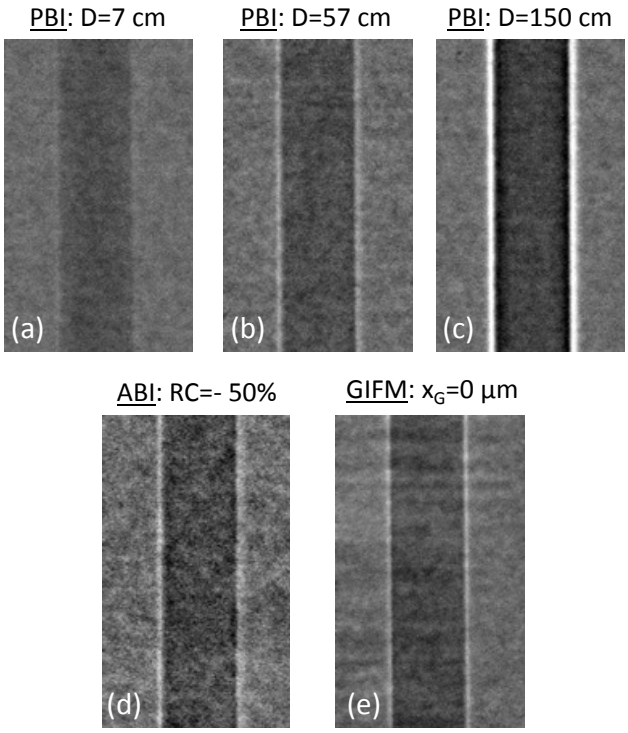

Fig. 7.10. Expanded views of experimental images of the vertical 350 µm diameter nylon wire: PB images at sample-detector distances of 7 cm (a), 57 cm (b) and 150 cm (c), AB image at -50% position along the RC (d), GIFM image at x_G = 0 µm (e). AB and GIFM images have been acquired at a sample-detector distance of 57 cm. The grayscale level has been adjusted in the same way for the various images.

The profiles across the vertical wire images acquired with the PBI, ABI and GIFM techniques at a 57 cm sample-detector distance (figs 7.10(b,d,e)) are plotted in figure 7.11. The shown profiles have been averaged over 40 vertical pixels in order to reduce the importance of the statistical noise. It is possible to see from figure 7.11 that both the wire absorption and the edge signals are very similar in the images acquired with the three techniques at the same propagation distance. These results indicate that the propagation-based signal in the direction perpendicular to the refraction sensitivity direction in ABI and GIFM is not affected by the presence of the optical elements (the analyzer crystal and the diffraction gratings), at least in these experimental conditions. This result is important because it experimentally proves that free propagation of the beam after the sample can be effectively used in the ABI and GIFM techniques to increase the image signal in the direction to which the analyzer crystal and the diffraction gratings are not sensitive.

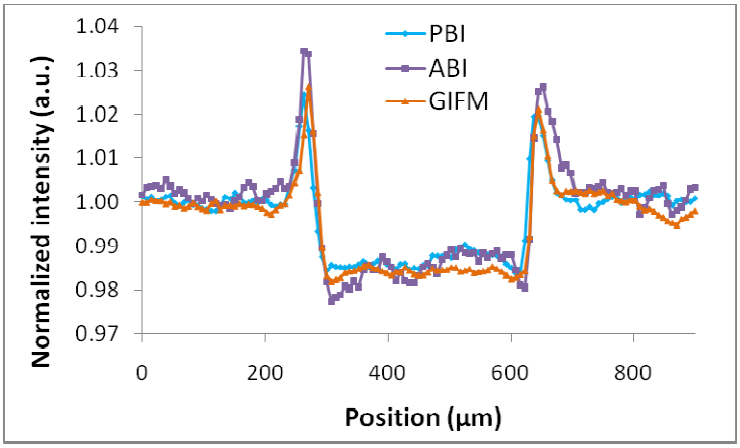

Fig. 7.11. Horizontal profiles across the images in figs. 7.10(b,d,e), acquired at a sample-detector distance of 57 cm. The presented profiles have been averaged over 40 lines in order to reduce the contribution of statistical noise.

7.4.2 Extraction of quantitative images

Extraction algorithms have been applied to the images obtained with the PBI, ABI and GIFM techniques in order to separate the different physical contributions to the contrast. In the case of PBI, the mixed transfer function and transport of intensity (mixed CTF-TIE) approach, described in chapter 2 (section 2.4.2), has been used, in conjunction with the homogeneity prior regularization method (Langer et al., 2010). For ABI, the Gaussian-curve fitting (GCF) method was chosen, since it was proven in chapter 4 to provide the most accurate results in many different experimental conditions. The so-called phase stepping method was used for the processing of GIFM images.

The resulting images are presented in figures 7.12 and 7.13, respectively for the 350 μm nylon wire and for the small groove in plexiglass. The grayscale has been adjusted independently for each image in order to optimize the visualization of the considered details. By using the GCF algorithm in ABI and the phase-stepping method in GIFM, images depicting the absorption, the refraction and the ultrasmall-angle (USAXS) contributions can be directly extracted. Maps of the object phase shift can be in turn calculated from the refraction images, as we saw in chapter 4, by using the "pure integration", the "averaged integration" or the "constrained least-squares" (CLS) methods. The CLS algorithm (with a value for the regularization parameter of $\gamma=10^{-5}$) was employed for the calculation of the ABI and GIFM phase images presented in figures 7.12 and 7.13. In the case of the PBI technique, the phase image is instead directly extracted, while the USAXS map cannot be computed. The absorption image does not need to be calculated for this technique because the experimental image acquired at a propagation distance of 7 cm already represents an image of the sample absorption. The phase contrast contribution is in fact almost negligible when the detector is placed so close to the sample.

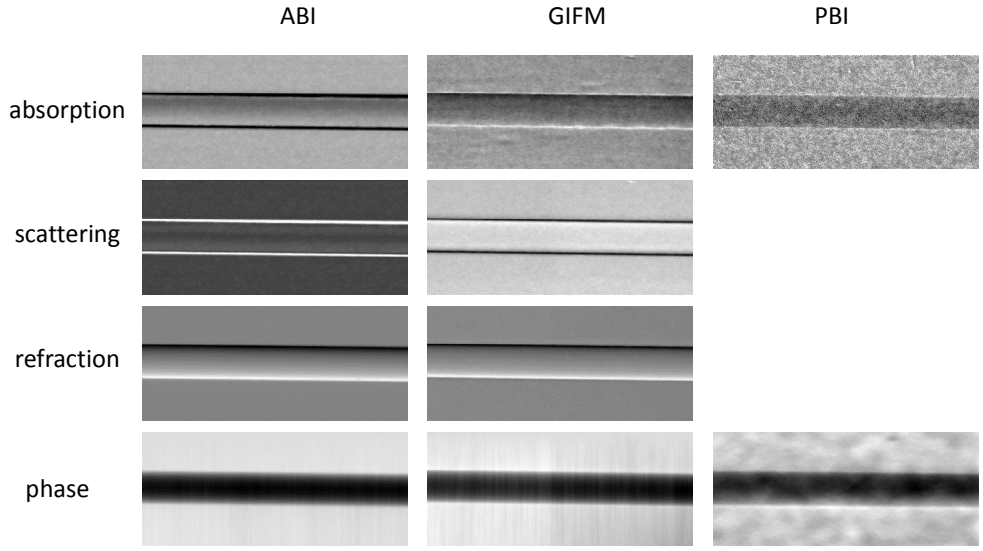

Fig. 7.12. Absorption, ultrasmall-angle scattering (USAXS), refraction and phase images extracted for the 350 µm nylon wire in the ABI, GIFM and PBI techniques. The Gaussian curve fitting (GCF) extraction algorithm is used in ABI, the phase stepping in GIFM, the CTF-TIE mixed algorithm with the homogeneity prior regularization in PBI. In this last case, the showed absorption image is the image acquired for a propagation distance of 7 cm.

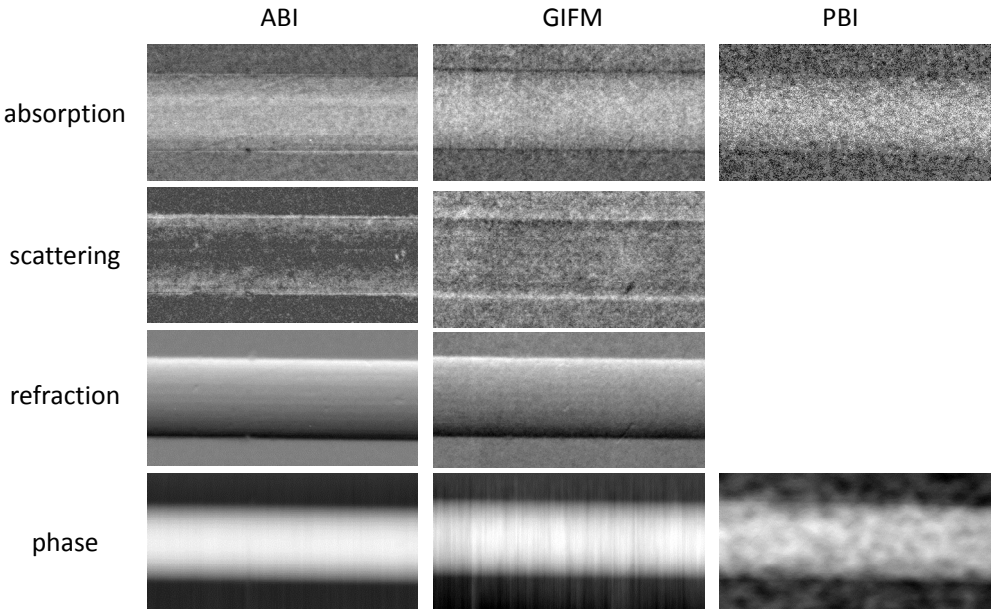

Fig. 7.13. Absorption, ultrasmall-angle scattering (USAXS), refraction and phase images extracted for the small groove in plexiglass in the ABI, GIFM and PBI techniques. The Gaussian curve fitting (GCF) extraction algorithm is used in ABI, the phase stepping in GIFM, the CTF-TIE mixed algorithm with the homogeneity prior regularization in PBI. In this last case, the showed absorption image is the image acquired for a propagation distance of 7 cm.

In the absorption images obtained with the different techniques, the wire (fig. 7.12) appears darker than the background because the beam is (very slightly) attenuated, while the groove (fig. 7.13) is brighter because it corresponds to a slightly reduced thickness inside the plexiglass phantom. Furthermore, the ABI and GIFM images show strong edge signals, especially in the case

of the nylon wire, which can be related to contamination effects arising from the considerable amount of refraction at these positions. In GIFM the observed signal can be attributed to propagation-based contrast. The sample-detector distance is in fact non-negligible and the signal introduced by free-space propagation is not accounted for by the phase stepping separation method. As a result, the GIFM absorption images show a contrast similar to the PBI images reported in figure 7.4. The wire absorption image computed in ABI, instead, presents an opposite edge contrast compared to the previous case. This effect, already discussed in chapters 4 and 5, can be attributed to the violation of the geometrical optics approximation, on which the GCF extraction algorithm is based. At the objects edges, in fact, especially in the case of the nylon wire, the phase gradients are very large and are rapidly varying, and therefore the conditions for the geometrical optics approximation are not fulfilled. An asymmetry of the absorption signal inside the wire is also visible in ABI and GIFM images. A possible explanation for this effect is refraction contamination arising from the uncertainty on the effective positions of the analyzer (in ABI) and of the gratings (in GIFM). It has to be noted that all the discussed artefacts are strongly enhanced by the fact that the absorption signal is very small and the refraction signal is very large.

The signal in the ABI USAXS images is very intense (bright) at the objects edges, especially in the case of the wire (fig. 7.12). As already discussed in chapters 4 and 5, this effect can be attributed to the rapid variations of the refraction angles at these positions. For this reason X-rays refracted at relatively different angles can fall within a single pixel. The scattering GIFM images obtained for the nylon wire are characterized by dark edges (fig. 7.13). In this case, in fact, the same effect described above produces a decrease in the visibility, since each pixel of the edge is not characterized by a definite refraction angle but by a relatively broad angular distribution. The different edge signals of the groove scattering image could be attributed to either a non-accounted effect of the free-space propagation, or to an uncertainty in the gratings positions.

The signal in the ABI and GIFM refraction images is qualitatively very similar, but the noise contribution appears higher for GIFM. As a result, in the computed phase images the typical integration streak artefacts are more evident in GIFM compared to ABI. A comparison with the phase images calculated with the PBI technique shows that a different kind of noise appears in this case, due to the completely different processing method used for obtaining the phase image (including the fact that in this case the phase contrast signal is not unidirectional like in the previous case). It is important to remark that the amplitude of the artefacts in the phase images is related, in the case of the ABI and GIFM techniques, to the signal-to-noise ratio of the refraction images, and in the case of PBI to the signal-to-noise ratio of the raw acquired images.

The profiles of the ABI and GIFM refraction angle images are presented in figures 7.14(a,b,c) for the 200 μm wire, the 350 μm wire and the groove, respectively. The values have been calculated by averaging 50 horizontal pixels in order to reduce the noise. Simulated refraction curves are also reported. Theoretical refraction angle profiles were calculated by considering the values of δ for nylon (in the case of the wires) and for plexiglass (in the case of the groove) at 26 keV, and the estimated thickness of the sample at each point of the image. The wires were

modeled as cylinders while the groove was modeled as a part of cylinder. The so-computed theoretical values were then convolved with Gaussian functions of different widths, in order to simulate the loss in resolution due to the real detector and optics. The simulated curves that best fit the GIFM profiles in figures 7.14(a,b) are those obtained by assuming an 11 µm spatial resolution. This result is very reasonable and can be explained by the finite resolution of the detector, which is expected to be slightly larger than the 7.5 µm pixel size (Coan et al., 2006). The ABI profiles in figures 7.4(a,b) are instead much broader, leading to an estimated spatial resolution of about 17-19 µm. In this case the resolution is in fact affected by the PSF of the analyzer crystal (see chapter 2, section 2.5.4), which is placed between the sample and the detector. The value of the FWHM of the analyzer PSF projected onto the detector is on the order of $2p \cdot \sin\theta$, where p is the crystal extinction depth and θ is the angle between the incident beam and the analyzer. For a photon energy of 26 keV and for the Si(333) reflection, $2p \cdot \sin\theta$ is equal to 8.06 µm (XOP, http://www.esrf.fr/computing/scientific/dabax/). The refraction profiles computed in ABI and GIFM for the two nylon wires agree very well with the simulated profiles. In the case of the groove, instead, the agreement is good except at the edges. This can be explained by the fact that the modeling of the grooves as parts of cylinders is only a rough estimation of their real shape. The results of figure 7.14(c) suggest that the refraction angles are overestimated by the adopted schematization.

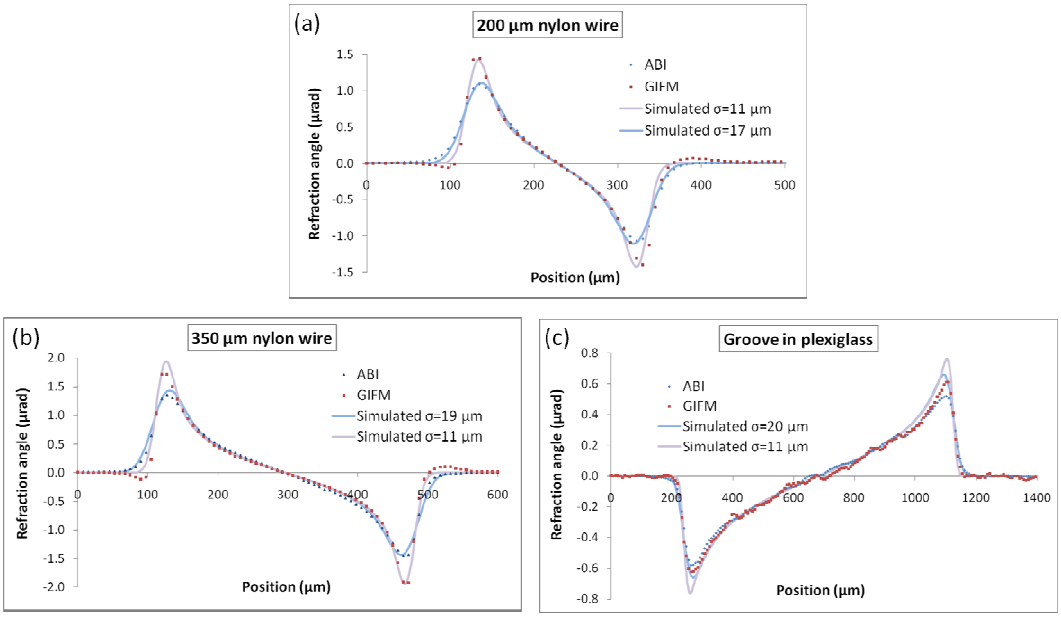

Fig. 7.14. Refraction angle profiles computed in the ABI and GIFM techniques by using respectively the GCF algorithm and the phase stepping method: (a) 200 µm nylon wire, (b) 350 µm nylon wire, (c) small groove in plexiglass. Simulated refraction profiles, calculated assuming different spatial resolutions, are also reported (see text for details).

The FOM values for the refraction signal in the three objects was also computed, in the same way as for the raw images, by considering regions of 30 pixels in the peak. The obtained FOM

values for ABI are 2.6-2.9 times higher than the corresponding values in GIFM. These results are similar to those obtained for the unprocessed ABI and GIFM images (figures 7.7 and 7.9).

Finally, phase profiles were obtained by integrating the refraction angle profiles, in the case of the ABI and GIFM techniques, and directly from the phase image for PBI. The results are plotted in figures 7.15(a,b,c), respectively for the 200 µm wire, the 350 µm wire and the groove. The theoretical profiles and the corresponding uncertainties at the centre of the different objects are also reported. The uncertainties on theoretical phase values have been calculated by estimating an uncertainty on the objects thickness of 5% for the wires and of 10% for the groove. The difference in the two values accounts for the fact that it is difficult to measure with good accuracy the depth of the small groove.

The phase profiles obtained with the different techniques generally agree well with the theoretical predictions. The ABI values are slightly larger than the GIFM for all the different objects, which suggests some small deterministic errors for one of the two techniques or both. It is not possible to state which of the three techniques provides the highest accuracy in the calculation of the phase, since the profiles are close to each other and the uncertainty on the theoretical values is relatively large.

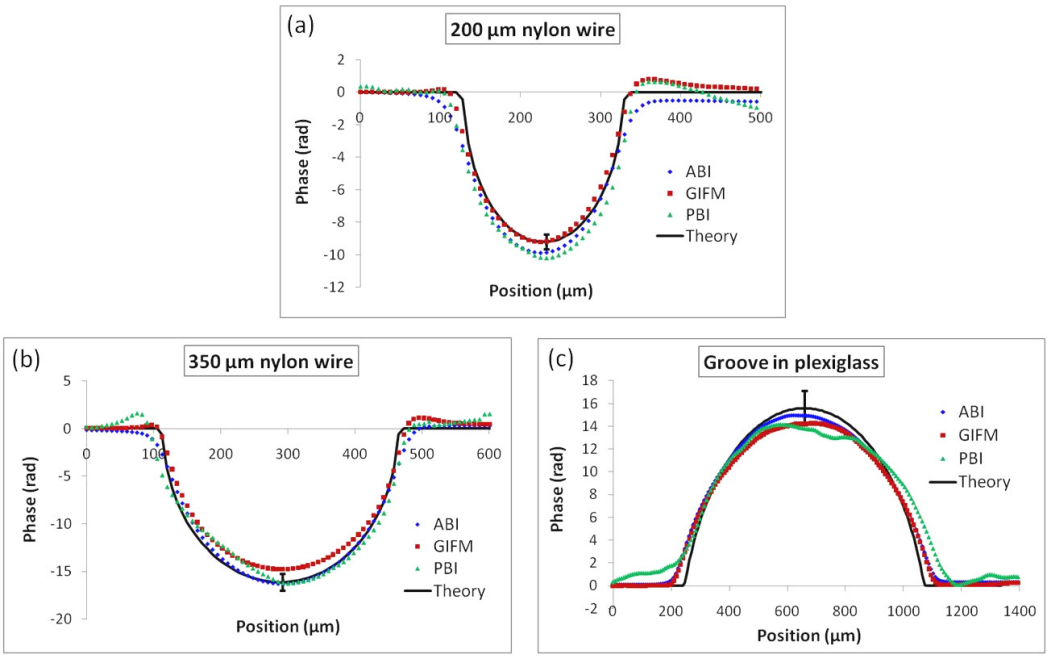

Fig. 7.15. Phase profiles computed in the ABI, GIFM and PBI techniques for three different objects: (a) 200 µm nylon wire, (b) 350 µm nylon wire, (c) small groove in plexiglass. Theoretical phase profiles are also reported. See text for details about the profiles calculation.

7.5 Conclusions

We have compared the signals provided by the PBI, ABI and GIFM techniques both theoretically, by considering the equations for the intensity incident on the detector in the different cases, and experimentally by analyzing the images of three test samples.

Analytical expressions for the signal-to-noise ratio (SNR) and the figure of merit (FOM) of the phase contrast signal have been obtained, under the assumptions that the photon counts on the detector can be described by a Poisson statistics, that the refraction angles for ABI and GIFM are small, and that the object is slowly varying and the propagation distance small for PBI. The derived expressions relate in a simple way the SNR and FOM values to quantities pertaining to the object itself (the refraction angle in ABI and GIFM, the Laplacian of the phase in PBI) and to quantities depending on the experimental setup and acquisition conditions. Key imaging parameters are the sample-to-detector distance for PBI, the second grating period, the fractional Talbot distance and the visibility for GIFM, and the rocking curve width for ABI. The spatial coherence of the incident beam and the PSF of the detector also affect the recorded signal.

We have shown that the SNR and FOM values for an edge are proportional, in the case of PBI, to the difference between the Laplacian of the phase at the two sides of the edge. In ABI and GIFM they are proportional, at positions of the analyzer on the slopes of the rocking curve (for ABI) and at positions of the gratings on the slopes of the intensity curve G (for GIFM) to the refraction angle itself. At working positions respectively at the top of the RC (for ABI) and at the top or bottom of the intensity curve G (for GIFM), the SNR and FOM values are instead linear with the square of the refraction angle, at a first approximation.

Important analogies therefore exist between the signal in the ABI and GIFM techniques. Besides the fact that their sensitivity is unidirectional, while PBI is sensitive to both directions in the detector plane, an important difference compared to PBI is represented by the fact that this technique measures a different quantity (the Laplacian of the phase) compared to ABI and GIFM (the refraction angle). This implies that these techniques are sensitive in a different way to different objects, and in particular to different object (spatial) frequencies. PBI is expected to have maximum sensitivity for higher frequencies than ABI and GIFM do.

We have also shown that the sensitivities of the three here-considered techniques present a different dependence upon the energy. The SNR, in fact, is inversely proportional to the square of the energy ($SNR \propto 1/E^2$) in PBI and GIFM, while it is inversely proportional to the energy ($SNR \propto 1/E$) in ABI. This means that ABI is particularly favoured with respect to the other techniques if high energies are considered.

The SNR and FOM values for the absorption signal are different from those that would be obtained in conventional imaging. The attenuation of the beam between the sample and the detector introduced by the gratings (in GIFM) or by the analyzer crystal (in ABI), in fact, reduces the number of counts on the detector and accordingly the SNR and FOM values. On the other side, the complete Compton scattering rejection in ABI and the partial Compton scattering rejection in

GIFM and PBI (increasing for large sample-detector distances) eliminate or reduce a source of noise typical of conventional absorption imaging.

PB images of two horizontal nylon wires of different diameter and of a small groove in a plexiglass phantom have been acquired at three different propagation distances. AB images of the same objects have been obtained at five positions of the analyzer along the rocking curve, while GIFM images have been acquired at nine relative positions of the two gratings along one fringe period. The FOM values for the refraction signal have been calculated from the experimental images. The results agree well with the theoretical predictions. In the considered experimental conditions, the ABI technique provides the largest sensitivity, while the PBI technique the lowest.

A vertical nylon wire has also been imaged. The ABI and GIFM refraction signals are absent from the recorded images because the wires edges are parallel to the sensitivity direction for both techniques. The propagation signal, instead, due to the finite sample-detector distance, is very similar to that obtained in PBI, which shows that it is not affected by the presence of the gratings and of the analyzer and thus can be used, by deliberately increasing the sample-detector distance, as a complement to the refraction signal recorded in the other direction.

Extraction algorithms have been applied to the experimental images acquired with the different techniques: the GCF algorithm for ABI, the phase stepping method for GIFM, the mixed CTF-TIE algorithm, with the use of the homogeneity prior regularization, for PBI. The computed images have been analyzed and the results discussed. Each technique is characterized by peculiar features concerning the quantities that can be extracted, the amplitude of the signal, the noise and the artefacts potentially affecting the images. Notably, in PBI the phase map is directly obtained while the scattering information is not extracted; in the considered case the calculation of an absorption image is not needed since the experimental image acquired with a propagation distance of 7 cm can be practically considered as an image of pure absorption. In ABI and GIFM the absorption, scattering and refraction images are extracted, and from this last image the phase map can be computed.

The refraction profiles obtained in ABI and GIFM images have been compared. The results show that in ABI the resolution is limited by the PSF of the analyzer crystal, which is placed between the sample and the detector. In GIFM, instead, the resolution is limited, in the present configuration, by the used detector. It is noteworthy to remark that, if a detector with higher resolution were used, the resolution of GIFM images would be anyway ultimately limited to one period of the second grating. Note, however, that in both ABI and GIFM these limitations can be overcome and higher spatial resolutions achieved by using magnification geometries. These can be obtained with the use of an asymmetric analyzer crystal in ABI, and with a source-to-sample distance of the order of the sample-to-detector distance ($L \sim d$) in GIFM.

The calculated phase profiles are all in good agreement with those predicted theoretically. All the methods, in these experimental conditions and with the considered extraction algorithms, are therefore able to provide accurate quantitative results.

References and links

P. Coan, E. Pagot, S. Fiedler, P. Cloetens, J. Baruchel, and A. Bravin, "Phase-contrast X-ray imaging combining free space propagation and Bragg diffraction", Journal of Synchrotron Radiation **12**, 241-245 (2005).

P. Coan, A. Peterzol, S. Fiedler, C. Ponchut, J. C. Labiche, and A. Bravin, "Evaluation of imaging performance of a taper optics CCD 'FReLoN' camera designed for medical imaging", J. Synchrotron Radiat. **13** (13) 260-270 (2006).

M. Langer, P. Cloetens, and F. Peyrin, "Regularization of Phase Retrieval With Phase-Attenuation Duality Prior for 3-D Holotomography", Ieee Transactions on Image Processing **19**, 2428-2436 (2010).

Y. I. Nesterets, T. Gureyev, and S. Wilkins, "Polychromaticity in the combined propagation-based/analyser-based phase-contrast imaging", Journal of Physics D: Applied Physics **38** (24), 4259-4271 (2005).

E. Pagot, S. Fiedler, P. Cloetens, A. Bravin, P. Coan, K. Fezzaa, J. Baruchel, and J. Härtwig, "Quantitative comparison between two-phase contrast techniques: Diffraction Enhanced Imaging and Phase Propagation Imaging", Phys. Med. Biol. **50** (4), 709-724 (2005).

K. M. Pavlov, T. E. Gureyev, D. Paganin, Y. I. Nesterets, M. J. Morgan, and R. A. Lewis, "Linear systems with slowly varying transfer functions and their application to x-ray phase-contrast imaging", J. Phys. D: Appl. Phys. **37** (19), 2746–2750 (2004).

K. M. Pavlov, T. E. Gureyev, D. Paganin, Y. I. Nesterets, M. J. Kitchen, K. K. W. Siu, J. E. Gillam, K. Uesugi, Y. Yagi, M. J. Morgan, and R. A. Lewis, "Unification of analyser-based and propagation-based X-ray phase-contrast imaging", Nucl. Instr. Meth. A **548** (1-2), 163-168 (2005).

F. Pfeiffer, T. Weitkamp, O. Bunk, and C. David, "Phase retrieval and differential phase-contrast imaging with low-brilliance X-ray sources", Nature Physics **2** (4), 258-261 (2006).

S. Webb, "The physics of medical imaging", F. Mould, ed. (Iop, Avon, 1988).

Conclusions

In this work, theoretical and experimental aspects of three phase-contrast imaging techniques, propagation-based imaging (PBI), analyzer-based imaging (ABI) and grating interferometry (GIFM), have been studied with the aim of evaluating their applicability in medical diagnostics.

The extraction of quantitative sample information in the analyzer-based imaging (ABI) technique has been considered first (chapters 4 and 5). The contrast in the AB images arises from the superposition of different physical contributions, related in particular to the sample absorption, refraction and scattering properties. The application of quantitative extraction algorithms for separating these effects may therefore enable a better image interpretation and to highlight particular object features otherwise difficult to visualize. Furthermore, accurate quantitative values may be very helpful for a precise characterization of the sample.

Among the several extraction algorithms proposed in the literature, five were chosen based on the following criteria: 1) the algorithms based on the geometrical optics, and among them, 2) the most used and cited in the literature. The geometrical optics was considered because under this approach a) a pixel-by-pixel relationship exists between the absorption, refraction and scattering properties in the object plane and the intensity recorded on the detector, and b) only the knowledge of the rocking curve (RC), which can be easily measured, is needed.

The validity conditions of the different algorithms were analyzed, and these were then applied to planar images of phantoms providing variable amounts of absorption, refraction and scattering (chapter 4). Nylon wires and a plexiglass grooves phantom (characterized by large refraction angles) were imaged superimposed to increasing layers of paper (providing different amounts of scattering). The obtained results were compared with the theoretical values computed by considering the geometry and composition of the phantoms. The agreement of the extracted absorption values with theory is good for all the considered algorithms, apart from the artefacts that can be observed at the objects edges, where the refraction angles are large. These are attributed to the violation of the validity conditions for the geometrical optics approximation, due to the fact that the refraction angles and their spatial variations are very large. Among the considered algorithms, only G-DEI, MIR and GCF allow separating the ultrasmall angle X-ray scattering (USAXS) contribution. The extracted signal is strong in the regions where the paper layers are present (i.e. where the amount of scattering is important) and also at the objects edges, since at these positions the refraction angles are rapidly varying and one single image pixel, due to its finite size, can record X-rays refracted at relatively different angles. As foreseen by analyzing the validity conditions of the G-DEI and MIR methods, when the scattering component is considerable the extracted images show a saturation effect that is instead not visible in GCF.

The comparison with the theory of the phase profiles across the nylon wires and the grooves phantom (calculated by integrating the corresponding extracted refraction profiles) indicates that

all the algorithms are able to provide accurate results when the refraction and scattering angles are small, while big differences are found when these angles are large. **In particular, the refraction angles tend to be underestimated**, because the validity conditions of the extraction algorithms may be violated in these conditions. The DEI method, for example, shows the worst agreement with theory because the approximations upon which it is based are valid only if the refraction angles are small and if scattering is negligible. GCF is the only algorithm that maintains a good agreement with the theory in all the considered conditions.

The analysis and the comparison of the different algorithms, under variable conditions of refraction and scattering, **clearly identify the GCF method as the one having the best agreement with the theory.** The main drawback of this method, however, is represented by the large required computation times, about 10 hours for a $10^3 \times 10^3$ pixels^2 image compared to few seconds for all the other methods.

The application of three methods for the calculation of the phase map from the refraction angle image has been investigated. The streak artefacts arising in the "pure integration" method can be reduced by the constrained least squares (CLS) and the "averaged integration" methods (the latter was proposed within this Thesis). **The calculated images show that the high spatial frequencies are best preserved by the CLS method, while the most accurate quantitative results are provided by the "averaged integration" method.**

The extraction algorithms were also applied to the images of a human bone-cartilage cylinder. Results indicate that the separation of the **absorption, refraction and scattering images may help in highlighting different features of the sample**. The refraction angle values extracted with the different algorithms do not differ substantially in the case of cartilage (even if the values are slightly underestimated in DEI) since the refraction angles are small. Instead, big differences arise for bone since the refraction angles are much larger than the full width at half maximum (FWHM) of the rocking curve. In agreement with the results obtained for phantoms, the refraction values are heavily underestimated in this case by the DEI and MIR methods.

Since the extracted projection images can be expressed in the form of line integrals, the same mathematical algorithms can be applied in combination with computed tomography (chapter 5). The three-dimensional maps of the object linear attenuation coefficient, of the vertical gradient of the refractive index decrement and of the second central moment of the object local angular response function can be obtained respectively from the absorption, refraction and USAXS angular projection images. In order to reach reasonable computation times, **a parallelization of the GCF method was implemented** by using Condor® **on the ESRF computers cluster**. The results obtained on plastics phantoms are in agreement with those obtained in the planar mode. All algorithms can provide accurate estimations of the linear attenuation coefficient, while big differences are found for the refractive index decrement when the considered refraction angles are large. **The GCF algorithm, as found in planar mode, shows the best agreement with theory**.

The same algorithms were also applied to CT images of a human bone-cartilage cylinder. The obtained images are extremely useful for depicting the structure of the bone and cartilage tissues. The bone trabecular meshwork is very well visualized in the absorption images, since bone is characterized by considerable absorption. The contrast in cartilage, instead, is particularly enhanced in the refraction images: not only the cartilage external edges are very well visible, but also the cartilage cells (chondrocytes) and groups of cells (chondrons) are clearly depicted. From these images, the refractive index decrements for the cartilage matrix and for the cartilage cells were computed. The first value is in very good agreement with that expected by considering the average elemental composition of cartilage; the second cannot be compared to a theoretical value because the composition of chondrocytes is not tabulated. **To our knowledge, this is the first time that these parameters characteristic of the cartilage tissue were calculated in the X-rays energy range.** This quantitative analysis of the cartilage properties may prove useful for improving the characterization of healthy and osteoarthritic cartilage tissues.

A semi-quantitative method for CT reconstruction requiring only one set of angular projections, acquired with the analyzer set in a fixed position, has also been demonstrated. Absorption and refraction properties cannot be separated under this approach: the reconstructed values, instead, are expressed by a linear combination of the linear attenuation coefficient and of the refractive index decrement. The validity conditions for the applicability of this method are best satisfied if the refraction and scattering angles are small, and if the analyzer crystal is positioned at one of the two slopes of its RC. Results obtained for two biological samples, a bone-cartilage cylinder and a breast mastectomy with a ductal carcinoma, show that, even if absorption and refraction information is not separated, the tissues structure is well depicted: this is very important for the early detection of diseases affecting these tissues, like for instance osteoarthritis and breast malignancies respectively. Due to the possibility of reducing the duration of the object scan, this method may prove very useful for many applications, like in in-vivo imaging, requiring short acquisition times.

In chapter 6, by exploiting the similarity between the signal in the ABI and GIFM techniques, a new acquisition and processing method for computed tomography was proposed for the GIFM modality. This procedure does not allow obtaining separate maps of the absorption and refraction introduced by the sample: the reconstructed values are given by a linear combination of the linear attenuation coefficient and of the refractive index decrement. Under this approach, the sample axial slices are computed by applying standard tomographic reconstruction methods like the filtered backprojection (FBP) algorithm directly to the angular projections acquired for a fixed position of the two gratings. The application of this method is mathematically correct if the refraction and scattering angles are small, so that the intensity function G can be accurately (locally) approximated by a straight line. The best results are expected to be obtained when the working point is at one of the two (positive or negative) slopes of the intensity function G, where

the second derivative is equal to zero (in order for the linear approximation to be more accurate) and the first derivative is maximized (so that the sensitivity to refraction is highest).

The reconstructed images of a bone-cartilage sample indicate that a good image quality, enabling a precise visualization of the sample tissues, can be obtained even if the absorption and refraction contributions are not separated. The two signals are somewhat complementary: the absorption signal is more observable in the internal region of the different sample structures, while refraction is large at the edges, where the value of the refractive index decrement varies. The advantages of this method derive from the fact that the gratings can be kept fixed during the acquisition, thus simplifying the imaging procedure, and that the times required for the object scan can be considerably reduced. **This can be an extremely important feature for in-vivo applications of grating interferometry, because shorter acquisition times can result in decreased motion artefacts and therefore in improved image quality.** The experimental results also suggest that this method may be less sensitive to noise than the commonly used phase stepping method, but further investigations are needed to clarify this point.

In chapter 7 a theoretical and experimental comparison of the PBI, ABI and GIFM techniques has been presented. **Analytical formulas for the signal-to-noise ratio (SNR) and for the figure of merit (FOM) for the refraction signal have been obtained from the expressions for the intensity incident on the detector in the different techniques**. The derived expressions can be simplified if it is assumed, in ABI and GIFM, that the refraction angles are small, and, in PBI, that the phase is a slowly varying function of the spatial coordinates and that the propagation distance is small. **The similarities of the ABI and GIFM techniques are evident**. Both techniques are sensitive to the phase variations only in one direction, perpendicular to the grating lines in GIFM and parallel to the diffraction plane in ABI, unlike the PBI technique, which is sensitive to phase changes in both directions. Furthermore, the SNR and FOM are at a first approximation proportional to the refraction angle, if the analyzer crystal is placed at one of the two slopes of the RC in ABI, and if the two gratings are set at a position corresponding to one of the two slopes of the intensity function G (see sections 7.2.3 and 7.2.4). They are instead at a first approximation proportional to the squared value of the refraction angle if the working point in ABI is set at the top position of the RC and if the working point in GIFM is set at the top or bottom positions of G. In PBI, instead, the signal is proportional at a first approximation to the phase Laplacian. **The nature of the detectable signal in PBI and in the ABI and GIFM techniques is therefore different**. This implies that these techniques are sensitive in a different way to different details, and in particular to the various spatial frequencies. PBI is expected to have maximum sensitivity for higher frequencies than ABI and GIFM do.

The theoretical FOM values for the refraction signal in the ABI and GIFM techniques can also be directly compared: the FOM has been calculated to be 9 times larger in ABI than in GIFM in the considered experimental configuration and for a X-ray energy of 26 keV. However, since its values are strongly dependent on the FWHM of the rocking curve in ABI and on the period of the

second grating and on the fractional Talbot distance in GIFM, the reported value can be very different in other experimental setups. The sensitivity is also dependent on the energy. In particular, since the RC FWHM in ABI is a decreasing function of the energy, **the sensitivity is expected to be sensibly larger in ABI than in GIFM when high energies are considered**.

Expressions for the SNR and FOM for the absorption signal in the three considered techniques have also been derived. Their values are not the same as in conventional absorption imaging for two main reasons: 1) on one side, the intensity incident on the detector in the ABI and GIFM techniques is reduced due to the presence, between the sample and the detector, respectively of the analyzer crystal and of the two gratings; therefore, since the number of detected photons is lower, the SNR and FOM are expected to be decreased; 2) on the other side, the Compton and small-angle scattered X-rays are completely eliminated in ABI and sensibly reduced in PBI and GIFM: the image quality is improved because of the reduction of the blurring due to scattering typical of conventional absorption imaging.

The experimental images obtained for plastics phantoms, two nylon wires and a groove in a plexiglass parallelepiped, are in agreement with the theoretical estimations. **The FOM values are largest in ABI and smallest in PBI**. Furthermore, in PBI these values are proportional to the propagation distance (approximation valid only for large Fresnel numbers N_F), while in ABI and GIFM they are largest when the working point is chosen respectively at the slopes of the RC and at the slopes of G.

The application of chosen extraction algorithms to the PBI, ABI and GIFM images demonstrates that all the three techniques can provide quantitatively accurate results when these algorithms are considered. However, it is evident that the experimental ABI results are affected by degradation in resolution that is due to the finite point spread function (PSF) of the analyzer crystal.

Summarizing, a detailed study on the accuracy of quantitative extraction algorithms in the ABI technique, in different experimental conditions and in both planar and tomographic modes, has been carried out. The ability of these algorithms in improving the visualization of biological tissues characterized by a complex geometry has been also assessed, and the possibility of extracting accurate quantitative sample information, for instance the sample linear attenuation and refractive index decrement, has been demonstrated. Concerning this last point, an interesting topic for future research may consist in investigating a possible correlation of these values with normal and pathological tissue conditions. Progresses in this direction may represent an important step forward for an easier image interpretation and, therefore, a more precise diagnosis. It is noteworthy to remark that this issue is not limited to the ABI technique but encompasses all the here-considered phase-contrast imaging techniques, which may be used for quantitatively characterizing the sample.

A new method for acquiring and reconstructing CT images in the GIFM technique has been proposed, which presents the advantages of simplifying the imaging procedure and of reducing the acquisition times. The considered method has been demonstrated to be able to provide, at least for the samples examined within this Thesis, an image quality comparable to that obtained with the commonly used phase stepping method, despite the fact that absorption and refraction contributions are not separated. Results suggest that, for a same dose delivered to the sample, the SNR for the proposed method may be higher than that for the phase stepping method. However, further investigations and experimental proofs are still needed. It would also be interesting to test the applicability of this new method to samples with different composition and structural characteristics, like breast for instance.

The nature and the amplitude of the signals in the PBI, ABI and GIFM techniques have been investigated in detail, both theoretically and experimentally. The analysis has particularly focused on crucial parameters like the achievable signal-to-noise ratio, figure of merit and spatial resolution. The application of the extraction algorithms in the different cases has been also studied. We believe that the obtained results concerning the different signals provided by the three here considered techniques may be useful for choosing the most adapted technique for a given application. We therefore hope that this work may represent an important step forward for a deeper understanding of these phase-contrast imaging techniques and for their application in the biomedical field.

Conclusions en français

Dans ce travail, certains aspects théoriques et expérimentaux de trois techniques de contraste de phase, la propagation-based imaging (PBI), la analyzer-based imaging (ABI) et la grating interferometry (GIFM), ont été étudiés dans le but d'évaluer leur applicabilité pour l'aide au diagnostic médical.

L'extraction d'informations quantitatives sur l'échantillon avec la technique analyzer-based imaging (ABI) a tout d'abord été considérée (chapitres 4 et 5). Le contraste dans les images obtenues par ABI est déterminé par la superposition de différents effets physiques, liés en particulier aux propriétés d'absorption, de réfraction et de diffusion de l'échantillon. L'application d'algorithmes d'extraction pour séparer ces effets peut donc favoriser une meilleure interpretation de l'image et permettre de mettre en évidence certaines charactéristiques de l'objet qui seraient autrement difficiles à visualiser. De plus, l'extraction de valeurs quantitatives précises peut être très utile pour une charactérization détaillée de l'objet.

Parmi les nombreux algorithmes d'extraction qui ont été proposés dans la littérature, cinq ont été choisis en se basant sur les critères suivants : 1) les algorithmes basés sur l'optique géométrique et, parmi eux, 2) les plus utilisés et cités dans la littérature. L'optique géométrique a été considérée puisque dans cette approximation a) une relation pixel par pixel existe entre les propriétés d'absorption, de réfraction et de diffusion de l'échantillon, et l'intensité enregistrée sur le détecteur, et puisque b) seulement la connaissance de la rocking curve (RC), qui peut être facilement mesurée, est requise.

Les conditions de validité des différents algorithmes ont été analysées, et ceux-ci ont été appliqués aux images planaires de fantômes donnant lieu à des quantités variables d'absorption, de réfraction et de diffusion (chapitre 4). Des fils en nylon et un fantôme de plexiglass contenant des sillons (caractérisés par de grands angles de réfraction) ont été imagés superposés à des couches de papier de différente épaisseur (donnant lieu à des quantités différentes de diffusion). Les résultats obtenus ont été comparés avec ceux théoriques calculés en considérant la géométrie et la composition des fantômes. L'accord entre les valeurs d'absorption extraites et la théorie est bon pour tous les algorithmes considérés, mis à part les artéfacts que l'on peut observer aux bords des objets, où les angles de réfraction sont grands. Ces artéfacts sont attribués à la violation des conditions de validité de l'approximation de l'optique géométrique, due au fait que dans ce cas les angles de réfraction et leurs variations spatiales sont très grands. Parmi les algorithmes considérés, seulement G-DEI, MIR et GCF permettent de séparer la contribution de la diffusion aux très petits angles (USAXS). Le signal extrait est fort dans les régions où les couches de papier sont présentes (c'est-à-dire, où la quantité de diffusion est importante) mais aussi aux bords des objets. En effet, dans ces positions les angles de réfraction varient rapidement et un seul pixel de l'image, à cause de ses dimensions finies, peut enregistrer des rayons X refractés à des angles relativement

différents. Comme prévu en analysant les conditions de validité des méthodes G-DEI et MIR, quand la composante de diffusion est considérable les images obtenues montrent un effet de saturation qui n'est pas visible avec le GCF.

La comparaison des profils de phase à travers les différents fantômes (calculés en intégrant les profils de réfraction correspondants) avec la théorie indique que tous les algorithmes sont capables de fournir des résultats corrects quand les angles de réfraction et diffusion sont petits, alors que d'importantes différences sont obtenues quand ces angles sont grands. **En particulier, les angles de réfraction ont tendence à être sousestimés**, car les conditions de validité des algorithmes d'extraction peuvent être violées dans ces conditions. La méthode DEI, par exemple, présente le pire accord avec la théorie. En effet, les approximations sur lesquelles elle est basée ne sont valables que pour des angles de réfraction petits et pour une diffusion négligeable. GCF est le seul algorithme qui garde un bon accord avec la théorie dans toutes les conditions considérées.

L'analyse et la comparaison des différent algorithmes, dans des conditions variables de réfraction et diffusion, **identifie clairement la méthode GCF comme celle qui présente le meilleur accord avec la théorie**. Cependant, le principal désavantage de cette méthode est sa lenteur d'exécution, environ dix heures pour une image de $10^3 \times 10^3$ pixels^2, comparé à quelques secondes pour toutes les autres méthodes.

L'application de trois méthodes pour le calcul de l'image de phase à partir de l'image de réfraction est examinée. Les artéfacts linéaires qui surgissent dans la méthode de simple intégration peuvent être réduits par la méthode utlisant une estimation aux moindres carrés (la méthode CLS) et la méthode d'"intégration moyennée" (la dernière a été proposée dans le cadre de cette Thèse). **Les images calculées montrent que la méthode CLS permet la meilleure préservation des hautes fréquences spatiales, alors que la méthode d'"intégration moyennée" fournis les valeurs quantitative les plus correctes.**

Les algorithmes d'extraction ont été aussi appliqués aux images d'un échantillon cylindrique d'os et cartilage humains. Les résultats indiquent que **la séparation des images d'absorption, de réfraction et de diffusion peut aider à mettre en évidence des détails différents de l'échantillon**. Les valeurs des angles de réfraction extraits par les différents algorithmes ne diffèrent pas considérablement dans le cas du cartilage (même si les valeurs sont légèrement sousestimées par la DEI) parce que les angles de réfraction sont petits. Au contraire, de grandes différences surgissent pour l'os, les angles de réfraction étant beaucoup plus grands que la largeur à mi-hauteur de la rocking curve. En accord avec les résultats obtenus pour les fantômes, les valeurs de réfraction sont fortement sousestimées dans ce cas avec les méthodes DEI et MIR.

Etant donné que les projections angulaires extraites peuvent être exprimées sous la forme d'intégrales de ligne, les mêmes algorithmes mathématiques peuvent être appliqués pour la tomographie (chapitre 5). Les distributions tridimensionnelles du coefficient d'atténuation linéaire, du gradient vertical de l'index de réfraction, et du deuxième moment central de la fonction de réponse angulaire locale de l'objet peuvent être obtenues respectivement par les projections

angulaires de l'absorption, de la réfraction et de la diffusion. Afin de rendre acceptables les temps de calcul, **une parallélisation de la méthode GCF a été implémentée** en utilisant Condor ® **sur les ordinateurs du cluster de l'ESRF**. Les résultats obtenus sur des fantômes de plastique sont en accord avec ceux qui trouvés en modalité planaire. Tous les algorithmes peuvent fournir des estimations correctes du coefficient d'atténuation linéaire, alors que de grandes différences sont rencontrées pour l'index de réfraction quand les angles de réfraction considérés sont grands. **L'algorithme GCF, comme dans le cas de la modalité planaire, est celui qui montre le meilleur accord avec la théorie.**

Les mêmes algorithmes ont été aussi appliqués à un échantillon cylindrique d'os et cartilage humains. La structure trabéculaire de l'os est très bien visualisée dans les images d'absorption, puisque l'os est caractérisé par une absorption considérable. Le cartilage, au contraire, est particulièrement mis en évidence dans les images de réfraction : non seulement ses bords externes sont bien visibles, mais aussi les cellules (chondrocytes) et les groupes de cellules (chondrons) apparaissent clairement. A partir de ces images, l'index de réfraction pour la matrice extracellulaire et pour les cellules du cartilage a été calculé. Le premier est en très bon accord avec la valeur théorique calculée en considérant la composition élémentaire moyenne du cartilage ; le deuxième ne peut pas être comparé à une valeur théorique puisque la composition exacte des chondrocytes n'est pas connue. **A notre connaissance, c'est la première fois que ces paramètres caractéristiques du tissu du cartilage ont été calculés dans cette gamme d'énergies des rayons X**. Cette analyse quantitative des propriétés du cartilage peut s'avérer utile pour améliorer la charactérisation du cartilage sain et du cartilage atteint par l'arthrose.

Une méthode semi-quantitative pour la reconstruction tomographique nécessitant seulement une série de projections angulaires, acquises avec le crystal analyzeur placé dans une position fixe, a aussi été démontrée. Les propriétés d'absorption et de réfraction ne peuvent pas être séparées dans cette méthode : les valeurs reconstruites, au contraire, peuvent être exprimées par une combination linéaire du coefficient d'atténuation linéaire et de l'index de réfraction. Les conditions de validité pour l'applicabilité de cette méthode sont satisfaites si les angles de réfraction et de diffusion sont petits, et si le crystal analyseur est positionné à un des deux flancs de sa RC. Les résultats obtenus pour deux échantillons biologiques, un cylindre d'os et de cartilage humains et une mastectomie totale avec un carcinome ductal, montrent que, même si l'absorption et la réfraction ne sont pas séparées, la structure des tissus est très bien visualisée. Ceci est très important pour la détection précoce des pathologies qui peuvent atteindre ces tissus, comme par exemple l'arthrose ou les cancers du sein. Puisqu'elle permet de réduire la durée du scan de l'object, cette méthode peut s'avérer très utile pour de nombreuses applications, comme l'imagerie in-vivo, qui nécessite un temps d'acquisition court.

Dans le chapitre 6, en exploitant les similarités entre le signal dans les techniques ABI et GIFM, une nouvelle méthode d'acquisition et de reconstruction pour la tomographie a été proposée pour la technique GIFM. Cette procédure ne permet pas de séparer les images

d'absorption et de réfraction : les valeurs reconstruites peuvent s'exprimer par une combinaison linéaire du coefficient d'atténuation linéaire et de l'index de réfraction. Dans cette approche, les coupes axiales sont calculées en appliquant des algorithmes de reconstruction standards comme la filtered backprojection (FBP) directement aux projections angulaires acquises à une certaine position fixe des deux réseaux de diffraction. L'application de cette méthode est mathématiquement correcte si les angles de réfraction et de diffusion sont petits, de façon que la fonction d'intensité *G* puisse être correctement approchée (localement) par une ligne. Il est estimé que les meilleurs résultats sont obtenus quand le point de travail est placé à un des deux flancs (positif ou négatif) de la fonction d'intensité G, où la dérivée seconde est égale à zéro (de façon à ce que l'approximation linéaire soit la plus correcte possible) et où la dérivée première est maximisée (de façon que la sensibilité à la réfraction soit la plus haute possible).

Les images reconstruites pour un échantillon d'os et de cartilage ont une bonne qualité et montrent qu'une précise visualisation des tissus de l'échantillon peut être obtenue même si l'absorption et la réfraction ne sont pas séparées. Les deux signaux sont en quelque sorte complémentaires : le signal d'absorption est plus évident dans les régions internes des différentes structures de l'échantillon, alors que la réfraction est importante aux bords (où la valeur de l'index de réfracton varie). Les avantages de cette méthode dérivent du fait que les réseaux de diffraction peuvent être maintenus fixes pendant l'acquisition, ce qui simplifie la procédure d'imagerie, et du fait que les temps requis pour le scan de l'objet peuvent être considérablement réduits. **Cette caractéristique peut être extrêmement importante pour des applications in-vivo de la technique GIFM, puisque des temps d'acquisition plus courts peuvent réduire les artéfacts de mouvement et donc améliorer la qualité de l'image**. Les résultats expérimentaux suggèrent que cette méthode pourrait être moins sensible au bruit par rapport à la méthode du phase stepping, qui est normalement utilisée, mais des études plus approfondies sont nécessaires pout clarifier ce point.

Dans le chapitre 7 une comparaison théorique et expérimentale des techniques PBI, ABI et GIFM a été présentée. **Des formules analytiques pour le rapport signal-sur-bruit (SNR) et la figure de mérite (FOM) pour le signal de réfraction ont été obtenues à partir des expressions de l'intensité incidente sur le détecteur dans les différentes techniques**. Les expressions obtenues peuvent être simplifiées si l'on suppose, en ABI et GIFM, que les angles de réfraction et de diffusion sont petits, et, en PBI, que la phase est une fonction qui varie lentement par rapport aux coordonnées spatiales et que la distance de propagation reste petite. **Les similarités entre les techniques ABI et GIFM sont évidentes**. Les deux techniques sont sensibles aux variations de phase seulement dans une direction, perpendiculaire aux lignes des réseaux de diffraction en GIFM et parallèle au plan de diffraction en ABI (contrairement à la technique PBI, qui est sensible au déphasage dans les deux directions). De plus, le SNR et la FOM sont en première approximation proportionnels à l'angle de réfraction, si le crystal analyseur est placé à un des flancs de la RC en ABI, et si les deux réseaux de diffraction sont placés à une position

correspondante à un des deux flancs de la fonction d'intensité *G* (voir sections 7.2.3 et 7.24). Ils sont au contraire en première approximation proportionnels au carré de l'angle de réfraction si le pic de la RC est considéré en ABI et si le pic ou le fond de *G* sont considérés en GIFM. En PBI, au contraire, le signal est proportionnel en première approximation au Laplacien de la phase. **L'origine du signal en PBI est donc différente de celui obtenu avec ABI et GIFM**. Ceci implique que ces techniques sont sensibles d'une façon différente à des détails différents, en particulier aux fréquences spatiales. On peut donc dire que la PBI présente la sensibilité maximale pour des fréquences plus hautes par rapport à la ABI et à la GIFM.

Les valeurs théoriques de la FOM pour le signal de réfraction dans les techniques ABI et GIFM peuvent être directement comparées : la FOM théorique est 9 fois plus large en ABI qu'en GIFM pour la configuration expérimentale considérée et pour une énergie de 26 keV. Cependant, puisque ses valeurs sont fortement dépendantes de la largeur à mi-hauteur de la RC en ABI et de la période du deuxième réseau de diffraction et de la distance fractionnaire de Talbot en GIFM, les valeurs présentées peuvent être très différentes dans d'autres montages expérimentaux. La sensibilité est aussi dépendante de l'énergie. En particulier, puisque la largeur à mi-hauteur de la RC en ABI est une fonction décroissante de l'énergie, **la sensibilité est estimée considérablement plus grande en ABI qu'en GIFM quand de hautes énergies sont considérées**.

Des expressions pour le SNR et la FOM pour le signal d'absorption dans les trois techniques considérées ont été dérivées. Leurs valeurs sont différentes de l'imagerie conventionnelle par absorption pour deux raisons principale. 1) D'un côté, l'intensité incidente sur le détecteur en ABI et GIFM est réduite à cause de la présence, entre l'échantillon et le détecteur, du crystal analyseur et des réseaux de diffraction respectivement ; ainsi, puisque le nombre de photons détectés est plus bas, le SNR et la FOM sont réduits. 2) De l'autre côté, les rayons X qui ont subi une diffusion Compton ou une diffusion aux petits angles sont complètement éliminés en ABI et considérablement réduits en PBI et GIFM : la qualité de l'image est améliorée à cause de la réduction du floutage, dû à la diffusion, typique de l'imagerie conventionnelle par absorption.

Les images expérimentales obtenues pour des fantômes de plastique, deux fils de nylon et un fantôme de plexiglass contenant des sillons, sont en accord avec les estimations théoriques. **Les plus grandes valeurs de FOM sont celles de la ABI et les plus basses celles de la PBI**. De plus, en PBI ces valeurs sont proportionnelles à la distance de propagation (approximation valide seulement pour des grands nombres de Fresnel N_F), alors qu'en ABI et GIFM les plus grandes valeurs sont obtenues quand des points sur les flancs respectivement de la RC et de *G* sont choisis.

L'application d'algorithmes sélectionnés aux images de PBI, ABI et GIFM démontre que toutes les trois techniques peuvent fournir des résultats quantitativement corrects quand ces algorithmes sont considérés. Cependant, il est évident que les résultats en ABI sont concernés par une dégradation de la résolution qui est dûe à la point spread function (PSF) du crystal analyseur.

En résumé, une étude sur la précision quantitative des algorithmes d'extraction dans la technique ABI, dans différentes conditions expérimentales et dans les modalités planaire et tomographique, a été effectuée. L'abilité de ces algorithmes à améliorer la visualization de tissus biologiques caractérisés par une géométrie complexe a été examinée, et la possibilité d'extraire des informations quantitatives précises sur l'échantillon a été démontrée. Pour ce qui concerne ce dernier point, une perspective intéressante consisterait à l'investigation d'une possible corrélation entre ces valeurs et les conditions normales et pathologiques du tissu. Des progrès en cette direction pourraient représenter un pas important pour une plus facile interprétation de l'image et donc un diagnostic plus précis. Il est important de remarquer que ce sujet n'est pas limité à la technique ABI mais comprend toutes les techniques de contraste de phase considérées ici, qui peuvent être aussi utilisées pour caractériser quantitativement l'échantillon.

Une nouvelle méthode pour acquérir et reconstruire les images tomographiques dans la technique GIFM a été proposée. Elle présente l'avantage de simplifier le scan de l'objet et de réduire les temps d'acquisition. Nous avons démontré que cette méthode est capable de fournir, pour les échantillons examinés dans cette Thèse, une qualité d'image comparable à celle obtenue avec la méthode traditionnellement utilisée du phase stepping, malgré le fait que les effets d'absorption et de réfraction ne soient pas séparés. Les résultats suggèrent que, pour la même dose délivrée à l'échantillon, le SNR pour la méthode proposée soit supérieur à celui de la méthode du phase stepping. Cependant, des investigations et test expérimentaux plus détaillés sont nécessaires. Il serait aussi intéressant de tester l'applicabilité de cette nouvelle méthode sur des échantillons avec une composition et une structure différentes, comme le tissue mammaire par exemple.

L'origine et l'amplitude des signaux dans les techniques de PBI, ABI et GIFM ont été étudiés en détail, théoriquement et expérimentalement. L'analyse s'est concentrée particulièrement sur des paramètres cruciaux comme le rapport signal-sur-bruit, la figure de mérite et la résolution spatiale. L'application des algorithmes d'extraction dans les différents cas a aussi été étudiée. Nous pensons que les résultats obtenus concernant les différents signaux fournis par les trois techniques de contraste de phase considérées peuvent être utiles pour déterminer quelle technique est la plus adaptée à une application donnée. Nous espérons donc que ce travail représente un important pas en avant vers une compréhension plus profonde des techniques de contraste de phase et pour leur application dans le domaine biomédical.

List of the publications produced in the framework of this Thesis

- P.C. Diemoz, P. Coan, I. Zanette, A. Bravin, S. Lang, C. Glaser and T. Weitkamp, "A simplified approach for computed tomography with an X-ray grating interferometer", Optics Express **19**(3), 1691-98 (2011).

- P.C. Diemoz, A. Bravin, C. Glaser and P. Coan, "Comparison of analyzer-based imaging computed tomography extraction algorithms and application to bone-cartilage imaging", Physics in Medicine and Biology **55**(24), 7663-79 (2010).

- P Coan, A. Wagner, A. Bravin, P.C. Diemoz, J. Keyriläinen and J. Mollenhauer, "In-vivo X-ray phase contrast analyzer-based imaging for longitudinal osteoarthritis studies in guinea pigs", Physics in Medicine and Biology **55**(24), 7649-62 (2010).

- P. Coan, F. Bamberg, P.C. Diemoz, A. Bravin, K. Timpert, E. Mutzel, J.G. Raya, S. Adam-Neumair, M.F. Reiser and C. Glaser, "Characterization of osteoarthritic and normal human patella cartilage by computed tomography X-ray phase-contrast imaging: a feasibility study", Investigative Radioloy **45**, 437-444 (2010).

- P.C. Diemoz, P. Coan, C. Glaser and A. Bravin, "Absorption, refraction and scattering in analyzer-based imaging: comparison of different algorithms", Optics Express **18**(4), 3494-3509 (2010).

- P. Coan, P.C. Diemoz, A. Bravin, T. Schlossbauer, M. Reiser, D. Habs, T. Schneider and C. Glaser, "Phase contrast imaging for medical diagnostics: towards clinical application with compact laser-based X-ray sources", World Congress on Medical Physics and Biomedical Engineering **25**(13), 200-203 (2009).